

# Resonant structures for vapor-cell atomic clocks

THÈSE N° 7859 (2017)

PRÉSENTÉE LE 5 OCTOBRE 2017  
À LA FACULTÉ DES SCIENCES ET TECHNIQUES DE L'INGÉNIEUR  
LABORATOIRE D'ÉLECTROMAGNÉTISME ET ANTENNES  
PROGRAMME DOCTORAL EN GÉNIE ÉLECTRIQUE

ÉCOLE POLYTECHNIQUE FÉDÉRALE DE LAUSANNE

POUR L'OBTENTION DU GRADE DE DOCTEUR ÈS SCIENCES

PAR

Anton Evgeniev IVANOV

acceptée sur proposition du jury:

Dr S.-R. Cherkaoui, président du jury  
Prof. A. Skrivervik, directrice de thèse  
Dr L.-G. Benier, rapporteur  
Prof. J. Bartolic, rapporteur  
Prof. F. Rachidi, rapporteur



ÉCOLE POLYTECHNIQUE  
FÉDÉRALE DE LAUSANNE

Suisse  
2017





Посвещавам на моите родители и моите учители



# Abstract

Vapor-cell atomic clocks based on double resonance are high-precision instruments that have strong potential for industrial commercialization. They offer performance which is superior to quartz oscillators and are already employed for synchronization-demanding applications in telecommunication and smart power grid networks. With a volume of up to few liters, these are devices compact enough to qualify for space applications related to global positioning. Moreover, a new generation of high-performance vapor-cell clocks based on Pulsed Optical Pumping scheme (POP) showed performance approaching that of much larger frequency standards.

For the case of the pulsed clock, the magnetic field homogeneity plays a central role in limiting the performance – in order to fully exploit the advantages of the novel POP scheme it is critical to apply a constant (amplitude) field distribution across the atomic sample. The main objective of the thesis is to find and characterize a cavity solution that is appropriate to apply in compact high-performance vapor-cell atomic clocks, and more particularly in the case of the pulsed optically pumped scheme.

In the currently existing solutions a relatively large type of cavity is utilized for which in order to obtain field homogeneity a small fraction of the field is sampled. A major drawback of this approach is the negatively affected compactness. Moreover, such a cavity is more restrictive to the useful volume of the atomic sample, and it is more complicated to stabilize in terms of temperature.

We propose a solution for which we managed to obtain a nearly constant microwave magnetic field distribution along the direction of the optical field with more than 97% of orientation uniformity across the atomic sample. Our approach is to implement a cavity with artificial magnetic conductor boundary conditions in order to take advantage of a beneficial field mode with two zero variation indexes.

Key words: double resonance atomic clocks, high-performance frequency standards, microwave cavities, homogeneous magnetic field distribution, artificial magnetic conductor boundary conditions



# Résumé

Les horloges atomiques à vapeur à double résonance sont des instruments de haute précision qui présentent un fort potentiel de commercialisation industrielle. Ils offrent des performances supérieures aux oscillateurs à quartz et sont déjà utilisées pour des applications exigeantes en synchronisation dans les réseaux de télécommunication et réseaux électriques intelligents. Avec un volume de seulement quelques litres, ce sont des appareils suffisamment compacts pour des applications spatiales liées au positionnement global. De plus, une nouvelle génération d'horloges à vapeur haute performance basées sur le système de pompage optique pulsé (POP) a montré des performances proches de celles de normes de fréquence beaucoup plus larges.

Pour le cas de l'horloge pulsée, l'homogénéité du champ magnétique joue un rôle central dans la limitation de la performance - afin d'exploiter pleinement les avantages du nouveau système POP, il est essentiel d'appliquer une distribution de champ constante (en amplitude) à travers l'échantillon atomique. L'objectif principal de la thèse est de trouver et de caractériser une solution de cavité appropriée à appliquer dans des horloges atomiques à cellules à vapeur compactes à haute performance et plus particulièrement dans le cas du schéma à impulsions optiques.

Dans les solutions actuellement existantes, on utilise des types relativement importants de cavités pour lesquelles, pour obtenir une homogénéité de champ, une petite fraction du champ est échantillonnée. Un inconvénient majeur de cette approche est la réduction de la compacité. En outre, une telle cavité est plus restrictive pour le volume utile de l'échantillon atomique, et il est plus compliqué d'être stable en termes de température.

Nous proposons une solution pour laquelle nous avons réussi à obtenir une distribution de champ magnétique micro-ondes presque constante dans la direction du champ optique avec plus de 97 % d'uniformité d'orientation sur l'échantillon atomique. Notre approche consiste à implémenter une cavité avec des conditions aux limites des conducteurs magnétiques artificiels afin de profiter d'un mode de champ bénéfique avec deux indices de variation zéro.

---

Mots clés : horloges atomiques à double résonance, normes de fréquence de haute performance, cavités hyperfréquences, répartition magnétique homogène, conditions limites des conducteurs magnétiques artificiels

# Acknowledgements

The pursuit of a Ph.D. is a type of endeavor impossible without the constant help and support of numerous people. First and foremost I would like to thank Prof. Anja K. Skrivervik who was my thesis director and the reason to be in *Laboratoire d'Electromagnétisme et Acoustique* (LEMA) in the first place. Her guidance was indispensable both from a scientific and personal point of view. She brought structure to my work and taught me many of the tools needed to become an independent researcher, providing enough creative freedom at the same time.

The multidisciplinary nature of the thesis has been a deeply satisfying aspect of the work and I am especially grateful for the chance to collaborate with the group of Prof. Gaetano Mileti from *Laboratoire Temps-Fréquence*, University of Neuchâtel. A special credit goes to Dr. Christoph Affolderbach with whom we had many fruitful discussions on the atomic side of things.

I would like to express my sincere gratitude to all the jury members for reading my thesis and for their helpful remarks. In particular, I thank Prof. Juraj Bartolić, Dr. Laurent-Guy Bernier and Prof. Farhad Rachidi who kindly accepted to be the thesis referees and who provided me with a very valuable feedback.

My sincere appreciation to Prof. Juan R. Mosig who is a real source of inspiration for all of us, a gifted pedagogue and without question one of the main reasons why LEMA felt so friendly. A special credit goes to Eulalia, who did her magic and found an accommodation even before my arrival in Lausanne. Big thanks to Mercedes and Daniela who always manage to solve all sorts of administrative puzzles with a smile on the face.

LEMA and later *Microwaves and Antennas Group* MAG have provided a liberal, open-minded and cosmopolitan environment which I find essential for the development of the scientist's identity. During my stay in the lab I was lucky to have some of the best office mates one can think of. I spent a lot of pleasant and productive hours with Marc and Eduardo, who very well pretended to like my eccentric humor, with Danelys, who tried her best to make me enjoy salsa and with Miroslav – a truly broad personality. Thankfully Apostolos and Mina were always nearby to set some limits and put me back on track. Thank you all.

## Acknowledgements

---

I would like to express my honest gratitude to one very prominent figure – Dr. Santiago Capdevila. His humble but proactive approach and willingness to help was prolific on so many levels. Always ready for a scientific discussion, with a very broad expertise, Santiago, you were like a magnifying glass for my logical reasoning – thank you for the inspiration.

A very special thank to you Joana, my honest appreciation, that you did not spare time and energy to be there for everyone in the difficult moments. Big thanks to my friend Tomislav, an excellent experimentalist and a very wise man who helped me sober my intrinsic technological optimism. I will always remember the brave philosophical discussions we had with Hamed, the unique sense of humor of Lei, the broad erudition of Baptiste and the positive mindset of Ioannis. I learned so much from Jovanche, from his sincere personality and down to earth approach. I am also very thankful to Michele, for his genuine scientific perspective and for keeping the research spirit high. My deep respect to Eden, who helped me recognize myself in the new environment of Switzerland and who allowed me to rigorously reexamine many of my tenets. I will allays miss his stimulating intelligence and his strong understanding of nature. I am thankful to Maria with whom we had many passionate discussions which helped me agitate my worldview. A special credit to Husein, for his sharp critical thinking and spicy sense of humor. Many thanks to Tatjana and Esteban, for their high ethics and for keeping the fresh spirit of the lab. Thanks also to Pedro, for his scientific curiosity regarding my project, and to Przemyslaw, for the many interesting talks we had in the mountain. And last but not least a big thank to the whole acoustics crew: Gilles, Sami, Etienne, Baptiste, Romain, and Hervé who, among other virtues, also brought a true artistic feeling with their music.

Clearly, my thesis would not have been possible without the general support of many people outside the lab. Thank you Orion for being always so endlessly generous, thank you Bademova for your warm and trustworthy personality. Special thanks to Sotiris, Erio, Ioanis Jr., Philippe, David. A big thank to Marie Dominique, my all time favorite French teacher, who tried her best to teach me not only French but also the virtues of communism.

I will use this moment to also express my gratitude to my teachers that inspired me to start this journey in the first place. I am involved in research because I was very lucky to have Prof. Zhivko Kiss'ovski to mentor my first encounter with the quest of science. It was an absolute pleasure to work with him, his humble attitude and his deep understanding of physics left a very positive influence on me. I will also not forget my physics teacher – Mrs. Violeta Tacheva, who is not only a talented educator but also a genuinely passionate Physicist.

Finally, I am deeply indebted to my family, particularly my parents and my sister, for their unconditional support throughout these years. Without you, it would not have been possible to accomplish any of this work – Благодаря!

*Lausanne, August 2017*

A. I.



# Contents

<b>Abstract (English/Français)</b>	<b>3</b>
<b>Acknowledgements</b>	<b>7</b>
<b>Acronyms and Abbreviations</b>	<b>11</b>
<b>List of Symbols</b>	<b>13</b>
<b>Notation and Conventions</b>	<b>15</b>
<b>1 Introduction and research context</b>	<b>17</b>
1.1 Accuracy and stability of oscillators . . . . .	18
1.2 The atom as a stable frequency source . . . . .	20
1.2.1 A simple three-level system . . . . .	21
1.3 The Rb clock based on double resonance . . . . .	23
1.3.1 Double resonance operation . . . . .	25
1.3.2 The physics package . . . . .	26
1.3.3 Sources of frequency instability related to the cavity . . . . .	28
1.3.4 Design guidelines . . . . .	31
1.3.5 Objectives and outline . . . . .	33
<b>2 Microwave cavities for DR atomic clocks</b>	<b>35</b>
2.1 General cavity theory . . . . .	35
2.1.1 Generalized cross section with translational symmetry . . . . .	36
2.1.2 Modes in a cylindrical cavity with a circular cross section and PEC boundaries . . . . .	40
2.1.3 The standard cylindrical cavity with PEC boundaries . . . . .	40
2.2 General design criteria and characterization . . . . .	48
2.2.1 Definition of the driving fields . . . . .	48
2.2.2 Figures of Merit . . . . .	50
2.3 Figures of merit in the case of the cylindrical cavity loaded with a cylindrical vapor cell . . . . .	53
2.4 Figures of merit – how to find the optimal case . . . . .	57
2.4.1 The case of a standard cylindrical geometry . . . . .	57

## Contents

---

<b>3</b>	<b>Cavities with modified geometry</b>	<b>61</b>
3.1	State-of-the-art development . . . . .	61
3.1.1	Size reduction . . . . .	61
3.1.2	Temperature stability . . . . .	69
3.1.3	A focus on the loop-gap geometry . . . . .	70
3.2	Physics of the loop-gap cavity . . . . .	74
3.2.1	Lumped element point of view . . . . .	74
3.2.2	Field point of view . . . . .	77
3.2.3	Figures of merit in the case of the loop-gap geometry . . . . .	83
3.3	Characterization of the existing cavities . . . . .	86
3.3.1	Field imaging experiment . . . . .	87
3.3.2	Field misalignment . . . . .	92
3.3.3	Double-stem design . . . . .	96
<b>4</b>	<b>Implementation of AMC boundary conditions</b>	<b>105</b>
4.1	Generic cavity with AMC boundaries . . . . .	105
4.2	Loop-gap geometry with AMC . . . . .	121
4.2.1	Implementation of AMC based on planar structures . . . . .	122
4.2.2	Implementation of a variable tuning in the case of the loop-gap geometry . . . . .	128
4.3	Complete cavity design . . . . .	131
4.3.1	Description of the proposed design . . . . .	131
4.3.2	Cavity modes . . . . .	132
4.3.3	Second design proposal – cavity with corrugations . . . . .	137
4.3.4	Feeding mechanism . . . . .	139
4.3.5	Quality of the obtained field . . . . .	140
4.3.6	Design realization and stage of development . . . . .	145
	<b>Summary and conclusions</b>	<b>147</b>
	<b>Prospective work</b>	<b>153</b>
<b>A</b>	<b>Field misalignment</b>	<b>155</b>
<b>B</b>	<b>Vapor cell study. Stability of the resonance condition</b>	<b>159</b>
B.0.1	Variation of the vapor cell dimensions . . . . .	159
B.0.2	Variation of the cell permittivity $\epsilon_d$ . . . . .	161
	<b>Bibliography</b>	<b>174</b>
	<b>Publications</b>	<b>175</b>

# Acronyms and Abbreviations

<b>AHM</b>	Active Hydrogen Maser
<b>AOM</b>	Acousto-optic Modulator
<b>AMC</b>	Artificial Magnetic Conductor
<b>AR</b>	Aspect Ratio
<b>BC</b>	Boundary Condition
<b>CCD</b>	Charge-coupled device
<b>DR</b>	Double Resonance
<b>EF</b>	Efficiency Factor
<b>EPR</b>	Electron Paramagnetic Resonance
<b>EM</b>	Electromagnetic
<b>FOF</b>	Field Orientation Factor
<b>FF</b>	Filling Factor
<b>FEM</b>	Finite Element Method
<b>GPS</b>	Global Positioning System
<b>MRI</b>	Magnetic Resonance Imaging
<b>NMR</b>	Nuclear Magnetic Resonance
<b>OD</b>	Optical Density
<b>PEC</b>	Perfect Electric Conductor
<b>PHM</b>	Passive Hydrogen Maser
<b>PMC</b>	Perfect Magnetic Conductor
<b>PCB</b>	Printed Circuit Board
<b>POP</b>	Pulsed Optical Pumping
<b>RAFS</b>	Rubidium Atomic Frequency Standard

## Acronyms and Abbreviations

---

<b>TL</b>	Transmission Line
<b>TE</b>	Transverse Electric
<b>TM</b>	Transverse Magnetic
<b>TC</b>	Temperature Coefficient
<b>VNA</b>	Vector Network Analyzer

## List of Symbols

$\epsilon_0$	Permittivity of vacuum
$\epsilon_r$	Relative permittivity
$\lambda$	Free space wavelength
$\lambda_g$	Guided wavelength
$\mu_0$	Permeability of vacuum
$\mu_r$	Relative permeability
$\sigma$	Allan deviation
$\tau$	Integration time
$\Omega$	Rabi frequency
$c$	Speed of light in vacuum
$\hbar$	Reduced Planck constant
$f_{\text{cut}}$	Cutoff frequency
$f_{\text{Rb}}$	Frequency of clock transition
$f_{\text{res}}$	Resonance frequency
$k$	Wavenumber of the free space
$k_c$	Transversal propagation constant
$k_z$	Longitudinal propagation constant
$Q$	Quality factor
$S_{ij}$	Scattering parameter associated to input port $i$ and output port $j$
$T$	Temperature
$W_e$	Electric energy
$W_h$	Magnetic energy
$Y_t$	Modal admittance
$Z_t$	Modal impedance



# Notation and Conventions

Everywhere in this document the following conventions are used: Scalar quantities are considered *italic*. Vector quantities are **boldface italic**. The norm of the vector is hence:

$$|\mathbf{A}| = \frac{\mathbf{A}}{\hat{\mathbf{A}}} = \left( \sum_i |A_i|^2 \right)^{1/2}. \quad (1)$$

If  $\alpha(t) = |A_0| \cos(\omega t + \varphi)$  is a real-valued sinusoid, it is considered equal to  $\text{Re}\{Ae^{j\omega t}\}$ , where  $A = \sqrt{2}|A|e^{j\varphi}$  is a phasor,  $|A|$  is the RMS effective value and hence for the time average we obtain:

$$\overline{\alpha^2(t)} = \frac{1}{T} \int_0^T \alpha^2(t) dt = \text{Re}\{AA^*\}, \quad (2)$$

where  $A^*$  is the complex conjugate of  $A$ . The engineering convention  $e^{j\omega t}$  used is compatible to the one applied in physics  $e^{-i\omega t}$  by directly substituting  $j \rightarrow -i$ . The corresponding phasor representation associated to the spatial and time dependence in the standard basis is given by:

$$\mathbf{A}(\mathbf{r}, t) = \sqrt{2} \begin{pmatrix} |A_x| \cos(\omega t - \boldsymbol{\beta} \cdot \mathbf{r} + \varphi_x) \\ |A_y| \cos(\omega t - \boldsymbol{\beta} \cdot \mathbf{r} + \varphi_y) \\ |A_z| \cos(\omega t - \boldsymbol{\beta} \cdot \mathbf{r} + \varphi_z) \end{pmatrix} e^{-\boldsymbol{\alpha} \cdot \mathbf{r}} = \sqrt{2} \text{Re}\{\mathbf{A}(\mathbf{r}) e^{j\omega t}\} = \sqrt{2} \text{Re}\{\mathbf{A} e^{-\boldsymbol{\gamma} \cdot \mathbf{r}} e^{j\omega t}\}, \quad (3)$$

where

$$\mathbf{A} = \begin{pmatrix} |A_x| e^{j\varphi_x} \\ |A_y| e^{j\varphi_y} \\ |A_z| e^{j\varphi_z} \end{pmatrix}, \quad (4)$$

is the vector-phasor,  $\boldsymbol{\gamma} = (\alpha + j\beta)\hat{\mathbf{p}}$  is the propagation constant defined along the direction of propagation  $\hat{\mathbf{p}}$ , assuming the same direction for the attenuation  $\alpha$ .

The units are considered according to the International System of Units (SI); GHz and mm are used in some cases. The angular frequency is denoted by  $\omega$ . An engineering convention ( $f$ ) is chosen for the temporal frequency, in contrast with the notation typically used in physics ( $\nu$ ).





# 1 Introduction and research context

Synchronization and time-keeping have a crucial role in the modern world with ever-increasing number of applications which require frequency stabilities that are beyond the limits of currently-employed quartz oscillators: telecommunication applications, smart grid power networks, global positioning systems, high-frequency trading to name a few. Traditionally, frequency standards based on vapor cells and double resonance are recognized as excellent solutions when high frequency stability needs to be combined with compactness [1]. Their performance is roughly between the large-scale laboratory clocks [2] or commercial Cs clocks [3] and the quartz oscillators widely employed in end user products [4] (see figure 1.1). This type of clocks have been steadily improved in the last decades resulting in commercial products that today reach fractional frequency instability of few  $10^{-15}$  (in terms of Allan deviation), over time scales (integration time)  $\tau \geq 10^4$  s [5]. Recently a new generation of vapor-cell clocks based on Pulsed Optical Pumping (POP) achieved state-of-the-art long-term stability [5] in laboratory conditions. Generally the microwave cavity has an important role in the operation of vapor cell clocks and has been in the focus of serious studies. For the case of the pulsed clock, the magnetic field homogeneity plays a central role in limiting the performance [5, 6, 7] and hence the cavity needs to be engineered accordingly. In this thesis we address the challenges related to the design of what is considered the "heart" of such clocks – the microwave cavity resonator.

In the first, introductory, part of the thesis we provide the basis required in order to put into perspective the goal of this research. First we briefly discuss what defines a good clock. This is followed by a basic introduction to the idea of how atoms can be used as such. We then focus on the particular type of clocks relevant for our application, namely: the rubidium atomic clock based on a vapor cell and Double Resonance (DR). We show the principle of operation, the role of the microwave cavity is introduced, as well as the general components of the clock. This is followed by a short discussion that provides some physical basis needed to understand which cavity aspects are important in our studies. Finally we wrap up by stating the general design guidelines, and the thesis outline.

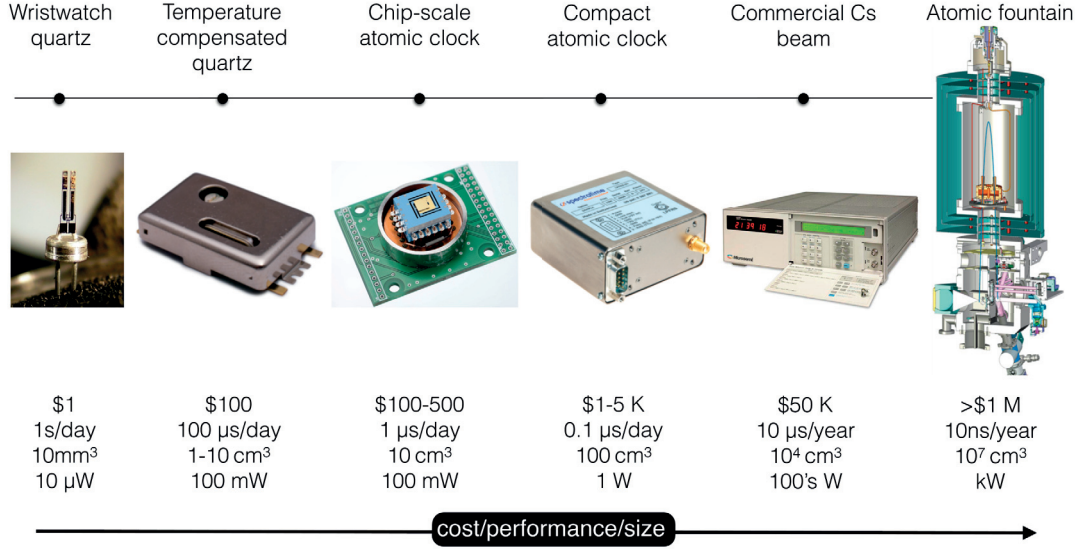


Figure 1.1 – A diagram showing the main variety of the frequency standards that are currently available. In each case the cost, the timing error, the volume and the power needed is shown. Put into perspective, it can be considered that the higher the performance, the larger and the more expensive the final device is.

## 1.1 Accuracy and stability of oscillators

A timekeeping device (oscillator, clock) can be described with its instantaneous frequency at time  $t$  :

$$f(t) = f_0 [1 + \epsilon + y(t)], \quad (1.1)$$

where  $f_0$  is the reference frequency (corresponding to the "true" frequency of the ideal oscillator),  $\epsilon$  is the systematic bias and  $y(t)$  is a term related to statistical fluctuations. The two general concepts that can be used to describe the timekeeping performance of the oscillator are accuracy and stability: the oscillator is *accurate* if  $\epsilon = 0$ , while if  $y(t) = 0$  the oscillator is 100% *stable* and there is no random process affecting the operation. Accuracy describes the difference between the measured and the ideal performance (that would be provided by a reference source with zero uncertainty) and can be defined both in terms of time and frequency:

$$\frac{\Delta t}{\tau} = \frac{t_{\text{measured}} - t_{\text{referent}}}{\tau}, \quad y = \frac{f_{\text{measured}} - f_{\text{referent}}}{f_{\text{referent}}}, \quad (1.2)$$

where  $y$  is referred as fractional frequency. Both descriptions are dimensionless and can be used equivalently to tell us how good an oscillator is in providing the frequency for which it was intended. Stability, on the other hand, is a measure of how well an oscillator can produce frequency (or time) with the same accuracy for a given time interval.

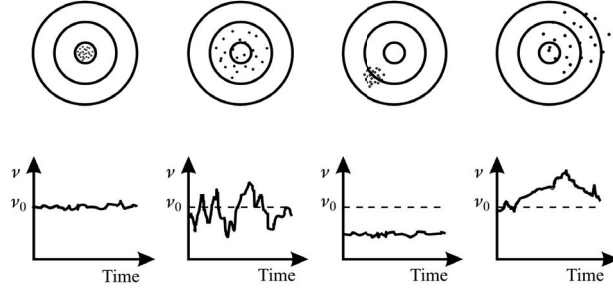


Figure 1.2 – Intuitive illustration of the concepts of stability and accuracy (taken from [8]). The fully accurate and stable device is given by the first panel from the left; a frequency unstable device might be accurate on occasion (second case); one can imagine a device which is not accurate but its frequency does not drift over time (third case); it is also possible to have low accuracy and low stability at the same time (fourth case).

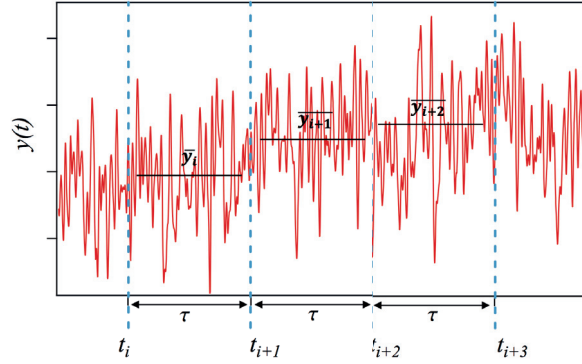


Figure 1.3 – Fluctuations of the frequency in time. The plot corresponds to a typical signal observed in the operation of an atomic clock, where  $y(t)$  is the fractional instantaneous frequency. The result is taken from [9].

In other words stability tells how much the frequency stays the same over the course of time and is hence a measure of the reproducibility. In figure 1.2 we include an instructive visual description which is often used to illustrate these concepts [4].

For the time scales of interest, the frequency output of the atomic standard is obtained as a function of time – figure 1.3. The signal can be divided into equally spaced frequency readings each  $\tau$  long, where  $\tau$  is the averaging time ( $\tau = t_{i+1} - t_i$ ) so that we have:

$$\overline{y}_i = \frac{1}{\tau} \int_{t_i}^{t_{i+1}} y(t) dt, \quad (1.3)$$

which is the average fractional frequency attributed to the  $i$ -th interval. Since the fluctuations of the oscillator frequency are statistical in their nature, this requires a corresponding figure of merit in order to describe the stability performance.

One such a figure of merit, used, is Allan deviation: [10, 11]:

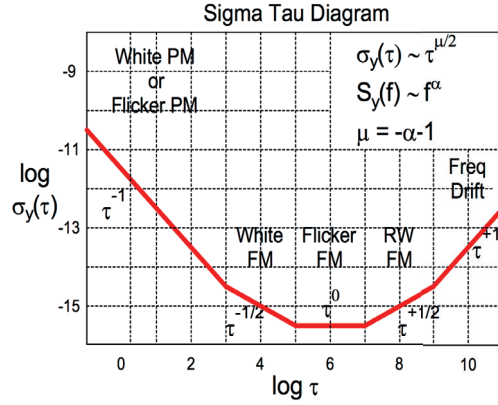
$$\sigma_y(\tau) = \sqrt{\frac{1}{2(N-1)} \sum_{i=1}^{N-1} (\bar{y}_{i+1} - \bar{y}_i)^2}, \quad (1.4)$$

where  $N$  is the number of acquired frequency readings. The main reason of introducing it is due to the fact that the conventional deviation does not converge for increasing sample size  $N$ , but the Allan deviation does converge. The difference with respect to the conventional standard deviation is that the average fractional frequency for a given frequency reading is not compared to the overall average fractional frequency of the oscillator. Instead it is based on the difference between the (averaged) fractional frequency found for two consecutive readings. In this case, due to the dependence on the averaging time, the properties of the noise can be revealed – figure 1.4a.

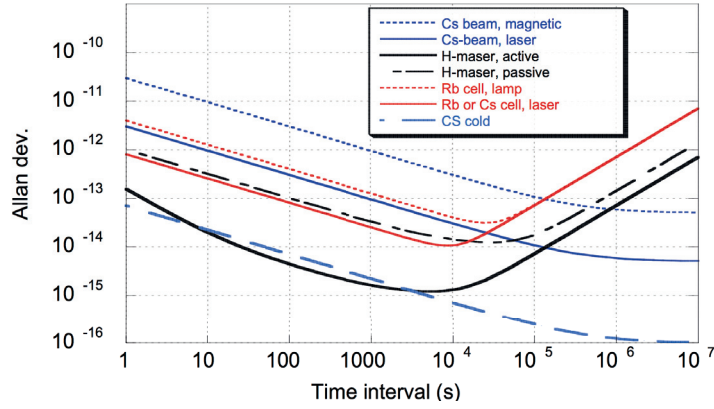
In the case of the vapor-cell atomic clock that we are concerned with, based on the averaging time  $\tau$ , we can consider three separate operational regimes: short term stability (1-100 s), medium term stability (100-1000 s) and long-term stability (1000 s - one day and beyond). In order to put it into perspective, we show (figure 1.4b) what is the performance associated to some real-world atomic clocks. For example, the reported passive hydrogen maser and the Rb vapor cell clock (based on a discharge lamp) are currently used in the Galileo positioning system. It can be seen that there are (non-laboratory) vapor-cell clocks based on laser optical pumping that already perform close to passive masers (considering short and medium term frequency stability). This, their cost and the fact that they are more compact is currently a big incentive for their further improvement.

### 1.2 The atom as a stable frequency source

Imagine we want to realize a hypothetical clock (in other words a frequency standard) that is 100% stable. This could be done if a physical process is found whose frequency is fully-independent from the external world. For example, a high-performance, commercial, temperature stabilized, quartz oscillator is characterized by a frequency stability of about  $1 \times 10^{-12}$  for integration times of 1-10 s [4]. However, temperature susceptibility and high sensitivity to mechanical vibrations limit its performance and make it unsuitable for highly demanding applications (e.g. the on-board requirement of frequency stability for the synchronization of GPS is a limiting factor for the resolution of the coordinate determination [12]). In order to overcome the limitations of the quartz, the system can be locked to a more stable oscillator based on atomic resonance. Instead of using the resonance vibrations of a crystal, an atomic oscillator employs the resonant interaction of individual atoms (or molecules) with external electromagnetic (microwave or/and optical) fields. Among the big variety of such frequency standards the vapor-cell atomic clock based on double resonance (DR) and rubidium atoms is a rather compact and relatively low-cost device which makes it very suitable for applications like GPS. The general idea is to create an atomic oscillator based on an appropriate (not sensitive to external perturbation) magnetic resonance transition from the hyperfine energy levels of alkali atoms (typically Rubidium for the case of DR vapor-cell clocks).



(a) A sigma-tau diagram. Each separate noise process is characterized by a particular slope. The image is taken from [10].



(b) Allan deviation found for different types of frequency standards. Courtesy: CUSO, Programme doctoral en Physique – Printemps 2014, "Atomic clocks: basic principles and applications".

Figure 1.4 – Allan deviation as function of the sampling time.

### 1.2.1 A simple three-level system

Below, we briefly describe what is the general idea behind the double resonance atomic clock operation. In order to simplify, we can first consider the basic (and fictional) case of two-level atom that can be described by its ground and excited states  $|g\rangle$ ,  $|e\rangle$  with their energy levels  $E_g$  and  $E_e$  accordingly (figure 1.5a). For an externally applied electromagnetic field chosen to be resonant to the energy difference between the two levels:  $\omega_{\text{ext.}} = \omega_0 = (E_e - E_g)/\hbar$ , where  $\hbar$  is the reduced Planck constant, an oscillation between the two states of the atom can be observed with frequency (interpreted as the frequency at which the electron population oscillates between the two levels) that depends on the frequency detuning of the driving field and on a frequency  $\Omega$  called "Rabi frequency".

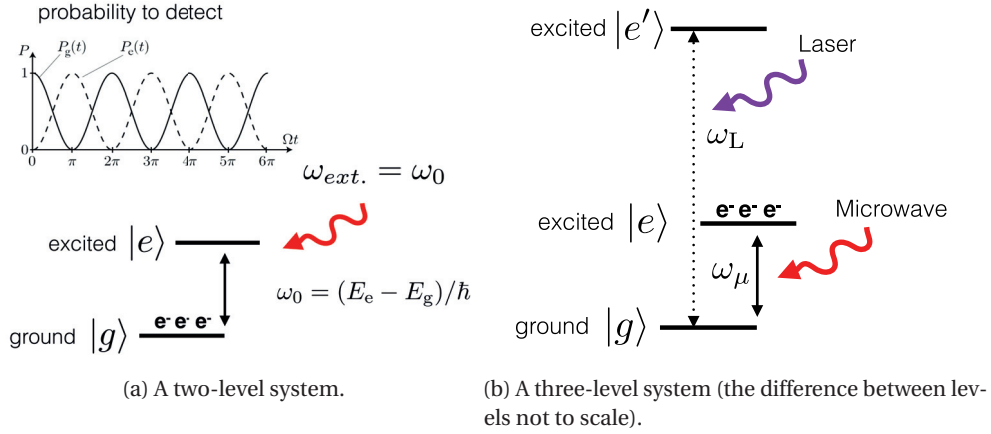


Figure 1.5 – Highly-simplified models of the atomic oscillator. The mechanisms of the EM field-atom interaction to consider are: absorption, stimulated and spontaneous emission. Absorption of EM energy results in electrons populating levels with energy higher than the ground state; stimulated emission is the opposite process resulting in identical but opposite atomic transition (both the absorption and stimulated transitions have identical probability and depended on the interaction time). Spontaneous emission is negligible at microwave frequencies, while it is the dominant effect for the optical transition. In the diagram,  $\omega_\mu$  and  $\omega_L$  are the angular frequencies of the externally applied microwave and optical fields correspondingly.

The latter is proportional to the amplitude of the external field and it can be interpreted as a frequency measure of the transition probability between the 2 states. A pulse  $\Omega t = \pi$  corresponds to a complete population of the excited state, while a pulse  $\Omega t = \pi/2$  corresponds to a superposition between the ground and excited states and hence a probability of 1/2 for the atom to be observed in one of them. In the case of Rb DR clocks this energy difference is in the microwave range. However, because the atoms are not perfectly isolated the atomic resonance cannot be used: the atoms are typically kept in the form of thermal vapor with temperature  $\approx 60$  deg C which results in  $|e\rangle$  and  $|g\rangle$  being equally populated keeping us from detecting the resonance signal whose amplitude scales with the difference of the populations. This is handled by considering an auxiliary level  $|e'\rangle$  resulting in the three-level system shown in figure 1.5b. The corresponding energy  $E_{e'}$  is chosen to be resonant for a field with much higher frequency (e.g. optical field at  $\lambda \approx 780$  nm). If the levels are selected such that the lifetime (the time for which the atom has the electron in the given excited state) for level  $|e\rangle$  is longer than for level  $|e'\rangle$ , continuously applying the optical field (optical pumping) will result in a net population of the  $|e\rangle$  level larger than that of  $|g\rangle$  (a condition known as population inversion). Having the atoms polarized in this way allows us to simultaneously apply the microwave field in order to drive the oscillation between  $|g\rangle$  and  $|e\rangle$  which in turn populates the ground state (by stimulated emission) and leads to absorbance of light – the opacity of the Rb vapor as a function of the microwave frequency is known as a DR signal which can be used as a high stability locking signal for the microwave frequency.

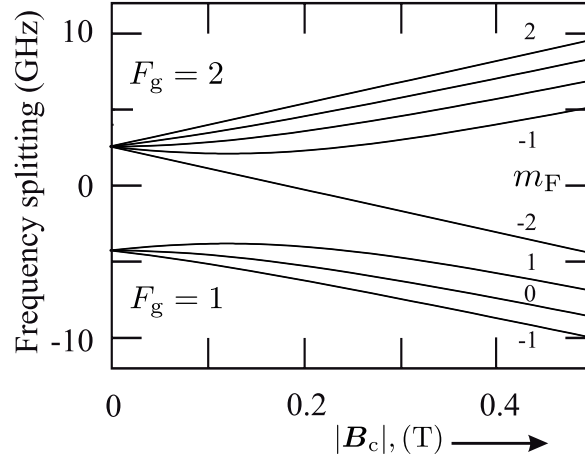
Therefore, by applying two resonance fields (hence the name double resonance) it is possible to drive the atomic oscillator and moreover detect the useful clock signal. Furthermore, since the light photons have a much higher energy than the microwave photons, detecting the light gives a stronger signal.

### 1.3 The Rb clock based on double resonance

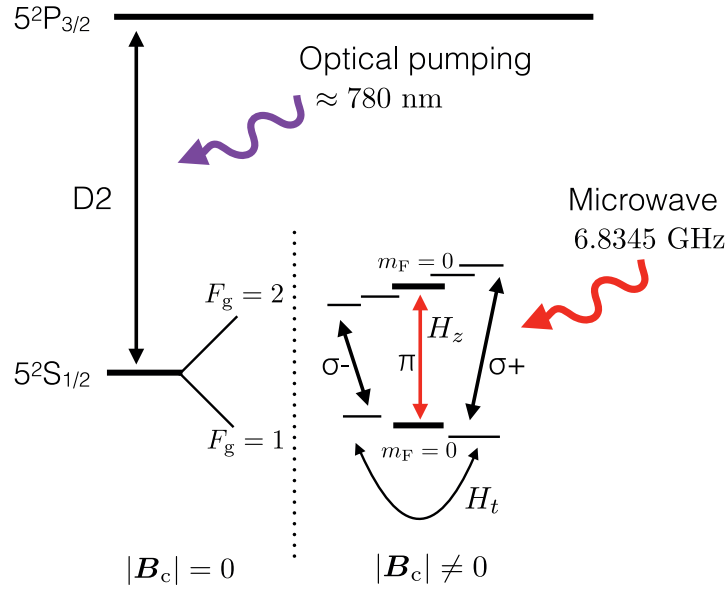
For a DR vapor-cell clock the above-described three-level system is typically implemented for rubidium where in this case the microwave transition is realized in the hyperfine-split ground state of the isotope  $^{87}\text{Rb}$ . The angular momentum in the ground state ( $5^2\text{S}_{1/2}$ ) of  $^{87}\text{Rb}$  is given by the spin of the unpaired electron in the outermost shell[13]:  $J = 1/2$ , while the nuclear spin is  $I = 3/2$ . The coupling of both angular momenta results in the (degenerate) hyperfine states described by total angular momenta  $F_g = 1$  and  $F_g = 2$ . Since the levels are subject to Zeeman splitting, the degeneracy is lifted by an externally applied static magnetic field (figure 1.6a) resulting in the sub-levels shown in figure 1.6b ( $\mathbf{B}_c \neq 0$ ). The corresponding transitions are of a magnetic dipole type which means that they are driven by the magnetic part of the external microwave electromagnetic field (note here we do not mean the static magnetic field). Moreover, the microwave field drives these transitions selectively according to the direction of the static magnetic field (also known as a quantization axis). For example, in the case shown in figure 1.6b the  $\pi$ -transition is driven by the microwave magnetic field which is parallel to the externally applied static magnetic field  $B_c$ . On the other hand, transitions  $\sigma_-$  and  $\sigma_+$  are driven by the left-handed and right-handed circularly polarized magnetic field components that are both orthogonal to the direction of the quantization axis. In our case, the transition used to provide the beneficial clock oscillation (clock transition) is chosen to be:  $|F_g = 1, m_F = 0\rangle \longleftrightarrow |F_g = 2, m_F = 0\rangle$  (the  $\pi$ -transition in figure 1.6b), so that it has the least dependency (and hence a low energy shift between the levels) of possible perturbations of the external magnetic field. The transition is driven by an externally applied microwave magnetic field with a frequency of  $\approx 6.8345$  GHz.

After we introduced the main operating principle, we can now wrap up: The clock is based on a three-level system that, in principle, interacts with three electromagnetic fields: an optical pumping field is used in order to create population imbalance and to read the useful signal; a static magnetic field is applied to define a quantization axis so that the oscillator levels are well-defined; the clock transition is driven by a microwave (magnetic) field with a frequency of about  $f_{\text{Rb}} \approx 6.834$  GHz, where the field is oriented along the direction of the static magnetic field. It is also worth noting, that all fields interacting with the atoms need to be meticulously controlled since naturally their insatiabilities will affect the performance of the atomic oscillator.





(a) Energy difference as function of the external static magnetic field (often referred as "C-field") in the case of  $^{87}\text{Rb}$  (taken from [8]).



(b) Energy levels of  $^{87}\text{Rb}$  ground state and  $5^2P_{1/2}$  excited state (D2 line). The Zeeman sub-levels are shown on the right.

Figure 1.6 – Energy levels of  $^{87}\text{Rb}$  relevant for the operation of the clock.



### 1.3.1 Double resonance operation

In the classical DR scheme, both the laser light (historically light source based on a discharge lamp is used, now substituted by highly stable lasers) and the microwave field are applied simultaneously (continuous mode) [14]. However, a scheme where both fields are separated in time is also possible (Ramsey scheme) where the Rb clocks based on such a principle are known as Pulsed Optical Pumping (POP) clocks [15]. Since our project is also intended to improve the performance of a microwave cavity used in the implementation of such a clock, it is worth while to briefly introduce its principle of operation.

**Pulsed clock operation** The operation of the pulsed clock consists of three stages, separated in time: preparation, interrogation and detection (figure 1.7). Without an externally applied EM field, the energy distribution in a thermal vapor results in equally populated  $|g\rangle$  and  $|e\rangle$  levels. In the preparation stage a light (laser) pulse resonant to the energy difference between levels  $|e\rangle$  and  $|e'\rangle$  is applied. After sufficient time, a significant atom population imbalance between level  $|g\rangle$  and  $|e\rangle$  is created, hence the two-states needed for the atomic oscillator are defined. The laser is then switched off, and a resonant microwave magnetic field is applied to the atoms in the form of two coherent  $\pi/2$  pulses separated in time (figure 1.7 – interrogation). This field drives the atomic resonance, where the durations of the pulses and the separation (called Ramsey time) are in the millisecond range. Finally, a laser pulse of light is applied, resulting in the useful absorption signal (a Ramsey-type signal with a line-width of  $\approx 100$  MHz) shown in the figure.

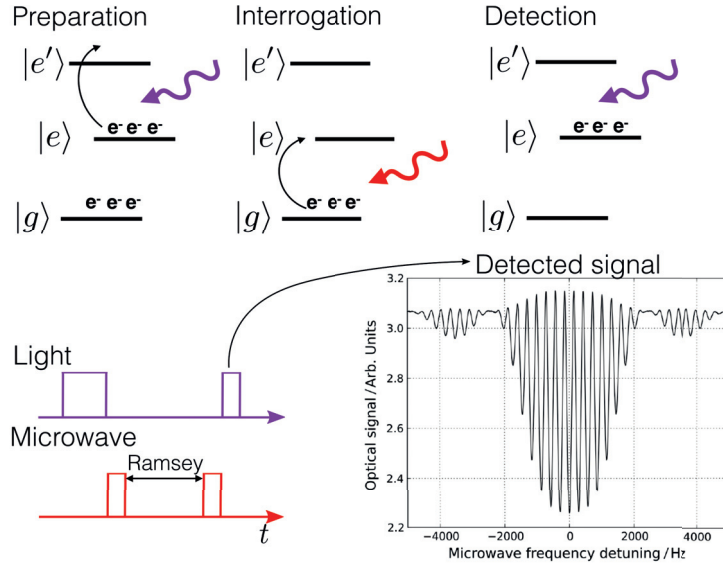


Figure 1.7 – A scheme of the clock operation for the magnetic resonance transition in the  $^{87}\text{Rb}$  atom applied in the pulsed regime. The atoms are represented by a three-level system. The amount of light absorption is directly related to the pulse area. The detected signal is characterized by a specific pattern referred as "Ramsey fringes".

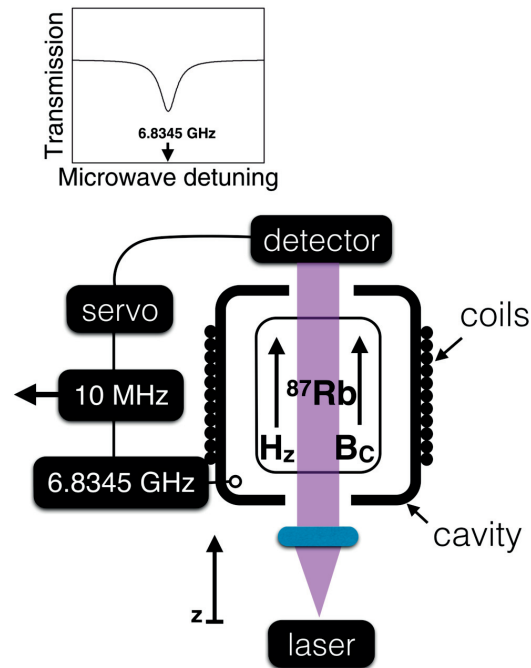
Therefore, by cycles of sweeping the microwave magnetic field and detecting the light absorption we can constantly lock the frequency of the input signal to the magnetic resonance transition and hence stabilize the clock's output frequency. Finally it is worth noting that since the atomic states correspond to the Zeeman sub-levels, they can be classically seen as magnetic dipoles that according to the populated level ( $|g\rangle$  or  $|e\rangle$ ) are characterized by opposite directions of the total magnetic dipole moment. Although this interpretation is not fully valid (in contrast to the classical view the orientation of the atomic magnetic dipoles is quantized) it is sufficient to get intuitive understanding. Only when the microwave frequency is resonant to the energy difference  $\Delta E_{1,2}$ , the electrons will populate the "empty" level  $|e\rangle$  (associated with a 180 degree flip of the magnetic dipoles).

### 1.3.2 The physics package

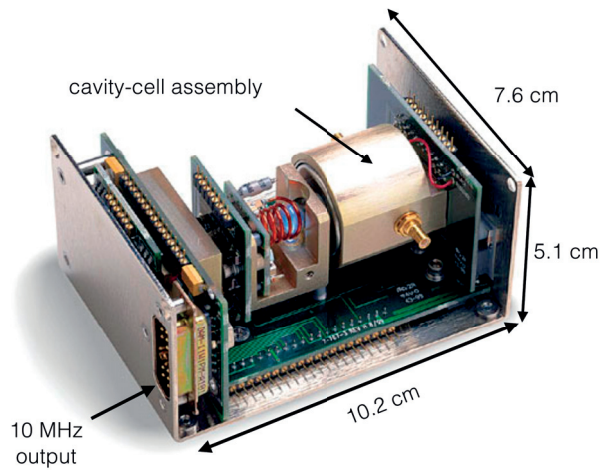
The above-explained EM field-atom interaction is physically realized in the, so-called, physics package of the clock for which a schematic can be seen in figure 1.8a. The rubidium atoms are enclosed in a dielectric cell. Pyrex or quartz dielectrics are used since they are transparent for the light. In principle, the vapor cell in our case contains an additional buffer gas (e.g. argon) which is added in order to increase the efficiency of the optical pumping and prevent effects of depolarization due to diffusion at the cell walls. The microwave field driving the required atomic transition is provided by a cavity with a resonance frequency tuned to the atomic transition  $f_{\text{RD}}$ . The cell is positioned inside the cavity where two apertures (with radius of  $\approx 10$  mm) are included to allow the laser beam to penetrate, interact with the atoms and get detected by the photo-detector (positioned on the top side of the cavity in figure 1.8a). The static magnetic field required for the Zeeman splitting is provided by DC-coils so that the field is oriented along the central axis of the cavity. In this case, for the chosen clock transition, the microwave magnetic field component, aligned to the direction of the (central) axis drives the atomic clock oscillations. The cavity is magnetically-shielded, and also layers of thermal insulation are used in order to reduce heat loss. The obtained optical signal is used with a servo correction feedback in order to stabilize a quartz oscillator. This is how the resulting 10 MHz (standard) clock output signal is created.

Many different variations of the general structure can be found. For example, a discharge lamp may be used instead of a laser (typically for lower performance devices). A realization of a commercially sold device, based on a discharge lamp, is shown in figure 1.8b. Finally, it is worth noting that the microwave cavity is the component with the largest volume and hence it can predetermine the footprint of the final device (not to consider the presence of a protective magnetic shield that surrounds the cavity, which is nevertheless determined by the size of it).

### 1.3. The Rb clock based on double resonance



(a) A scheme of the physics package used in a DR atomic clock. The cavity is usually surrounded by magnetic and temperature shields not shown for clarity. The full detail of the physics package can be seen in figure 3.1b.



(b) A vapor-cell clock (Rb-based) commercially sold by Stanford Research Systems. Photo, Courtesy: Stanford Research Systems.

Figure 1.8 – Physics package of a DR atomic clock.

### 1.3.3 Sources of frequency instability related to the cavity

After introducing the main principle as well as the elements of the physics package, in this section, we briefly explain what are the important aspects of the cavity design that need to be considered assuming DR clock implementations with high stability performance.

In terms of short term stability (1 - 100 s) the Rb clock performance strongly depends on the signal-to-noise ratio (S/N). For example, in the case of the continuous DR regime, the corresponding instability is inversely proportional to the discriminator slope  $D$  (see 1.9a). The latter can be approximated as:  $D \approx A/\Delta f$ , where  $A$  and  $\Delta f$  are the amplitude and the line-width attributed to the optically detected signal (both shown in figure 1.9a). Physically,  $\Delta f$  is centered around  $f_{\text{Rb}}$  and corresponds to the Q-factor attributed to the atomic transition (typically observed values are in the range of few KHz, hence the atomic Q-factor is in the order of  $10^7$ ). The short-term stability can be evaluated as [17]:

$$\sigma_{\text{S/N}}(\tau) = \frac{N_{\text{psd}} \Delta f}{\sqrt{2} A f_{\text{Rb}}} \frac{1}{\sqrt{\tau}} = \frac{N_{\text{psd}}}{\sqrt{2} A Q_a} \frac{1}{\sqrt{\tau}}, \quad (1.5)$$

where  $Q_a$  is the atomic Q-factor,  $N_{\text{psd}}$  is the detection noise power spectral density defined for a photocurrent signal ( $\text{pA} \times \text{Hz}^{-1/2}$ ) and  $\tau$  is the integration time. The cavity plays an important role here since a large S/N ratio means that a large number of atoms is needed to contribute to the beneficial signal. This is why high-performance DR clocks tend to relay on large vapor cells (however it is clear that the cell cannot be arbitrary big either since we are restricted in terms of pressure, temperature gradients, size limitations etc.). The cavity needs therefore to provide a field distribution that covers the whole volume of such a large cell. Moreover, a resonance cavity is an intrinsically restricted structure (geometrically) that will, in principle, provide a good quality field (selectively driving the clock transition) only to a small fraction of its volume. For the example shown in figure 1.9a, an improvement by a factor of two for the short-term stability was reported ( $4 \times 10^{-13} \tau^{-1/2}$ ), attributed to the newly developed cavity that was used. The latter was designed to provide a large number of atoms (a cell volume of  $0.012 \text{ dm}^3$  was reported) where  $\approx 88\%$  of the magnetic field was found (both numerically and experimentally) to contribute to the clock-transition.

In POP clocks, a big advantage is the temporal separation between the optical and the microwave pulse interaction, resulting in a very low light perturbation and hence a potential for a much improved short-term stability:  $1.6 \times 10^{-13} \tau^{-1/2}$ , for  $\tau = 1 - 10^4 \text{ s}$  was reported in [5] for one of the first realizations of such a clock and consecutively  $2.1 \times 10^{-13}$  was demonstrated in [7]. Effectively, the atoms do not change their position inside the vapor cell (a buffer-gas is typically used hence the atoms are considered localized for time intervals relevant for the POP operation), the spatial field inhomogeneity associated to the standing wave in the cavity will result in the Rb atoms being subject to different (effective) microwave pulse areas (see figure 1.7). This has a potential to reduce the contrast of the Ramsey signal (in practice the central fringe is used). Since the contrast is proportional to the signal-to-noise ratio [18], the ability of the cavity to provide a spatially homogeneous field (that drives the clock transition) has a direct consequence in the performance of the clock.

In the pulsed case the short term stability can be obtained by [7]:

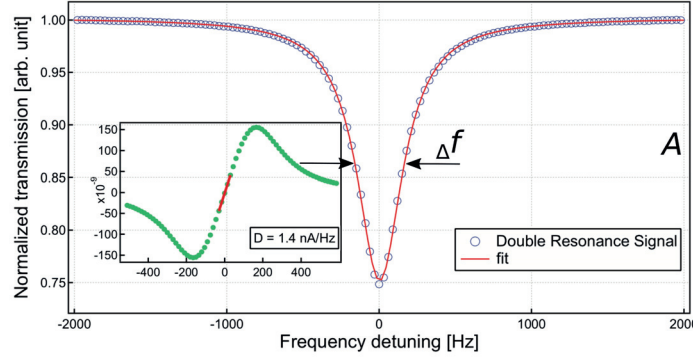
$$\sigma_{S/N}(\tau) = \frac{1}{\pi Q_a R_{sn}} \sqrt{\frac{T_c}{\tau}}. \quad (1.6)$$

In the above equation the signal-to-noise ratio is  $R_{sn} = C \sqrt{\eta N_{opt}}$  where  $\eta$  is the photodetector efficiency,  $C$  is the contrast,  $N_{opt}$  is the number of photons at detection and  $T_c$  is the time required for the repetition of the pulse sequence. For example, for the experimentally obtained signal shown in figure 1.9b, the contrast is  $C = 35\%$  where  $\sqrt{\eta N_{opt}} \approx 8.85 \times 10^4$  resulting in a signal-to-noise ratio of  $\approx 30000$ . The simulated result predicts that if all atoms in the volume are driven by a microwave magnetic field with a constant amplitude, an improvement is expected for the contrast of the central Ramsey fringe. Considering that the atomic Q-factor is fixed, from eq. 1.6 one can obtain that a stability improvement of  $\approx 30\%$  is expected in terms of the short-term performance.

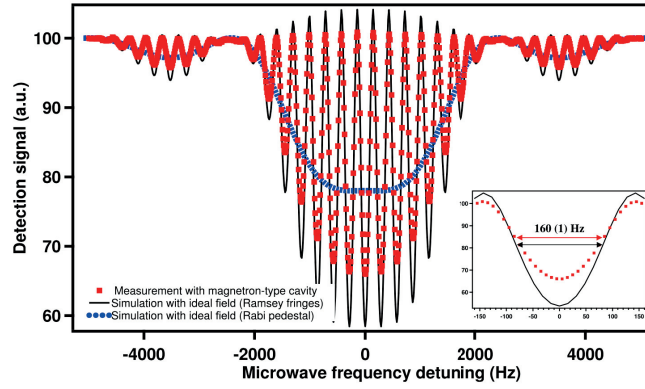
Concerning medium to long-term frequency stability, two major physical effects can be directly contributed to the cavity: position shift and cavity pulling effect. The former is known from continuous mode DR implementations in the cases where buffer gases are used and is explained in more a detail in [19]. The main idea is that both the light beam (due to absorption) and the microwave field (due to the standing wave) can vary significantly in the active volume used to produce the beneficial DR signal, and hence can result in a spatial variation of the atomic resonance frequency (technically the Rabi frequency with the atoms being driven). Both effects may couple in such a way that the non-homogeneities of the light field sample regions (in a power-dependent way) of a non-homogeneous microwave field resulting in a signal that is a weighted average of the resonance frequencies of the single atoms (which can in turn shift the DR line). When buffer gases are not used, the atoms are free to move, averaging out the power gradients associated to the light propagation. The cavity pulling effect is a source of frequency instability associated to temperature. If we consider the simple case of a driven resonance if the the driving force is slightly off-resonance with respect to the intrinsic  $f_{res}$  a small frequency shift (pulling) is observed in the response. Similar situation occurs in the case of atomic frequency standards – since the cavity driving the atomic oscillator is not perfectly tuned to the atomic resonance it results in the frequency shift generally simplified as in [20]:

$$f - f_{atom} = A \frac{Q_{cavity}}{Q_{atom}} (f_{cavity} - f_{atom}), \quad (1.7)$$

where the constant  $A$  describes the level of oscillation, the frequency shift is  $f - f_{atom}$ , the detuning of the cavity is  $f_{cavity} - f_{atom}$  and  $Q_{cavity}$ ,  $Q_{atom}$  are the Q-factors of the cavity and the atomic resonance correspondingly. The reason why over time this effect leads to instability is among others the temperature fluctuation of the cavity resonance frequency. Furthermore, from the general result shown in eq. 1.7 it is evident that different types of clocks are influenced by a different amount depending on the requirements that hold for the Q-factor.



(a) The optically detected DR signal has appr. Lorentzian shape;  $A$  and  $\Delta f$  are the amplitude and full-width-half-maximum (FWHM) of the DR signal.  $D$  is the slope of the corresponding error signal (shown in green) used for locking. Image taken from [16].



(b) Ramsey pattern fringes observed in the operation of a POP clock. The black curve corresponds to a hypothetical case for which all atoms "see" the same amplitude of the magnetic field. The red curve shows an experimentally obtained signal. Image taken from [7].

Figure 1.9 – Optically detected signal (DR signal) in the case of continuous and pulsed regimes. The signal corresponds to the opacity of the Rb vapor as a function of the microwave frequency driving the atomic oscillator; it is normalized to the frequency of the clock transition and hence zero detuning is manifested by maximum light absorption.

Since in our case the clock is passive, a low Q-factor is possible and, moreover, it is highly desirable in order to minimize this effect [7].

After we introduced the major effects directly relevant for the cavity design it is worth noting that, in principle, there is a plethora of physical effects, reported in the literature, through which the clock frequency stability can be affected. Understanding these effects as of a crucial importance for the characterization of a frequency standard.

Some of them include: amplitude and frequency instabilities associated to the laser; effects associated to the vapor e.g. collisions between the atoms, collisions between the atoms and the buffer gas as well as the atoms and the walls of the cell; the phase noise of the microwave frequency synthesizer (Dick effect), various processes associated to the error signal; non-uniform phase distribution arising from losses in the cavity; specific long-term effects attributed to aging and related to the design of the cavity are reported e.g. in [21].

#### 1.3.4 Design guidelines

In order to conclude, we state the general requirements that define an optimal cavity in our case:

**Resonance frequency** The resonance frequency of the microwave cavity must coincide precisely with the frequency of the ground state transition chosen for the clock operation:  $f_{\text{res}} = f_{\text{Rb}} \approx 6.8345$  GHz. Due to its size and materials used, the vapor cell represents a significant dielectric loading for the cavity and hence has a strong potential to influence the resonance frequency. Moreover, the processes used for production of the vapor cell (and the cavity itself) are often associated with considerable tolerances. In order to ensure that the required resonance frequency is met even if such tolerances are present, a variable tuning mechanism needs to be included. Such a tuning needs to be achieved for the vapor cell present inside the cavity and with enough range around the required clock frequency.

**Temperature coefficient** Even small variation of the temperature can sufficiently dilate the cavity material as well as the cell. This affects the performance of the clock since the resonance frequency of the cavity can vary slightly with temperature (Temperature Coefficient TC), which typically requires a complicated temperature control. Therefore, the design of the cavity needs to be intrinsically stable in terms of temperature (the temperature performance can vary significantly for different structures) which would minimize the requirements for active temperature control. The TC needs to be in the range of  $\text{TC} = 10\text{-}100$  kHz/K. Too high temperature coefficient has the potential to significantly impact the clock stability via the cavity pulling effect.

**Quality factor** A moderate Q-factor in the range  $Q = 100\text{-}200$  is sufficient and preferable, since the cavity pulling effect will be suppressed in this way ([14] ch. 7.3.3). Nevertheless efficient power transfer is required hence the cavity needs to be characterized by an input impedance close to the standard  $50\ \Omega$ .

**Power requirements** The power requirement for the optimal clock operation is  $\text{few} \times 10^{-7}$  W and  $\text{few} \times 10^{-8}$  W for the amplitude of the magnetic field in the continuous and pulsed regimes correspondingly. Previous designs [16] show that, in practice, the input power applied to the cavity in the operation of the clock is about  $-20$  dBm and  $-33$  dBm correspondingly from which the power absorbed from the Rb atoms is in the range of  $\text{few} \times 10^{-8}$  W.



**Quality of the microwave field** The cavity mode, used, needs to be characterized by identical phase of the magnetic field for all points inside the active volume of the cavity, meaning that no field node should be present. For our clock we are not concerned with minimizing small phase variations that, for example, can arise from losses.

The cavity mode needs to have a magnetic field with uniform orientation – ideally 100% oriented along the direction of the static C-field, otherwise the field will couple unwanted sigma transitions ( $\sigma_-$ ,  $\sigma_+$ ) reducing the signal-to-noise ratio.

The amplitude of this field needs to be homogeneous in the active volume sampled by the laser light. The requirements for uniformity and homogeneity need to be fulfilled for a vapor cell that is relatively large (a volume of  $\approx 0.012 \text{ dm}^3$  is considered as optimal to use in our case).

**Overall size and structural requirements** The size of the cavity is a serious design restriction since it is intrinsically related to the resonance condition and the quality of the field. In principle, compact sizes are always preferred, since this means a better temperature control, compact magnetic and temperature shields and for example would allow for such a clock to qualify easily for an on-board satellite application. In our studies, we aim at keeping the total volume of the cavity lower than the typically used cylindrical structures. For example, the volume of the cavity found in [16] is considered as a good reference point in terms of volume ( $0.044 \text{ dm}^3$ ).

In terms of structure, we note that the cavity is opened at both sides – two apertures with a radius of  $\approx 10 \text{ mm}$  need to be present in order to allow for the pumping light. This is a major source of power loss hence extensions need to be included in order to minimize leakage. Finally, the design needs to be flexible (preferably it should have various degrees of freedom since this will help in meeting the stringent requirements), the DC coils needed for the static magnetic field as well as the magnetic shields need to be easily accommodated. Moreover, for practical reasons, the cavity needs to allow operation with various cells. This means that retrofitting and compensation of potential tolerances should be possible in a straightforward way.

The above described requirements are intended to summarize the crucial points of the design. They are reexamined in a more thorough detail further in various parts of this thesis. The requirements for the quality of the field are extensively discussed in section 2.2.2, where we define various figures of merits utilized to determine the optimal design.



### 1.3.5 Objectives and outline

The goal of this thesis is to improve the performance of microwave cavities in applications related to vapor-cell atomic clocks based on double resonance. This includes characterization of currently employed structures as well as proposing entirely new solutions with much improved characteristics. The organization of the thesis is included below.

**Chapter 2** In this chapter we give the electromagnetic theory basis needed for the class of resonating structures which are interesting for our application – cavities obtained from waveguide sections.

First we consider the general case of arbitrary cross section and translational symmetry for which we describe the fields in the cavity. At this stage it is recognized that due to a duality feature of the ideal boundary conditions considered (PEC/PMC), a TE mode characterized by a longitudinal modal number zero is physically possible. We then move to a more specific case, namely, the typically-employed cylindrical cavity, for which we report the modal distribution as well as the various characteristics associated to the resonance condition.

The next major part of this chapter shows in detail how the cavity is connected to the performance of the clock from an electromagnetic point of view. First we describe the driving fields that apply directly to the transitions in the clock operation. Various figures of merit used as design criteria are then defined, more specifically, related to the quality of the field. A special remark is made for the homogeneity of the amplitude. In the last part of this chapter we utilize performance diagrams that, in an intuitive way, allow us to find the optimal performance case. The content of this chapter is already well-known, however its intention is to provide both the theory and the tools needed in the design process.

**Chapter 3** The first part of this chapter reports in detail the state-of-the-art related to the development of various relevant cavities found in the literature. First, we consider geometries known in the atomic clock domain where the reported solutions are classified according to their compactness and temperature performance. Moreover we focus on a special-kind of geometry (the loop-gap), for which we report solutions known in the atomic clock domain as well as in the domains of nuclear magnetic resonance and electron paramagnetic resonance. This type of structure is important in our studies since our final design is based on a version of it.

The second part of this chapter is entirely related to the physics of the loop-gap cavity. We introduce the structure from a lumped point of view as well as from a point of view of the field performance. A particular attention to the field homogeneity is paid for various configurations of the structure, including the problems that can arise from the physics package requirements. We then put into perspective its performance by evaluating it using the figures of merit previously introduced. In terms of contribution we consider the study to be of some relevance for the atomic clock community, particularly because we have not previously found an in-depth comparison of the homogeneity performance.

The last part of this chapter is related to experiments that were performed for two cavity designs previously realized. In the first case an optical imaging experiment was conducted (by a different scientific group) which revealed some unexpected field distribution mostly attributed to the unwanted clock transitions. In line with that, we report an extensive numerical study where, in an attempt to debug the experiment, we have considered the effect of a potential misalignment between the electromagnetic fields. For the second cavity design, we have performed a measurement of the cavity temperature stability. A complementary numerical study was also considered and it is reported. Finally we investigate tolerance issues which are found to degrade the resonance. In terms of contribution, the effect of the misalignment was not previously studied. It revealed some interesting effects related to the figures of merit and it is useful since it provides a basis for understanding future experiments. The approach we used in order to model the temperature coefficient proved to be useful since a possibility for a potential improvement of the temperature performance was revealed.

**Chapter 4** The last chapter of this thesis proposes various implementations of atomic clock cavity based on Artificial Magnetic Conductor (AMC) boundary conditions.

In the first half of this chapter we show, that such a solution can be in principle implemented for arbitrary cross section by utilizing close to quarter-wavelength dielectric loadings. We then focus on the circular cross section which allows us to study the structure analytically. The performance is evaluated both in terms of uniformity and homogeneity. The issues associated to sensitivity of the dimensions are considered important for these kind of structures and are accordingly discussed. The expected temperature sensitivity is evaluated as well as the effect that the apertures have on the field distribution.

In the second part of this chapter we investigate an implementation of AMC boundaries in the case of the loop-gap geometry which is also our choice for the final design. Besides the solution based on a dielectric material, we investigate a possibility to implement AMC based on a planar structure. The very important issue of frequency tuning is covered where we report a specifically designed solution that utilizes the loop-gap structure and we discuss the proposed design in full detail. Moreover, we describe two additional (optional) features: the possibility to add corrugations and the option for a distributed feeding, both used for additional suppression of unwanted modes. Finally, we evaluate the obtained performance and report the current stage of the realization.

In terms of novelty, this chapter represents the biggest contribution in this thesis. To the best of our knowledge this is the first attempt to relate the concept of AMC to atomic clock applications. We managed to achieve a nearly constant microwave magnetic field distribution along the direction of the optical field with more than 97% of orientation uniformity across the atomic sample. The proposed tuning mechanism, the additionally developed planar AMC solution and the fact that the structure is intrinsically not too restricted in terms of volume allow to meet the excellent performance for a surprisingly large interval of possible dimensions.

## 2 Microwave cavities for DR atomic clocks

### 2.1 General cavity theory

In this chapter we include a brief introduction to the general electromagnetic theory related to microwave cavities. More specifically, we are interested in cavities obtained from waveguide sections. In the domain of DR atomic clocks this is the utilitarian choice – such geometries can easily accommodate vapor cells with various sizes and moreover the required magnetic field distribution can be obtained without being much perturbed by the presence of the vapor cell [21]. First, we describe the general electromagnetic solution and discuss the boundary conditions relevant for our application. We then cover some characteristics associated to the resonance condition and explain the general design criteria. Finally, appropriate figures of merit are defined providing the basis required for the evaluation of the cavity design in terms of the clock performance.

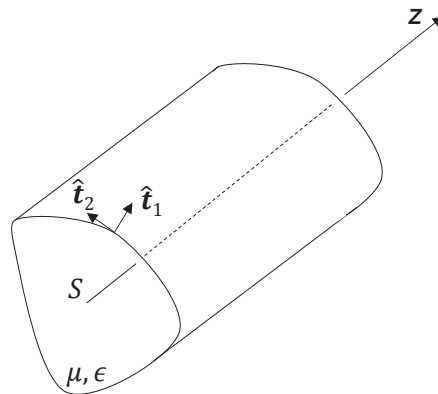


Figure 2.1 – The generalized cylindrical waveguide is shown in a curvilinear coordinate system  $t_1, t_2, z$ , with unit vectors  $\hat{t}_1, \hat{t}_2$  used to define the transverse cross section and  $\hat{z}$  chosen along the direction of wave propagation (hereafter referred as "longitudinal").

### 2.1.1 Generalized cross section with translational symmetry

In the general case, a cavity is a fully electromagnetically bounded volume where the electromagnetic field is described by discrete solutions that fulfill Maxwell's equations. For the type of cavities that we are interested in, due to a translational symmetry, the problem of obtaining the EM field distribution can be separated in two parts: initially the propagation of the guided wave is determined and then additional boundary conditions are applied along the direction of energy propagation. Here, this general procedure is briefly described.

Lets first consider the generalized case of a cylindrical waveguide characterized by an arbitrary cross section and a translational symmetry in the direction of the guided wave propagation – figure 2.1. Everywhere inside the volume, the EM field can be obtained as the steady-state solution of the source-free vector Helmholtz equation, and it is given in the phasor form as:  $\mathbf{E}(\mathbf{r})e^{j\omega t}$ ,  $\mathbf{H}(\mathbf{r})e^{j\omega t}$ . This is a well-known problem [22] that can be analytically solved assuming a field decomposition into transverse and longitudinal (along  $z$ ) parts. It is sufficient to find the eigenmodes of the transverse problem, assuming boundary conditions associated to the contour that describes the waveguide cross section. Once the transverse field components are obtained, the Maxwell's equations can be applied in order to calculate the dependent longitudinal ones. The above explained orthogonal decomposition is generally valid for isotropic media and permits variation of  $\epsilon$  and  $\mu$  in both transverse and longitudinal direction. In the case of transversely inhomogeneous medium, hybrid modes need to be taken into account [23].

In the most simple case of a bounded, fully homogeneous medium (uniform waveguide) the complete solution for the independent transverse field can be obtained as a superposition of separate TM and TE modes:

$$\mathbf{E}_t(t_1, t_2, z) = \sum_i V_i^{\text{TM}}(z) \mathbf{e}_i^{\text{TM}}(t_1, t_2) + \sum_i V_i^{\text{TE}}(z) \mathbf{e}_i^{\text{TE}}(t_1, t_2), \quad (2.1)$$

$$\mathbf{H}_t(t_1, t_2, z) = \sum_i I_i^{\text{TM}}(z) \mathbf{h}_i^{\text{TM}}(t_1, t_2) + \sum_i I_i^{\text{TE}}(z) \mathbf{h}_i^{\text{TE}}(t_1, t_2). \quad (2.2)$$

where  $\mathbf{e}_i^{\text{TM}}(t_1, t_2)$ ,  $\mathbf{h}_i^{\text{TM}}(t_1, t_2)$  and  $\mathbf{e}_i^{\text{TE}}(t_1, t_2)$ ,  $\mathbf{h}_i^{\text{TE}}(t_1, t_2)$  are the transverse TM and TE eigenvectors corresponding to the  $i$ -th solution with explicit form dependent on the chosen shape of the waveguide cross section. The expressions for the separate TM and TE distributions are given below:

<b>TM</b> $H_z = 0; \quad \mathbf{H}_t, \mathbf{E}_t, E_z \neq 0$
---

The transversal components are given by:

$$\mathbf{E}_t^{\text{TM}}(t_1, t_2, z) = \sum_i V_i^{\text{TM}}(z) \mathbf{e}_i^{\text{TM}}(t_1, t_2), \quad \mathbf{e}_i^{\text{TM}}(t_1, t_2) = -\nabla_t \phi_i(t_1, t_2); \quad (2.3)$$

$$\mathbf{H}_t^{\text{TM}}(t_1, t_2, z) = \sum_i I_i^{\text{TM}}(z) \mathbf{h}_i^{\text{TM}}(t_1, t_2), \quad \mathbf{h}_i^{\text{TM}}(t_1, t_2) = \hat{\mathbf{z}} \times \mathbf{e}_i^{\text{TM}}(t_1, t_2); \quad (2.4)$$

The longitudinal components are given by:

$$\mathbf{E}_z^{\text{TM}}(t_1, t_2, z) = -\frac{1}{j\omega\epsilon} \nabla_t \cdot (\hat{\mathbf{z}} \times \mathbf{H}_t^{\text{TM}}(t_1, t_2, z)) \hat{\mathbf{z}} = \sum_i I_i^{\text{TM}}(z) Z_{t,i}^{\text{TM}} e_{z,i}^{\text{TM}}(t_1, t_2) \hat{\mathbf{z}}, \quad (2.5)$$

where

$$e_{z,i}^{\text{TM}}(t_1, t_2) = \frac{1}{j\omega\epsilon Z_{t,i}^{\text{TM}}} \nabla_t \cdot \mathbf{e}_i^{\text{TM}}(t_1, t_2) = \frac{1}{jk_{z,i}^{\text{TM}}} \nabla_t \cdot \mathbf{e}_i^{\text{TM}}(t_1, t_2). \quad (2.6)$$

In the above expressions  $Z_{t,i}^{\text{TM}}$  is the characteristic impedance of the  $i$ -th TM mode,  $k_{z,i}^{\text{TM}}$  and  $k_{c,i}^{\text{TM}}$  are the longitudinal and transversal propagation constants:

$$k_{z,i}^{\text{TM}} = \sqrt{k^2 - k_{c,i}^{\text{TM}}}, \quad Z_{t,i}^{\text{TM}} = \frac{k_{z,i}^{\text{TM}}}{\omega\epsilon} = \frac{1}{Y_{t,i}^{\text{TM}}}. \quad (2.7)$$

**TE**  $E_z = 0; \quad \mathbf{H}_t, \mathbf{E}_t, H_z \neq 0$

The transversal components are given by:

$$\mathbf{E}_t^{\text{TE}}(t_1, t_2, z) = \sum_i V_i^{\text{TE}}(z) \mathbf{e}_i^{\text{TE}}(t_1, t_2), \quad \mathbf{h}_i^{\text{TE}}(t_1, t_2) = -\nabla_t \psi_i(t_1, t_2); \quad (2.8)$$

$$\mathbf{H}_t^{\text{TE}}(t_1, t_2, z) = \sum_i I_i^{\text{TE}}(z) \mathbf{h}_i^{\text{TE}}(t_1, t_2), \quad \mathbf{e}_i^{\text{TE}}(t_1, t_2) = \mathbf{h}_i^{\text{TE}}(t_1, t_2) \times \hat{\mathbf{z}}; \quad (2.9)$$

The longitudinal components are given by:

$$\mathbf{H}_z^{\text{TE}}(t_1, t_2, z) = \frac{1}{j\omega\mu} \nabla_t \cdot [\hat{\mathbf{z}} \times \mathbf{E}_t^{\text{TE}}(t_1, t_2, z)] \hat{\mathbf{z}} = \sum_i V_i^{\text{TE}}(z) Y_{t,i}^{\text{TE}} h_{z,i}^{\text{TE}}(t_1, t_2) \hat{\mathbf{z}}, \quad (2.10)$$

where

$$h_{z,i}^{\text{TE}}(t_1, t_2) = \frac{1}{j\omega\mu Y_{t,i}^{\text{TE}}} \nabla_t \cdot \mathbf{h}_i^{\text{TE}}(t_1, t_2) = \frac{1}{jk_{z,i}^{\text{TE}}} \nabla_t \cdot \mathbf{h}_i^{\text{TE}}(t_1, t_2). \quad (2.11)$$

## Chapter 2. Microwave cavities for DR atomic clocks

In the above expressions  $Z_{t,i}^{\text{TE}}$  is the characteristic impedance of the  $i$ -th TE mode and  $k_{z,i}^{\text{TE}}$  and  $k_{c,i}^{\text{TE}}$  are the longitudinal and transversal propagation constants:

$$k_{z,i}^{\text{TE}} = \sqrt{k^2 - k_{c,i}^{\text{TE}}} \quad Z_{t,i}^{\text{TE}} = \frac{\omega\mu}{k_{z,i}^{\text{TE}}} = \frac{1}{Y_{t,i}^{\text{TE}}}. \quad (2.12)$$

The modal description shown, follows the approach developed in [23] where the scalar functions  $\phi$  and  $\psi$  (referred in the literature as mode functions) can be found tabulated for different geometries in [24]. Both expressions for the TE and TM case are convenient due to the fact that  $V_i(z)$  and  $I_i(z)$  can be, in principle, interpreted as the equivalent, modal voltage and current waves. This allows the use of a Transmission Line (TL) approach in order to describe the propagation along the  $z$ -direction:

$$V_i(z) = V_i^+ e^{-jk_{z,i}z} + V_i^- e^{+jk_{z,i}z}, \quad (2.13)$$

$$I_i(z) = I_i^+ e^{-jk_{z,i}z} - I_i^- e^{+jk_{z,i}z} = \frac{1}{Z_{t,i}} \left( V_i^+ e^{-jk_{z,i}z} - V_i^- e^{+jk_{z,i}z} \right), \quad (2.14)$$

which are the traveling wave solutions that fulfill the telegrapher's equations [25] where  $e^{-jk_{z,i}}$  and  $e^{+jk_{z,i}}$  correspond to the forward and backward propagating waves. In order to obtain the cavity solutions we can apply boundary conditions to the longitudinal  $z$  direction. For completeness, here we include the two main boundary conditions (BC) used in our analysis as seen from a field point of view or alternatively from a transmission line point of view:

**Perfect Electric Conductor PEC:**  $E_t = 0$  and  $V_i = 0$  (short circuited plane).

**Perfect Magnetic Conductor PMC:**  $H_t = 0$  and  $I_i = 0$  (open circuited plane).

If we consider  $d$  to be the height of the cavity (defined along  $z$ ), the coordinate system fixed to the bottom (at  $z = 0$ ) and hence the two boundaries are considered at  $z = 0$  and  $z = d$ . The solutions corresponding to the PEC and PMC are therefore given by:

PEC at  $z = 0$ ,  $V_i(z = 0) = 0$

$$V_i(z) = V_i^+ (e^{-jk_{z,i}z} - e^{+jk_{z,i}z}) = -2jV_i^+ \sin(k_{z,i}z), \quad (2.15)$$

$$I_i(z) = \frac{V_i^+}{Z_{t,i}} (e^{-jk_{z,i}z} + e^{+jk_{z,i}z}) = 2Y_{t,i}V_i^+ \cos(k_{z,i}z), \quad (2.16)$$

where applying PEC at  $z = d$  we obtain  $k_{z,i}d = p\pi$ .

$$\text{PMC at } z = 0, I_i(z = 0) = 0$$

$$V_i(z) = Z_{t,i} I_i^+ (e^{-jk_{z,i}z} + e^{+jk_{z,i}z}) = 2Z_{t,i} I_i^+ \cos(k_{z,i}z), \quad (2.17)$$

$$I_i(z) = I_i^+ (e^{-jk_{z,i}z} - e^{+jk_{z,i}z}) = -2j I_i^+ \sin(k_{z,i}z), \quad (2.18)$$

where applying PMC at  $z = d$  we obtain  $k_{z,i}d = p\pi$ .

In table 2.1, we summarize the cases for the length  $d$  of the cavity corresponding to the four possible combinations of the PEC/PMC boundary conditions applied along the  $z$ -direction.

$z = 0$	PEC	PEC	PMC	PMC
$z = d$	PEC	PMC	PEC	PMC
$d$	$\frac{p\pi}{k_{z,ip}}$	$(2p+1)\frac{\pi}{2k_{z,ip}}$	$(2p+1)\frac{\pi}{2k_{z,ip}}$	$\frac{p\pi}{k_{z,ip}}$

Table 2.1 – The length of the cavity  $d$  is given for combinations of PEC/PMC boundary conditions applied at  $z = 0$  and  $z = d$ ;  $i$  and  $p$  are the transverse and longitudinal modal numbers and hence the longitudinal propagation constant attributed to the cavity solutions can be indexed as:  $k_{z,ip}$ .

The cavity field components in the case of PEC at  $z = 0$  and  $z = d$  are given by:

$$\begin{aligned} \mathbf{E}_{t,ip} &= -2j V_i^+ \sin(k_{z,ip}z) \mathbf{e}_i(t_1, t_2), \\ \mathbf{H}_{t,ip} &= 2 Y_{t,i} V_i^+ \cos(k_{z,ip}z) \mathbf{h}_i(t_1, t_2), \\ E_{z,ip}^{\text{TM}} &= 2 V_i^+ \cos(k_{z,ip}z) e_{z,i}^{\text{TM}}(t_1, t_2), \\ H_{z,ip}^{\text{TE}} &= -2j V_i^+ Y_{t,i} \sin(k_{z,ip}z) h_{z,i}^{\text{TE}}(t_1, t_2). \end{aligned} \quad (2.19)$$

The cavity field components in the case of PMC at  $z = 0$  and  $z = d$  are given by:

$$\begin{aligned} \mathbf{E}_{t,ip} &= 2 V_i^+ \cos(k_{z,ip}z) \mathbf{e}_i(t_1, t_2), \\ \mathbf{H}_{t,ip} &= -2j Y_{t,i} V_i^+ \sin(k_{z,ip}z) \mathbf{h}_i(t_1, t_2), \\ E_{z,ip}^{\text{TM}} &= -2j V_i^+ \sin(k_{z,ip}z) e_{z,i}^{\text{TM}}(t_1, t_2), \\ H_{z,ip}^{\text{TE}} &= 2 V_i^+ Y_{t,i} \cos(k_{z,ip}z) h_{z,i}^{\text{TE}}(t_1, t_2). \end{aligned} \quad (2.20)$$

The above-described solutions are periodic in  $z$  with modal index  $p$  – an integer number. It is of interest to analyze the case of  $p = 0$ , which will turn useful for our further studies.

In the case of PEC at  $z = 0$  and  $z = d$  we have:

- TE $_{i \neq 0, p=0}$  modes

We have:  $E_{z,i0} = 0$ ,  $E_{t,i0} = 0$  and since  $\nabla \times \mathbf{E} = 0$  the magnetic field is zero and such a TE mode is not physical.

- TM $_{i \neq 0, p=0}$  modes

We have:  $H_{z,i0} = 0$ ,  $E_{t,i0} = 0$ ,  $\mathbf{H}_{t,i0} = 2Y_{t,i} V_i^+ \mathbf{h}_i(t_1, t_2)$ ,  $E_{z,i0} = 2V_i^+ e_{z,i}(t_1, t_2)$ , which is a possible mode with a constant field along  $z$ .

In the case of PMC at  $z = 0$  and  $z = d$  we have:

- TE $_{i \neq 0, p=0}$  modes

We have:  $E_{z,i0} = 0$ ,  $\mathbf{H}_{t,i0} = 0$ ,  $E_{t,i0} = 2V_i^+ \mathbf{e}_i(t_1, t_2)$ ,  $H_{z,i0} = 2V_i^+ Y_{t,i} h_{z,i}(t_1, t_2)$ , which is a possible mode with a constant field along  $z$ .

- TM $_{i \neq 0, p=0}$  modes

We have:  $H_{z,i0} = 0$ ,  $\mathbf{H}_{t,i0} = 0$  and since  $\nabla \times \mathbf{H} = 0$  the electric field is zero and such a TM mode is not physical.

It can be seen that the TE $_{i \neq 0, p=0}$  and TM $_{i \neq 0, p=0}$  modes are related to the duality between the PEC-PMC boundaries, when applied at the transverse sides of the cavity. For us the TM $_{i \neq 0, p=0}$  case is of a special interest, because it implies a field distribution which is beneficial for the clock. This aspect is covered in chapter 4.

### 2.1.2 Modes in a cylindrical cavity with a circular cross section and PEC boundaries

After the general theory was introduced, we now focus on a more specific geometry relevant for our application. The cylindrical cavity with a circular cross section (parametrization of the dimensions is found in figure 2.2) is a particular choice that sufficiently fulfills the requirements of size and shape related to the implementation of the physics package (see section 1.3.2) [14, 21]. In this case, the field is considered in cylindrical coordinates where in the transverse direction the mode is described by  $m, n$  indexes related to the number of circumferential and radial variations correspondingly. Being a canonical geometry, for such a cavity, it is possible to analytically obtain the modes (figure 2.3).

### 2.1.3 The standard cylindrical cavity with PEC boundaries

In this structure it is the family of TE modes that can be practically used to provide the required driving field along the direction of the quantization axis (typically aligned to the central axis of the cavity). More specifically, such a cavity working at the TE $_{011}$  mode is an example of the most often-applied and well-studied geometries in the domain of DR atomic clocks as well as atomic fountains [14]. Therefore, in our studies, we assume it as a referent structure and a performance benchmark.



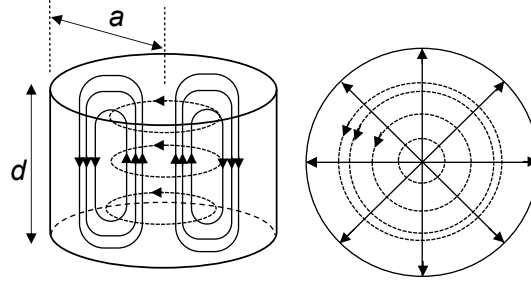


Figure 2.2 – Electric (dashed) and magnetic (solid) field lines of the  $TE_{m=0,n=1,p=1}$  mode in a cylindrical resonator cavity with a radius  $a$  and a height  $d$ . An Aspect Ratio (AR) is defined as  $2a/d$ .

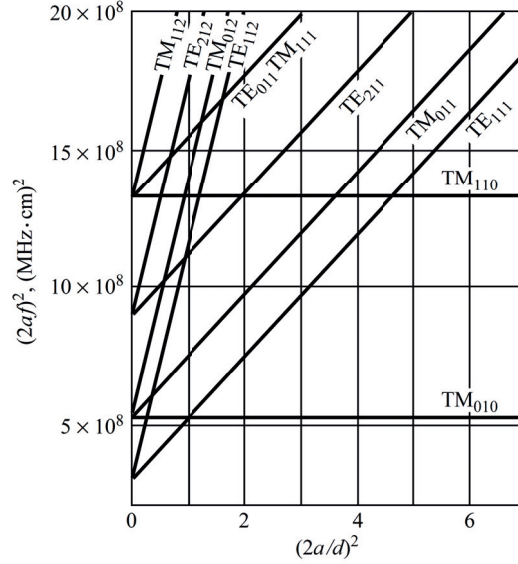


Figure 2.3 – A mode chart for the (circular) cylindrical cavity – originally published in [22]. PEC boundary conditions are considered to apply at all cavity walls. For a given mode we have  $(2af_{mnp})^2 = (\frac{cx_{mn}}{\pi})^2 + (\frac{cp}{2})^2 (\frac{2a}{d})^2$ , where  $f_{mnp}$  is the resonance frequency,  $x_{mn} = \chi'_{mn}$  for the  $TE_{mnp}$  modes and  $x_{mn} = \chi_{mn}$  for the  $TM_{mnp}$  modes;  $\chi_{mn}$  is the  $n$ -th root of  $J_m$ .

### Field components

For the circular cross section, assuming PEC boundary conditions, the solution corresponding to the  $TE_{mnp}$  mode is given in the cylindrical coordinate system  $(\rho, \phi, z)$ . In this case from eq. 2.8:  $\nabla_t \psi_i(t_1, t_2)$  becomes  $\nabla_t \psi_i(\rho, \phi)$  and hence taking into account the cylindrical coordinates we have:

$$\frac{\partial}{\partial \rho} \psi_i(\rho, \phi) \hat{\rho} + \frac{1}{\rho} \frac{\partial}{\partial \phi} \psi_i(\rho, \phi) \hat{\phi} = \nabla_t \psi_i(\rho, \phi). \quad (2.21)$$

## Chapter 2. Microwave cavities for DR atomic clocks

---

For the circular cross section, the scalar function  $\psi_i$  has the form [24]:

$$\psi_{mn}(\rho, \phi) = \sqrt{\frac{\epsilon_m}{\pi}} \frac{1}{\sqrt{\chi'_{mn} - m^2}} \frac{1}{J_m(\chi'_{mn})} J_m\left(\frac{\chi'_{mn}\rho}{a}\right) \begin{cases} \cos(m\phi) \\ \sin(m\phi) \end{cases}, \quad (2.22)$$

where  $\epsilon_m = 1$  for  $m = 0$  and  $\epsilon_m = 2$  for  $m \neq 0$ . Both degenerate components are assumed: one of odd and one of even angular dependence accordingly. Since the first part is independent on the coordinates we can write:

$$\psi_{mn}(\rho, \phi) = H_0 J_m\left(\frac{\chi'_{mn}\rho}{a}\right) \begin{cases} \cos(m\phi) \\ \sin(m\phi) \end{cases}, \quad (2.23)$$

where  $\chi'_{mn}$  is the  $n$ -th non-vanishing root of the derivative of the  $m$ -th order Bessel function and  $m = 0, 1, 2, 3, \dots$ . Substituting 2.22 in eq. 2.21 and considering eq. 2.8 we obtain for the  $\hat{\rho}$ -component of the  $mn$ -th mode:

$$h_\rho(\rho, \phi) = -H_0 k_c J'_m\left(\frac{\chi'_{mn}\rho}{a}\right) \begin{cases} \cos(m\phi) \\ \sin(m\phi) \end{cases} \quad (2.24)$$

and accordingly for the  $\phi$ -component:

$$h_\phi(\rho, \phi) = \pm H_0 \frac{m}{\rho} J_m\left(\frac{\chi'_{mn}\rho}{a}\right) \begin{cases} \sin(m\phi) \\ \cos(m\phi) \end{cases}, \quad (2.25)$$

where the transverse propagation constant  $k_c$  attributed to the chosen mode is given by  $\frac{\chi'_{mn}}{a}$  for the considered TE family of modes. Therefore, from eq. 2.9, for the transverse components of the magnetic field we obtain:

$$\begin{aligned} H_\rho(\rho, \phi, z) &= -I_i^{\text{TE}}(z) k_c H_0 J'_m\left(\frac{\chi'_{mn}\rho}{a}\right) \begin{cases} \cos(m\phi) \\ \sin(m\phi) \end{cases}, \\ H_\phi(\rho, \phi, z) &= \pm I_i^{\text{TE}}(z) \frac{m}{\rho} H_0 J_m\left(\frac{\chi'_{mn}\rho}{a}\right) \begin{cases} \sin(m\phi) \\ \cos(m\phi) \end{cases}. \end{aligned} \quad (2.26)$$

For the transverse components of the electric field from 2.9 we have:

$$\mathbf{e}(\rho, \phi) = \mathbf{h}(\rho, \phi) \times \hat{\mathbf{z}} = h_\phi \hat{\boldsymbol{\rho}} - h_\rho \hat{\boldsymbol{\phi}} \quad (2.27)$$

and hence from eq. 2.8 we obtain:

$$\begin{aligned} E_\rho(\rho, \phi, z) &= \pm V_i^{\text{TE}}(z) \frac{m}{\rho} H_0 J_m \left( \frac{\chi'_{mn} \rho}{a} \right) \begin{cases} \sin(m\phi) \\ \cos(m\phi) \end{cases}, \\ E_\phi(\rho, \phi, z) &= V_i^{\text{TE}}(z) k_c H_0 J'_m \left( \frac{\chi'_{mn} \rho}{a} \right) \begin{cases} \cos(m\phi) \\ \sin(m\phi) \end{cases}. \end{aligned} \quad (2.28)$$

In order to obtain the longitudinal component of the magnetic field we take eqs. 2.11 and 2.8 where:

$$h_z(\rho, \phi) = -\frac{1}{j} \frac{1}{k_z} \nabla_t \cdot \mathbf{h}(\rho, \phi) = -\frac{1}{j} \nabla_t^2 \psi(\rho, \phi) \quad (2.29)$$

and hence from the (reduced) Helmholtz equation:  $\nabla_t^2 \psi(\rho, \phi) = -k_c^2 \psi(\rho, \phi)$  we have:

$$h_z(\rho, \phi) = \frac{1}{j} \frac{k_c^2}{k_z} \psi(\rho, \phi) \quad (2.30)$$

and from eqs. 2.10 and 2.23 we finally obtain:

$$H_z(\rho, \phi, z) = -j V_i^{\text{TE}}(z) \sqrt{\frac{\epsilon}{\mu} \frac{k_c^2}{k_0}} H_0 J_m \left( \frac{\chi'_{mn} \rho}{a} \right) \begin{cases} \cos(m\phi) \\ \sin(m\phi) \end{cases}, \quad (2.31)$$

where for the characteristic impedance we have:  $Z_t = k_0 Z_0 / k_z$  in which  $Z_0 = \sqrt{\mu/\epsilon}$  and  $k_0 = \omega \sqrt{\mu\epsilon}$  are the intrinsic impedance and propagation constant attributed to the isotropic, lossless and homogeneous medium characterized by material constants  $\epsilon$  and  $\mu$ .

Assuming the mode of interest  $\text{TE}_{m=0, n=1, p=1}$  and using the boundary conditions (eq. 2.15 and 2.16) for the standing wave in the cavity we obtain:

$$\begin{aligned} H_z(\rho, \phi, z) &= \sqrt{\frac{\epsilon}{\mu} \frac{k_c^2}{k_0}} H_0 J_0 \left( \frac{\chi'_{01} \rho}{a} \right) \begin{cases} -2V^+ \sin(K_z z) \\ -2jV^+ \cos(K_z z) \end{cases}, \\ H_\rho(\rho, \phi, z) &= Y_t K_c H_0 J'_0 \left( \frac{\chi'_{01} \rho}{a} \right) \begin{cases} -2V^+ \cos(K_z z) \\ 2jV^+ \sin(K_z z) \end{cases}, \\ E_\phi(\rho, \phi, z) &= K_c H_0 J'_0 \left( \frac{\chi'_{01} \rho}{a} \right) \begin{cases} -2jV^+ \sin(K_z z) \\ 2V^+ \cos(K_z z) \end{cases}, \\ H_\phi(\rho, \phi, z) &= 0, \\ E_z(\rho, \phi, z) &= 0, \\ E_\rho(\rho, \phi, z) &= 0, \end{aligned} \quad (2.32)$$

where, for completeness, the two convenient cases for the coordinates are shown: the bottom of the cavity being at  $z = 0$  and  $z = d/2$  accordingly. It is worth noting that in eq. 2.32 the magnetic and electric fields are  $\pm 90$  deg out of phase, which is the case when a lossless cavity is considered and relates to the current and voltage waves being  $\pm 90$  deg out of phase in an equivalent lossless  $LC$  circuit model. A scheme of the field distribution can be seen in figure 2.2. The longitudinal and transverse magnetic field components are shown in figures 2.4, 2.5 and 2.6 accordingly.

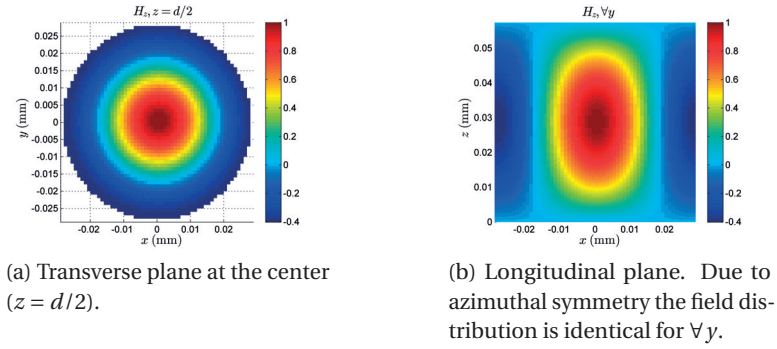


Figure 2.4 –  $H_z$  field component.

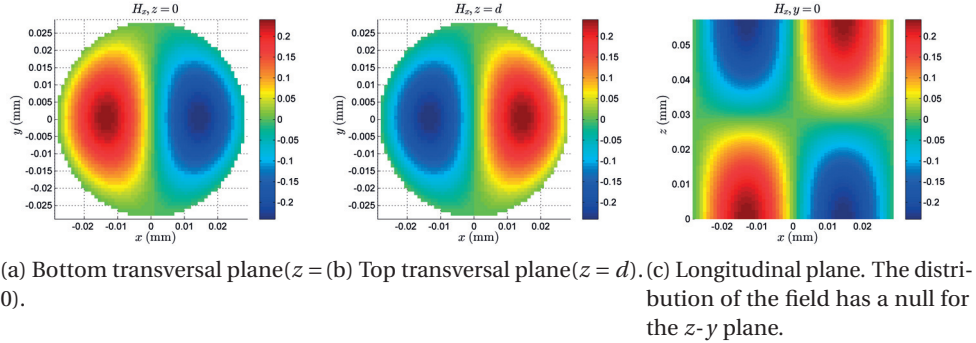


Figure 2.5 –  $H_x$  field component.

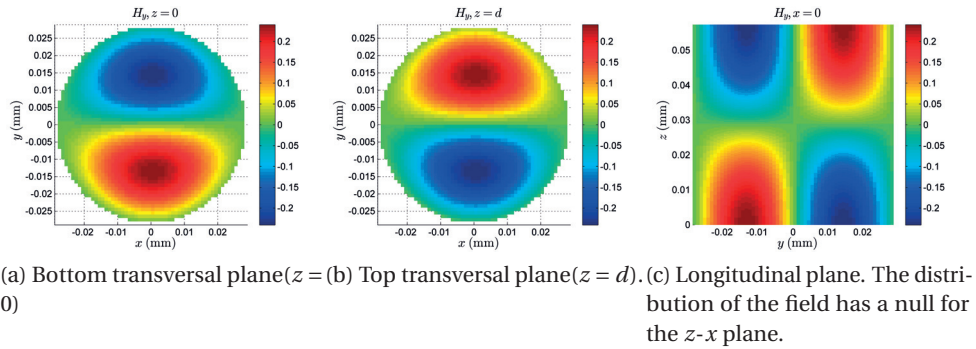


Figure 2.6 –  $H_y$  field component.

### Resonant frequency and quality factor

From an electromagnetic point of view, the physically observable quantities associated to the microwave cavity are the resonance frequency and the quality factor. For the resonance frequency we can write:

$$f_{\text{res, TE}_{01p}} = \frac{1}{2\pi\sqrt{\mu\epsilon}} \left[ \left( \frac{\chi'_{01}}{a} \right)^2 + \left( \frac{p\pi}{d} \right)^2 \right]^{\frac{1}{2}} = \frac{k_{mnp}}{2\pi\sqrt{\mu\epsilon}}, \quad (2.33)$$

where  $k_{mnp}$  can be seen as a resonance wavenumber related to the  $m, n, p$  mode such that:

$$k_{mnp}^2 = k_c^2 + k_z^2. \quad (2.34)$$

The quality factor  $Q$  is defined as:

$$Q = 2\pi \frac{\text{energy stored}}{\text{energy dissipated per cycle}} = 2\pi f_{\text{res}} \frac{W}{P_t}, \quad (2.35)$$

where  $P_t$  is the total dissipated power at resonance which is proportional to the losses in the cavity. Therefore in the case of resonance without losses  $P_t = 0$  and hence  $Q \rightarrow \infty$ . The energy stored  $W$  is the sum of the electric  $W_e$  and magnetic  $W_m$  time-averaged energies given in the steady-state case as:

$$W_e = \frac{\epsilon}{4} \int_{V_c} |\mathbf{E}|^2 dV \quad (2.36)$$

and

$$W_m = \frac{\mu}{4} \int_{V_c} |\mathbf{H}|^2 dV, \quad (2.37)$$

where, at resonance, we have:  $W_e = W_h = W$ . Generally, power is lost in several ways: due to the finite conductivity walls of the cavity  $P_c$ ; dielectric losses in the vapor cell  $P_d$ ; loss due to the Rb vapor presence  $P_v$ ; radiation losses from the apertures  $P_r$ . Therefore, separating the total power lost, we can write for the Q-factor:

$$\frac{1}{Q_u} = \frac{1}{Q_c} + \frac{1}{Q_d} + \frac{1}{Q_v} + \frac{1}{Q_r}, \quad (2.38)$$

where  $Q_u$  is called unloaded Q-factor and can be understood as the intrinsic Q-factor of the cavity without assuming external energy coupling (undriven resonance). Below we discuss ways to estimate the contribution of these terms.

### Losses due to finite conductivity

It is known [25] that when instead of PEC boundaries, finite conductivity is considered, the conducting surface of the cavity can be represented by a complex surface impedance defined as  $Z_s = (1 + j)R_s$ .

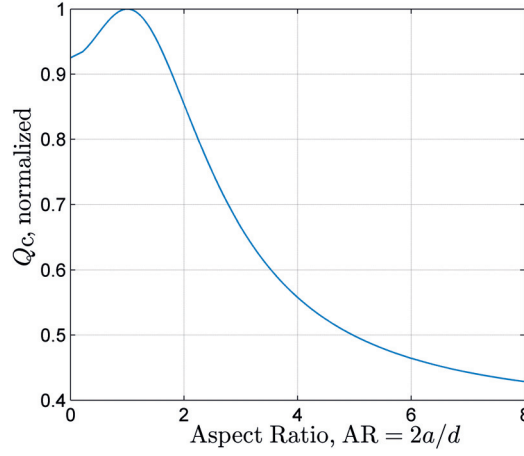


Figure 2.7 – Normalized value of the Q-factor related to the metallic losses shown for a variety of cylindrical TE<sub>011</sub> realizations with  $f_{\text{res}} = f_{\text{clock}}$ .

The  $R_s$  term can be physically understood as an equivalent surface resistance and it is given by:

$$R_s = \left( \frac{\mu_0 \omega_r}{2\sigma} \right)^{1/2} = \frac{1}{\sigma \delta}, \quad (2.39)$$

where  $\sigma$  is the conductivity and  $\delta$  is the skin depth. The quality factor can be obtained as in [25]:

$$Q_c = \frac{2 \int_V |\mathbf{H}|^2 dV}{\delta \int_S |\mathbf{H}_t|^2 dS}. \quad (2.40)$$

In table 2.2 we show the maximum values that can be obtained for the  $Q_c$ , assuming a TE<sub>011</sub> cavity with conducting walls. In figure 2.7 we report how the  $Q_c$  depends on the cavity dimensions.

Material - cavity walls	$\sigma, (S/m)$	$Q_c$
copper	$\approx 5.97 \times 10^7$	$\approx 3.7 \times 10^4$
aluminum	$\approx 3.5 \times 10^7$	$\approx 2.8 \times 10^4$

Table 2.2 – Maximum Q-factor ( $Q_c$ ) that can be achieved in the case of a TE<sub>011</sub> cavity operating at the required clock frequency  $f_{\text{Rb}}$ . Two typical cases are shown: a cavity made of copper and aluminum correspondingly.

### Losses in the dielectric

When the cavity is loaded with a vapor cell having lossy dielectric walls (characterized by complex dielectric constant  $\epsilon = \epsilon' + j\epsilon''$ ) the solution given in eq. 2.32 is generally no longer valid.

We can consider however the much simpler case of a cavity completely filled with a lossy dielectric material for which we have the analytical result [25]:

$$Q_d = \frac{\omega_r W}{P_d} = \frac{\epsilon'}{\epsilon''} \frac{\int_{V_{\text{cavity}}} |\mathbf{E}|^2 dV}{\int_{V_{\text{cavity}}} |\mathbf{E}|^2 dV} = \frac{1}{\tan \delta}, \quad (2.41)$$

where  $\tan \delta$  is the loss tangent. Since the volume of the cavity is always lower than the volume of the cell, this expression serves as the lower limit case for  $Q_d$ . Assuming that the vapor cell will not perturb significantly the  $\text{TE}_{011}$  mode we then have [21]:

$$Q_d = \frac{\omega_r W}{P_d} = \frac{\epsilon'}{\epsilon''} \frac{\int_{V_{\text{cavity}}} |\mathbf{E}|^2 dV}{\int_{V_{\text{cell}}} |\mathbf{E}|^2 dV}. \quad (2.42)$$

In table 2.3 we show what are the corresponding values in the case of two materials that are extensively used for the production of the vapor cells - quartz and Pyrex (borosilicate glass).

Material (cell)	$\epsilon'/\epsilon_0$	$\epsilon''/\epsilon_0$	$\tan \delta$	$Q_d$
Quartz	3.25	0.028	0.0086	116
Pyrex	4.82	0.026	0.0054	185

Table 2.3 – Characteristics of dielectric materials typically used in the production of the vapor cells applied in DR atomic clocks. All values are shown for the required clock frequency,  $Q_d$  corresponds to the case of  $\text{TE}_{011}$  cavity that is fully-loaded with a dielectric material (lower limit).

### Loaded Q-factor and resonance frequency shift

It can be readily seen that the most significant contribution for the losses comes from the dielectric. The effect of the Rb vapor can be separated to losses inside the vapor cell and losses due to a possible metal deposition on the cell walls. However, these effects are small and do not have a significant contribution [21]. Furthermore, the radiation loss can be made negligible if cutoff pipes are considered at the apertures required for the optical pumping. Therefore, by neglecting these minor terms, from 2.38, we can obtain:

$$Q_u = \frac{Q_c Q_d}{Q_c + Q_d}. \quad (2.43)$$

The above-mentioned loss effects are intrinsic and independent on the external energy coupling. In order to take into account the case of a cavity coupled to the external generator we can consider the loaded Q-factor given by:

$$Q_l = \left( \frac{1}{Q_u} + \frac{1}{Q_{\text{ext}}} \right)^{-1} = \frac{Q_u}{Q_u/Q_{\text{ext}} + 1}, \quad (2.44)$$

where  $Q_{\text{ext}}$  is the external Q-factor that accounts for the losses in the load and the coupling mechanism and hence for  $Q_{\text{ext}} \rightarrow \infty \Rightarrow Q_l = Q_u$ .

It is worth noting that in the case of losses, the resonance frequency of the cavity will be shifted from the one given in 2.33. This effect is attributed to the losses themselves as well as to the strength of the energy coupling. An extensive study, including a dedicated lumped element equivalent circuit, can be found in [21].

## 2.2 General design criteria and characterization

After the main physical quantities associated to cavities (field distribution, resonance frequency and Q-factor) were introduced in section 2.1, the next step is to relate them to the atomic clock application. In this section we show how the clock operation relates to the fields in the cavity, what requirements hold as well as ways to evaluate the performance.

### 2.2.1 Definition of the driving fields

It was shown (section 1.3.1) that for the DR regime in our case, the atomic response is characterized by three magnetic resonance transitions:  $\sigma_-$ ,  $\pi$  and  $\sigma_+$  that can be described with their corresponding Rabi frequencies which, following the formalism from [26], can be expressed as:

$$\begin{aligned}\Omega_-(\mathbf{r}) &= \frac{\sqrt{3}\mu_B}{\sqrt{2}\hbar} B_-(\mathbf{r}), \\ \Omega_\pi(\mathbf{r}) &= \frac{\mu_B}{\hbar} B_\pi(\mathbf{r}), \\ \Omega_+(\mathbf{r}) &= \frac{\sqrt{3}\mu_B}{\sqrt{2}\hbar} B_+(\mathbf{r}),\end{aligned}\tag{2.45}$$

where  $\mu_B$  is the Bohr magneton and  $\hbar$  is the reduced Planck constant. The external fields  $B_-$ ,  $B_\pi$ ,  $B_+$  are referred as "driving fields" and are defined as a function of the standing magnetic field at a given point  $\mathbf{r}$  inside the volume:

$$\begin{aligned}B_-(\mathbf{r}) &= \mathbf{B}_{xyz}(\mathbf{r}) \cdot \hat{b}_- = \frac{1}{\sqrt{2}} [B_x(\mathbf{r}) + jB_y(\mathbf{r})], \\ B_\pi(\mathbf{r}) &= \mathbf{B}_{xyz}(\mathbf{r}) \cdot \hat{b}_\pi = B_z(\mathbf{r}), \\ B_+(\mathbf{r}) &= \mathbf{B}_{xyz}(\mathbf{r}) \cdot \hat{b}_+ = \frac{1}{\sqrt{2}} [B_x(\mathbf{r}) - jB_y(\mathbf{r})],\end{aligned}\tag{2.46}$$

where the magnetic field provided by the cavity is expressed in the standard basis and the circular complex basis is defined with its unit vectors as:

$$\hat{b}_- = \frac{1}{\sqrt{2}} (\hat{x} + j\hat{y}), \quad \hat{b}_+ = \frac{1}{\sqrt{2}} (\hat{x} - j\hat{y}), \quad \hat{b}_\pi = \hat{z}.\tag{2.47}$$

In our case, the operation of the clock is based on the  $\pi$ -transition, driven by the magnetic field component directed along a quantization axis (see section 1.3.1). In eq.2.47 and 2.46 we consider the axis of the cavity aligned to the quantization axis and hence the chosen transition is driven only by the longitudinal magnetic field  $H_z$ .



## 2.2. General design criteria and characterization

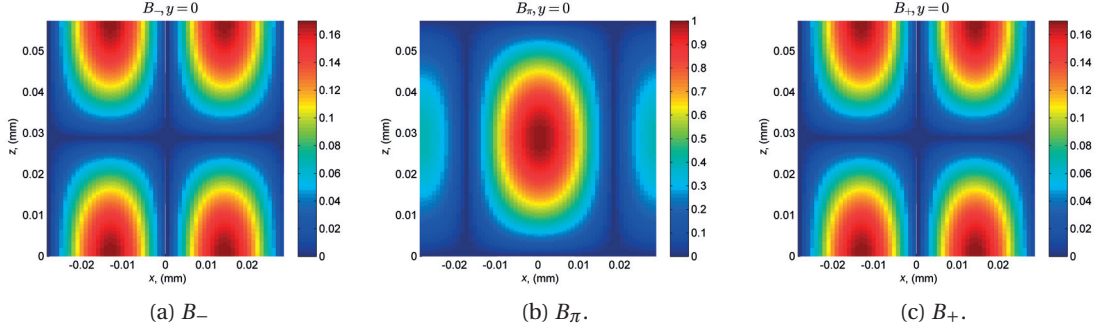


Figure 2.8 – Calculated driving fields inside a  $TE_{011}$  cavity with  $AR = 1$ . All driving fields are characterized by azimuthal symmetry and hence all longitudinal planes are identical to the shown.

Since the linearly polarized transverse magnetic field in the cavity can be seen as a superposition of oppositely circularly polarized standing waves, it is evident that in eq. 2.46,  $B_-$  can be considered as the "left-handed" and  $B_+$  as the "right-handed" circularly polarized component in the plane perpendicular to the cavity axis. Because for the standing wave there is no propagation vector defined, we have used a convention that defines the polarization with respect to the orientation of cavity axis considered from the point of view of the laser source towards the detector. We note, that this description is the opposite to the one used in the physics literature – usually the direction in that case is defined towards the source. In the case of the simple cylindrical geometry, it is straight-forward to calculate the field distribution and to directly obtain the corresponding driving fields: figures 2.8 and 2.9.

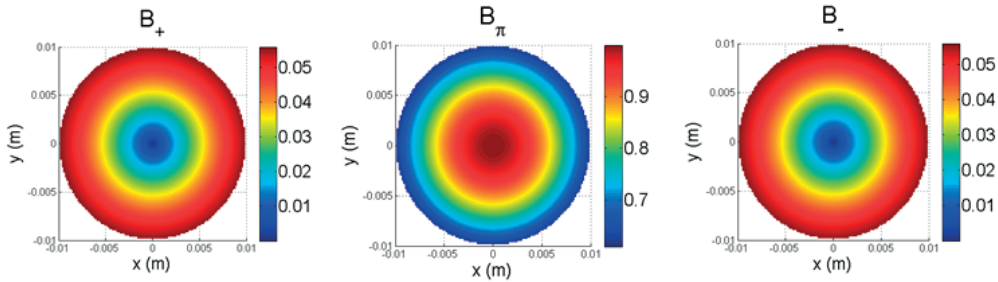


Figure 2.9 – Calculated 2D field profiles corresponding to the driving fields that interact with the atoms inside the vapor cell. The field amplitudes are averaged along the direction of the laser light –  $z$  and are shown normalized to the maximum (found in the center for the case of the  $TE_{011}$  mode). Each component is color-coded separately.

### 2.2.2 Figures of Merit

In this section, we first introduce various figures of merit that can be used to evaluate the performance of the cavity in line with the performance of the clock. Then we consider the case of the cylindrical geometry with a cylindrical vapor cell, for which we evaluate the efficiency, the amount of field alignment to the chosen quantization axis and the homogeneity of the field amplitude.

In section 1.3.3 it was explained that, for the case of the Rb clock, the frequency stability can be related to the atomic Q-factor and the signal-to-noise ratio. It can be readily seen that the design of the cavity needs to allow for a high signal-to-noise ratio, while at the same time it needs to permit a high atomic Q-factor associated to the atomic resonance. In the following section we will discuss two main properties of the microwave cavity that both have an impact on the clock signal contrast and thus on the clock stability: the uniformity (orientation) of the microwave magnetic field and the amplitude homogeneity of the same field.

#### Field uniformity

One way to improve the signal-to-noise ratio is to increase the fraction of Rb atoms that interact with the proper driving field. Therefore, a good design is able to provide only the required  $B_\pi$  component over the biggest possible volume of the vapor cell. From figure 2.9 it can be qualitatively seen that while the biggest part of the magnetic field in the cavity is attributed to the clock transition, part of the field also drives the unwanted  $\sigma_-$  and  $\sigma_+$  transitions. Because the cavity has a relatively low Q-factor with respect to the atomic resonance, the transverse magnetic field is able to drive the unwanted  $\sigma_-$  and  $\sigma_+$  transitions which are characterized by frequencies close to the frequency of clock transition. In figure 2.10 we show the contribution of the unwanted transitions to the total optical signal, detected in continuous-wave DR mode.

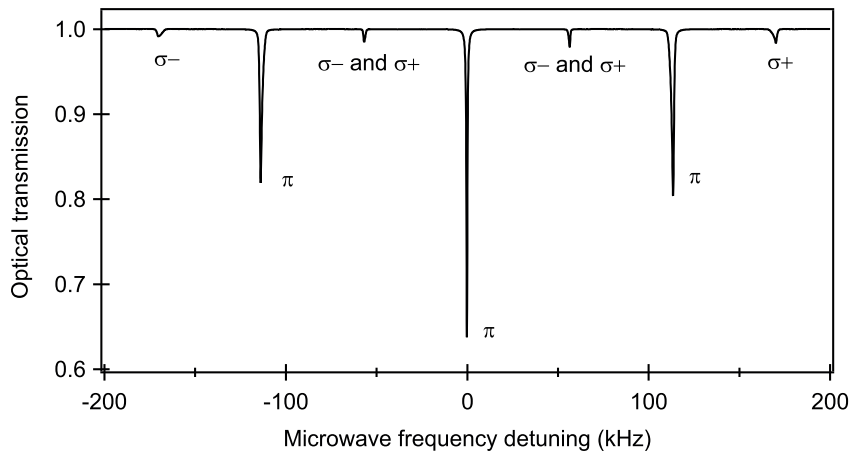


Figure 2.10 – A Zeeman-split spectrum of the atomic microwave transition recorded in a continuous-wave DR mode. The central line, around the zero frequency detuning, corresponds to the required clock transition for which the cavity needs to be designed to maximize.

– **Filling Factor** First we introduce a figure of merit known as Filling Factor (FF) which is traditionally used to describe the amount of cavity-atom coupling in active masers [14] (chapter 6.2, 6C):

$$FF = \frac{V_{\text{Rb}} \langle |H_z|^2 \rangle_{\text{Rb}}}{V_{\text{cavity}} \langle |\mathbf{H}|^2 \rangle_{\text{cavity}}} = \frac{V_{\text{Rb}}}{V_{\text{cavity}}} \frac{\left( \frac{1}{V_{\text{Rb}}} \int_{V_{\text{Rb}}} |H_z| dV \right)^2}{\left( \frac{1}{V_{\text{cavity}}} \int_{V_{\text{cavity}}} |\mathbf{H}|^2 dV \right)} = \frac{\left( \int_{V_{\text{Rb}}} |H_z| dV \right)^2}{V_{\text{Rb}} \int_{V_{\text{cavity}}} |\mathbf{H}|^2 dV}. \quad (2.48)$$

Physically it shows how much of the total energy provided by the cavity is used to drive the clock transition. Both terms  $\langle \rangle_{\text{Rb}}$  and  $\langle \rangle_{\text{cavity}}$  correspond to averaging over the related volume, with all volume elements considered having equal weight and static magnetic field defined along the  $z$ -axis such that  $|H_z| \equiv |H_\pi|$ . For the conditions in the maser the atoms are in a random motion in the volume of the cell and hence 'see' the spatially averaged strength of the standing wave field. In eq. 2.48 this effect is considered in the numerator where  $\langle |H_z|^2 \rangle$  is the square of the average over the cell volume. It is known that in vapor cell clocks, due to the buffer-gas added to the cell, the atoms can be considered spatially localized (stationary) for timescales relevant for the DR signal [16]. Therefore, hereafter it is appropriate to consider figures of merit that explicitly take into account such a localized-atom approximation.

– **Filling Factor (stationary atoms)** We introduce a modified version of the FF in the case of stationary atoms [20]:

$$FF_s = \frac{V_{\text{Rb}} \langle |H_z|^2 \rangle_{\text{Rb}}}{V_{\text{cavity}} \langle |\mathbf{H}|^2 \rangle_{\text{cavity}}} = \frac{\int_{V_{\text{Rb}}} |H_z|^2 dV}{\int_{V_{\text{cavity}}} |\mathbf{H}|^2 dV}. \quad (2.49)$$

– **Efficiency Factor** For completeness, we can also define Efficiency Factor (EF), as the amount of energy (attributed to  $H_z$ ) that is available to the atoms, relative to the total volume of the cavity:

$$EF = \frac{\int_{V_{\text{Rb}}} |H_z|^2 dV}{\int_{V_{\text{cavity}}} |\mathbf{H}|^2 dV}. \quad (2.50)$$

– **Field Orientation Factor** In order to obtain a measure of the field orientation across the vapor cell which is more appropriate for DR atomic clocks, Field Orientation Factor (FOF) can be defined as in [16] and [27]:

$$FOF = \frac{\int_{V_{\text{Rb}}} |H_z|^2 dV}{\int_{V_{\text{Rb}}} |\mathbf{H}|^2 dV}. \quad (2.51)$$

One advantage of this figure of merit is that it can be directly experimentally verified – the experimental FOF can be obtained from the equation:

$$FOF_{\text{exp}} = \frac{\int S_\pi df}{\int S_\pi df + \int S_{\sigma_-} df + \int S_{\sigma_+} df}, \quad (2.52)$$

where  $\int S_\pi df$  and  $\int S_{\sigma_{+,-}} df$  can be determined from the detected optical signal and correspond to the signal transmission strength that can be obtained by integration of the curves along the frequency detuning – figure 2.10. While the FF shows how much of the cavity field is used, the FOF is related to the quality of  $H$ -field orientation inside the active volume of the cavity and it is hence directly related to the clock signal.

From definitions 2.48 and 2.50 it can be seen that the requirement for a high signal-to-noise ratio and hence a large active volume  $V_{\text{Rb}}$  comes on the expense of a reduced cavity-atom coupling. Therefore, a trade-off exists between the size of the vapor cell and the amount of useful field provided by the chosen cavity geometry.

### Figures of merit related to the homogeneity

The homogeneity of the  $H_z$  field amplitude across the vapor cell is of a high importance for the signal-to-noise ratio and thus for the achievable clock stability. For example, a variations of the amplitude results in a spatial region of the localized atoms experiencing incomplete transitions during the interrogation phase. In a pulsed operation mode this leads to a reduction of the clock signal amplitude [7]. The spatial distribution of the field is a subject to boundary conditions and it is hence impossible for the ensemble of atoms to interact with equal field amplitude. Furthermore, a position-dependent microwave power shift of the clock transition can lead to an inhomogeneous broadening of the clock signal, which may reduce the atomic Q-factor and degrade the clock stability. The field homogeneity is therefore an important characteristic that needs to be specifically targeted in the cavity design.

– **Field histogram** A direct way to estimate the theoretical homogeneity of the field is to obtain a 2D field map and to plot the isoclines (contour plot). This approach is intuitive but has a limited application since we often want to compare very different geometries. Instead, a field histogram approach, known also in the magnetic resonance community [28], is suitable to apply in order to assess the total field homogeneity. In this case, the field is uniformly sampled over the active volume of the cavity with a resolution allowing an accurate field representation. The variation of the obtained  $|H_z|$  distribution can be represented by a histogram  $N(|H_z|)$  vs  $|H_z|$ , where  $N(|H_z|)$  is the number of sampling points having the field in the interval  $(|H_z| - \delta) \leq |H_z| \leq (|H_z| + \delta)$ ;  $\delta$  is the resolution of the histogram, chosen lower than the resolution of the obtained field. Because different geometries are characterized by different distributions a normalization is considered: the horizontal axis corresponds to  $(|H_z| - (|H_z|)_{\text{max}}) / (|H_z|)_{\text{max}}$  which is the relative deviation of the field amplitude,  $(|H_z|)_{\text{max}}$  being the field obtained in the center. The relative number of sampled points with field amplitudes in a chosen variation range  $(N(|H_z|) / N_{\text{total}})$  corresponds to the amount of volume inside the cell that sees field with the corresponding variation. Therefore, since the atoms are considered localized and uniformly distributed, this volume corresponds to the relative amount of atoms. In figure 2.11, a typical example of such a histogram is shown for the case of the cylindrical cavity. Since the maximum value is found in the center  $(|H_z|)_{\text{max}}$ , the histogram is in the range -1 to 0. However, this range is different for other geometries where the maximum is not necessary in the center.

### 2.3. Figures of merit in the case of the cylindrical cavity loaded with a cylindrical vapor cell

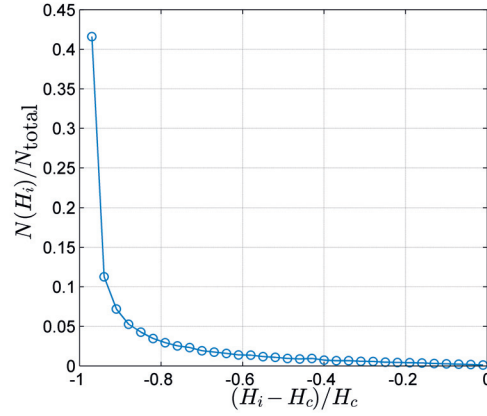


Figure 2.11 – A histogram plot.  $H_c$  corresponds to the field amplitude found in the center.

– **Bulk homogeneity** For given cell dimensions, it is possible to calculate the total field homogeneity by comparing the total energy available in the volume to the ideal case of zero variation:

$$h = \frac{\int_{V_{\text{Rb}}} |H_z|^2 dV}{\int_{V_{\text{Rb}}} (|H_z|^2)_{\text{max}} dV}. \quad (2.53)$$

In this case a hypothetical, ideal cavity is able to provide a constant field to all atoms and it is hence characterized by  $h = 1$ . While eq. 2.53 corresponds to a simple measure of the homogeneity, the histogram approach gives a more detailed information about the specific variation inside the volume.

### 2.3 Figures of merit in the case of the cylindrical cavity loaded with a cylindrical vapor cell

It was already mentioned that the often preferred type of a microwave cavity is the one of a simple circular shape where in practice it is fabricated from metal and thus approximating the PEC boundary conditions. In this cylindrical geometry, the vapor cell can be easily accommodated and the coils required for the static magnetic field can be precisely machined directly to the walls. In principle, for the case of a translational symmetry, one can always design a cylindrical cavity that resonates at the frequency of interest  $f_{\text{clock}}$ , starting from an arbitrary radius  $a$  and obtaining the corresponding cavity height  $d(a)$ . From eq. 2.33 for a given  $a$  we can find the length of the cavity  $d$  that fulfills the requirement  $f_{\text{res}}$ :

$$d = \sqrt{\frac{(pa_{\frac{c}{2}})^2}{(af_{\text{res}})^2 - (\chi'_{01 \frac{c}{2\pi}})^2}}. \quad (2.54)$$

Therefore, a cavity with  $a = a_{\text{cutoff}}$  is characterized by  $d \rightarrow \infty$  and  $K_z \rightarrow 0$ .

In figure 2.12a we report the dimensions related to a variety of possible realizations of such a cylindrical cavity resonating at  $f_{\text{Rb}}$ . The corresponding volume is shown in figure 2.12b, where it is convenient to include both dimensions by defining a parameter called Aspect Ratio:  $\text{AR} = \frac{2a}{d}$ . In this discussion we consider the vapor cell to be cylindrical, situated in the center of the cavity and with dimensions defined relative to the dimensions of the cavity for the chosen AR – figure 2.13a.

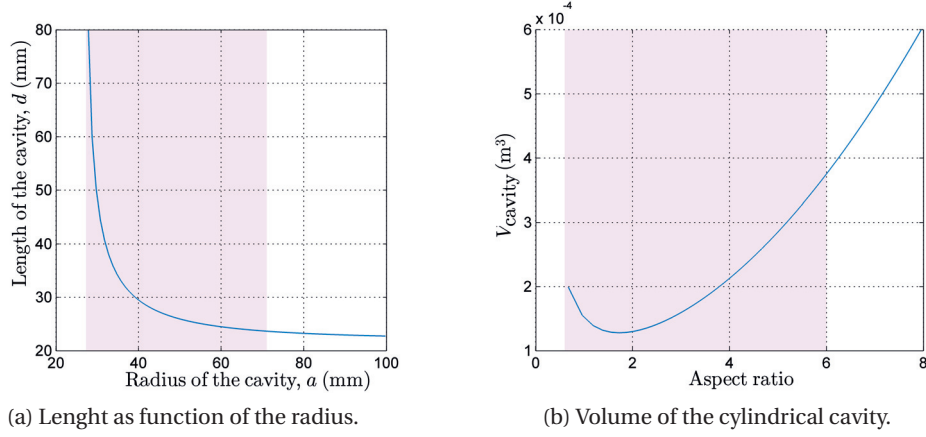


Figure 2.12 – Possible dimensions of a  $\text{TE}_{011}$  cylindrical cavity with  $f_{\text{res}} = f_{\text{Rb}} = 6.834 \times 10^9$  Hz.

For the mode of interest, the distribution of the favorable  $H_z$  field is such that a 180 phase change occurs at  $\approx 0.62a$ , independent on the chosen AR (represented by the shaded area in figure 2.13b). Therefore, the size of the vapor cell will be considered according to  $0 \leq b \leq 0.62a$ . In figure 2.14 the cavity volume is shown relative to the volume of a realistic vapor cell that is used in practice. The cell is considered with its center aligned to the center of the cavity, such that it allows for the largest number of atoms to interact with the required field component –  $H_z$ . In the figures 2.12a, 2.12b and 2.14 the shaded area corresponds to the somewhat practically realizable geometries with aspect ratios in the range:  $0.5 \leq \text{AR} \leq 6$ .

### Homogeneity of the cylindrical cavity

For a cavity based on a translational symmetry, it was discussed that the field distribution can be separated into transverse (along the cavity radius), and longitudinal (along the cavity height). The former is predetermined by the shape of the cross-sectional boundary condition, hence, in our case, the Bessel function of the first kind and order zero. The intrinsic field variation associated to the circular cross section is shown on a homogeneity plot that can be seen in figure 2.15. It is calculated via the histogram approach (as explained in section 2.2.2), however we show the cumulative field variation – e.g. 0.8 on the  $x$ -axis corresponds to values in the range  $(|H_z|)_{\text{max}} \leq 0.8(|H_z|)_{\text{max}}$ . As expected, the sinusoidal field dependence along the  $z$  axis further reduces the homogeneity. It is important to note that since it is the shape of the field that determines the spread of values, both curves shown are independent on the aspect ratio as long as the whole volume of the cavity is considered. The next step is to investigate the field homogeneity in the case of a cavity with a vapor cell included.

### 2.3. Figures of merit in the case of the cylindrical cavity loaded with a cylindrical vapor cell

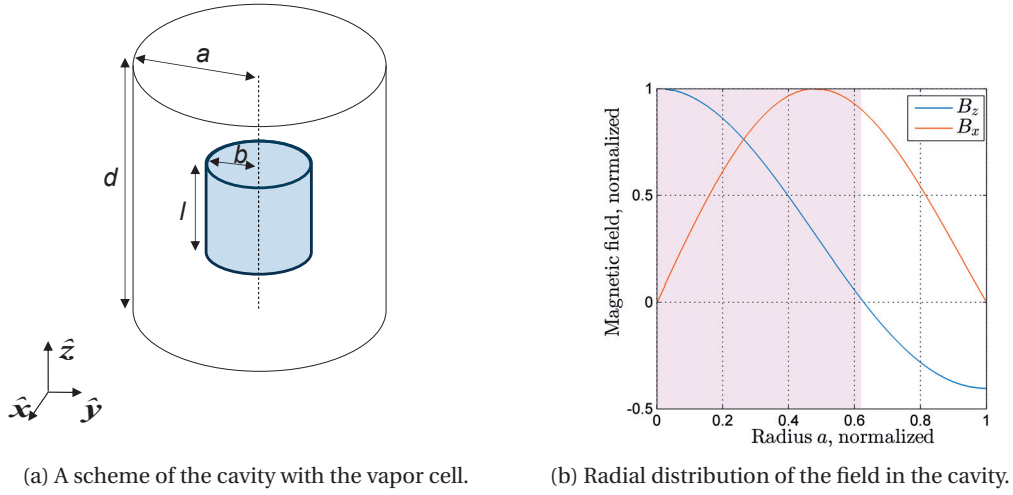


Figure 2.13 – A scheme of the standard cavity with the vapor cell included.

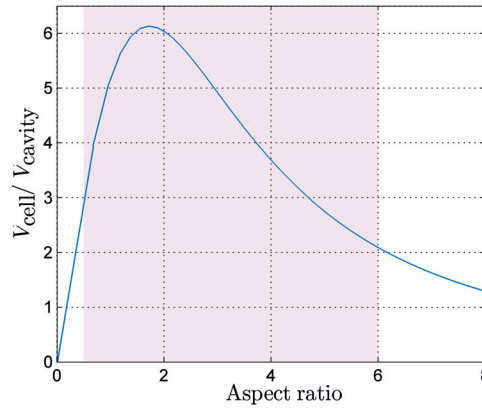


Figure 2.14 – Relative amount of the usable active volume, as function of the AR for a  $\text{TE}_{011}$  cylindrical cavity with  $f_{\text{res}} = 6.834 \times 10^9$  Hz. The dimensions of the cell are: radius  $b = 0.01$  m, height  $l = 0.02$  m.

Let's first consider a cavity loaded with a cell having a zero height. By reducing the relative radius  $b/a$  of this 2D cell, we observe improvement of the homogeneity on the expense of the amount of useful field "picked" by the cell. This effect is calculated and shown for two different values of cell radius, represented by the dashed lines in figure 2.16a. If for a fixed radius of the cell, its relative length  $l/d$  is increased, the field homogeneity degrades due to the additional sinusoidal variation along the  $z$  direction. The worst homogeneity is then found in the case of  $l = d$  (the solid lines in figure 2.16a). The shaded region corresponds to the interval  $0 \leq l/d \leq 1$ . In figure 2.16b we show the field variation as function of the normalized cell length  $l/d$ .



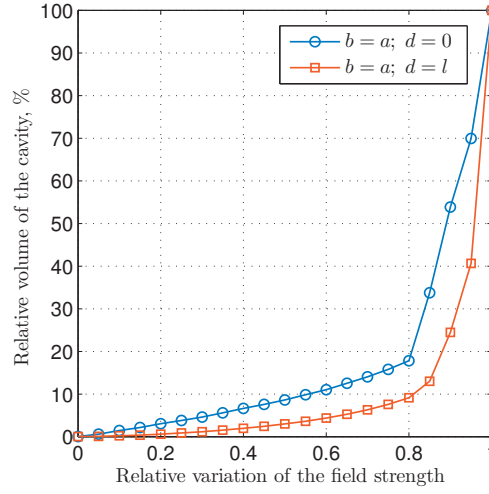
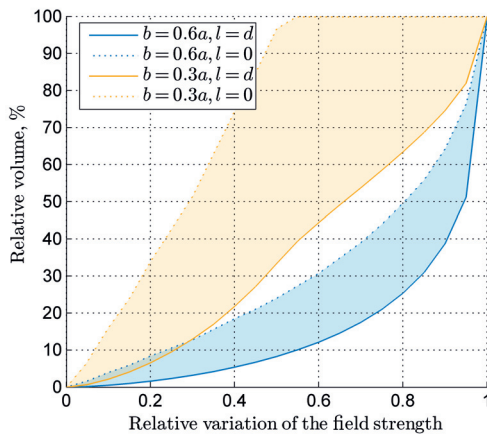


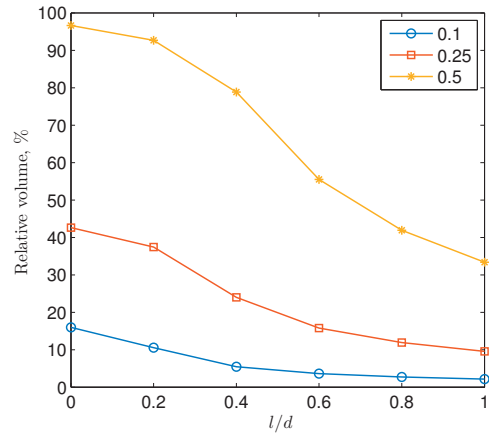
Figure 2.15 – Homogeneity plot of the  $H_z$  field amplitude calculated based on the field histogram approach. The relative amount of the cavity volume that can be attributed to the normalized variation of the field amplitude is shown  $(1 - |H_z|/(|H_z|)_{\max})$ . For example, 0.8 on the  $x$  axis corresponds to the range  $(|H_z|)_{\max} \leq x < 0.8(|H_z|)_{\max}$  and hence it can be obtained what is the relative amount of the volume that will interact with  $|H_z|$  field varying by not more than 80% from the maximum. The case  $d = 0$  is attributed to the 2D distribution only.

For the case of the cylindrical cavity the previously discussed metric, bulk homogeneity, can be analytically obtained [21]:

$$h = \frac{\int_{V_{\text{Rb}}} H_z(r, \phi, z)^2 dv}{\int_{V_{\text{Rb}}} H_z(0, 0, 0)^2 dv} = \frac{1}{2} \left( 1 + \frac{\sin(\pi l/d)}{\pi l/d} \right) \left[ J_0^2 \left( p'_{01} \frac{b}{a} \right) + J_1^2 \left( p'_{01} \frac{b}{a} \right) \right]. \quad (2.55)$$



(a) Homogeneity plot.



(b) Homogeneity as a function of the vapor cell length shown for three variation intervals. The radius of the considered vapor cell is  $b = a \times 0.3$ .

Figure 2.16 – Homogeneity in the  $\text{TE}_{011}$  cavity for vapor cells with different size.



## 2.4 Figures of merit – how to find the optimal case

In this part of the study we want to evaluate the performance of the geometry and draw some conclusions for the most optimal case. To do that, the full range of the possible dimensions for the cavity and the cell needs to be covered. This is most conveniently done using 2D color maps that can be associated to the corresponding figures of merit (figures: 2.17 – 2.21). For the chosen cavity geometry each color map is related to a specific figure of merit shown for a sweep of the possible dimensions of the vapor cell. The cell is considered cylindrical with both radius and height normalized to the cavity ones, where the radius is shown on the  $x$ -axis and the height is along  $y$ . In order to be able to compare the performance among different geometries, contour plots of common cell volumes are shown where each curve corresponds to the volume of a vapor cell normalized to the volume of the referent vapor cell (with standard dimensions: radius  $b = 10$  mm and length  $l = 20$  mm). Therefore, the standard cell is represented by the unit curve.

### 2.4.1 The case of a standard cylindrical geometry

In order to fully cover the range of possible geometries we have chosen to plot three separate cases for the aspect ratio:  $AR = 1, 3, 6$ . The 2D plots associated to the figures of merit related to the field uniformity are shown in figures 2.17, 2.18 and 2.19, while the ones related to the homogeneity of the field are shown in figures 2.20 and 2.21. It is immediately seen that the  $FF$  and  $FF_s$  are somewhat proportional to the volume of the cell, while the "purity" of the driving field (FOF) and the homogeneity are degrading with increasing of the cell volume. Therefore the 2D diagrams represent a trade-off between the amount and the quality of the microwave field required for the clock transition.

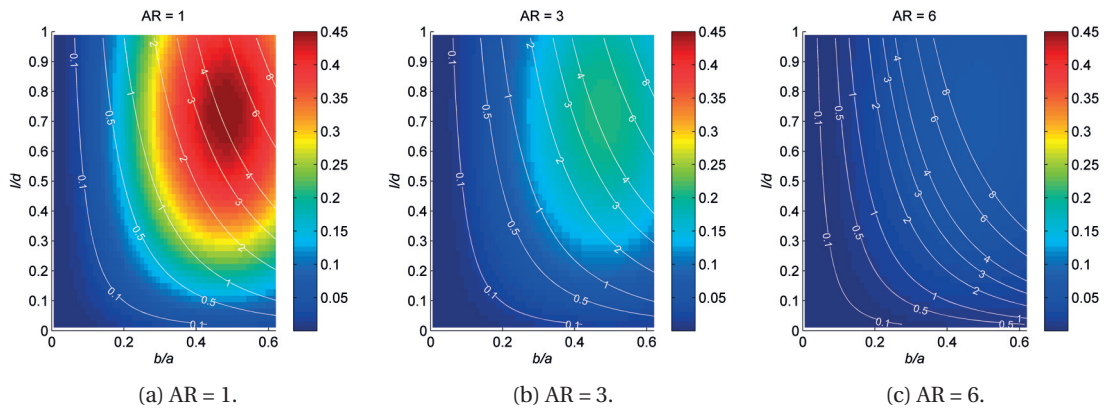


Figure 2.17 – Filling Factor (FF) calculated for the case of the cylindrical cavity.

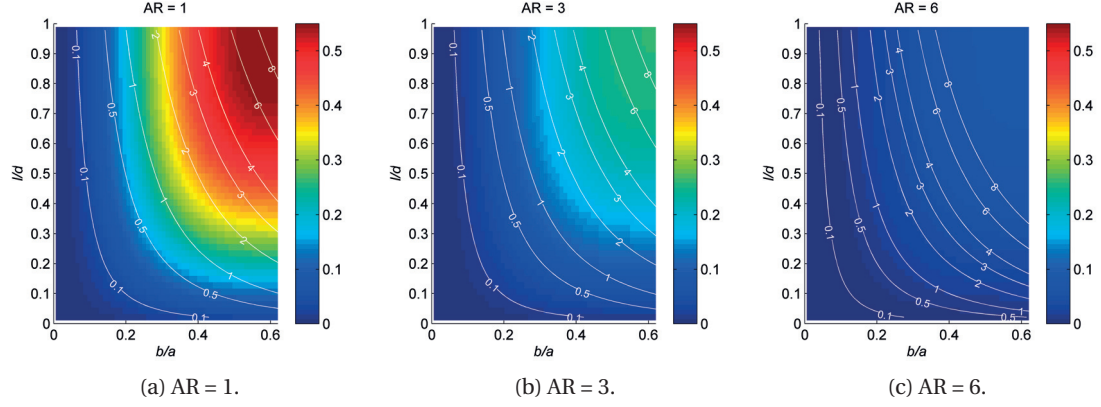


Figure 2.18 – Filling Factor for the case of stationary atoms ( $FF_s$ ) calculated for the cylindrical cavity.

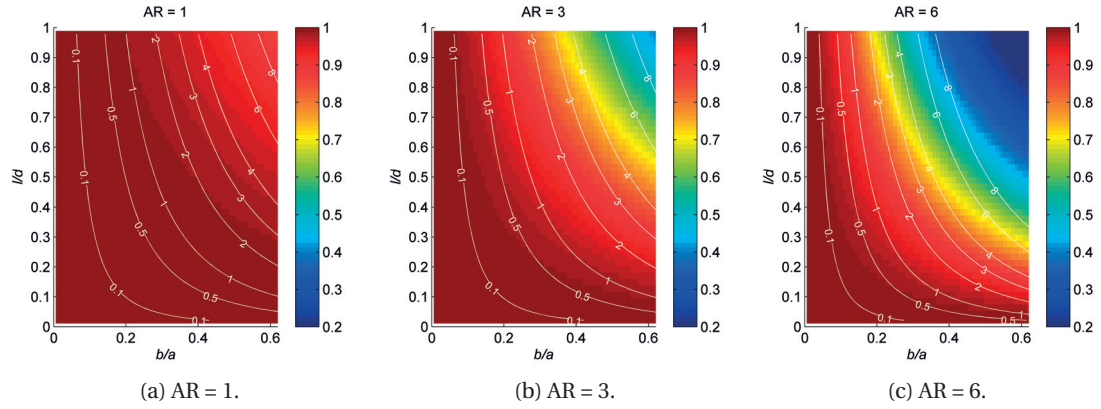


Figure 2.19 – Field Orientation Factor (FOF) for the case of the cylindrical cavity.

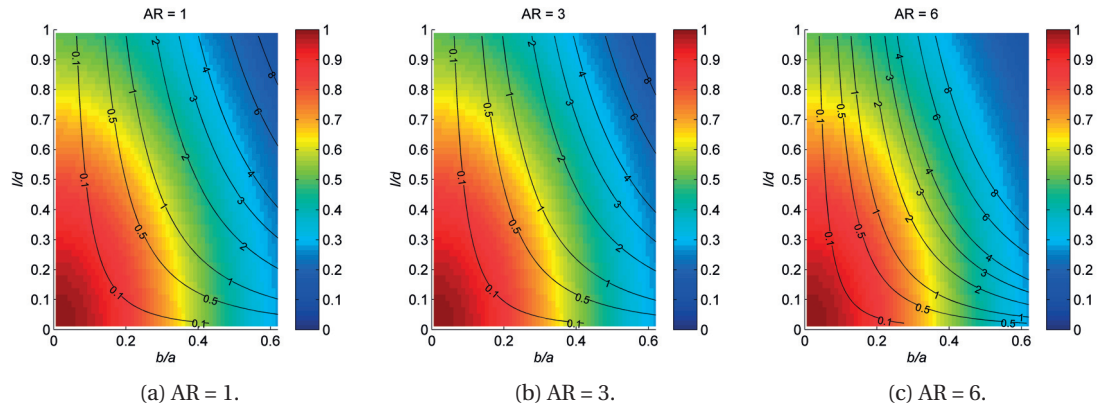


Figure 2.20 – Bulk homogeneity (in [21] it is originally referred as "uniformity index" as defined in eq. 51.). An ideal cavity with a fully-homogeneous field amplitude is characterized by unity.

## 2.4. Figures of merit – how to find the optimal case

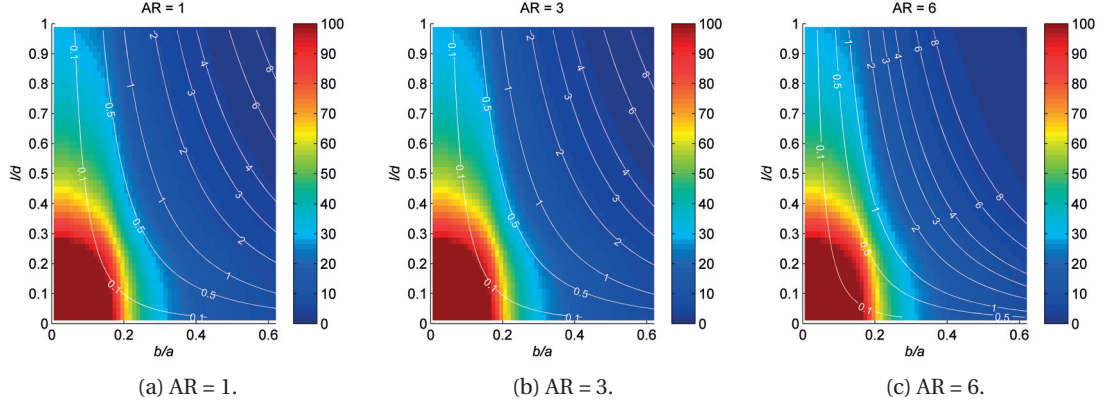


Figure 2.21 – Relative amount of the active volume that "sees" field amplitude with 10% variation from the maximum. The figure is calculated based on the field-histogram approach explained in section 2.2.2.

The filling factor (figures 2.17, 2.18) can be interpreted as the coupling strenght between the magnetic field provided by the cavity and the resonance clock transition. It is hence a measure of the design efficiency – if all other parameters are fixed a cavity with a lower FF would require more microwave power compared to a cavity for which the FF is higher.

It was shown [16] that the FOF is a reliable estimator (preferable to the FF) of the double-resonance performance. However, from a cavity point of view, the high-performance could not be attributed solely to high FOF because the latter does not hold information about the absolute amount of favorable field. If the quality of the field is kept constant the larger is the volume of the vapor cell the more atoms contribute to the resonance absorption and hence the signal-to-noise ratio is increased. Therefore we are, in principle, interested in maximizing the number of (coherent) atoms interacting with the beneficial field .

From figure 2.19a can be seen that for the circular cavities with a small AR the FOF is very high even for vapor cells with a very large volume (situated at the upper right corner of the diagrams). When the aspect ratio is increased, the FOF is degraded (figures 2.19b and 2.19c). This is attributed to the fact that the field driving the unwanted sigma-transitions is mostly situated in the vicinity of the bottom and top of the cavity and these geometries being short, introduce too much unwanted field even for relatively short vapor cells. This is the reason why in terms of FOF, in the case of the cylindrical geometry, it is generally preferable to choose a vapor cell having a smaller radius. This is easily seen in figure 2.19c where for a constant volume, vapor cells with lower radius have an advantage in terms of FOF. From figures 2.20 and 2.21 can be seen that the homogeneity of the field (amplitude) is faster degraded by increasing the cell radius than by increasing the cell height. This is expected considering the different field distribution along the radius and the height of the cell. From the family of the contour lines it can be seen that an optimal case is to choose vapor cells with  $AR \approx 1$ . It is worth noting, that in the case of cavities with high aspect ratio (ex.  $AR = 6$  in figure 2.20c) the homogeneity is improved at the expense of a degraded FOF.



## 3 Cavities with modified geometry

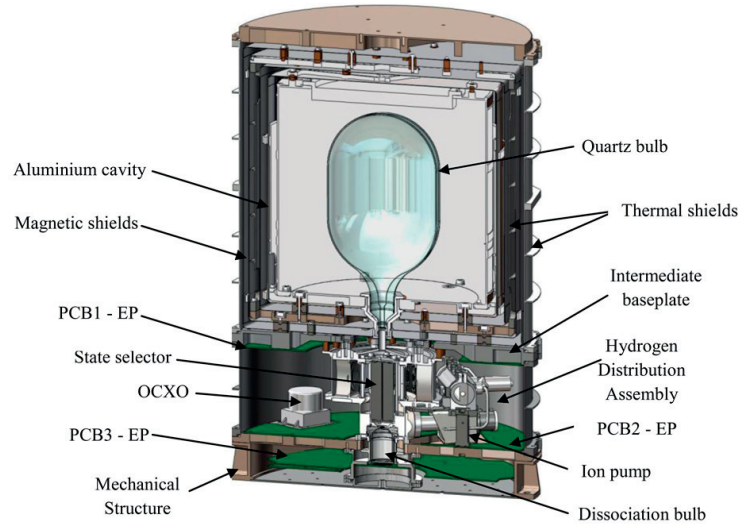
### 3.1 State-of-the-art development

In order to investigate what general directions have been taken to improve the design of the microwave cavity we first focus on the two types of frequency standards based on a microwave resonance: masers and passive Rb clocks. In this context we will discuss cavities developed in order to allow miniaturization as well as improved temperature performance. We will then focus on a specific class of geometries (the loop-gap) for which it is suitable to consider various developments in the domains of Electron Paramagnetic Resonance (EPR), Nuclear Magnetic Resonance (NMR) and Magnetic Resonance Imaging (MRI).

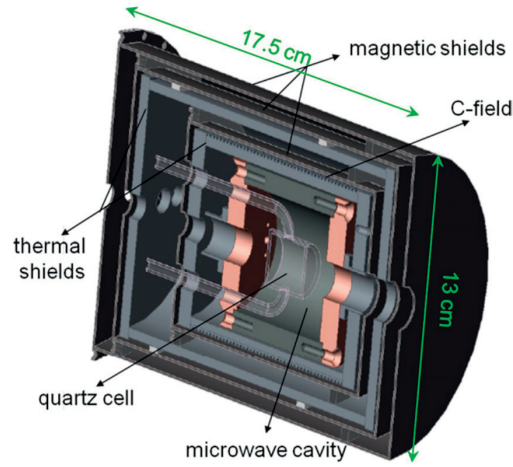
#### 3.1.1 Size reduction

Historically, the first realizations of such atomic standards have been based on the empty cylindrical cavity (discussed in-depth in section 2.3) which is an application dating over fifty years ago [30]. The first and foremost incentive for the development of new types of microwave resonance structures comes from space applications for which, in the beginning, the typical physics package of the maser has proven to result in a fairly large and impractical device [15]. From figure (3.1) is obvious that the volume of the physics package (and hence of the final device) is largely dictated by the size of the cavity. From the discussion in the previous chapter is evident that it is, in principle, impossible to obtain a reduction of the size without affecting various aspects of the physics package and hence the performance of the clock: the signal-to-noise ratio (related to the amount of Rb atoms and hence the size of the vapor cell), the efficiency, the temperature stability of the resonance frequency and the Q-factor to name a few. In the development of the cavity design, a trade-off between miniaturization and performance is dictated by the application of interest.

In order to reduce the size of the atomic clock cavity, historically, three main approaches have been taken. A cavity with a non-traditional structure and (or) a mode can be considered. Alternatively, the classically used geometry can be dielectrically loaded with. Finally, a cavity miniaturization based on a loop-gap structure is also possible.



(a) Hydrogen maser [29] (courtesy of SpectraTime, Switzerland).



(b) Vapor-cell Rb frequency standard working in a pulsed regime, originally published in [5].

Figure 3.1 – Schematic view of the physics package in the case of a hydrogen maser and a pulsed Rb clock. In both cases a standard  $TE_{011}$  cavity geometry is used.

#### Non-traditional structures

A good example where the first approach is taken is the cylindrical geometry operating at the  $TE_{111}$  mode. At this mode the cavity is characterized by a longitudinal (along  $z$ ) magnetic field distribution that is zero along the central axis and increases towards the walls. The volume of the  $TE_{111}$  cavity is almost half of the conventional, which is why this structure has attracted attention for application in masers [31] – shown in figure 3.2 (A). A considerable disadvantage of this mode is that the field lines are in directions opposite with respect to the central axis which is the reason why usually for maser applications an additional dielectric septum is added in order to separate the two halves and prevent atoms to sample across both regions. In this way the two parts can be roughly considered to contribute equally to the quality of the observed signal. In principle it is possible to apply the idea to the double resonance Rb clock, because of the presence of a buffer gas that significantly reduces the mobility of atoms and therefore, in that case, a septum is not necessary. This approach is taken in [40], where a highly compact volume of the cavity is obtained:  $\approx 20 \text{ cm}^3$ . However, such a configuration of the field is not favorable in terms of optical pumping, where it is usually convenient to position the light beam in the center of the cavity. A very compact structure appropriate for Rb standards was proposed in [32] and [41] – shown in figure 3.2 (B). It is based on a modified coaxial structure, for which the central electrode is offsetted towards the circumferential wall of the cavity in order for the central region to be used for the dielectric cell. Since this cavity operates at the TEM mode, the field lines pass through the vapor cell and hence can be used to excite the atoms. With a volume of  $\approx 1 \text{ cm}^3$ , this is on a par with the most compact resonators available for miniature Rb standards. Another design based on a rectangular geometry and  $TE_{101}$  mode can be found in [33]. Similar to [31], this mode is characterized by a minimum of the magnetic field in the center of the cavity and a maximum that is close to the metal walls. However in this particular structure a dielectric slab is inserted such that the field lines are displaced towards the center and hence enough magnetic flux (with the proper orientation) is allowed to pass through the vapor cell and couple to the atomic resonance (figure 3.2 (C)). The overall volume of this device is  $\approx 4.6 \text{ cm}^3$  while the useful volume is  $\approx 3.3 \text{ cm}^3$  which makes it an appropriate choice mostly for miniature standards based on Rb. It is worth noting that this structure is characterized by a relatively homogeneous magnetic field distribution [42]. However, the rectangular cross section is not the most practical choice to accommodate a vapor cell with a circular cross section.

#### Cavities with dielectric filling

It is possible to reduce the size of the cavity by introducing a dielectric filling. This approach is typically used in the case of space-born maser applications. The main idea is to start from the classical  $TE_{011}$  cavity and introduce a thin and hollow dielectric cylinder (a tube) along the axis. In this case the vapor cell (the bulb of the maser) is situated inside the dielectric tube with a radius limited by the radius of the tube. While in principle the modes in such a radially-stratified structure are hybrid, for a zero azimuthal modal number, pure TE modes still exist and the field distribution can be obtained analytically [43, 34] – shown in figure 3.2 (D).



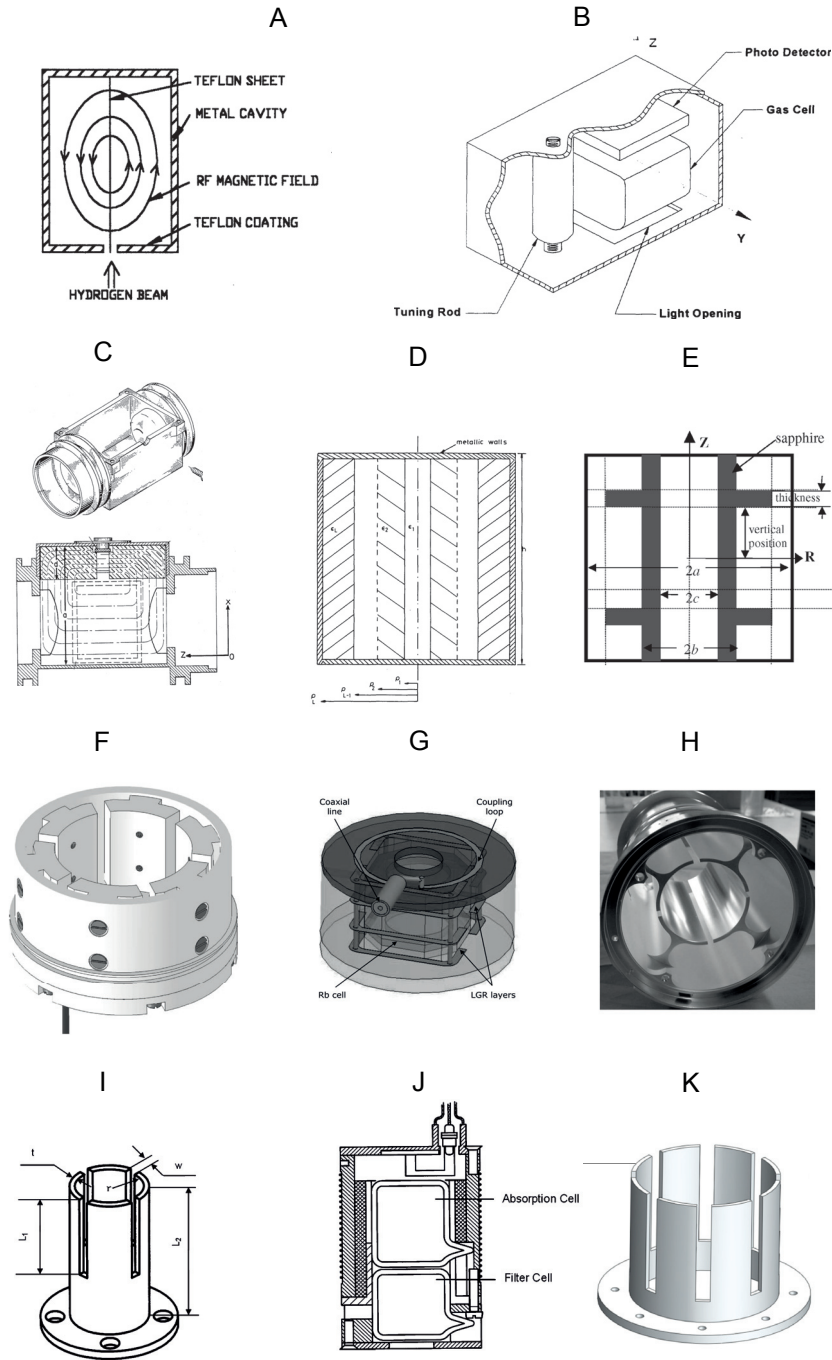


Figure 3.2 – Various notable geometries reported in the literature: (A)  $TE_{111}$  septum cavity [31]; (B) sub-miniature cavity [32]; (C)  $TE_{101}$  cavity [33]; (D) radially stratified dielectric-loaded cavity [34]; (F) 6-gap compact loop-gap geometry [16]; (G) "microloop-gap resonator" [35]; (E) sapphire-loaded cavity [36]; (H) loop-gap geometry employed in the PHM of Galileo [37]; (I), (J), (K) a type of loop-gap structures similar to the one employed in the RAfs of BeiDou [38, 39].



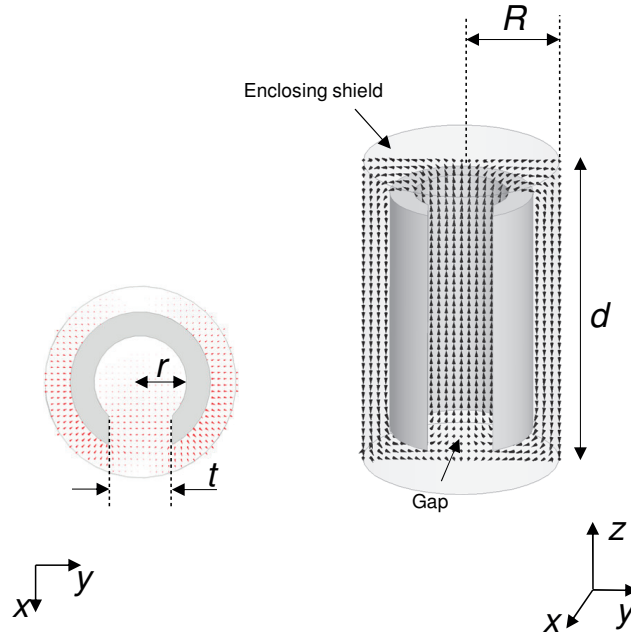
A very important concern, specific to the active maser application, is the requirement for a self-oscillation which could only be obtained for cavities with very high Q-factors ( $\approx 10000$ ). This is the reason why the material preferred for dielectric loading is typically sapphire ( $\tan \delta \approx 1 \times 10^{-7} \div 1 \times 10^{-6}$ ). However, it was shown [44] that the introduction of additional dielectric losses is much lower than the decrease of the conduction losses resulting from the reduction of the volume (and hence the metal surface of the cavity). This means that until a certain threshold is reached, the size of the cavity can be reduced without degrading the Q-factor. A proof of concept of a cavity with a volume approximately 4 times lower than the volume of the standard  $TE_{011}$  geometry was first reported in [44]. Further developments have resulted in a better control of the Q-factor as well as the filling factor (as defined in eq. 2.48). A very compact design of the cavity with a volume of  $\approx 9.7 \text{ cm}^3$  is obtained by combining the rather compact  $TE_{111}$  cavity with an additional dielectric filling [45]. Since in the case of Rb frequency standards, the Q-factor is not a critical aspect but rather a matter of power efficiency, dielectric filling can be applied more easily.

Above, we discussed what are the approaches taken for miniaturization of the cavity used for the physics package of DR atomic clocks as well as masers. The options described, are all valuable since they relate directly to our application goals. There is, however, one particular solution which has a central role in our studies – the loop-gap cavity.

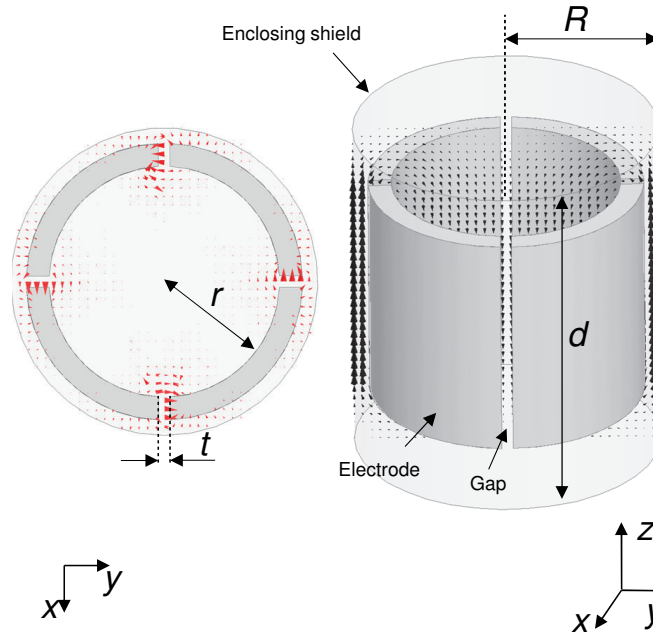
#### The loop-gap

As suggested by the name, its most prominent feature is a metallic loop (ring) with at least one gap (also referred as a slot). In order to form a cavity and increase the Q-factor, the structure is typically contained in a hollow metallic cylinder. In a very simplified way this design can be assumed to resonate due to a combination of magnetic and electric energy attributed to the inductance of the loop and the capacitance of the gap correspondingly. In figure 3.3a we show the overall structure and the resonance mode favorable for the atomic clock application. Physically, the volume can be reduced, for the mode of interest, mainly because the balance of electric and magnetic energy associated to resonance is achieved through the electrode structure and is hence less restricted by the overall dimensions. Typically such geometries have a reduction of the volume between 3 and 4 times compared to the standard cylindrical geometry, while the useful volume of the cavity is about 25% (in comparison, the useful volume of the standard  $TE_{011}$  cavity is just 5%).

The two structures shown in figure 3.3 correspond to two possible realizations of the loop-gap cavity that are very different. However, it can be seen that in both cases the distribution of the obtained field is favorable for the atomic clock application – the magnetic field is aligned to the z-axis and there is a significant amount of the volume where a cylindrical vapor cell can be conveniently situated. The dimensions are chosen such that the resonance frequency matches  $f_{\text{Rb}}$ , for both geometries, however, while the volume of the 4-loop structure is around three times larger than the 1-loop one, the vapor cell that can be accommodated in the center is almost eight times larger than the case of the 1-loop cavity. Furthermore, both have identical height showing that for the selected mode the resonance frequency is not much influenced by the height  $d$ .



(a) A loop-gap structure with one gap. Dimensions:  $t = 4$  mm,  $r = 2.9$  mm,  $d = 23$  mm,  $R = 6$  mm.



(b) A loop-gap structure with four gaps. Dimensions:  $t = 0.73$  mm,  $r = 7.5$  mm,  $d = 23$  mm,  $R = 10$  mm.

Figure 3.3 – Generic loop-gap structures. The red and black arrows depict the electric and magnetic field distribution correspondingly. The magnetic flux that is in opposite direction to the central one is hereafter referred as "return flux". At the top and the bottom sides empty cylindrical extensions are considered.

It can be readily concluded that this type of cavity is characterized by a significant flexibility and it is hence suitable to apply in various scenarios where different level of miniaturization vs. performance trade-off is demanded. In the domain of atomic clocks the first appearance of a structure similar to the loop-gap is found in the case of maser applications [46, 47]. In this realization the loop-gap part was obtained by four relatively thin electrodes that can be considered directly attached to the volume of the vapor cell. A significant reduction of the cavity volume was found: eight times with respect to the standard cavity and moreover, one miniature structure with a volume of  $\approx 20\text{cm}^3$  was reported. We note however, that the vapor cell accommodated in the first case was reduced by a factor of  $\approx 12$ , which is dictated mainly by the distribution of the magnetic field and can in principle reduce the signal-to-noise ratio and hence the performance of the clock.

Initially, for the case of the loop-gap structure, the resonance condition was obtained in a somewhat empirical fashion with further works related to a theoretical prediction of the resonance frequency [48] as well as a semi-analytical evaluation of the field distribution [49]. The first attempts to understand the relatively complicated loop-gap are based on a magnetron theory and hence the name "magnetron cavity" is mostly used in the domain of atomic clocks. Using this approach, a realization of a loop-gap cavity with low losses was obtained and applied in (active) maser implementation [50]. In this case, a more complicated structure was considered – an additional dielectric between the electrodes was included. Furthermore, four small (relative to the wavelength) gaps are chosen in order to comply to the approximations required by the theory. It is interesting to note that, currently, a loop-gap geometry is employed in the maser design used for the Galileo navigation system (an example of the realized design can be seen in [51, 52, 37], the latter is shown in figure 3.2 – H). In this case, a Passive Hydrogen Maser (PHM) is enough to fulfill the system specifications and hence a cavity characterized by a low Q-factor is chosen:  $\approx 7000$  (relative to the requirement in active masers). In order to insure high performance, the size of the vapor cell is selected to be relatively large ( $40\text{ cm}^3$ ) where the volume of the cavity is approximately 40% of the standard cylindrical geometry and the filling factor is  $\approx 0.4$  as reported in [53]. It is worth noting that, recently, a provisional design based on the loop-gap geometry was reported as a candidate for the masers proposed for GLONASS-K [54], the next generation of the Russian-made, global positioning system.

As previously explained, for the case of DR Rb clocks, the Q-factor of the cavity is not directly affecting the frequency stability which makes the implementation of the loop-gap geometry a very preferable option. One of the earliest applications can be found in [55] and [56] for the case of a DR Rb clock based on a discharge lamp pumping. Similar design was shown in [57] where a structure with 8 electrodes was additionally loaded with a dielectric material in order to improve the temperature coefficient of the cavity. While in [55] and [57] no exact dimensions are reported, the shown structures are estimated to be in the highly-compact range ( $V_{\text{cell}} \approx 3.5\text{cm}^3$ ) [56]. The fact that the volume of the cavity is considerably filled with a highly thermally conductive material (the metal electrodes) can lead to a potential improvement of the thermal performance of the clock and, moreover, it allows for advantageous faster warm-up times [56]. A more recent iteration of a similar structure can be found in [38] – shown in figure 3.2 (I), (J).

This design aims at increasing the filling factor by employing a larger number of electrodes (versions of up to 8 electrodes are reported). In order to make it feasible, the gaps between the electrodes are directly machined to a hollow cylinder forming a slotted tube. However, the lower end of the tube is kept solid in order to provide a structural support. According to the authors such a structure is easier to machine and has advantages in terms of precision and rigidity. In order to reduce the temperature coefficient, an additional dielectric ring is included in the vicinity of the caps close to the upper part of the vapor cell. The reported volume of the cavity is  $\approx 15\text{cm}^3$ , where the volume of the accommodated cell is  $\approx 4\text{cm}^3$ . The concept was further developed by the same group, resulting in a sub-miniature version of the design [58] with a volume of the cavity  $\approx 8\text{cm}^3$ . In a more recent study a theoretical evaluation of the signal-to-noise ratio was used in order to shine light on the optimal performance of their structure [59]. A slightly modified design was proposed, where by increasing the volume of the cell by 25% the signal-to-noise ratio of the clock was increased by a factor of two. It is also worth noting that a version of this cavity is chosen for the RAFS of the Chinese positioning system – BeiDou [27]. In the work of another group, a 6-electrode gap structure (figure 3.2 (F)) was realized and applied in a high-performance DR clock [16]. This compact cavity ( $V_{\text{cavity}} \approx 35\text{cm}^3$ ) was specially developed in order to accommodate an enlarged cell with a diameter of 25 mm and a volume of  $12\text{cm}^3$ . Due to the high signal-to-noise ratio as well as the relatively high field homogeneity of the cavity the performance of this clock was found to be on a par with the currently used space RAFS and PHM [16]. Furthermore, it was successfully applied in the case of a POP clock for which the high level of magnetic field homogeneity was experimentally confirmed [6]. Another, much more compact, resonator, the so-called  $\mu$ -LGR, was developed by the same group (figure 3.2 (G)). It is a hybrid version based on a dielectric filling – multi-layer stack of loop-gap resonator structures are directly printed on a temperature-compensated substrate [35]. Because a novel, micro-fabricated cell is used (with a volume of just  $0.05\text{cm}^3$ ) the volume of this resonator is as low as  $0.9\text{cm}^3$ . The chip-scale size and the use of planar technology that can be easily mass-industrialized make this device a good candidate for the new generation of highly-miniaturized atomic standards. One of the most recent loop-gap applications found in the literature: [39] – a realization of the above-discussed slotted-tube version of the loop-gap structure, is made by the same group (figure 3.2 (K)). It is a larger 8-gap structure designed for a high signal-to-noise ratio and hence accommodating a relatively large cell (the inner cavity radius is  $r = 30\text{mm}$ , the cell volume is  $\approx 14\text{cm}^3$ ). For this cavity a high FOF of 0.91 was numerically obtained and further confirmed experimentally [27].

Finally, in order to put into perspective the above-described geometries, we can map the cavities according to their overall volume and the volume that is useful for the operation of the clock (figure 3.4). It can be seen that in terms of the vapor cell volume (and hence the amount of useful signal) the loop-gap geometry is the most suitable choice for high-performance clocks. It is significantly more compact than the standard cavity yet it is capable of obtaining a comparable performance in terms of field distribution (this is evaluated in section 3.2.3).

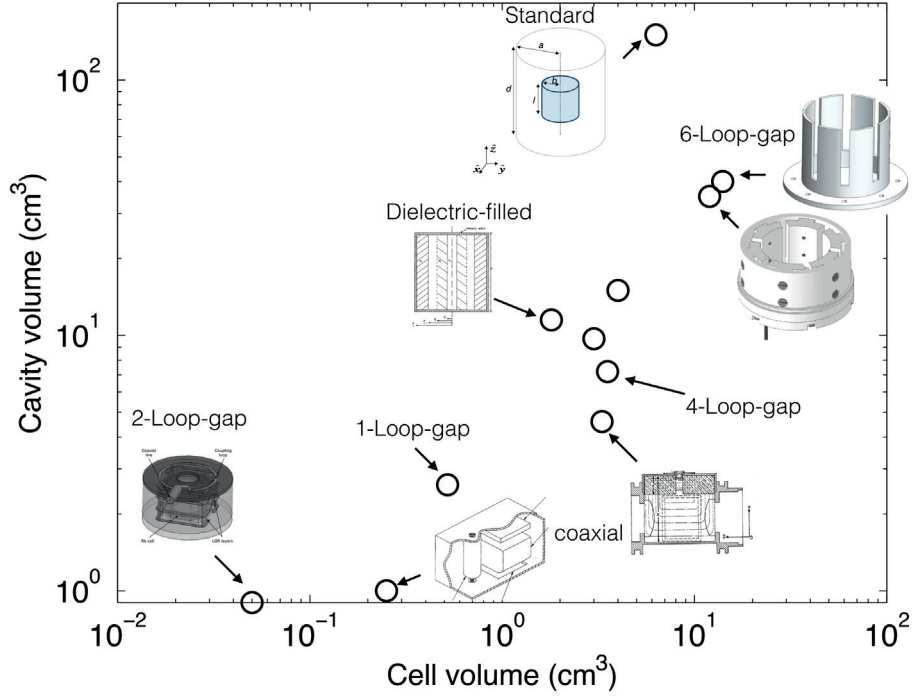


Figure 3.4 – Cavity volume versus cell volume shown for various prominent geometries. The cases named "1-Loop-gap" and "4-Loop-gap" correspond to the structures shown in figure 3.3.

From figure 3.4 it is interesting to see that the loop-gap geometry was applied in very different realizations in terms of compactness. A discussion of this intrinsic flexibility is further included (section 3.2).

### 3.1.2 Temperature stability

The problem of obtaining a high temperature stability has been traditionally important for maser applications where the frequency stability is limited by the temperature variation due to pulling effect (see section 1.3.3). In order to reduce the temperature sensitivity of the resonance frequency several strategies have been employed: active thermal control of the physics package is often utilized, the thermal behavior of the vapor cell can be engineered and a fine tuning mechanism via modification of the atomic Q-factor can be applied.

With the advent of a new generation high performance Rb clocks, the pulling effect is considered to be of a significant importance since it can lead to a noticeable degradation of the medium and long-term performance(see section 1.1.3.2.3 in [15]). Therefore the temperature stability is increasingly important characteristic of the cavity design – it can be shown that for such a Rb clock, in order to obtain a fractional frequency stability in the range of  $10^{-14}$ , the stability of the cavity frequency needs to be in the range of 200 Hz, assuming that the cavity Q-factor is in close to 500.

In [21], a theoretical evaluation of the temperature sensitivity of the resonance frequency (also known as a Temperature Coefficient, TC) can be found for the classical  $TE_{011}$  geometry loaded with a dielectric cell. It can be calculated that in the case of a cavity made of aluminum and loaded with the standard vapor cell (made of quartz), the temperature coefficient is:  $TC \approx -180 \text{ KHz K}^{-1}$ . The negative sign is attributed to the physical fact that with the increase of the temperature, the expansion of the cavity dimensions lowers the resonance frequency. In the case of the  $TE_{111}$  geometry, the temperature coefficient is in the similar range:  $|TC| \approx 220 \text{ KHz K}^{-1}$  [57]. In order to counteract, a precise temperature electronic control would need to obtain a temperature stability in the  $10^{-3} \text{ K}^{-1}$  range. This is a stringent requirement, especially on the board of a satellite where a local fluctuation of several degrees is typical. One straight-forward way to reduce the TC of the cavity is to choose a material with low thermal expansion – ex. if titanium is used the TC can be reduced nearly 4 times for the case of the  $TE_{011}$  geometry. It can be shown that the TC is proportional to the amount of dielectric loading [21], mainly due to the spatial expansion of the dielectric material as well as the temperature dependence of the dielectric constant. This is a significant problem when a dielectric filling is used to miniaturize the cavity. In order to tackle it, an additional dielectric material can be introduced for which the temperature coefficient has an opposite slope (with respect to the sapphire used for loading). In this way it is possible to partially compensate the temperature variation of the resonance frequency as well as the variation of the Q-factor [60, 61], where a value as low as  $|TC| \approx 10 \text{ KHz K}^{-1}$  can be obtained.

For the case of the previously discussed loop-gap structure, based on the slotted-tube design, a very good temperature stability was measured [57]:  $|TC| = 28 \text{ KHz K}^{-1}$ . However, it is worth noting that this result is not inherent to the slotted structure itself, but it is instead contributed to the additional dielectric ring included. In [38] is reported that the TC of the slotted tube itself, is negative and on a par with the  $TE_{111}$  used as a reference. It is in principle possible to take advantage of the design flexibility of the loop-gap in order to reduce the TC. This idea was recently adopted in [62] where a theoretical model of the temperature variation was used in order to optimize the TC of a loop-gap structure used in a PHM application. By an appropriate choice of materials used for the various metal loop-gap components the temperature coefficient of this structure was reduced from  $-30 \text{ KHz K}^{-1}$  to  $2.59 \text{ KHz K}^{-1}$ . One of the most recent results is reported for the previously described magnetron cavity structure [16], for which the experimentally obtained TC was found to be  $-33 \text{ KHz K}^{-1}$  [63].

#### 3.1.3 A focus on the loop-gap geometry

One domain where the loop-gap geometry is heavily employed is Electron Paramagnetic Resonance (EPR) – a material characterization technique based on interaction with unpaired electrons. The large majority of EPR measurements is made with microwaves in the 9-10 GHz range, where cavities based on the loop-gap geometry have long been the field of interest [64]. Another domain in which various versions of the loop-gap are popular is Nuclear Magnetic Resonance (NMR) in which the spins of atomic nuclei are excited instead of the electron spins.



While in principle the resonators in NMR are large and operate at lower frequency, for a static magnetic field with high strength the Larmor frequency is in a range suitable for a cavity-type resonators [65, 66]. In the two applications, the cavity needs to be designed such that both the uniformity of the magnetic field alignment and the field homogeneity need to be well-controlled. It is therefore instructive to consider these domains and take into account the corresponding contributions related the loop-gap (and alike) geometries.

The first modern use of the loop-gap structure was introduced for applications in NMR experiments [67], where it was thought as a replacement of the solenoid/capacitor resonators which are not applicable above 100 MHz (figure 3.5 (A)). A two-gap structure is utilized in a way for which instead of employing the magnetic field along the central axis (as the case shown in figure 3.3) the transverse magnetic field is used. In this case, an out-of-phase, coaxial mode is excited between the two loops (here they are more like-half loops) such that the field in the center is well aligned and convenient to use. An alternative solution based on a 1-gap structure was proposed in [68] where, in this case, the guided mode is  $TE_{01}$ -like described by the electric field perpendicular everywhere to the central axis and with the magnetic field longitudinal to it (the field distribution is similar to the relevant for the clock application – figure 3.3). In this first attempt, the structure is modeled so that the electric and magnetic fields are fully separated: the former is considered concentrated in the gap, it is treated as fully uniform and the fringing fields are neglected; the latter is considered attributed to the loop only. This allows for a relatively simple lumped representation of the problem to be used in order to obtain the resonance frequency – the gap is treated as a gap capacitor while the loop is modeled as a single-turn coil. Such a rather intuitive treatment of the cavity resonance problem is an approach known from the early days of magnetron analysis [69] and it can be very instructive in order to understand the general operational principle of the microwave cavity [70]. In EPR the first appearance of the loop-gap structure (as well as the name "loop-gap") can be found in [71]. In this work, the number of gaps was increased and it was shown that they can be modeled as capacitances connected in series. Furthermore, the effects of the fringing fields, associated to the gap, were taken into account in the expressions for the resonance frequency and the quality factor. In [72] the effect of the longitudinal fringing fields that exist in the empty cylindrical extensions (as shown in figure 3.3) was considered for the first time and, moreover, different options were discussed for the feeding and the tuning mechanisms. In [73] the loop-gap model was refined by also including the inductive effect attributed to the gap. In this work the high flexibility of the loop-gap was illustrated where the structure was successfully designed to operate at 35 GHz. In the domain of EPR the complete field problem was considered for the case of a compact loop-gap structure [74]. A full wave analysis was also performed in [75] where the longitudinal field variation (along the axis of the cavity) was neglected and the problem was solved by approximating the central field distribution using a superposition of cylindrical modes modified in order to account for the gaps. Based on this approach, an estimation of the magnetic field homogeneity was obtained for the case of a small internal radius (few mm) and a small size of the gap.

In [76], by using a similar method, the effect of the fringing fields at both extensions was modeled. Both sides of the loop-gap being under cutoff the fringing field was represented as a superposition of evanescent cylindrical TE modes.

Great topological variety exists for the case of the loop-gap geometry – figure 3.5. For example, in EPR, relatively simple structures based on one or two gaps can be employed: [81, 82, 83, 84]. Various methods can be used in order to produce them. One interesting example of a potentially cheap to produce design is based on etching a planar sheet and then folding it so that the cylindrical loop-gap structure can be formed [85]. The "slotted-tube resonator", an example of a two-gap structure, is known from NMR [67]. It is utilized so that the transverse magnetic field is employed and it is typically designed for the 300-500 MHz range. The same idea can be found in some EPR applications, where the 1-10 GHz range is employed instead [86]. Low frequency versions (500 MHz) are also known in the domain of Magnetic Resonance Imaging (MRI) [87]. For EPR applications, a desired feature of the loop-gap design is the large amount of spatial separation between the electric and magnetic fields. As seen from figure 3.3, the electric field is quite localized in the gap where the fringing electric field is often the factor limiting the performance [64]. In order to mitigate this effect, a so-called bridged loop-gap was developed [83, 82] where a variable electrical shield is positioned close to the gap. One advantage of this structure, that was realized, is the possibility for a frequency tuning ([88]). This idea was further elaborated by creating an additional concentric loop-gap structure used in a cavity for NMR application [89].

One of the main reasons why the loop-gap structure has been so extensively studied in EPR is its naturally high filling factor (the definition been identical to the efficiency factor defined by us for the case of atomic clocks – section 2.2.2). The filling factor is related to the useful signal which makes it a crucial aspect in the design of the resonator. Generally, in the loop-gap case, the filling factor is relatively high and can be increased by making the return-flux cross section large (by enlarging the metal shield) relative to the central part [64]. In order to be able to engineer and obtain a better control on the return flux, the loop-gap geometry can be based on several (reentrant) loops that share the same gap. In this way, instead through the shield, the magnetic flux closes through one or several loops. Various such topologies can be found in the literature e.g. 2-loop 1-gap [90]; 3-loop 2-gap [77, 91]; 5-loop 4-gap [78, 92], where the latter case shows how structurally close these structures can be to the classical magnetron geometry. It is also worth noting that the electrodes (loops) are not limited to curvilinear shapes – e.g. in [79] various loop-gap structures with a rectangular cross section were developed. An extensive depiction of many possible geometries used in practice is reported in [93]. One interesting geometry is the so called "bimodal loop-gap resonator" [80] shown in figure 3.5 (F). It consists of two axially separated loop-gap regions which are fed separately. The structure is known to exhibit a parallel/anti-parallel modal behavior [72] (hence its name). By controlling the phase and amplitude of the two feeds, a circular polarization can be created which means that this configuration allows to employ the  $\sigma_-$  and  $\sigma_+$  transitions.



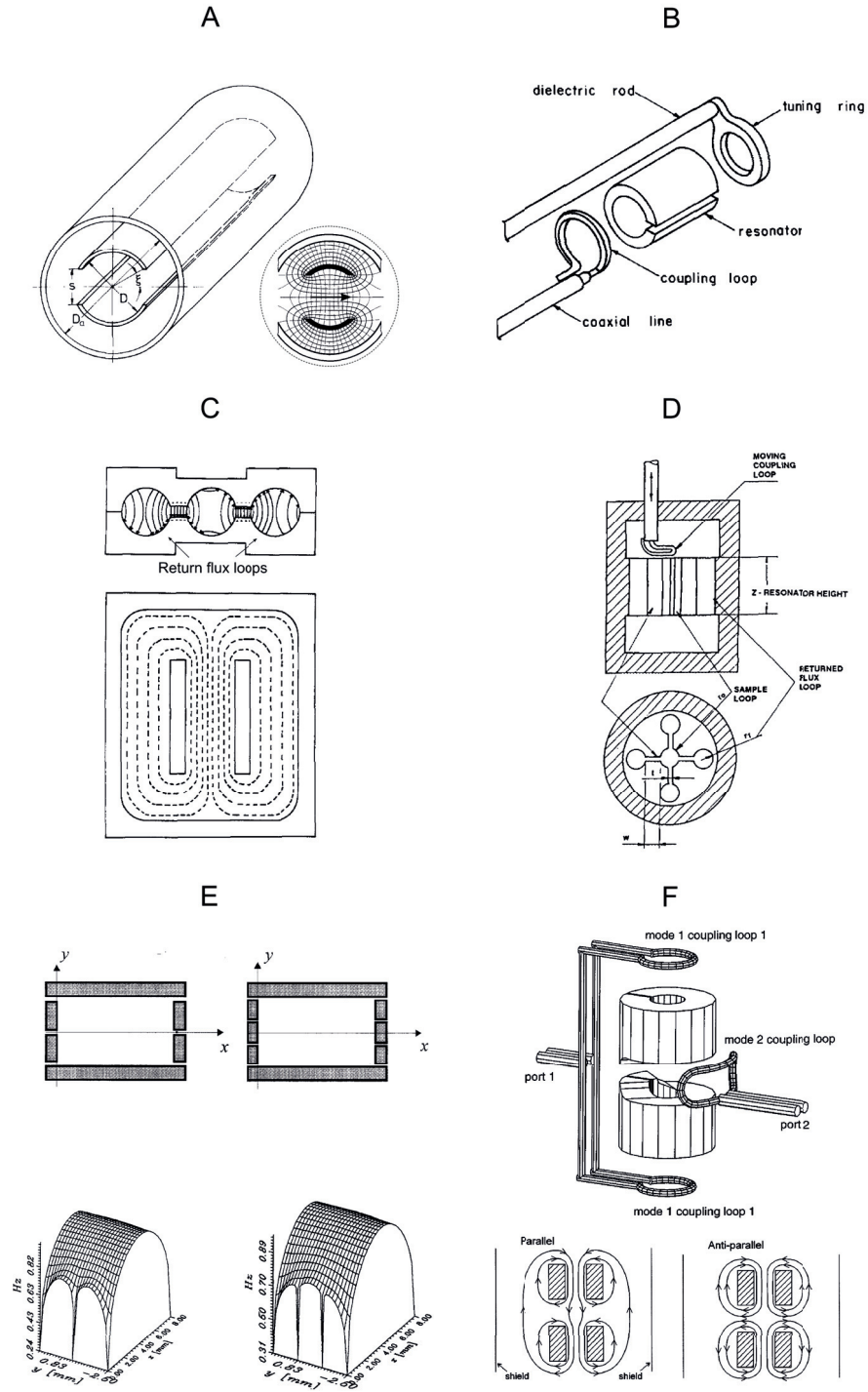


Figure 3.5 – Various notable loop-gap geometries reported in the literature: (A) "slotted-tube resonator" [67], the direction of the magnetic field is indicated by the arrow; (B) 1-gap structure [68]; (C) 3-loop 2-gap structure [77]; (D) 5-loop 4-gap structure [78]; (E) loop-gap based on rectangular electrodes [79]; (F) bimodal loop-gap [80].

In the first realizations of the various loop-gap geometries, the feeding was usually obtained via an inductive loop attached to the end of the coaxial cable – typically coupled through the return magnetic flux. An alternative approach is to feed the cavity through an iris situated at the shield of the loop-gap. An overview of the feeding mechanism and one possible implementation of the latter can be found in [94]. Finally, we report a more recent work where a rather extensive model of the iris is developed in [95]. In that case, its dimensions were optimized so that the homogeneity of the field was unaffected by its presence. Moreover, the shift of the resonance frequency, existing due to the iris, was modeled and connected to the lumped representation of the loop-gap.

### 3.2 Physics of the loop-gap cavity

For the engineering problem of properly exciting a large volume (relative to  $\lambda_{\text{Rb}}$ ) of Rb atoms there are two separate ways to look at the requirements. In terms of the magnetic field distribution, in order to obtain high filling factor and high field homogeneity the best would be to position the vapor cell in the vicinity of a solenoid resonator. On the other hand, the frequency and Q-factor requirements suggest fully enclosed structures for which the magnetic field is inherently non-homogeneous and far too localized to be able to excite all atoms properly. The loop-gap can be considered as a structure that is somewhat able to successfully combine both type of requirements. Unfortunately it is not possible to analytically analyze even the simplest among the great variety of possible loop-gap geometries. When the cavity is considered with its circuit (system) characteristics,  $f_{\text{res}}$  and Q-factor, analysis is possible based on a number of approximations. However, in order to fully obtain the characteristics related to the field distribution, numerical modeling is preferable.

#### 3.2.1 Lumped element point of view

It is of interest to study how the resonance frequency of the loop-gap depends on its dimensions. First we can start with the very simplified expressions for the circuit equivalence [71], which nevertheless provide us with a good physical intuition:

$$C = \frac{\epsilon w z}{t n}, \quad L = \frac{\mu_0 \pi r^2}{z}, \quad (3.1)$$

where  $C$  and  $L$  are the approximated capacitance and inductance,  $r$  is the internal radius of the loop-gap region,  $n$  is the number of gaps,  $t$  is the length of the gap,  $w$  is the thickness of the loop elements (not the frequency  $\omega$ ) and  $z$  is the height. This simplest case is shown in figure 3.6a. Since  $C$  and  $L$  scale opposite with  $z$ , the intrinsic frequency associated to the loop-gap is described by only the transverse dimensions and is given by:

$$f_{\text{int}} = \frac{1}{2\pi} \sqrt{\frac{n t}{\pi r^2 \epsilon \mu w}}. \quad (3.2)$$

From eq. 3.1 is evident that the capacitance is attributed to the gaps (considered identical).

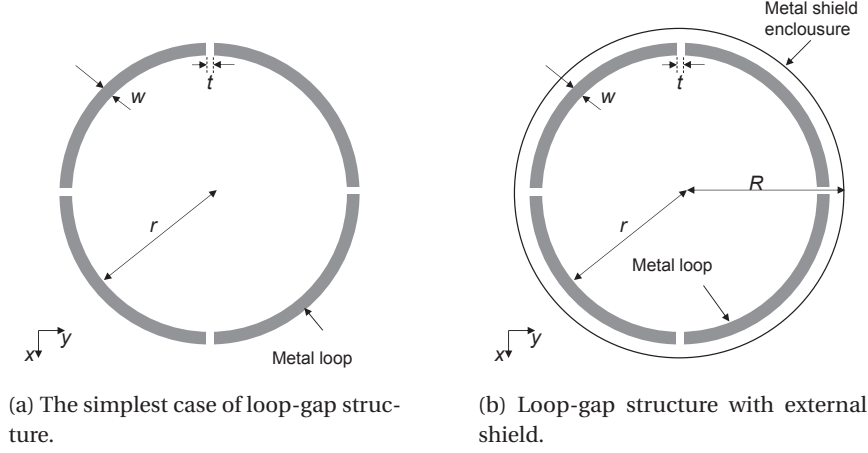


Figure 3.6 – Parametrization of the loop-gap structure. An example with four gaps ( $n = 4$ ) is shown.

It is seen that a number  $n$  of such capacitances add in series where each of them is proportional to the ratio of the thickness to the gap size:  $w/t$  (for a chosen dielectric). On the other hand, the inductance  $L$  scales naturally with the amount of magnetic flux, which is proportional to the area, and hence the  $r^2$  dependence (non-magnetic medium is considered).

So, from this very simplified description, it is evident that there is no interdependence between the two expressions in eq. 3.1 (apart from  $z$  that cancels) which is why, naturally, this structure is so flexible in terms of  $f_{\text{res}}$ . In order to demonstrate that, let's compare the dimensions of the loop-gap to the cylindrical case. For the frequency of interest  $f_{\text{Rb}}$  (here it is equivalent to the cutoff frequency from a wave guide point of view) the radius of the canonical structure is  $a = a_{\text{cut}} \approx 26.757$  mm, as reported in section 2.1.2. We can theretofore calculate the value of the equivalent  $L$  that a loop-gap with identical radius has. The expression for  $C$  can be then used in order to combine the width of the loops  $w$  as well as the size  $t$  and the number of gaps  $n$ . In this way, for the frequency of interest, a balance for the reactance is reached  $|X_L| = |X_C|$ . From figure 3.7 can be seen that, for example, if we want to reduce the radius by a factor of two, relative to the canonical case, we need to select a certain number of gaps where, for each case,  $t$  is fixed. As expected, since the gap capacitances add in series, a larger number of gaps translates as a lower gap distance. From this simple  $LC$  analysis can be concluded that if we want to compact the cavity, reducing the equivalent reactance is the way to go.

A more precise treatment of the problem approximates the resonance frequency as the following:

$$f_{\text{int}} = \frac{1}{2\pi} \sqrt{\frac{nt}{\pi r^2 \epsilon \mu w}} \sqrt{1 + \frac{r^2}{R^2 - (r+w)^2}} \sqrt{\frac{1}{1 + 2.5t/w}}, \quad (3.3)$$

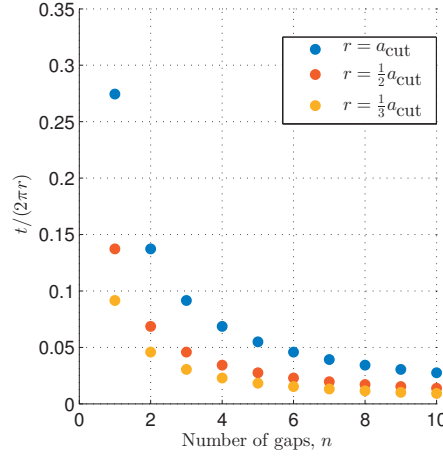


Figure 3.7 – Size of the gap  $t$  as function of the number of gaps  $n$  such that  $f_{\text{Rb}}$  is obtained. Three separate values for the radius are considered defined relative to the radius of the canonical structure  $a_{\text{cut}}$ . The y-axis is case-wise normalized to the circumference of the loop-gap. The thickness of the loop is fixed to  $w = 1$  mm. The parametrization of the structure is according to the reported in figure 3.3.

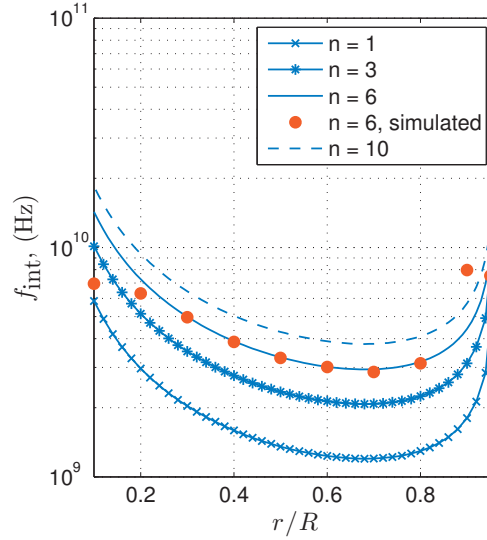


Figure 3.8 – Intrinsic resonance frequency of the loop-gap structure shown as a function of the internal radius  $r$ . All dimensions are as the reported in table 4.4, the normalization considered is with respect to  $r = 16.8$  mm. The outcome of eq. 3.3 is compared to a result from a full-wave eigen simulation performed via ANSYS HFSS<sup>®</sup>. By applying PMC boundaries at both planes of the loop-gap cross section, the numerically found frequency has the same physical meaning as the modeled in eq. 3.3.

where the first term is the resonance frequency of the  $LC$  circuit and the two other terms improve the approximation by accounting for the effect of the metal shield (shown in figure 3.6b) and the fringing fields accordingly [71].

Although approximate, for the mode of interest, these expressions are found to describe the loop-gap relatively well. From figure 3.8 can be seen that the frequency range is bounded by  $f_{\text{int}} \rightarrow \infty$ . It is worth noting that in the case when  $r \rightarrow R$  the frequency is infinity because of the second term in eq. 3.3. However this is not physical since in this case the gaps are shorted-out and hence the intrinsic frequency of the loop-gap approaches the cutoff associated to the shield radius  $R$ . The latter is especially valid when the thickness  $w$  is small and it is confirmed in the simulated result shown in figure 3.8. Of practical value is the amount of error between the approximation model given by eq. 3.3 and the results obtained from simulations (reported in figure 3.8).

At this stage, it is curious to explore what is the most compact structure that can be made to resonate at the  $f_{\text{Rb}}$  (at the required mode) and still being able to accommodate the standard vapor cell (with radius  $b = 10$  mm). This can be studied by expressing the external radius  $R$  from eq. 3.3 and plotting the loop thickness  $w$  as well as the gap size  $t$  for a fixed  $n$  and considering the frequency of interest  $f_{\text{int}} = f_{\text{Rb}}$ . We show the corresponding result in figure 3.9, where we have considered four different cases ( $n = 2, 4, 6, 10$ ) that are of a practical interest. It can be roughly concluded that structures with fewer gaps are more sensitive to the width, while in the case of a large number of gaps the gap size plays a bigger role in the miniaturization. This is easily seen by comparing the case of  $n = 2$  (figure 3.9a) with the case of  $n = 10$  (figure 3.9d). In the former, the gradient is roughly in horizontal direction (a decreasing  $w$ ), while in the latter it is somewhat vertical and hence reducing the cavity size is mainly obtained by reducing the gap size. It can be concluded that in terms of compactness, in principle, the structure with two gaps is the best candidate. However, different structure may be more suitable depending on the tolerances associated to the realization. We want to emphasize that the solution shown in figure 3.9 needs to be considered carefully – in figure 3.8 we showed that when the external and internal radius  $R$  are too close, the result is not physical. Finally, the variety of the geometries needs to be evaluated in terms of field quality, for which a full-wave simulation is the optimal choice.

#### 3.2.2 Field point of view

The loop-gap cavity not being a canonical structure, we base our full-wave study on a commercial software (Ansys HFSS<sup>®</sup>) using FEM. The first simplification that can be used is to neglect the longitudinal field distribution (along  $z$ ), and only consider the resonating field in the transverse direction. This is, in other words, equivalent to the case where the top and bottom plates of the cavity are situated infinitely far. Since we are interested in a  $\text{TE}_{011}$ -like mode (the field distribution shown in figure 3.3), by applying PMC boundary conditions at the top and bottom plates of the cavity, the longitudinal modal number becomes zero – the mode is independent of  $z$ . Also there is no region where the magnetic field lines turn, the magnetic field is entirely along  $z$  and the currents flow azimuthally (perpendicular to  $z$ ). The resonance frequency in such a cavity is the cutoff frequency related to the cross section and it is hence physically equivalent to the one modeled via eq. 3.3.

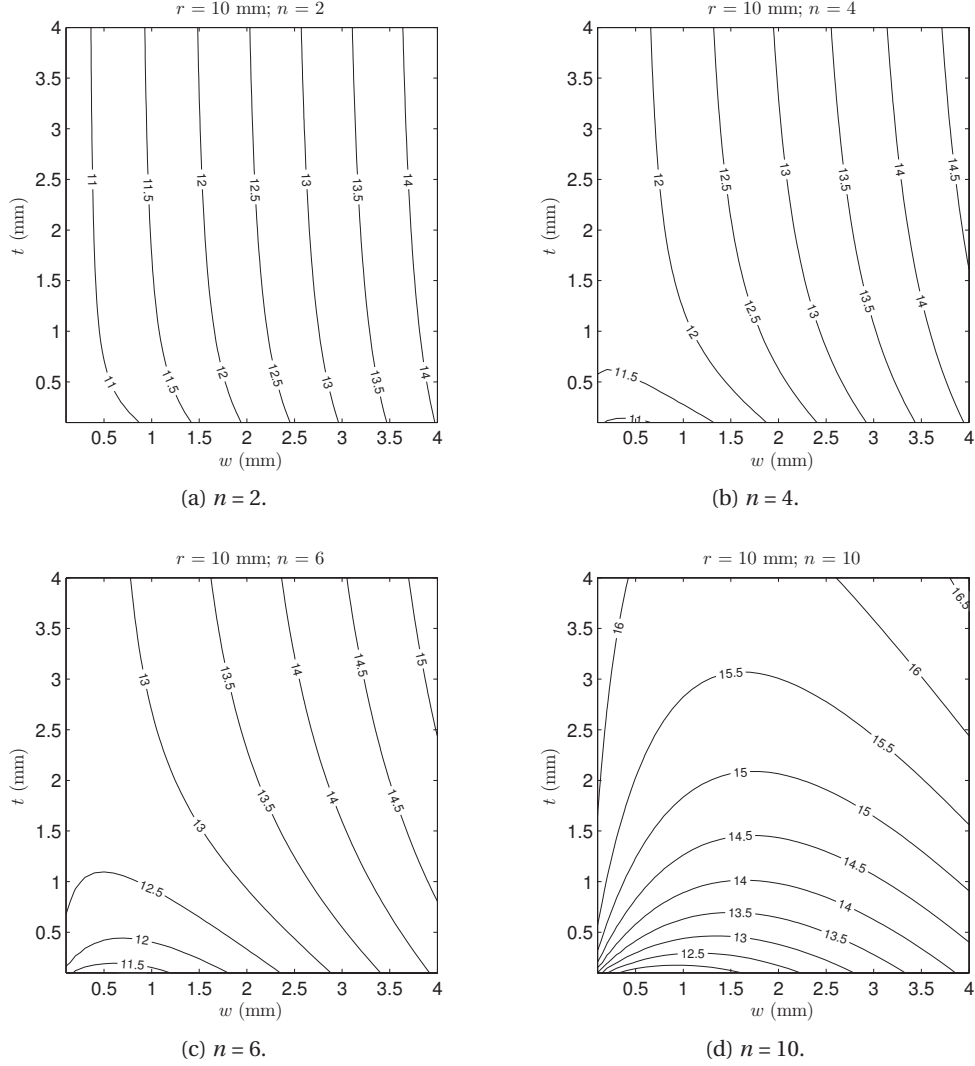


Figure 3.9 – A plot of the required loop width  $w$  and the gap size  $t$  so that the structure resonates at  $f_{Rb}$  for a given external radius  $R$  (represented by the contour lines). The internal radius  $r$  is considered identical to the radius of the standard cell:  $r = b = 10$  mm. Physically meaningful values are:  $w < (R - r)$  for the width and  $t < (2 \pi r)/n$  for the size of the gap.

It is worth noting, however, that such a transversal decoupling of the wave solution has to be applied with some care when the condition for translational symmetry is not fully fulfilled. In the case of the loop-gap cavity a relatively small hollow region exists on both sides of the loop-gap, however this part is under cutoff (as long as the external radius  $R$  is kept relatively small) and hence for the purpose of this analysis we neglect the contribution of the associated fringing fields.

### 3.2. Physics of the loop-gap cavity

case	$n$	$r$ (mm)	$R$ (mm)	$w$ (mm)	$t$ (mm)	$f_{\text{num}}$ (GHz)	$f_{\text{mod}}$ (GHz)	hom. $h$
1	2	10	14	2.5	9.9	6.838	4.3026	0.620
2	2	10	14	0.15	7.98	6.844	3.4558	0.626
3	4	10	14	2.75	3.676	6.839	5.9677	0.616
4	4	10	14	0.55	3.25	6.848	4.866	0.617
5	6	10	14	2.75	1.5	6.84	6.33	0.606
6	10	10	14	2.75	0.674	6.838	6.63	0.605

Table 3.1 – Dimensions, resonance frequency and field homogeneity for various loop-gap structures,  $f_{\text{num}}$  corresponds to the numerically obtained frequency,  $f_{\text{mod}}$  is calculated from eq. 3.3,  $h$  is the amount of bulk homogeneity evaluated as described in section 2.2.2.

Based on this approach, we can find the eigenmodes using the eigen solver of Ansys HFSS<sup>®</sup>. This allows us to obtain the transverse field distribution and to test the predictions from the  $LC$  model. Moreover, this approach is sufficiently fast since the computational region is reduced significantly (in principle the problem is reduced to the 2D domain). It is worth noting that since a loop-gap with  $n$ -loops has a  $n$ -fold rotational symmetry, a further reduction of the computational domain is possible. Furthermore, applying the PMC boundaries helps us restrict the number of solved (unwanted) modes and also increases the solution speed.

**Structures with different number of gaps** Using the above-mentioned analysis we can now investigate the homogeneity of the loop-gap structure and compare it to the case of the simple cylindrical geometry. In this study we consider loop-gap geometries with  $n = 2, 4, 6, 10$  number of electrodes. In all cases we fix both the external and internal radii:  $R = 14$  mm,  $r = 10$  mm. The choice of these dimensions is made such that the external radius is reduced more than 2 times with respect to the standard geometry (for the practical case of  $AR = 1$ ) while at the same time the internal radius allows the accommodation of the standard vapor cell (with a radius  $b = 10$  mm). These structures are reported in detail in table 3.1.

Going back to the circuit model (figure 3.9), we see that, for fixed  $r$ ,  $R$  and  $n$ , we have two ways to reach the required  $f_{\text{res}}$ . We can use thicker electrodes (loops) but reduce the gap thickness  $t$ . Alternatively, we can use a combination of thin electrodes and a relatively large gap instead. For example, in the currently considered  $n = 2$  case we are in the bottom of the  $R = 14$  curve (figure 3.9a) or very high when thinner electrodes are considered. In the simulations, we take two such cases of thick/thin electrodes (table 3.1): cases 1 and 2 for  $n = 2$  and cases 3 and 4 for  $n = 4$ . It can be seen that the model fails to predict well the frequency for low  $n$ . The last two entries in table 3.1 correspond to loop-gaps with  $n = 6$  and  $n = 10$  for which the predicted resonance frequency is somewhat closer to the simulated one. We present the obtained transverse field distribution in figure 3.10. The first observation is that the amplitude found in the area between the electrode and the lateral wall is several times bigger than the central region. Structures with many gaps tend to decrease this effect, which makes them generally more efficient. In all cases considered, the homogeneity is on a par with the standard cylindrical cavity (for which  $h \approx 0.064$ ).



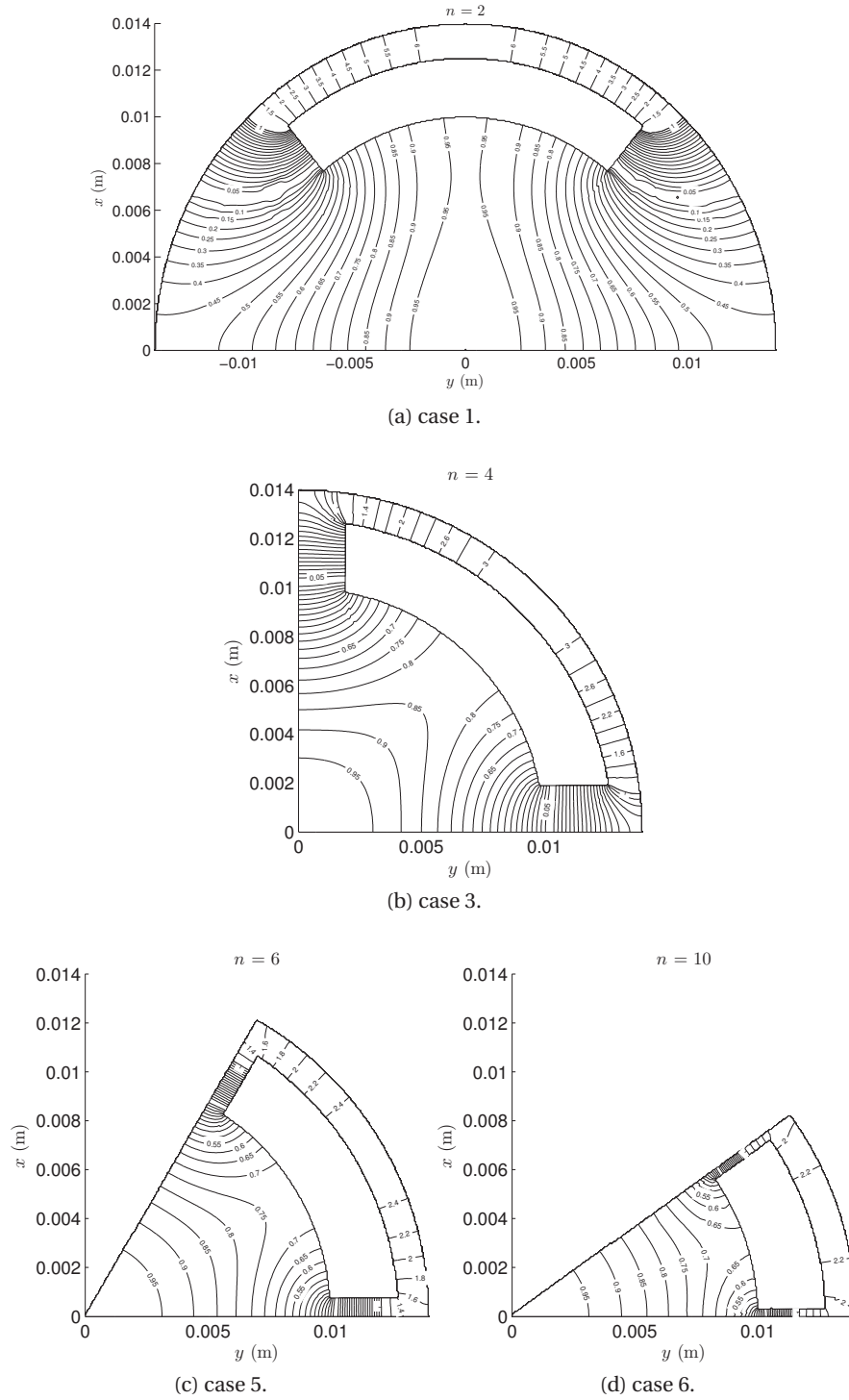


Figure 3.10 – Contour plots corresponding to the  $H_z$  amplitude. A normalization to the amplitude found in the center ( $x = 0, y = 0$ ) is considered. In each case, the result is shown according to the symmetry used – the symmetry planes are applied across the center of the gap (perpendicular to the plot). All dimensions are given in table 3.1 where the useful part of the cross section is the circular region with a radius  $r = 10$  mm.



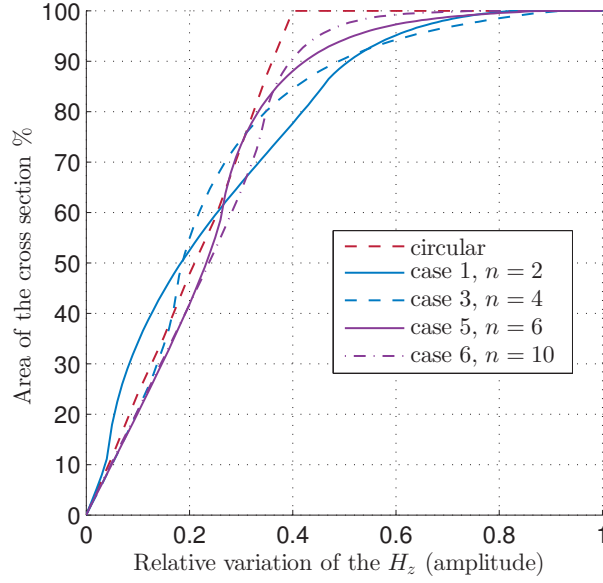
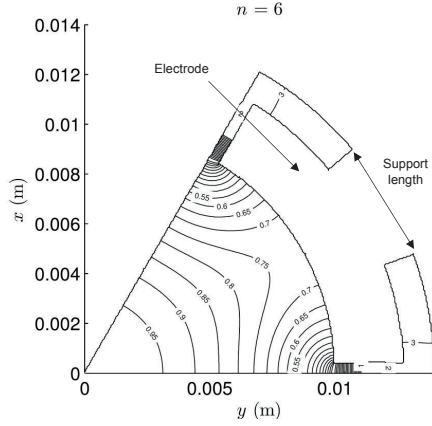
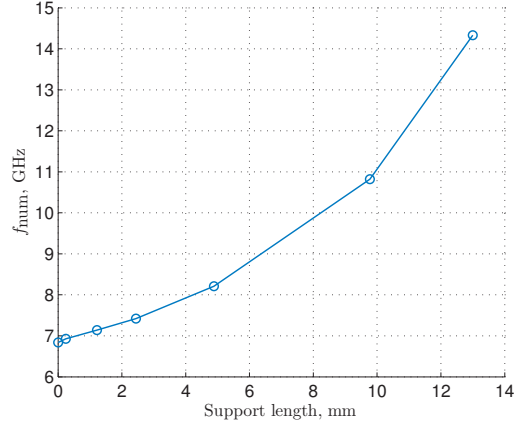


Figure 3.11 – Homogeneity profiles calculated for the  $H_z$  amplitude following the procedure explained in section 2.3. In each case, the normalization of the field is with respect to the amplitude found in the center.

The thickness of the electrodes is found to have a negligible effect on the field distribution (in figure 3.10 the cases of thin electrodes are omitted being very similar to the shown). What is more, the number of gaps/electrodes is found to have a rather small effect, where a slight homogeneity degradation is seen for a larger number of gaps. The latter is a rather unexpected since, intuitively, a larger number of electrodes somewhat confines better the field "leaking out" of the central region. However, it can be seen that the larger the number of electrodes the more the relative amplitude variation from the center towards the wall of the electrode. As an attempt to better quantify this behavior we can calculate the homogeneity profiles introduced in section 2.3. The result is shown in figure 3.11 where we compare the loop-gap structures from figure 3.10 to the simple cylindrical geometry with  $AR = 1$ . Since in this analysis we do not have a  $z$ -dependence, the plots show what is the amount of field variation attributed to the cross section only. Because the useful region of the loop-gap is the central part, in all cases (incl. the simple cylindrical geometry), the area is normalized to a circular cross section with a radius  $r$  of 10 mm, which is the typical vapor cell used in practice. For the case of the simple geometry a linear relationship exists between the field variation and the amount of the useful area, which is expected due to the azimuthal symmetry. For the loop-gap structures this behavior is mostly seen in the center, while close to the gaps the field leakage changes the slope of the curve. The higher the number of the gaps the closer the loop-gap is to the behavior of the standard geometry. It is interesting to see, however, that in case 1 ( $n = 2$ ), although we have a lot of leakage, the beginning of the curve is peaked hence maximizing the area that "sees" field in the interval of  $\approx 10\%$  variation.



(a) Contour plot corresponding to the  $H_z$  amplitude.



(b) Influence of the support length on the frequency of the loop-gap.

Figure 3.12 – A loop-gap geometry with electrodes attached to the lateral walls given for:  $n = 6$  mm,  $R = 14$  mm,  $r = 10$  mm,  $w = 2.75$  mm,  $t = 1.5$  mm.

This might be a useful characteristic considering the fact that, in principle, the largest part of the favorable signal comes from the center of the vapor cell.

**The influence of the electrode support** In all loop-gap structures considered until now we assumed that the electrodes are "floating". For structural reasons, however, the easiest way to build the cavity is by attaching them electrically to the lateral wall (figure 3.12a). As can be seen the magnetic field distribution is unaffected in the central region. The frequency increases with increasing of the gap size as shown in figure 3.12b.

**The influence of the vapor cell** In the first approximation the presence of the vapor cell reduces the resonance frequency but in general no significant change of the field distribution is expected. This is confirmed by the result shown in figure 3.13, where the frequency is found to decrease with  $\approx 15\%$  when a vapor cell with a standard thickness and dielectric material is used. In order to counteract this effect, the thickness  $t$  of the gaps is increased, for which case the field distribution is shown. It can be seen that the effect of the vapor cell is marginal and mostly localized at the vicinity of the gaps. The change of the overall homogeneity is found to be marginal as well.

**Longitudinal field distribution** In all the above investigations for the loop-gap geometry we excluded the effect of the longitudinal field distribution. The most straightforward way to consider the real cavity is by applying PEC boundaries directly to the top and bottom of the loop-gap cross section (considered empty). In this case, the resonance frequency can be obtained in a way similar to the canonical structure (see eqs. 2.34 and 2.33) and the procedure to design the loop-gap cavity can be now fully established: the overall height and radius are chosen according to the vapor cell used; the loop-gap structure can be roughly determined

using the lumped model; PMC boundaries and symmetry can be used to numerically obtain the cutoff frequency such that for the fixed height  $d$  the value needs to be:

$$f_{\text{cut}} = \frac{c}{2\pi} \sqrt{\left(\frac{2\pi f_{\text{res}}}{c}\right)^2 - \left(\frac{p\pi}{d}\right)^2}, \quad (3.4)$$

where  $c = 1/\sqrt{\epsilon_0\mu_0}$  is the speed of light in vacuum,  $f_{\text{res}} = f_{\text{Rb}}$ , and the longitudinal wave number corresponds to half the guided wavelength for  $p = 1$ .

One complication comes from the fact that, in practice, the lateral walls of the loop-gap cavity are often chosen to extend above the central (loop-gap) region resulting in the empty top and bottom segments (see figure 3.3). This is required e.g. for the tuning of the cavity or in order to accommodate the vapor cell. In this case the problem can be analyzed via the equivalent transmission line model shown in figure 3.14. The same approach is also known as a transverse resonance method [25] and, for example, can be used to analyze discontinuity problems [96, 97]. In this case, each cavity segment can be described via its corresponding length, characteristic impedance and propagation constant attributed to the mode of interest. It can be shown that, at resonance, for the left-oriented  $\vec{Z}_{\text{in}}$  and the right-oriented  $\vec{Z}_{\text{in}}$  input impedances we have the equality  $\vec{Z}_{\text{in}} = -\vec{Z}_{\text{in}}$  that can be defined for a chosen coordinate  $z$  along the TL. Using this approach, we have calculated the resonance frequency for extensions with various heights – the results are reported in table 3.2.

### 3.2.3 Figures of merit in the case of the loop-gap geometry

For the case of the loop-gap geometry no analytical solution is available. Instead we use a full-wave simulation performed with Ansys HFSS<sup>®</sup>. The field data is calculated for a relatively dense mesh and it is exported to MATLAB<sup>®</sup> in order to generate the 2D-diagrams related to the figures of merit. In this way we are able to directly compare very different geometries.

cell $\epsilon_r$	$t$ (mm)	$f_{\text{num}}$ (GHz)
1 (no cell)	1.5	6.84
4	1.5	5.786
4	2.55	6.842

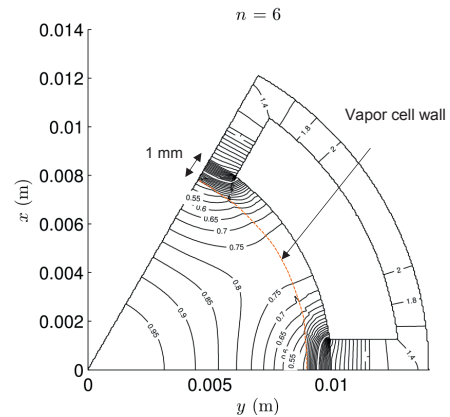


Figure 3.13 – A contour plot corresponding to the  $H_z$  amplitude shown for a loop-gap geometry with vapor cell included;  $n = 6$  mm,  $R = 14$  mm,  $r = 10$  mm,  $w = 2.75$  mm,  $t = 1.5$  mm. The thickness of the cell is 1 mm.

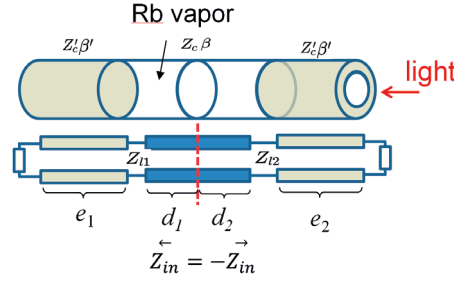


Figure 3.14 – A scheme of the resonance transmission line model. The central region corresponds to the loop-gap segment. The two extensions are considered identical and with a circular cross section. The aperture can be modeled with an equivalent reactance. The Rb vapor is indicated for illustrative purpose only.

ext. height (mm)	TL model (GHz)	Numerical (GHz)
0	6.852	6.81
1.5	4.897	4.858
4.5	4.842	4.698
6.5	4.783	4.7

Table 3.2 – Resonance frequency obtained for a loop-gap cavity with empty extensions at both end sides of the loop-gap region. The radius of the extensions is identical to the external radius of the loop-gap region:  $R = 14$  mm is the external radius;  $r = 10$  mm is the internal radius,  $w = 2.75$  mm is the thickness of the electrode;  $t = 0.54$  mm is the gap size;  $d = 30.5$  mm is the height of the loop-gap region.

The loop-gap geometry, considered here, is based on 6 electrodes and it is characterized by an external radius of  $R = 18$  mm and a length of  $d = 33$  mm (see Figure 9. in [98]). In the plots, the limit for the radius of the vapor cell is determined the internal radius of the electrodes. The volume of the cell used in [16] is approximately 1.5 times larger than the volume of the standard cell previously mentioned and is hence represented by the corresponding contour curve. The radius of the apertures required for the optical pumping is approximately one half of the external cavity radius. By comparing figures 3.15a and 3.15b with 2.17 and 2.18 it can be seen that, in the case of the loop-gap structure considered, the FF and  $FF_s$  are about half of the cylindrical  $AR = 1$  case and hence this structure is less efficient. However, we note that the FOF is relatively high – around 90% for a vapor-cell with a normalized volume of 1.5 (figure 3.15c). From figure 3.16 can be seen that, in terms of homogeneity, the loop-gap geometry performs equally well to the cylindrical cavity with  $AR = 1$ . The latter can be seen as a big advantage of the loop-gap since, the high field homogeneity does not come on the expense of a very large volume – the loop-gap cavity considered has an overall volume which is more than 4 times smaller compared to the cylindrical,  $AR = 1$ , cavity.

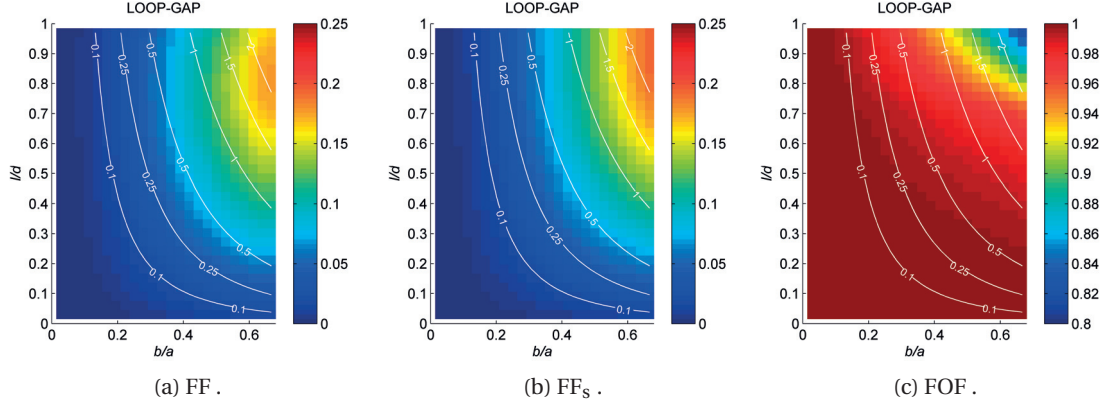


Figure 3.15 – 2D diagrams associated to the figures of merit related to the field uniformity shown for the case of a cavity based on a loop-gap geometry.

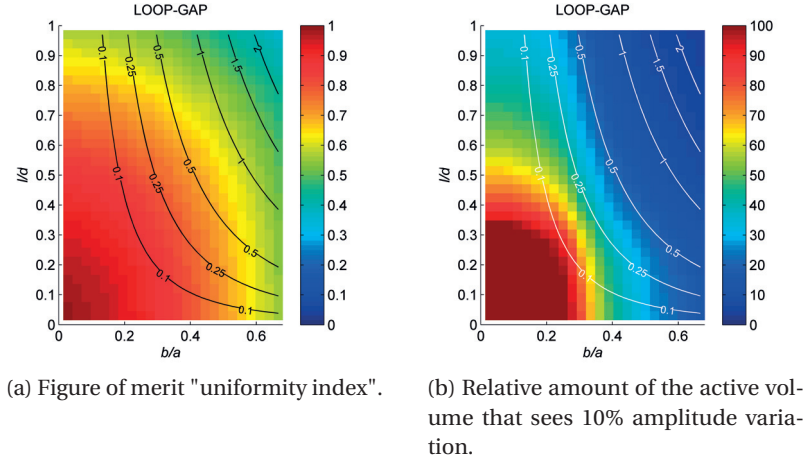


Figure 3.16 – 2D diagrams associated to the figures of merit describing the amount of homogeneity shown in the case of a cavity based on a loop-gap geometry.

#### The case of the loop-gap geometry with PMC boundaries

The final consideration in this part of the study is to test the performance of the structure when PMC boundary conditions are applied at the top and bottom sides of the cavity. From figures 3.17a and 3.17b can be seen that the filling factor is improved with respect to the non-PMC case. Furthermore, in the case of the PMC, the FOF is close to unity, regardless the volume of the considered vapor cell (figure 3.17c). This is due to the fact that the return flux is improved: the magnetic field lines need not turn at the PMC surface and hence they do not contribute to the unwanted field components. In terms of homogeneity, as expected, the longitudinal variation of the field amplitude is close to zero (figures 3.18a and 3.18b). By comparing figures 3.18a and 3.16a, it can be noted that while in the longitudinal direction the field is significantly improved for the PMC case there is as well slight degradation in traverse direction. The latter effect is attributed to the presence of the vapor cell (included in the simulation).

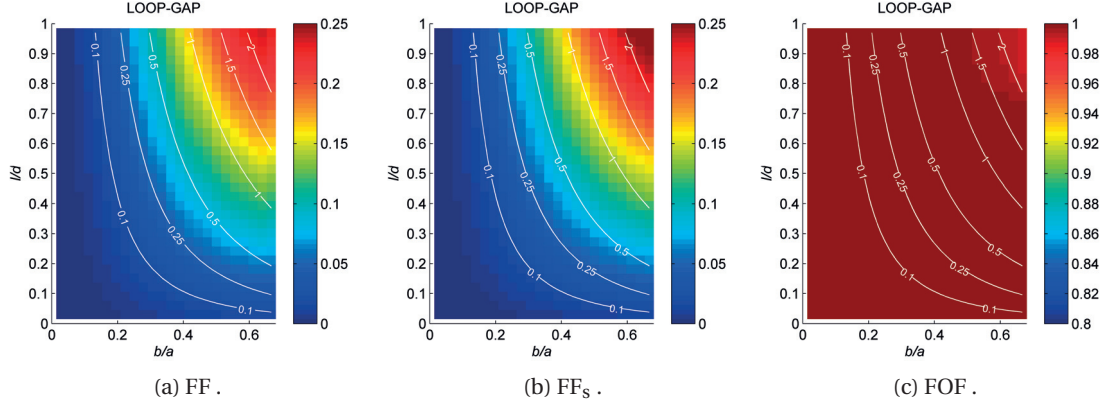


Figure 3.17 – 2D diagrams associated to the figures of merit related to the field uniformity shown for the case of a cavity based on a loop-gap geometry and PMC boundary conditions.

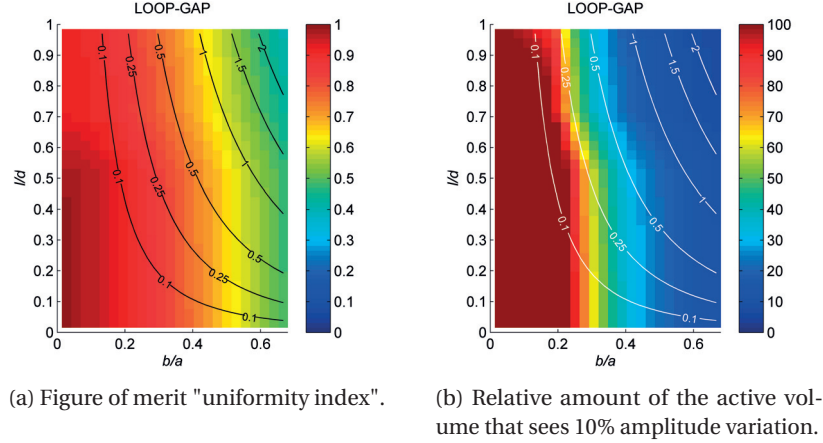


Figure 3.18 – 2D diagrams associated to the figures of merit related to the homogeneity of the field amplitude in the case of a cavity based on a loop-gap geometry and PMC boundary conditions.

Therefore in order to maximize the positive effect of the boundary condition modification a more optimal design corresponds to a longer vapor cell which will allow a more homogeneous field if the central region is used in the clock operation. However, it is worth noting that from of point of view of the clock implementation the length of the cavity-cell package is also limited by potential temperature issues.

### 3.3 Characterization of the existing cavities

Part of this thesis is related to the study and the characterization of two currently employed cavity structures. A loop-gap geometry based on six electrodes was reported previously in [16] and it was successfully implemented for both continuous [16] and POP applications [7].

A version of this cavity was retrofitted in order to accommodate a modified design of the vapor cell based on two stems. In order to differentiate, this design is referred as "double-stem design".

In this section we report various studies related to the above-mentioned structures in the following order: First we investigate the results of a field imaging experiment that was used in order to experimentally evaluate the field distribution in the case of the first (original) loop-gap geometry. Next we briefly describe the double-stem design, we report its performance and comment on potential sensitivity issues related to the realization. Finally, we discuss results obtained for the temperature coefficient of this cavity.

#### 3.3.1 Field imaging experiment

The role of the magnetic field homogeneity in the clock performance puts importance not only on the cavity itself but also on the experimental verification of the field distribution. A modern approach to obtain the magnetic field distribution attributed to the clock transition is to directly use the atoms as sensors. The method was first demonstrated for the case of cold atoms, where imaging of the near-field distribution around a coplanar waveguide was obtained [99]. It was then shown to be suitable for imaging in hot atomic vapor cells [100, 101]. The method was recently used to measure the microwave magnetic field distribution for one of our currently employed cavities [102] (reported originally in [16]). Such an experiment can be very insightful in terms of optimizing the cavity performance and it is therefore worthed to analyze the experimentally obtained results and see how they relate to our a numerically obtained analysis.

**General description of the method and the experimental setup** First, lets introduce the main physical principle behind this method in a qualitative fashion – an in-depth description can be found in [99]. The imaging of the magnetic field is performed, somewhat, similar to the operation of the POP clock – the interaction of the atoms with the optical/microwave field is separated in time, where the fields are applied in pulses. First, a pulse of laser light is applied in order to prepare the atoms in the same state – the  $F_g$  ground state is depopulated (see the explanation for the relevant atomic transitions discussed in section 1.3.1). After this is achieved, the light is switched off and a pulse of microwave magnetic field is then applied. Becasue the microwave field is tuned to the required frequency of transition (e.g. 6.8345 GHz with the magnetic field directed along the quantization axis for the  $\pi$ -transition) the pulse induces a cyclic process of population/depopulation (in the hyperfine structure) which happens with (Rabi) frequency in the KHz range. For the laser light this (Rabi) oscillation shows through the optical density  $OD$  (defined as in [101]:  $OD = -\ln(I_t/I_0)$ , where  $I_t$  and  $I_0$  is the transmitted and incident power per unit area). This means that after the microwave pulse (its duration  $dt_{\mu w}$  can be varied) is switched off and a second optical pulse is then applied (probing pulse), the amount of detected light will depend on the duration of the microwave pulse. If we repeat this process multiple times, by changing the duration  $dt_{\mu w}$  we are able to reconstruct the time-domain oscillations of the optical density (the signal is shown in 3.19).



Once this signal is obtained, the data can be fitted in order to find the Rabi frequency – [102]:

$$\Delta OD = A - B \exp\left(-\frac{dt_{\mu w}}{\tau_1}\right) + C \exp\left(-\frac{dt_{\mu w}}{\tau_2}\right) \sin(\Omega dt_{\mu w} + \phi), \quad (3.5)$$

where  $A$  is an offset constant (gives the intrinsic optical density of the Rb vapor for the conditions of the experiment but without the applied microwave field), the amplitudes  $B$ ,  $C$  and the time constants  $\tau_1$  and  $\tau_2$  are related to the relaxation processes,  $\Omega$  is the frequency and  $\phi$  is the phase of the Rabi oscillations. Because we can directly relate the microwave magnetic field to the Rabi frequency (see eq. 2.45), the detected signal shown in 3.19 is in principle all the information needed to deduce the amplitude of the field driving the given transition. In our case, the driving fields provided by the cavity that can be imaged are related to the  $\sigma_-$ ,  $\sigma_+$  and  $\pi$ -transitions (see eq. 2.46). In order to resolve this in a spatial way, a matrix detector (CCD camera) is used where the temporal signal from figure 3.19 is obtained for each of the  $n \times n$  pixels of the camera. This technique was first applied for a thin optical medium, e.g. [99] and [101], where the microwave field varies negligibly along the light propagation. However, in the currently considered case, a thick vapor cell is used [102]. The obtained image, in this case, corresponds to the amplitude of the microwave magnetic field integrated by the light along the full height of the vapor-cell ( $\approx 23$  mm along the  $z$ -axis of the cavity) – according to the Beer-Lambert law [102].

A simplified scheme of the setup used for the field imaging experiments is depicted in figure 3.19. A diode laser is stabilized to the Rb D2 transition so that it drives atoms in  $F_g = 2$  (see section 1.6), and its light is pulsed using an acousto-optical modulator. The resulting light beam traverses the microwave cavity containing the Rb vapor cell. The cell and the cavity are temperature-stabilized to around 60 deg C and the static magnetic field (the C-field) is applied parallel to the direction of the laser propagation and the central axis of the cavity (the  $z$ -axis). Imaging lenses are used to enlarge the laser beam to the size of the accessible cell diameter, and to image the transmitted beam onto the CCD camera chip. A switchable microwave source is used to apply the microwave to the cavity.

**Results** In figure 3.20 we show the experimentally obtained 2D image of the microwave magnetic field driving the  $\pi$ -transition (in our case  $B_\pi \equiv B_z$  since the quantization axis is considered perfectly aligned to the axis of the cavity). The image covers a circular cross section with a radius of 5 mm, aligned to the central axis of the cavity. Each pixel gives an averaged value of the field amplitude integrated over the 25 mm length of the relatively thick cell. If we assume that  $B_z(z)$  is identical for all points from the cross section, it is clear that in this case the image shown in figure 3.21 will correspond to the transverse field distribution. The numerically obtained distribution shown in figure 3.21 is calculated from a simulation of the cavity where the whole complexity of the structure is considered: vapor cell, stem of the vapor cell, feeding [103]. Similar to the experiment, we integrate the field along the length of the vapor cell, where in the figure we show a contour plot corresponding to the amount of amplitude variation relative to the maximum (found in the center).



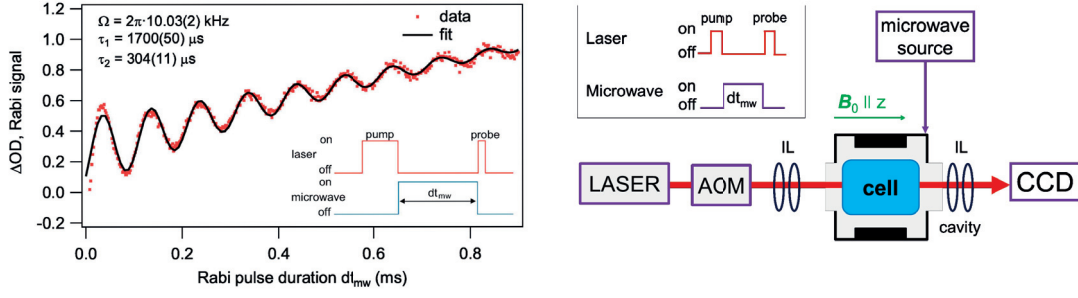


Figure 3.19 – (left) The effect of the Rabi oscillations on the  $OD$  of the atomic medium, shown in the time domain – image taken from [102]. In practice, the Rabi oscillations will modify the absorption partially – typically, a fraction of the light passes through the medium and is detected as a background signal. This is taken into account in the figure where the normalization is such that:  $OD = 0$ , when no microwave field is applied. (right) The experimental setup used for the field imaging. AOM – acousto-optical modulator; IL – imaging lenses.

From the contour plot can be seen that within the area corresponding to the image we have  $\approx 15\%$  variation. It is seen that the amplitude variation of the  $B_\pi$  component over the area sampled in the experiment is  $\approx 20\%$  which is slightly higher due to the off-centered maximum. In fact, both the experimental and numerical amplitude profiles show an off-center (relative to the image center) displacement of the maximum field towards the upper left corner. This can be seen in figure 3.21 where we compare both by overlapping the contour plot with the image. The relative  $x$  and  $y$  coordinates are approximately scaled according to the experimental imaging conditions. By doing a simulation study, assuming the fields are perfectly aligned to the cavity axis, the spatial shift of the field maximum was determined to mostly depend on the position of the cell stem – its position at the time of the experiment is shown in figure 3.21. This result is not unexpected since, inside the volume of the cavity the stem of the vapor cell represents a major dielectric inhomogeneity. Moreover, the fact that for this cavity, the mechanism of tuning is associated to rotation as well as insertion of the dielectric cell, makes it rather difficult to precisely control the distribution and compensate certain inhomogeneities. In terms of a  $B_\pi$  distribution, this experiment can be thought as a confirmation of the simulation. Moreover, given the structure and dimensions of the cavity, the variation of the field is similar to the generic case of the previously discussed 6-gap geometry – see figure 3.10. The peak is found in the center where, for a sufficiently small radius, the field is azimuthally symmetric and no leakage from the gaps is seen.

In figure 3.22 we show what is the obtained distribution of the unwanted  $B_-$  and  $B_+$  driving fields. In the case of the experiment, the  $B_-$  distribution appears offsetted towards the the bottom left of the  $xy$ -plane. The image obtained for the  $B_+$  component is not symmetric to the one found for  $B_-$  and moreover, the maximum is found very close the center.

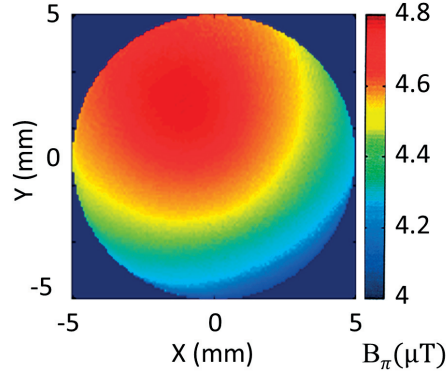


Figure 3.20 – Experimentally obtained distribution of the  $B_\pi$  component (amplitude) found in the center of the vapor cell.

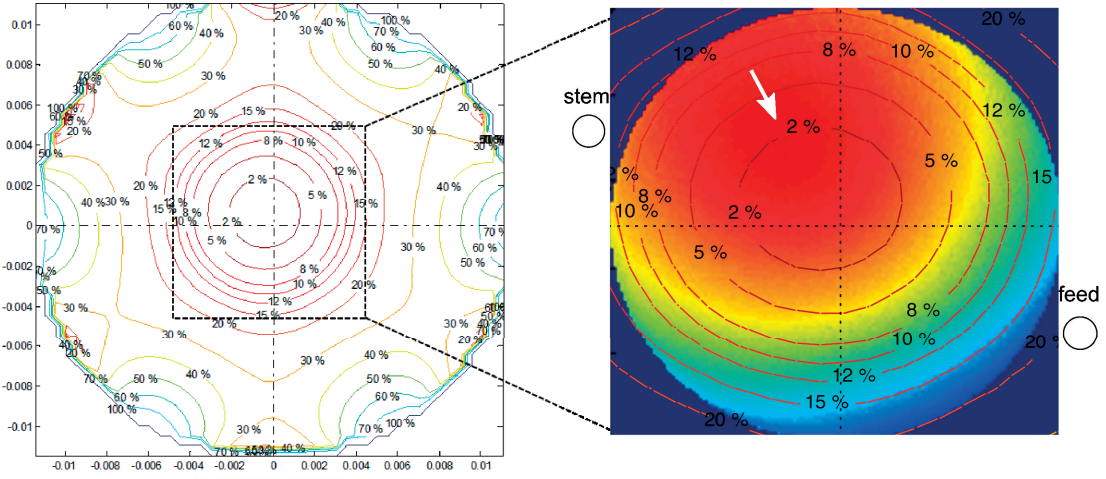


Figure 3.21 – (left) A contour plot of the simulated  $B_\pi$  field (amplitude) calculated for the complete cross section of the vapor cell. (right) Comparison between the simulated and the experimentally obtained profiles. The position of the stem and the feeding loop are indicated as they would be seen, relative to the  $xy$ -plane of the image, at the time of the experiment. The arrow emphasizes the offset of the field maximum.

In principle, for the considered mode in this cavity, it is expected to obtain identical and azimuthally symmetric  $B_{+,-}$  fields with a minimum found in the center – much like in the case of the canonical geometry (figure 2.8). From figure 3.22 can be seen that such a behavior can be approximately attributed to the case of the  $B_-$  (apart from the relatively large offset), however this is clearly not the case for the  $B_+$  image. On the contrary, for the simulated images, we are able to see the expected minimum of the field, although a slight asymmetry is found between the two components. The latter can be qualitatively understood by looking at figure 3.23 where we show the  $B_{+,-}$  components at separate planes along the height of the vapor cell.

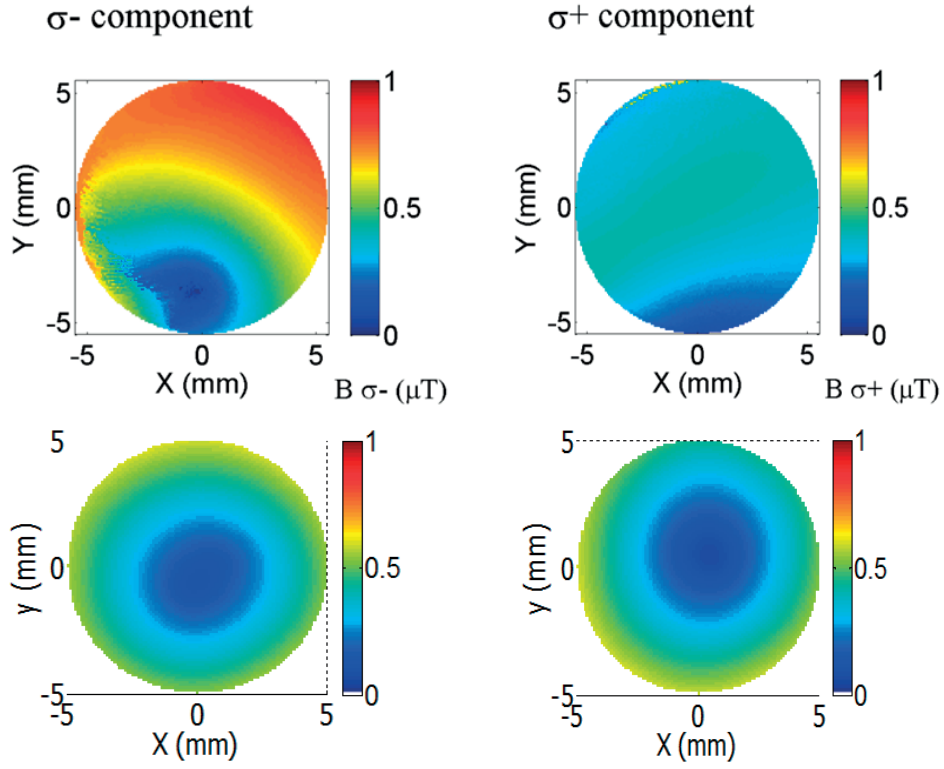


Figure 3.22 – Distribution of the  $B_{+,-}$  components. (top) Experimentally obtained images; (bottom) Simulated images.

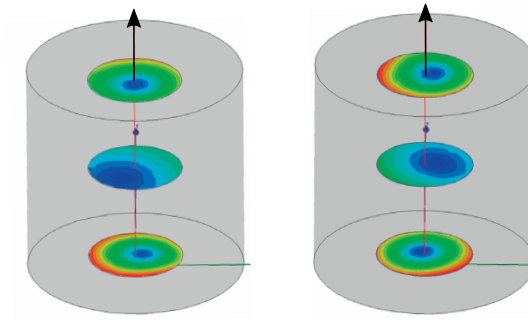


Figure 3.23 – Simulated field amplitude ( $B_{-}$  is shown on the left;  $B_{+}$  is shown on the right) found along different heights inside the vapor cell:  $0.1l$ ,  $0.5l$  and  $0.9l$ , where  $l$  is the cell height. A common normalization is considered for the color-coding. The arrows indicate the direction of the light propagation.

While for the different planes considered the distribution is found to be non-symmetric in azimuth, the integration along  $z$  averages out this effect resulting in the, close to symmetric, images for the simulated field shown in figure 3.22.

We note that in the simulations we were not able to reconstruct the behavior seen in the experiments for the  $B_{+,-}$  components. The fact that the light is integrated along the cavity height washes out the effect of the non-symmetries that can in principle arise due to the feed or the stem. One possible explanation of this behavior would be to consider that a potential misalignment between the static magnetic field, the light beam and the axis of the cavity was present at the time of the experiment.

### 3.3.2 Field misalignment

In the previous section it was shown that the fields driving the unwanted  $\sigma_{+,-}$  transitions may have a non-negligible amplitude in the most important part of the cavity volume and hence may play a significant role in the clock performance. It was speculated that a potential misalignment between the fields required for the operation of the clock (the microwave field, the static magnetic field and the optical beam) can be the reason for such a behavior. While in principle, in the clock operation, such a misalignment is usually taken care of, it is still interesting to investigate it in line with the imaging experiment. For that matter, in this section we study this effect theoretically for which, in order to simplify, the canonical cylindrical cavity (TE<sub>011</sub> mode) is considered.

**Description of the general misalignment problem** We make the following assumptions: A perfectly collimated (parallel) light beam of a uniform intensity profile is considered. The light source is situated at the bottom opening of the cavity where the cavity walls are considered to be non-reflecting for the light. The static magnetic field is considered to be fully-homogeneous everywhere inside the cavity — the fringing field is neglected and therefore the quantization axis, defined by the C-field vector, is equal for all atoms. The cavity is illustrated in the scheme shown in figure 3.24, where we first report the field amplitude found in the ideal case for which no misalignment exists. The microwave magnetic field is calculated with respect to a coordinate system aligned to the central axis of the cavity. It is decomposed along the C-field direction and the driving fields  $B_-$ ,  $B_+$  and  $B_\pi$  are obtained. In the field calculation, the effect of the Rb vapor, the dielectric cell and the light apertures are neglected. Similar to the experiment, the field images are obtained by integrating along the full height of the vapor cell (a cell with a standard height of 20 mm is considered).

**Misalignment of the C-field** We allow a misalignment of the C-field by the rotation scheme shown in figure 3.25. For  $\theta = 0$ , the effect of a rotation at  $\phi$  or  $\psi$  is identical since the  $B_-$ ,  $B_+$  and  $B_\pi$  components all have azimuthal symmetry. The symmetry is broken in the rotation  $\theta \neq 0$ , which is easily seen for the driving  $B_-$  and  $B_+$  fields inside the cavity shown in figure 3.26a and for the corresponding averaged images shown in 3.26b. As a result of the rotation, the field at the top and bottom of the cavity is kind of mirrored (see the  $xy$ -planes reported in 3.26a). However, the effect is somewhat averaged along the direction of the light beam, resulting in the field images shown in figure 3.26b. It is seen that even for small angles the unwanted driving fields can have a complicated shape with a non-negligible amplitude found in the center.

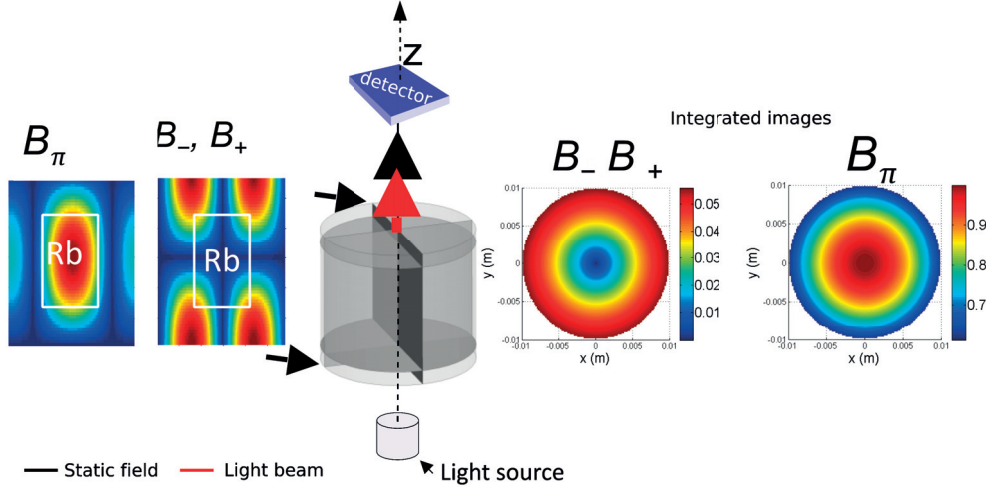


Figure 3.24 – A Scheme of the cavity with the light source and the detector. Both the light beam (represented by the red arrow) and the C-field (represented by the black arrow) are considered aligned to the central cavity axis. The obtained  $B_{-,+}$  components are symmetric and result in integrated images that are identical. A common normalization is considered for the  $B_{+,-}$  and  $B_\pi$  components.

Once the azimuthal symmetry is broken, the integrated images will be further rotated for  $\psi \neq 0$ , but are invariant to rotation at  $\phi \neq 0$ . Moreover, the averaged images obtained for  $B_-$  and  $B_+$  are always identical, regardless of the chosen direction for the C-field. The amount of clock signal degradation, due to increased coupling of  $B_-$  and  $B_+$ , is determined by the  $\theta$  angle only. Therefore, the FOF (shown in figure 3.27a) is invariant to rotation at  $\phi$  and  $\psi$ . Any misalignment of the C-field will equally increase the coupling to the both  $\sigma_-$  and  $\sigma_+$  transitions. For completeness, we include figure 3.27b, where we shown how the  $\theta$ -rotation affects the homogeneity of the field (we have chosen to report the amount of active volume for which the amplitude field variation is in the interval of 35% relative to the maximum). It is obvious that the range of angles included is far from the clock operation requirements. However, it is interesting to see that at a very large angle ( $\theta = 60$  deg) the homogeneity is improved (clearly, this effect cannot be used, since for such angles the FOF factor is very low). However, it is curious to note that such an effect might be worth further investigation since optimal structures may exist for which the field homogeneity can be improved in this way.

**Misalignment of the light beam** A laser beam misalignment will result in a horizontal displacement of the averaging direction, spread of the shape of the peak of the averaged field and, depending on the detector area, a reduced amount of the useful signal. The displaced direction of the laser light and thus the direction of the integration can be represented by applying a shear mapping to the initial grid for which the field is calculated – figure 3.28. In figure 3.29 we report what is the general effect of such a misalignment. It can be seen that, at the detector plane, the field is displaced away (from the center of the image) due to the tilt of the optical beam.

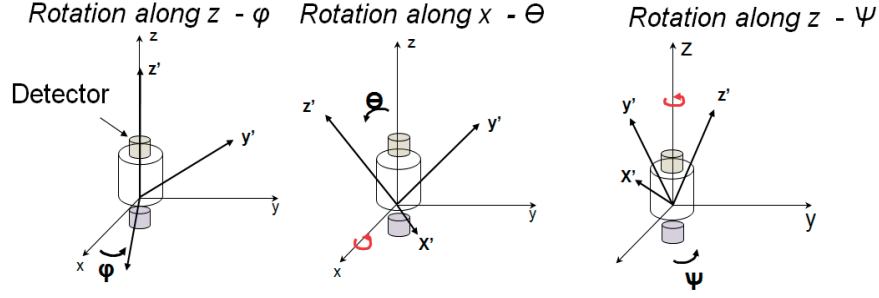
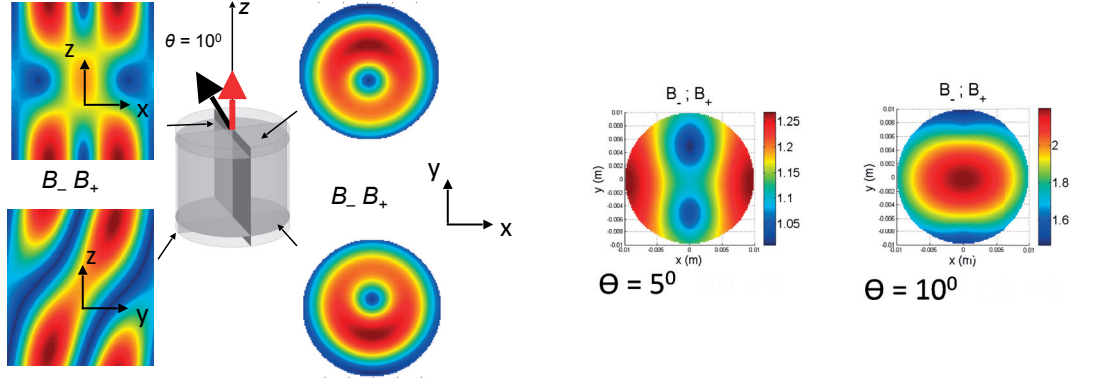


Figure 3.25 – The cavity is initially fixed to a coordinate system  $xyz$ . The coordinate system  $x'y'z'$  is obtained by three consecutive rotations related to the angles  $\phi, \theta, \psi$  each corresponding to rotation along a particular axis ( $z-x-z$  rotation convention for extrinsic rotation as defined in [105]). The rotated quantization axis is considered to be along  $z'$ .

For the  $B_\pi$  component this means that the maximum is not found at the center while for the  $B_+$  and  $B_-$  components, on the contrary, we see that such an effect may result in a non-negligible amplitude in the center. Assuming the C-field is perfectly aligned, due to symmetry, any further azimuthal rotation of the displaced beam results in field images that are rotated but will not change the shape of the field profile [104]. Thus, in this case, the total amount of the driving fields interacting with the atoms depends only on the amount of radial displacement and can be seen in figure 3.30. It is curious to note that  $B_{-,+}$  and  $B_\pi$  decrease in slightly different rates as function of the beam tilt. Due to that, the FOF is found to slightly improve for small tilt angles, on the expense of less overall signal detected. It is also worth noting that such a misalignment of the laser beam has the potential to spread the shape of the detected field distribution (although this effect is difficult to see for the relatively small angle shown in figure 3.29a). In attempt to quantify it, we evaluate what is the field homogeneity in the volumetric region that is sampled by the tilted light beam. In figure 3.29b we show how much of the active volume (hence the relative number of atoms, if they are considered homogeneously distributed) will interact with the  $B_\pi$  field that varies 30% with respect to the maximum. It is seen that, in principle, the homogeneity is improved, however the absolute amount of signal is reduced since for large angles the light samples a very narrow region. It is worth noting that this effect might lead to an overestimation of the field homogeneity if the misalignment at the experiment is non-negligible.

**Final discussion** It was shown that a small field misalignment between the required fields has indeed the potential to influence the outcome of the imaging experiment. Based on the discussion above, we think that the most plausible explanation for the experimental result shown in figure 3.22 might be a possible misalignment of the laser beam with respect to the cavity axis. In this case, the amount of radial field displacement from the center (the amount of displacement of the maximum for  $B_\pi$  and the amount of displacement for the minima for  $B_+$  and  $B_-$  seen on the experimentally obtained images is  $\approx 2 - 3$  mm) can be attributed to a possible tilt of the laser beam.

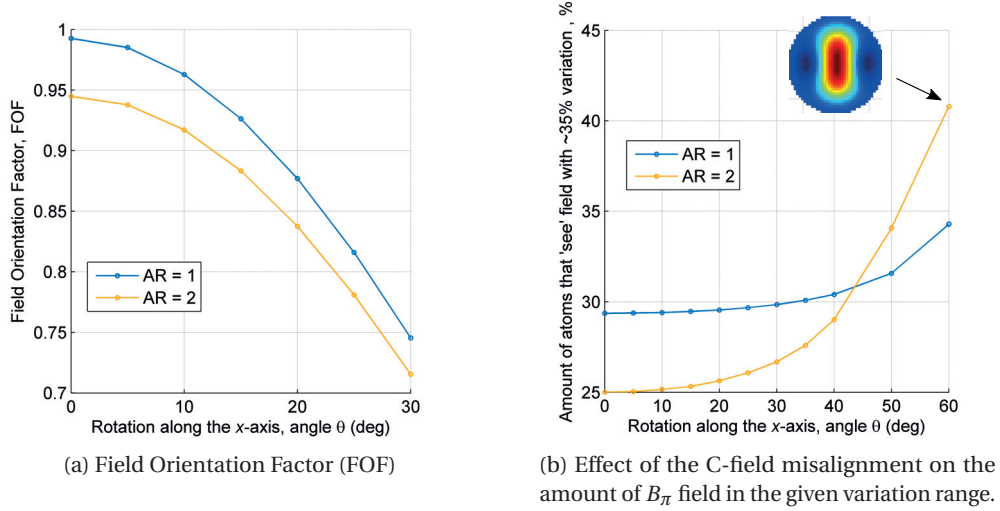




(a) Amplitudes of the  $B_{-,+}$  components corresponding to the planes inside the cavity

(b) Integrated images. The light beam is considered aligned to the central cavity axis; the normalization is relative to the corresponding fields found in the case of the perfectly aligned cavity.

Figure 3.26 – Effect of the C-field misalignment on the  $B_{+,-}$  driving fields.



(a) Field Orientation Factor (FOF)

(b) Effect of the C-field misalignment on the amount of  $B_\pi$  field in the given variation range.

Figure 3.27 – Figures of merit as function of the C-field misalignment (at angle  $\theta$ ) considered for two separate aspect ratios of the cavity.

It is worth noting, however, that in all cases of the theoretically studied misalignment we observe identical images for the  $B_-$ ,  $B_+$  (one exception would be to consider a phase difference between the transverse field components – see appendix A). On the other hand for the experimental images shown in figures 3.21 and 3.22 we can see a certain sense of azimuthal rotation between the  $B_\pi$ ,  $B_-$  and  $B_+$  field distributions. One possible explanation for this would be to consider the presence of mechanical noise in the process of data acquisition.

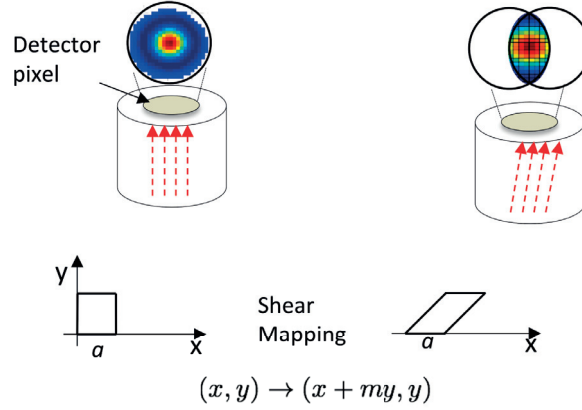
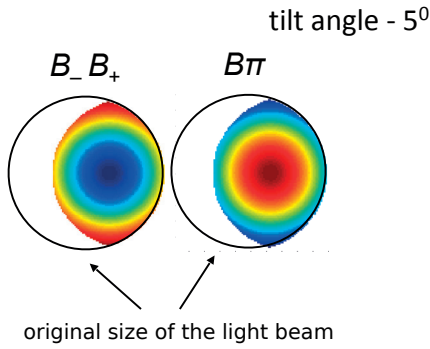
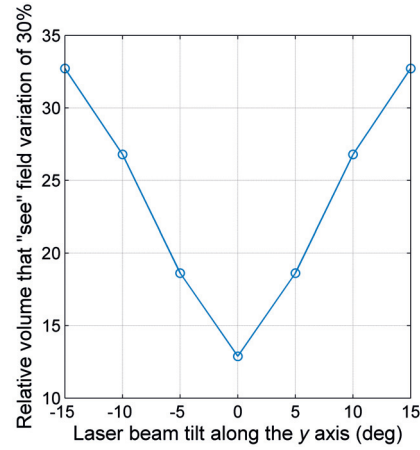


Figure 3.28 – The displaced direction of the laser light is obtained by applying shear mapping to the initial rectangular grid used (details included in appendix A).



(a) Integrated images for  $B_{+,-}$  and  $B_{\pi}$ . The circles define the laser beam footprint in the perfectly aligned case.



(b) Relative amount of the active volume (relative number of atoms, if they are considered homogeneously distributed) that sees  $B_{\pi}$  field with amplitude that varies 30% with respect to the maximum.

Figure 3.29 – Effect of the laser beam misalignment. A circular cavity with a radius  $a$  of 30 mm and a height  $d$  of 48.5 is considered. The radius of the laser beam is 15 mm, the C-field is oriented along the  $z$ -axis.

### 3.3.3 Double-stem design

**Description of the design** The design of the double-stem cavity is based on a six-electrode loop-gap geometry similar to [16] which here we overview only briefly. From the schematic representation shown in figure 3.31 can be seen that the structure is based on a cylindrical geometry, additionally loaded with six electrodes that form the azimuthally-symmetric loop-gap.



### 3.3. Characterization of the existing cavities

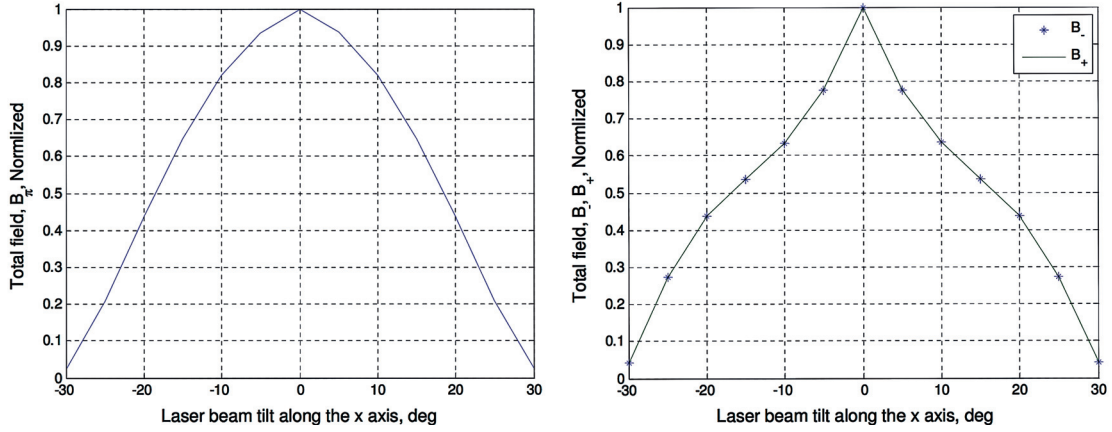


Figure 3.30 – Total amount of the driving field interacting with the atoms as a function of the laser beam tilt.

The mode of interest is a  $TE_{011}$ -like where in the central volume the magnetic field has a maximum and is directed along  $z$ . The cell with the Rb vapor is therefore accommodated in the center, where a quartz cell based on two-stems is considered. The pumping light passes the structure through two quartz slabs positioned at the openings and required to reduce the temperature gradient. An additional feature of this cavity is the existence of cutoff tubes at both openings, needed to reduce the field leakage.

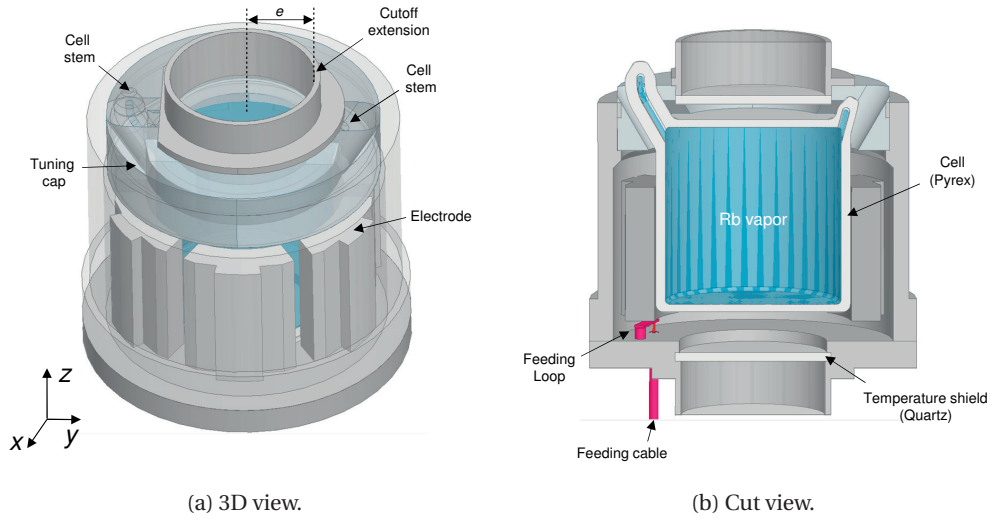
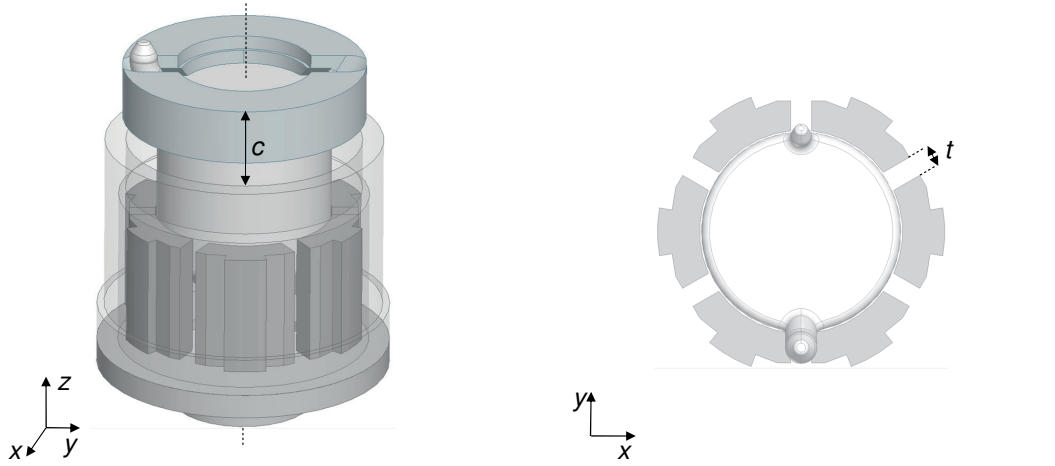


Figure 3.31 – A scheme of the basic structure of the chosen cavity design.



(a) A scheme of the cavity tuning used. It is based on insertion of the dielectric cell and hence changing the distance  $c$  (referred as a tuning gap distance).

(b) All gaps between the electrodes have the same size  $t$ .

Figure 3.32 – Parameters used to obtain the required resonance condition.

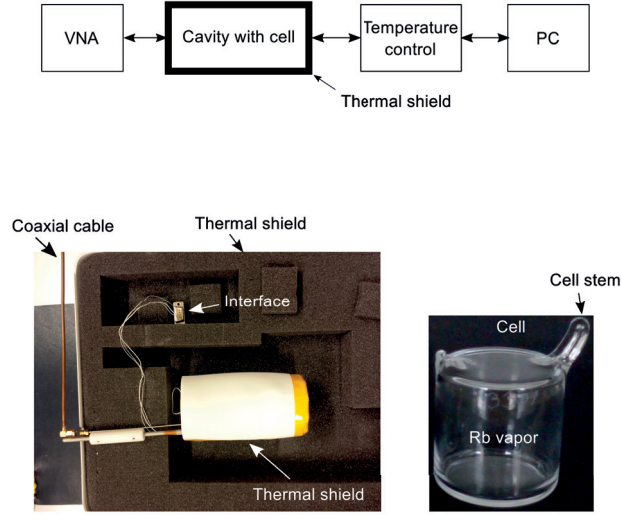
While the main part of the cavity is unchanged with respect to the original geometry [16], the structure needs to be reconsidered mainly due to the following reasons:

- Since the design of the vapor cell is based on two stems, the amount of dielectric filling present in the top part of the structure is increased and furthermore an additional opening is required in the top cap. While we do not observe a big difference in the structure of the modes, there is a potential for some unwanted modes to perturb the performance since, in principle, this type of cavity is not operating at the fundamental mode.
- Another major difference that can perturb the performance, with respect to the original design [16], is the lack of dielectric lens required for the pumping light.
- Finally, as the least sensitive aspect we consider the presence of additional cutoff tubes.

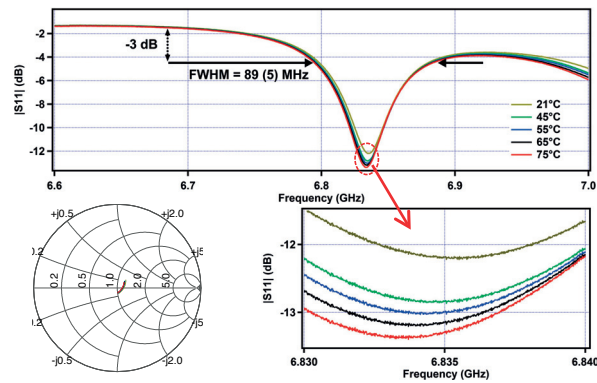
**Measurement of the temperature coefficient** As it was previously discussed (in section 3.1.2), one important design aspect of the loop-gap geometry is its generally increased temperature stability. In fact, one of the major reasons for the here-considered design is the improved temperature performance – the shorter reservoir stems of the vapor cell result in approximately ten times lower stem temperature coefficient [106]. Here we report what is the temperature stability of this cavity. In figure 3.33a we show what experimental setup was used to in order to perform the measurement of the TC. The cavity is loaded with the glass cell shown in the figure. The cell is manually crafted (using a glass blowing technique) and it is with a diameter of 25 mm and a height of 25 mm.

### 3.3. Characterization of the existing cavities

It is filled with a buffer gas mixture (argon and nitrogen) with an overall pressure of 26 mbar where  $P_{Ar} : P_{N_2} = 1.6 : 1$ . During the experiment, the cavity-cell package is kept in a thermal shield, where the temperature is stabilized using a dedicated micro-controller. The considered range of operating temperatures is: 20:80 K, where each measurement is performed for a sufficient time interval ( $\approx 1$ h) so that the cavity is well thermally-stabilized. The resonance frequency is obtained from the  $S_{11}$  parameter, measured with a Vector Network Analyzer (VNA) – Hewlett Packard 8720D. In figure 3.33b we report the experimentally obtained result for five different operating temperatures.



(a) Experimental setup.



(b) Experimentally obtained  $S_{11}$  parameter shown for the considered temperature range.

Figure 3.33 – Measurement of the temperature coefficient.

The resonance frequency can be found as a function of the temperature from the minima obtained for the fitted data. In our case, a temperature coefficient of  $\approx -33(2)$  KHz/K was found [106] which, given the fact that no additional modification of the design is applied, is on a par with the top-performing structures that were reviewed in section 3.1.2.

**Modeling of the temperature coefficient** To better understand the temperature behavior of the loop-gap structure we have also studied the problem numerically. In principle, for the case of the magnetron cavity the variation of the resonance frequency as function of the temperature is a full-wave problem which can be appropriately studied via FEM simulations. Changing the operational temperature can be implemented in the simulations using thermal expansion coefficients that will scale the dimensions of the cavity and the vapor cell (figure 3.34). It is important to note that for the expected variation range (20–50) KHz/K, a simulation of the cavity for a 20 K temperature difference results in just a 0.005 % fractional change of the resonance frequency. This is a stringent convergence criterion and cannot be easily fulfilled even by a workstation-class computer (for the software used in our case – Ansys HFSS<sup>®</sup>). In order to reduce the computational domain, one possibility is to take an advantage of the 6-fold rotational symmetry of the cavity, which however proved not to be sufficient in our case. Instead, our approach is to consider the problem by utilizing a Transmission Line (TL) model – figure 3.35a. In this way we can separate the effect of the temperature variation and treat separately the transverse and the longitudinal (along  $z$ ) cases.

First, we model the loop-gap segment by assuming PMC boundary conditions at the top and bottom ends. In this case, the mode of interest is independent of  $z$  thus the height can be reduced arbitrary. This allows a full-wave eigen simulation with a very high precision to be performed for a thin slice of the loop-gap region (figure 3.35b). Using this approach, we can find the cutoff frequency as a function of the temperature  $f_{\text{cut}}(T)$ . Finally, the resonance frequency can be determined according to the relation:  $f_{\text{res}}(T) = \sqrt{[0.5c/l(T)]^2 + f_{\text{cut}}^2(T)}$ , where  $c$  is the speed of light in vacuum and the longitudinal temperature variation is included via the height of the cavity, scaled according the temperature:  $l(T)$ . Here we have made an approximation that the top and bottom extensions of the cavity are very thin and therefore the length of the central region is close to one half of the guided wavelength.

In a more complete description of the problem, the extension caps are boundary conditions that allow resonance for a shorter than a  $\lambda/2$  cavity and can be modeled as equivalent lumped impedances – figure 3.35a. Note that in the simulation used to obtain  $f_{\text{cut}}(T)$  we also consider the presence of the vapor cell (see figure 3.35b). In this case, in principle, such a simplified decomposition of the problem is not correct since in the transverse direction we have a non-homogeneous dielectric filling. Qualitatively this means that, when PEC boundaries are applied, the transverse field distribution is influenced by the height of the cavity. However, we consider this approach to be good enough, since the (transverse) distribution found for the realistic cavity (considered with cell, stems etc.) is close to the one obtained in the case shown in figure 3.35b. In figure 3.36a we show how the cutoff frequency depends on the temperature for a cavity similar to the experimentally investigated.

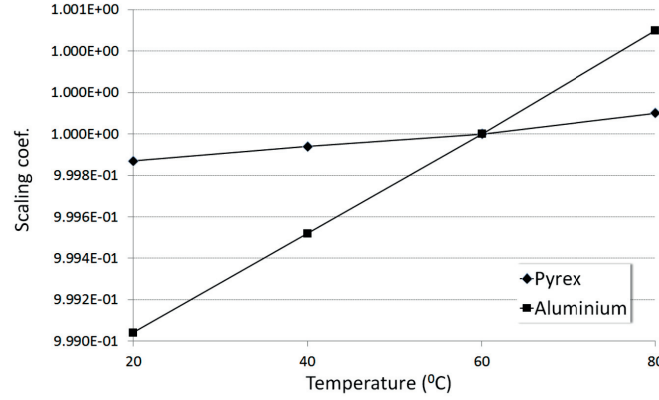


Figure 3.34 – The scaling factor used to model the temperature stability of the resonance frequency. The nominal case of  $T_0 = 60$  deg C is used as a reference. A given dimension  $d$  associated to the cavity can be obtained by scaling the nominal one:  $d(T) = d(T_0)(1 + \Delta T\alpha)$ , where the linear thermal expansion coefficient is:  $\alpha = 24 \times 10^{-6}\text{K}^{-1}$  for the Al alloy used and  $\alpha = 3.25 \times 10^{-6}\text{K}^{-1}$  for Pyrex. It is clear that variation of the temperature will then decrease/increase the dimensions for values for temperatures that are below/above the reference  $T_0$ .

The resonance frequency of the cavity is reported in figure 3.36b. In the figure, the case referred as "longitudinal" is obtained for a fixed cutoff frequency (no temperature variation in transverse direction) and scaled according to the temperature, length of the cavity  $l(T)$ . From figures 3.35b and 3.36a we see that the inverted temperature dependence for the longitudinal and transverse case combine, so that the slope of the resonance frequency is reduced ( $\approx -9$  KHz/K). The result for the numerically obtained TC is therefore about 3 times smaller compared to the experimentally obtained (figure 3.37). A possible explanation may be that the influence of the extensions is not considered in the temperature expansion.

**Final notes and discussion** In this section we covered an important characteristic of the cavity – the temperature stability of the resonance condition. The experimentally measured TC ( $-33$  KHz/K) confirms the expected temperature stability that the loop-gap cavities intrinsically have. The loop-gap being a relatively complicated structure, makes it difficult to have a direct physical understanding for the TC. Moreover, a complete simulation of the structure, with the full complexity of the design, is not possible in our case, since the expected frequency variation is typically found under the level of the numerical noise. The use of a TL-based approach allowed us to evaluate the TC numerically, which was found to qualitatively agree with the experiment. Although a considerable overestimation of the performance was predicted by the model (a rather simplified version of the original structure was assumed), it helped us reveal a nice feature. Namely, the temperature dependence was found to have an opposite behavior in the separately considered cases of transverse and longitudinal temperature variation. It is evident that such an inverse behavior can be utilized to engineer a cavity, characterized by a reduced temperature coefficient.

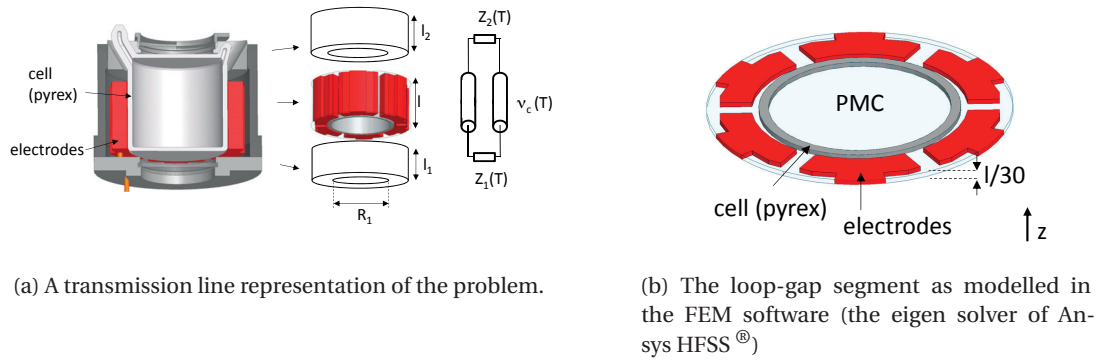
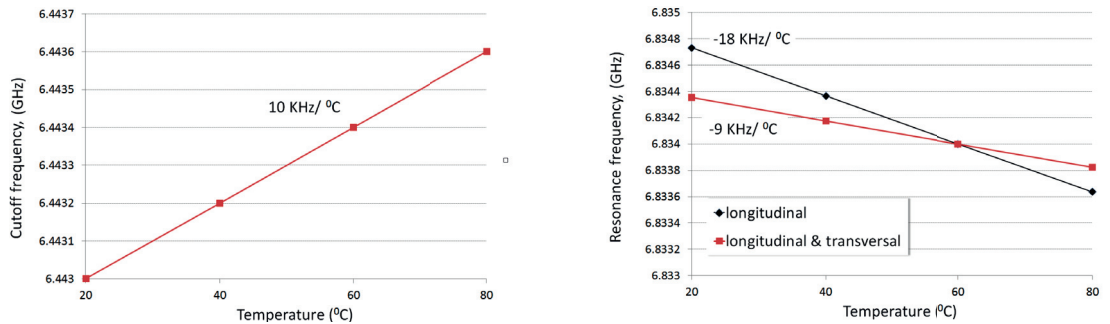
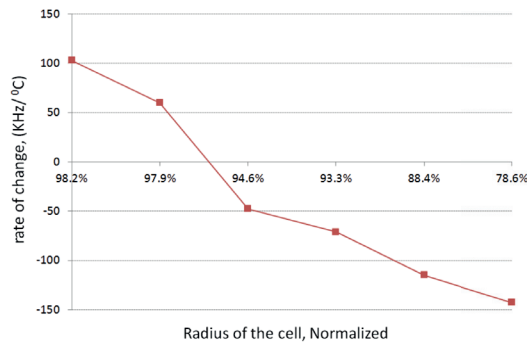


Figure 3.35 – The cavity can be simplified as a loop-gap waveguide segment characterized by a translational symmetry and enclosed by the top and bottom extension caps (considered empty). Physically, the resonance frequency can be determined if the guided wave propagation (assuming a single mode) and the impedances corresponding to the top and bottom caps are known functions of temperature.



(a) Cutoff frequency as a function of the temperature. The result is obtained from a FEM eigen simulation and corresponds to the temperature dependence associated to the transverse dimensions of the cavity.

(b) Resonance frequency as a function of the temperature.



(c) Slope of the  $f_{res}(T)$  obtained as function of the cell radius. The values for the cell radius are normalized to the inner radius of the electrodes.

Figure 3.36 – Simulated effect of the temperature.

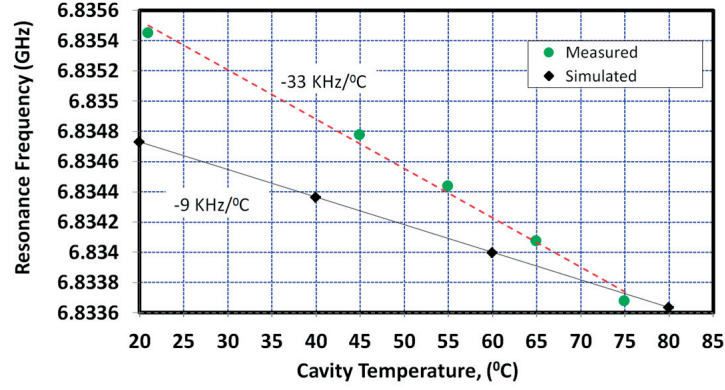


Figure 3.37 – Comparison between the experimentally measured and the simulated temperature coefficient.

For example, in figure 3.36 is shown the result from the initial study related to the control of the  $f_{\text{res}}(T)$  slope. From the plot can be concluded that, depending on the radius of the cell (the wall size is kept constant), opposite slopes can be obtained for the  $f_{\text{res}}(T)$  dependence. Finally, we note that from the experimentally obtained result for the  $S_{11}$  parameter (see figure 3.33b) it can be seen that the resonance condition is not fully optimal – the curve shows a partial modal overlap and, as a consequence, a relatively low Q-factor ( $Q = 70$ ) was measured. The main reasons for such a behavior are attributed to possible production tolerances, among which, we consider the ones associated to the vapor cell to be the most sensitive realization aspect. In appendix B we have included a rather extensive study of the sensitivity, related to the resonance condition and its potential for a modal overlapping.





## 4 Implementation of AMC boundary conditions

It was already discussed (see chapter 2.3) that for a vapor cell with fixed dimensions the longer the cavity is, the better the homogeneity (within the cell, along the  $z$  direction). In fact, in the non-physical limit where the top and bottom plates are infinitely far away (a cavity with an infinite height), the field is fully constant along the  $z$ -axis. This is because the guided wavelength of such a cavity is  $\lambda_g \rightarrow \infty$ , since we are in the beginning of the dispersion curve ( $k_z = 0$ ). Furthermore, in section 2.1 we showed that applying PMC boundaries at the top and bottom plates is a possible way to obtain the same result for a finite height  $d$  of the cavity. What is more, we saw that, in this case, the mode of interest can be considered independent on the cavity height. Being described by a longitudinal modal number  $p = 0 \Rightarrow \text{TE}_{010}$ , it follows that the only way to control the resonance frequency in such a cavity is via the radius of the cross section. Due to the improvement of the field homogeneity such a mode holds a great advantage in our application and it is worth investigating how to physically realize it. Therefore, in this chapter, we concentrate on a realistic implementation of a cavity with bottom and top PMC boundaries.

The engineering of such artificial boundary conditions, also known as artificial magnetic conductor (AMC), High Impedance Surface (HIS) or magnetic mirrors (in optics), has been an active topic of research for various applications mostly related to miniaturization in antennas [107] and microwave devices [108]; improvement of the field homogeneity in the case of electron paramagnetic resonance [109, 110, 111, 112], as well as for the use in quantum experiments [113] and optical applications [114]. In the first part of this discussion, we consider the general case of a cavity geometry based on a section of a waveguide which we analyze following the approach found in [109].

### 4.1 Generic cavity with AMC boundaries

It is somewhat intuitive, that if we want to mimic the effect of placing the top and bottom conducting walls at infinity, we would use a dielectric filling since the finite dimensions would appear longer than in the empty case. So let's start from this simple intuition and investigate how to obtain AMC boundaries based on dielectric filling. Let's consider a general cavity without the cell and loaded with two dielectric segments as shown in figure 4.1. In order to take advantage of symmetry, the coordinate system is positioned at the center of the central region:  $d/2$  and the two dielectric segments have identical height  $e$ .

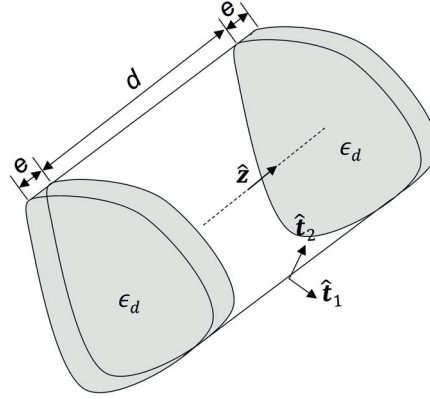


Figure 4.1 – A generalized cavity with translational symmetry and arbitrary cross section, loaded at the top and bottom with two cylindrical dielectric segments (depicted in gray). The cross section at the central region is identical to the regions with the dielectric filling. PEC boundary conditions apply to all external walls.

Furthermore, identical dielectric material is used for both segments, where the relative dielectric constant  $\epsilon_d$  can be arbitrary chosen while the central region is considered empty:  $\epsilon_{\text{central}} = \epsilon_0$ . For the TE family of modes the magnetic field in the central, empty, part is given by:

$$H_z(t_1, t_2, z) = \psi'(t_1, t_2) \cos(k'_z z), \quad -\frac{d}{2} < z < \frac{d}{2} \quad (4.1)$$

and for the dielectric segments we have:

$$H_z(t_1, t_2, z) = \psi(t_1, t_2) \sin \left[ k_z \left( \frac{d}{2} + e - |z| \right) \right], \quad \frac{d}{2} < |z| < \frac{d}{2} + e, \quad (4.2)$$

where, proceeding from the original mode of interest (with a longitudinal number  $p = 1$ ), expression 4.1 is chosen such that the field distribution has an even symmetry with respect to the center of the coordinate system. In eqs. 4.1 and 4.2,  $k'_z$  and  $k_z$  are the longitudinal propagation constants in the central part and in the dielectric segment accordingly. In order to keep the notation simple and the analysis more general we have chosen  $\psi'$ ,  $\psi$  to be the generalized transverse wave functions related to the two regions. Accordingly, it can be seen that eq. 4.2 fulfills the PEC boundary condition for the standard  $\text{TE}_{011}$  mode :

$$H_z(t_1, t_2, z = \frac{d}{2} + e) = 0.$$

As previously explained, the transverse-longitudinal decomposition of the solution implies that, for the structure shown in figure 4.1,  $\psi'$  and  $\psi$  both satisfy the 2-dimensional differential equations:

$$(\nabla_t^2 + k_c'^2)\psi' = 0 \quad \text{and} \quad (\nabla_t^2 + k_c^2)\psi = 0. \quad (4.3)$$

Where  $\nabla_t$  is the transverse gradient and the transverse propagation constants  $k_c'$  and  $k_c$  are determined by accounting for the boundary conditions:  $\partial\psi'/\partial n = 0$  and  $\partial\psi/\partial n = 0$  that need to be fulfilled at the circumferential PEC surface,  $n$  being the normal to the surface. Physically, this decoupling of the solution means that the transverse field distribution is independent from the longitudinal boundary. Therefore, since in the considered case the cross section of the cavity is identical for both regions, the field is governed by the same transverse constant  $k_c = k_c'$  and hence, referring to equation 2.12, we can write the longitudinal propagation constant as:

$$\begin{aligned} k_z'^2 &= \mu_0\epsilon_0\omega^2 - k_c'^2, \\ k_z^2 &= \mu_0\epsilon_0\epsilon_d\omega^2 - k_c^2. \end{aligned} \quad (4.4)$$

It is now clear that the effect of such a transverse discontinuity only alters the longitudinal propagation constant and therefore the longitudinal shape of the field.

The next step is to apply the relations from Maxwell's equations to the longitudinal field, in order to obtain the remaining transverse fields in each region:

Form eq. 4.1, in the central region  $-\frac{d}{2} < z < \frac{d}{2}$  we have:

$$\begin{aligned} \mathbf{E}_t'(t_1, t_2, z) &= -\frac{j\omega\mu_0}{k_c'^2} \cos(k_z'z) \hat{z} \times \nabla_t \psi'(t_1, t_2), \\ \mathbf{H}_t'(t_1, t_2, z) &= -\frac{k_z'}{k_c'^2} \sin(k_z'z) \nabla_t \psi'(t_1, t_2). \end{aligned} \quad (4.5)$$

Form eq. 4.2, in the top segment  $\frac{d}{2} < z < \frac{d}{2} + e$  we have:

$$\begin{aligned} \mathbf{E}_t(t_1, t_2, z) &= -\frac{j\omega\mu_0}{k_c^2} \sin\left[k_z\left(\frac{d}{2} + e - z\right)\right] \hat{z} \times \nabla_t \psi(t_1, t_2), \\ \mathbf{H}_t(t_1, t_2, z) &= -\frac{k_z}{k_c^2} \cos\left[k_z\left(\frac{d}{2} + e - z\right)\right] \nabla_t \psi(t_1, t_2). \end{aligned} \quad (4.6)$$

Until now, we considered the two regions separately. To link them, we must apply the boundary conditions at the dielectric interface. The longitudinal propagation constants as well as the relative amplitudes of the fields can be related by requiring continuity for both the transverse and longitudinal field components at  $z = \frac{d}{2}$ :

## Chapter 4. Implementation of AMC boundary conditions

- From  $H'_z(t_1, t_2, z = d/2) = H_z(t_1, t_2, z = d/2)$  or  $E'_t(t_1, t_2, z = d/2) = E_t(t_1, t_2, z = d/2)$  we can obtain:

$$\psi'(t_1, t_2) \cos(k'_z d/2) = \psi(t_1, t_2) \sin(k_z e); \quad (4.7)$$

- From  $H'_t(t_1, t_2, z = d/2) = H_t(t_1, t_2, z = d/2)$  we have:

$$k'_z \psi'(t_1, t_2) \sin(k'_z d/2) = k_z \psi(t_1, t_2) \cos(k_z e). \quad (4.8)$$

By expressing  $\psi'$  from eq. 4.7 and substituting it in eq. 4.8 we can obtain the following transcendental relation between the longitudinal propagation constants :

$$k'_z \tan(k'_z d/2) = k_z \cot(k_z e). \quad (4.9)$$

It is clear that, in terms of frequency, each dimension is characterized by an infinite number of solutions corresponding to the number of oscillations. We can thus rewrite eq. 4.4:

$$\omega_{mnp}^2 = (\mu_0 \epsilon_0)^{-1} (k_{c,mn}^2 + K_{z,p}^{\prime 2}) = (\mu_0 \epsilon_0 \epsilon_r)^{-1} (k_{c,mn}^2 + k_{z,p}^2), \quad (4.10)$$

where in the transverse plane the solution is controlled by a double integer infinity  $m, n$  (eq. 4.3) and in the  $z$  direction eq. 4.9 results in an infinite number of solutions denoted by  $p$ .

In principle, in order to obtain the resonance frequency, it is sufficient to solve eq. 4.9.

The next step is to consider the guided  $TE_{01}$  mode in the circular cross section for which the explicit form of  $\psi$  is given in eq. 2.22 and  $k_c$  is analytically known. The result is reported in figure 4.2 where we show what is the effect of adding dielectric segments to the previously considered empty  $TE_{011}$  cavity ( $AR = 1$ ,  $f_{\text{res}} = f_{\text{Rb}}$ ). From figure 4.2, it is seen that, as expected, by increasing  $e$ , the resonance frequency of the cavity is reduced with respect to the initial  $f_{\text{Rb}}$  at  $e = 0$ . The special case of a dielectric segment with  $\epsilon_d = 1$ , is simply equivalent to an increase of the cavity height  $d$ . In figure 4.2a this limit case is represented by the upper-most curve. From the figure is evident that for any  $\epsilon_d > 1$  a segment with a finite length exists such that the resonance frequency of the cavity lowers down to the cutoff corresponding to the radius  $a$ :  $f_{\text{res}} \equiv f_{\text{cut}}$ , which is the lower-limit of wave propagation in the central region. Note that for  $\epsilon_d = 1$  this is asymptotically achieved for  $e \rightarrow \infty$ . As expected, in these cases the guided wavelength in the central region is:  $\lambda_g \rightarrow \infty$  ( $k'_z = 0$  in figure 4.2b). We can investigate this case by plugging  $k'_z = 0$  in eq. 4.9 which gives:  $k_z = p\pi/2e$ , fulfilled for:  $p = 1, 3, 5$ . We then substitute this result in eq. 4.10 to obtain a discrete set of values for the dielectric length  $e$ :

$$(\mu_0 \epsilon_0)^{-1} k_{c,mn}^2 = (\mu_0 \epsilon_0 \epsilon_r)^{-1} [k_{c,mn}^2 + (p\pi/2e)^2], \quad (4.11)$$

$$e_a = \frac{p}{4f_{\text{cut}}} \frac{1}{\sqrt{\mu_0 \epsilon_0 (\epsilon_d - 1)}}. \quad (4.12)$$

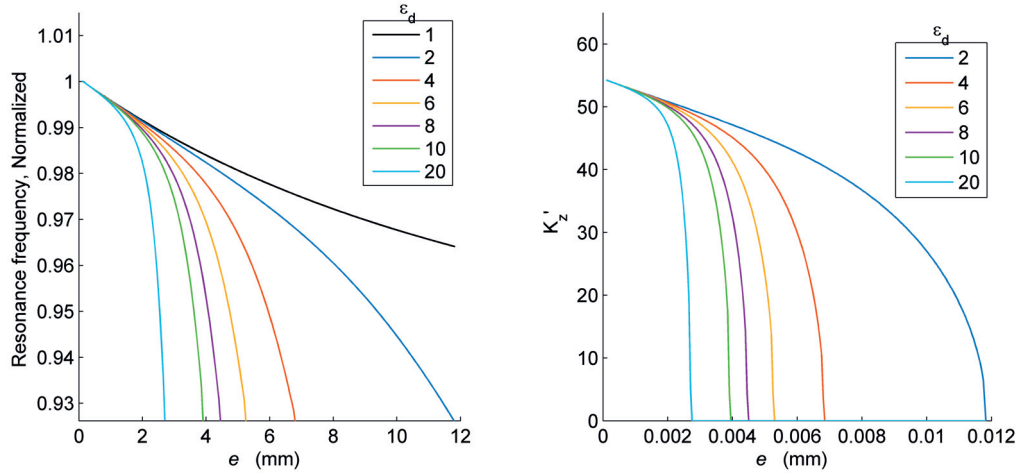
This is a remarkable result since it means that it is possible to create a cavity resonating at the desired frequency yet with a constant field distribution (in the central region).

It is enough to choose the transverse cross section such that the corresponding  $f_{\text{cut}}$  is the desired  $f_{\text{res}}$  of the cavity. Physically,  $e$  is the 1/4 of the (equivalent) guided wavelength  $\left(\frac{\lambda_0}{\sqrt{\epsilon_d - 1}}\right)$ . It is worth noting that the height of the cavity does not show in eq. 4.11 and therefore, in this special case, the mode depends only on the segment height  $e$  and not on the height of the cavity  $d$ . In the central region, such a behavior is described by a longitudinal modal number zero, the field "sees" PMC boundaries at the dielectric planes, and hence this corresponds to the previously discussed (chapter 2.1)  $\text{TE}_{010}$  mode (we refer to this cavity as a  $\text{TE}_{010}$  cavity).

### Application consideration

Above, we showed that a  $\text{TE}_{010}$  cavity is, in fact, possible to implement with arbitrary cross section. If we want to apply this concept to the atomic clock cavity, the simplest possible realization is to consider the canonical case – the cylindrical cavity based on circular cross section. In figure 4.3 we show a sketch of a possible implementation of such a cavity.

**Structure and dimensions** Because the pumping light needs to penetrate the Rb vapor and get detected, the cavity has to be open at both sides. As we will see later, this has the potential to degrade the performance of the boundary conditions and needs to be taken into account.



(a) Resonance frequency as function of the dielectric height  $e$ . Normalization to  $f_{\text{Rb}}$  is considered. The normalized cutoff frequency corresponding to the circular cross section for the given radius is:  $f_{\text{cut}}/f_{\text{Rb}} \approx 0.926$ .

(b) Longitudinal propagation constant  $k'_z$  in the central region shown as function of the dielectric height  $e$ .

Figure 4.2 – Resonance condition in a fully enclosed  $\text{TE}_{011}$  cavity considered with additional top and bottom segments homogeneously filled with dielectric. The family of curves corresponds to dielectric segments of different relative permittivity  $\epsilon_d$ . The dimensions of the cavity are: radius  $a = 28.9$  mm, height  $d = 57.7$  mm; the height of the dielectric segment is in the range of 0 – 11.8 mm.

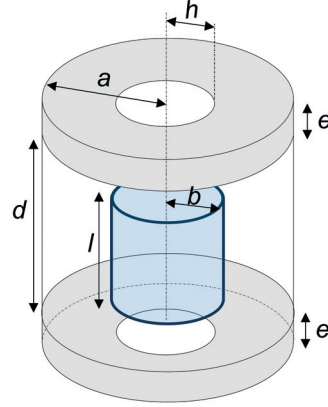


Figure 4.3 – A scheme of a possible realization of a  $TE_{010}$  cavity with artificial boundary conditions. The two, top and bottom, segments are homogeneously filled with dielectric and have a length  $e$ . The resonance frequency  $f_{\text{res}} = 6.834$  GHz corresponds to the clock transition. The cell is accommodated in the central region and it is depicted in blue. All external walls are conductive apart from the apertures required for the optical pumping (shown in white) at the top and bottom plates.

However, the following results are concerned with the general design criteria of such a dielectrically filled cavity and can be obtained analytically neglecting the apertures. In terms of the dielectric material, the segments need to be chosen with  $\epsilon_d \neq 1$  and need to be transparent for the laser light used ( $\approx 780$  nm). Good candidates are Pyrex and quartz which have additional advantage of reducing the temperature losses. In figure 4.4 we report what dimensions a loaded cavity with a given AR must have in order to resonate at the required  $f_{\text{Rb}}$ . The result is obtained by numerically solving eq. 4.10, for a fixed  $f_{\text{res}} = f_{\text{Rb}}$ , fixed AR and sweeping  $a$  and  $d$  in order to obtain the propagation constants for a given length of the segment  $d$ . The point  $e = 0$  corresponds to the standard unloaded geometry. As expected, depending on the amount of the dielectric filling, both  $a$  and  $d$  need to decrease since the resonance frequency is kept fixed. From the plot shown in figure 4.4 it is evident that for all lengths  $e \neq e_a$  the resonance frequency depends on the height as well as the radius. However, when the condition for the  $TE_{010}$  mode is obtained  $e = e_a$  (for a chosen dielectric) the resonance frequency is independent on the height  $d$ . The latter is the reason why all three AR curves converge to a single point, for a given dielectric. The height of the  $TE_{010}$  cavity is therefore only limited by the arbitrary chosen height of the cell  $l$  (and the distance  $e$ ). The dimensions of two potential cavities fulfilling the  $TE_{010}$  condition and based on the discussed materials, are summarized in table 4.1. By comparing the volume of the  $TE_{010}$  cavities to the optimal case (AR = 1) of the standard  $TE_{011}$  geometry (figure 2.14), it is seen that the volume of the  $TE_{010}$  cavity can be made almost two times smaller, for a cell with identical size.

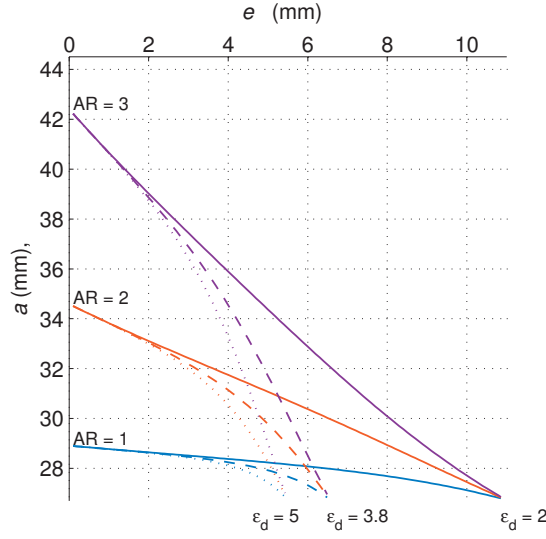


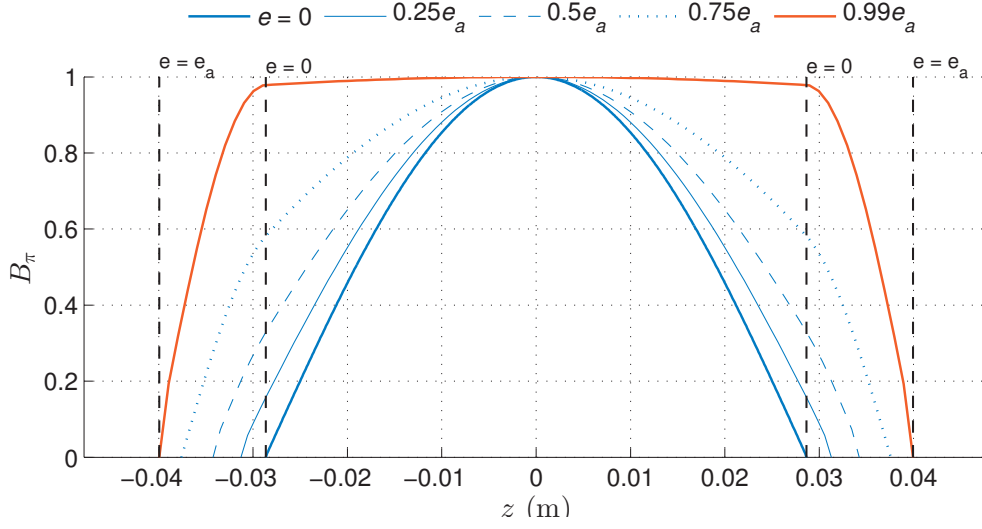
Figure 4.4 – Cavity radius  $a$  versus the dielectric segment height  $e$  for a  $TE_{011}$  cavity with  $f_{\text{res}} = f_{\text{Rb}}$ . Three different aspect ratios are considered ( $AR = 1, 2, 3$ ) as well as three dielectric materials:  $\epsilon_r = 2, \epsilon_r = 3.8$  (quartz) and  $\epsilon_r = 5$  (Pyrex). The height of the central region is:  $d = 2a/AR$ .

	Pyrex $z$	quartz $z$
$\epsilon_d$	$\approx 5$	$\approx 3.8$
$e_a$ (mm)	5.483	6.553
$d$ (mm)	25	25
$a$ (mm)	26.757	26.757
$V_{\text{cavity}}$ (cm <sup>3</sup> )	80.3	85
$V_{\text{cell}}/V_{\text{cavity}}$	0.074	0.078

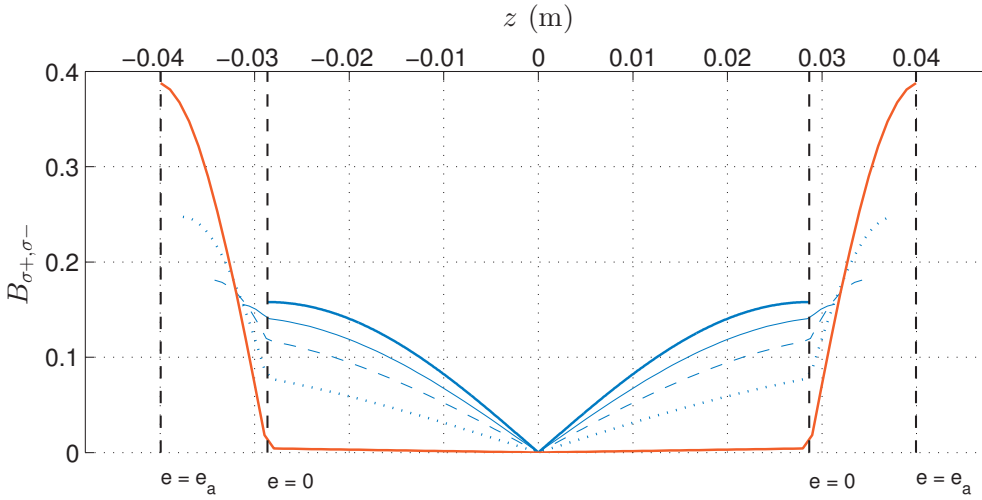
Table 4.1 – Dimensions of possible  $TE_{010}$  cavity implementations based on dielectric filling. A standard cell is considered with dimensions: radius  $b = 10$  mm and height  $l = 20$  mm. The light apertures have radius typically  $h = 10$  mm. The cutoff extensions at the apertures are neglected.

In fact, the lower limit of the cavity volume is at  $d = 0$  (24 cm<sup>3</sup>, if Pyrex is chosen), for which the resonance frequency is still  $f_{\text{Rb}}$ . On the other hand, the cavity can be made significantly longer if a dielectric cell with extended length is required, although, the latter is not a preferable option for high-performance clocks because of unwanted temperature gradients, it is clear that the  $TE_{010}$  cavity is a resonance structure that is unusually flexible in terms of size.

**Field distribution and performance** It is possible to analytically obtain the field distribution in the fully-enclosed, dielectrically loaded  $TE_{011}$  cavity, where in equations 4.1, 4.2, 4.5 and 4.6 the explicit form for the circular cross section is used (introduced in chapter 2.1, eq. 2.32).



(a) Longitudinal distribution profile of the wanted  $B_\pi$  field (amplitude) across the central axis of the cavity ( $r = 0$ ).



(b) Longitudinal distribution profile of the unwanted  $B_-$  and  $B_+$  fields (amplitude). In transverse direction the profile is taken at the radius of the cell ( $r = b$ ).

Figure 4.5 – Field distribution along the height of a cavity loaded with dielectric segments with different height  $e$ . The vertical dashed lines define the dimensions of the standard empty cavity ( $e = 0$ ) as well as the  $TE_{010}$  case ( $e = e_a$ ). All field components are normalized to the maximum for  $B_\pi$  found in the center. The dielectric material considered is with  $\epsilon_d = 2$ . The length  $e_a$  that fulfills the  $TE_{010}$  condition is obtained from eq. 4.12 and it is  $e_a \approx 11.9$  mm. The central part of the cavity is considered empty.

In figure 4.5 we report the longitudinal distribution of the driving fields for a cavity (the standard circular geometry with  $AR = 1$ ,  $a = 29$  mm and  $d = 57.4$  mm) loaded with dielectric segments with variable length. It is seen that the mode with zero amplitude variation ( $TE_{010}$ ) is defined in the central (empty) region of the cavity for  $e = e_a$ , while with respect to the dielectric



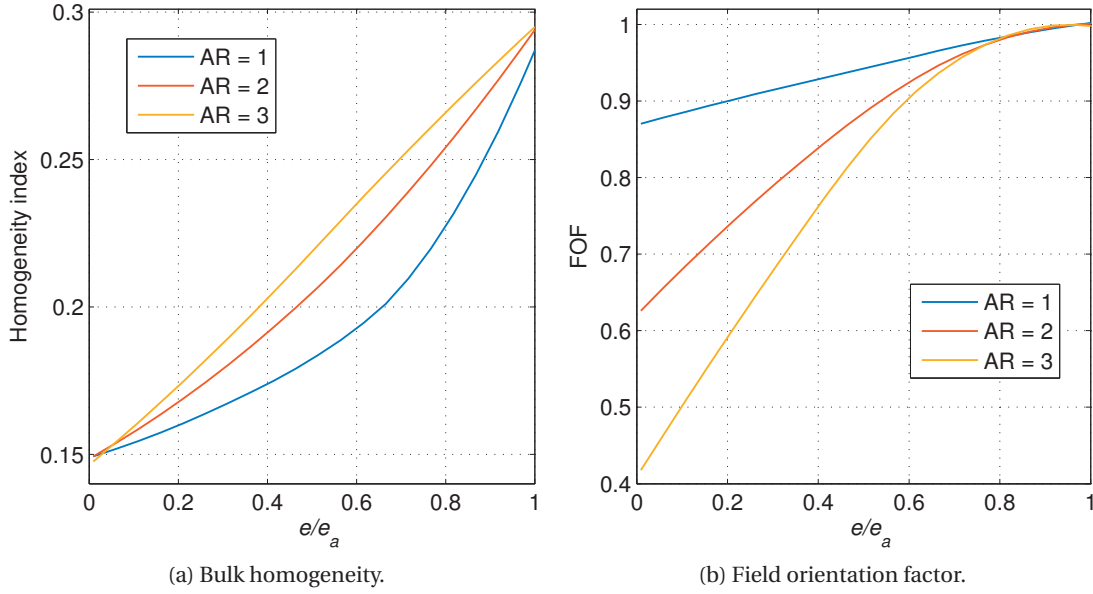


Figure 4.6 – Figures of merit as function of the segment length  $e$ . In the calculation, the biggest possible size of the vapor cell is considered: radius  $b = 0.6a$  and height  $l = d$ . The length of the dielectric segment is normalized as following:  $e/e_a$ . The resonance frequency is kept fixed to  $f_{\text{Rb}}$ .

region, the mode can be considered as  $\text{TE}_{011}$ . From the results for the field distribution, there are two important observations to be made: From figure 4.5a can be seen that adding dielectric segments to the standard cavity leads to the expected improvement of the longitudinal field homogeneity (in the central, empty region) for the wanted  $B_\pi$  field. On the other hand, from figure 4.5b we see that the unwanted driving fields are reduced in the central region of the cavity. The latter is directly seen from eq. 4.5, for which  $\mathbf{H}_t(t_1, t_2, z)$  is zero in the limit case. It can be now concluded that loading the cavity in such a way holds two advantages that are important for the atomic clock performance: improved homogeneity and increased field uniformity. In order to put it into perspective, in figure 4.6 we report what is the improvement of the corresponding figures of merit versus the height of the dielectric segments, considered for cavities with different AR (as previously reported in section 2.12). It can be seen that, as expected, the homogeneity of the available field is significantly improved – by a factor of two for  $e = e_a$ . Furthermore, the FOF is approaching one. This means that all available field in the central region drives only the wanted atomic resonance, which is fulfilled regardless the chosen AR. Finally, in figure 4.7, we report the field distribution for the AR = 1 case that can be directly compared to the one previously reported for the standard  $\text{TE}_{011}$  cavity (figure 2.8). It is worth noting that the results shown in figure 4.7 apply to the case of the biggest possible vapor cell. As it was previously explained (section 2.2.2), the performance of the cavity is a tradeoff between the amount of field (hence the improved signal-to-noise ratio) and the quality of the field (uniformity and homogeneity).

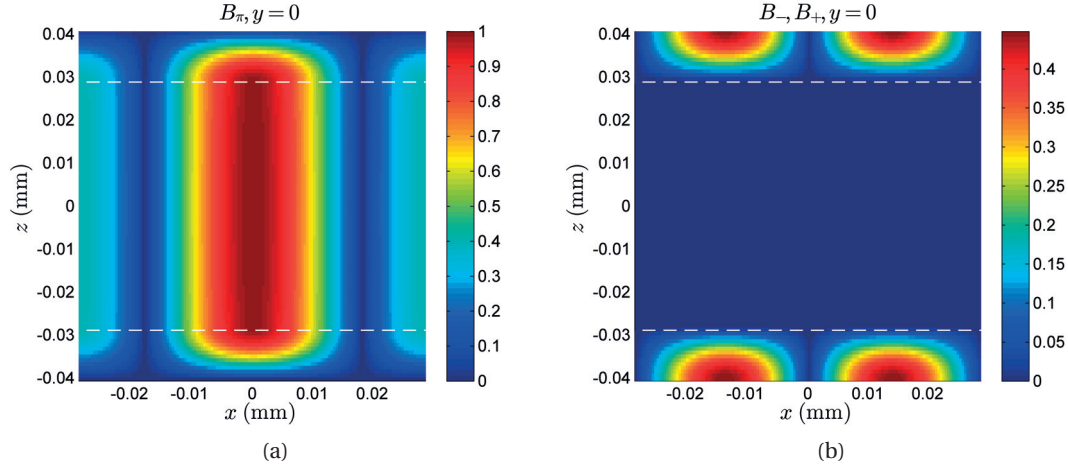


Figure 4.7 – Analytical solution for the driving fields inside the  $TE_{011}$  cavity with  $AR = 1$ . The boundary between the central empty region and the two dielectric segments is shown via the white dashed line. All external boundaries are considered PEC. In the central region, the mode is  $TE_{010}$  and it is characterized by zero variation of the  $B_\pi$  component and unwanted  $B_-$ ,  $B_+$  components with zero amplitude. All driving fields are characterized by azimuthal symmetry and hence all longitudinal planes are identical to the shown.

Therefore, in order to wrap up this discussion, let's see how the  $TE_{010}$  case compares to the previously discussed optimal case for the standard geometry. In figure 4.8 we show, side by side, the homogeneity performance in the standard case (figure 4.8a), for the  $TE_{010}$  cavity with  $AR = 1$  (figure 4.8b), as well as for a significantly compacted  $TE_{010}$  cavity with height comparable to the height of the vapor cell (figure 4.8c).

It can be seen that in the conventional cavity, when the standard cell is used (with a volume described by a contour line unity), the homogeneity is maximized for dimensions of the cell:  $b/a \approx 0.3$  and  $l/d \approx 0.4$ . Using the same cell, for the  $TE_{010}$  case, we have roughly 15% improvement regarding the field homogeneity. On the other hand, for the  $TE_{010}$  cavity the optimum corresponds to cells that are longer for a given volume for which the homogeneity can be improved up to two times. Therefore, for such a cavity, we have a strong incentive to increase the height of the vapor cell in order to take advantage of the enhanced longitudinal homogeneity of the magnetic field driving the atomic resonance. It is worth noting, however, that for practical reasons (mostly homogeneous control of the temperature) we are not free to arbitrarily choose the height of the vapor cells. From figure 4.8c can be seen that, as expected, the performance of the  $TE_{010}$  cavity is not affected by its height, meaning that a cavity with a volume reduced by a factor of almost two would be capable of obtaining the proper resonance condition and will still provide field with improved homogeneity. In terms of the FOF, the standard cavity performs good for the vapor cells that are typically used (figure 2.19).

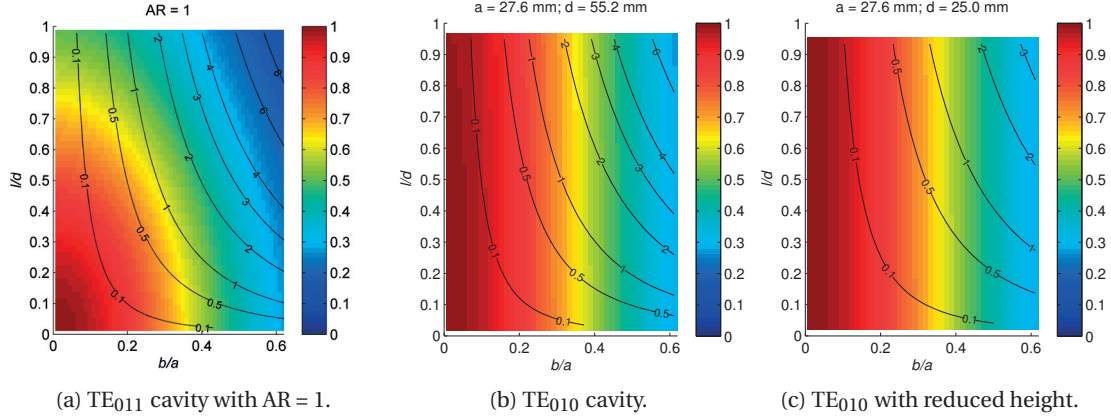


Figure 4.8 – Bulk homogeneity (also referred as "uniformity index" see [21] eq. 51) for given dimensions of the vapor cell. The height and the radius are normalized to the cavity ones:  $l/d$ ,  $b/a$ . The contour lines describe the volume of the cell and are normalized to the volume of the standard one (with dimensions:  $b = 10$  mm,  $l = 20$  mm).

The TE<sub>010</sub> case holds, therefore, a marginal improvement of the field uniformity (we have omitted the corresponding color diagram, since the FOF is unity). However, as we will see later, the effect is not negligible when structures with more complicated transverse cross section are considered.

After we showed the performance of the TE<sub>010</sub> cavity, we now concentrate on the practical issues that need to be resolved in a potential realization of such a cavity.

**Sensitivity** Since the cavity operates at the limit case, the structure is characterized by a high geometrical sensitivity which is a serious realization obstacle. This can be easily seen from the slope of the curves crossing the  $x$ -axis in figure 4.2. As expected, the higher the dielectric constant of the dielectric segment, the more sensitive the resonance condition is to its height. In order to quantify the level of precision needed, let's start from the requirement that holds for the Q-factor: if we assume a value of  $\approx 150$ , to be as near-optimal, this is equivalent to a resonance line-width:  $\Delta f \approx 50$  MHz. This means that we need to reach the resonance frequency with a relative error of  $\approx 0.5\%$ . In table 4.2 we report the numerically obtained sensitivity for a variety of dielectric materials. It is evident that the resonance requirement is easily fulfilled for a convenient range of dielectric materials. Furthermore, in terms of field performance, it can be qualitatively seen (figure 4.5) that  $50 \mu\text{m}$  deviation of the dielectric height has a negligible effect on the distribution of the fields.

Having calculated the amount of the relative error associated with the variation of the dielectric height, it is easy to evaluate what is the corresponding effect in terms of variation of the dielectric constant (real) value. We assume that the maximum precision of measurement is  $\pm 0.01$  (which is a realistic estimator for the method used in our lab: Fabry–Perot open resonator technique).

dielectric ( $\epsilon_r$ )	sensitivity (MHz/mm)	relative error (%)
2	73	0.05
4	210	0.15
6	330	0.24
8	645	0.47
10	1034	0.76
20	1290	0.94

Table 4.2 – Sensitivity of the resonance frequency related to the height of the dielectric segment. The relative error corresponds to the amount of frequency deviation from the  $f_{\text{Rb}}$  and it is obtained assuming a standard production precision of  $\pm 50 \mu\text{m}$ .

By using eq. 4.12 we can directly obtain that such a variation of the dielectric constant is equivalent to no more than  $\approx 10 \mu\text{m}$  for the dielectrics used – well within the requirement.

**Temperature coefficient** The next logical step of the sensitivity analysts is to calculate the temperature coefficient of the dielectrically loaded geometry. In order to simplify, we assume that the variation of the dimensions as function of the temperature is governed by linear thermal expansion coefficients (shown in table 4.3). All dimensions associated to the cavity structure can be thus scaled relative to a reference temperature  $T_0$ :

$$x'(T) = x + x\alpha(T - T_0), \quad (4.13)$$

where  $x'$  is a given dimension scaled for a chosen temperature  $T$ ,  $x$  is the nominal (original) dimension defined at  $T_0$  and  $\alpha$  is the expansion coefficient associated to the material. A reference temperature of  $T_0 = 60 \text{ C}$  is chosen, which is somewhat close to the optimal operational condition for the Rb vapor in our case. The dielectric segments are considered fixed (glued) to the top and bottom metal plates of the cavity. This means that they are free to expand (or shrink) with a separate expansion coefficient associated to the chosen dielectric. In order to obtain the variation along the height, we express the total cavity height as:  $L = d + 2e$  (see figure 4.3), which is then scaled as a function of the frequency. The scaled height of the central region  $d'$  can be then found:  $d'(T) = L'(T) - 2e'(T)$ , where  $e'(T)$  is the scaled height of the dielectric. In order to further simplify, we assume that both the radius of the cavity and the radius of the dielectric segments are scaled with the expansion coefficient of the metal. Using the described temperature parametrization and the relations from section 4.1 it is easy to solve numerically for  $f_{\text{res}}(T)$  – figure 4.9. As expected, increase of the temperature leads to expansion of the dimensions and hence decreases the resonance frequency.

In figure 4.10 we show the calculated temperature coefficient as a function of the dielectric filling. For the empty cavity, the temperature scaling of the radius and of the height has equal effect on the TC. The latter is found to be:  $\text{TC} \approx -164 \text{ KHz/K}$ , regardless of the aspect ratio. This result is comparable to the already reported (see section 3.1.2)  $\text{TC} \approx -180 \text{ KHz/K}$  (with the included vapor cell).

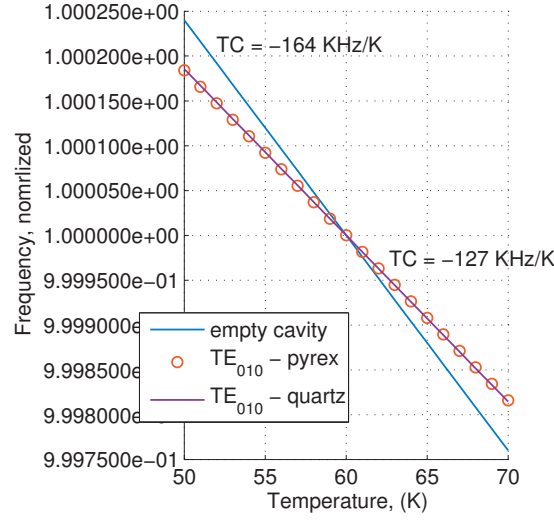


Figure 4.9 – Resonance frequency of the cavity versus temperature. The corresponding temperature coefficients obtained from the slopes are:  $TC \approx -164$  KHz/K for the empty cavity;  $TC \approx -127$  KHz/K for a  $TE_{010}$  cavity realized with Pyrex or quartz.

material	linear coefficient $\alpha$ ( $10^{-6} \text{ K}^{-1}$ )
aluminium	24
Pyrex	3.25
quartz	0.59

Table 4.3 – Thermal expansion coefficients for materials related to the implementation.

From figure 4.10 can be seen that increasing the height of the dielectric segments improves the TC. In order to understand why, it is easier to take the limit case (the  $TE_{010}$  condition at  $e = e_a$ ) for which a maximum improvement is reached. Imagine we first fix the length and scale only the radius by increasing the temperature. In this case, the cutoff frequency associated to the circular cross section will lower. From eq 4.12 can be seen that the height of the dielectric segment will then need to be larger. If we scale it with the same amount as the radius, the condition given by eq. 4.12 will be fulfilled again but for the lowered frequency. In this case, the TC of this cavity would be identical to the standard, empty, one. However, since the expansion coefficient of the dielectric is significantly lower and, as a result, the height of the dielectric is shorter than the required. This translates to a slightly sinusoidal field distribution in the central region and hence the cavity resonates slightly above the cutoff. This is why the frequency variation is partially compensated. Furthermore, the shorter the height of the central region is, the more this effect is pronounced – this is the reason why in figure 4.10 cavities with higher AR appear with lower TC. In figure 4.11 we report the TC found as function of the aspect ratio for different expansion coefficients.

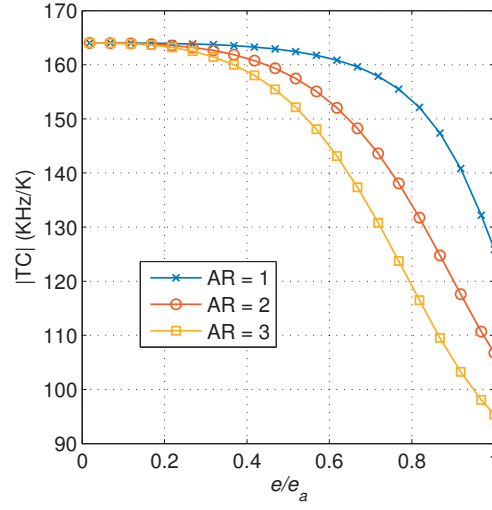


Figure 4.10 – Temperature coefficient as function of the dielectric loading for cavities with different AR. The height of the dielectric segment is swept from  $e = 0$  (empty cavity) to  $e = e_a$ , where  $e_a$  is the length for which the mode in the central region is  $TE_{010}$ . In each case, the nominal dimensions are considered such that  $f_{res} = f_{Rb}$  (as reported in figure 4.4). The dielectric material used is Pyrex.

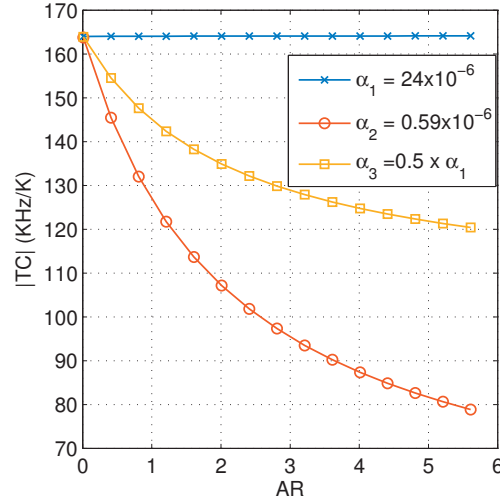


Figure 4.11 – Numerically obtained temperature coefficient as function of the aspect ratio shown for different expansion coefficients.

**Q factor** The unloaded Q-factor attributed to the losses in the conductor is obtained as in [109] and it is shown in figure 4.12. It is seen that for the frequency of interest, considering dielectric materials in the range  $\epsilon_r = 4 - 6$ , we can achieve between 60% and 70% of the performance associated to the most efficient case of the standard  $TE_{011}$  cavity (figure 2.7).

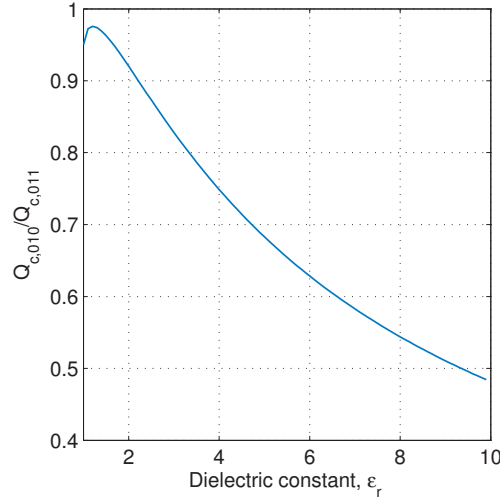


Figure 4.12 – Unloaded Q-factor of the  $TE_{010}$  cavity (with  $AR = 1$ ), attributed to conducting losses ( $Q_c$ ) and shown as function of the dielectric constant used for the loading. The normalization is considered with respect to the  $Q_c$  found for the standard  $TE_{011}$  geometry.

**Implementation of variable tuning in the case of AMC** Since the homogeneous mode is in principle independent on the height, a standard solution based on the electrical length is not optimal. In this case a frequency tuning can be obtained, by directly changing the cutoff of the central region or by perturbing the AMC boundaries. In order to be physically understood, we apply perturbation theory that was initially developed to study the sensitivity in the canonical case [109]. Assume that the height of the dielectric segments  $e$  is chosen to vary slightly from the optimal:  $e = e_a \pm e'$ , where  $e_a$  is the condition to obtain AMC given by eq. 4.12 and  $e'$  is a small dimension variation. In this case, a deviation from the expected homogeneous field is observed – figure 4.13.

In the first case (figure 4.13a) the field shows a slight sinusoidal variation similar to the case of PEC boundaries and therefore the resonance frequency is increased. In the second case (figure 4.13b) the field in the central region is slightly evanescent – the peak of the field is pulled towards the dielectric for which propagation starts lower in frequency. Therefore, in this case, the  $TE_{010}$  mode is characterized by a resonance frequency slightly lower than the cutoff frequency.

Since the AMC can be modeled as a parallel  $LC$  circuit, for the dielectric segment we have:  $W_e = W_h$ , where  $W_e$  and  $W_h$  stand for the electric and magnetic energy. Accordingly, for the dielectric volume of the perturbed AMC it can be calculated that in the first case we have  $W_h > W_e$  and accordingly,  $W_e < W_h$  in the second. It is now evident that the process of tuning can be associated with imbalance of the EM energy attributed to the equivalent AMC volume.

**The influence of the apertures** The apertures required for the interaction of the laser light with the Rb vapor represent a significant variation of the cross section and hence have the potential to perturb the performance of the homogeneous mode.



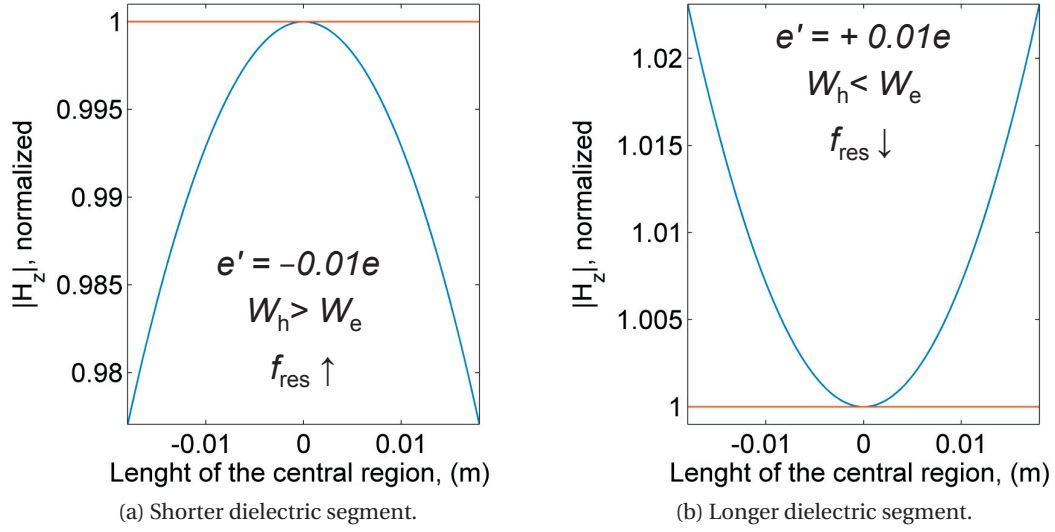
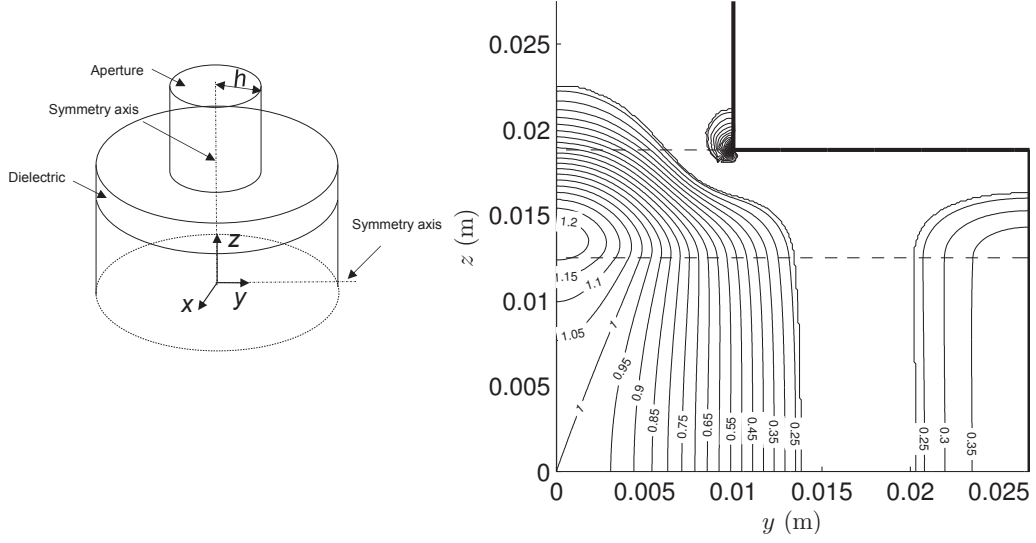


Figure 4.13 – The plots show the effect of the dielectric length on the  $H_z$  distribution in the homogeneous region of the cavity. The result is calculated for the central axis of a  $TE_{010}$  cavity with a radius of 26.7 mm and a length of 36.6mm. A dielectric material with  $\epsilon_r = 5$  is considered. The field profiles are normalized with respect to the center of the cavity and the constant field distribution corresponding to the ideal AMC case is shown in red.

It is convenient to study this effect by using numerical simulations where the height of the aperture can be made long and non-radiating (figure 4.14a) and eigen analysis can be applied. The field distribution is shown in figure 4.14b, where the cavity is with dimensions considered as the reported in table 4.1 and (realistic) apertures with a radius of 10 mm. It is intuitive to assume that, at the opening, the effective height of the dielectric segment is locally  $e > e_a$  and hence the field maximum is slightly moved towards the dielectric extension – similar to the case shown previously in figure 4.13b. From the contour plot it is easy to see that in the region of interest the transverse distribution of the  $H_z$  field is significantly affected. Close to the center the field lines are pulled towards the central axis, where this effect gradually decreases towards the circumferential cavity wall. We report this in detail in figures 4.15a and 4.15b where the result is calculated for apertures of variable radius. It can be seen that a very significant degradation of the field homogeneity is found for the central profile ( $\approx 34\%$  variation from the maximum) while for the field profile taken at half the radius, the variation is  $\approx 5\%$ . Furthermore it is seen that the shape of the two profiles is somewhat inverted, where for the central profile the field is peaked close to the dielectric region. In figure 4.15c we show what is the transverse field distribution attributed to  $H_z$  in the case of a 10 mm aperture. It is seen that the aperture leads to different transverse profiles along the height where the latter is in contrast to the case of the fully-enclosed geometry. We also note that the edge between the top wall and the aperture represents a significant extremity as can be seen from figure 4.14b.





(a) A scheme of the cavity and the (upper) aperture.

(b)  $H_z$  field lines.

Figure 4.14 – Due to symmetry, the field can be evaluated e.g. in the  $y$ - $z$  plane ( $x = 0$ ), where two symmetry axes at  $[y, z = 0]$  and  $[y = 0, z]$  are considered. The walls of the cavity and the aperture are depicted by the black lines. The dielectric filling ( $\epsilon_r = 4$ ) is represented in the field map via the dashed lines.

Given the above discussion, it is evident that such a high homogeneity degradation is in a stark contrast with the excellent performance of the canonical  $TE_{010}$  case. The most intuitive way to mitigate the effect of the apertures is to locally (at the vicinity of the aperture) reduce the thickness of the dielectric as shown in figure 4.16a. A result from a parametric study can be seen in figure 4.16. It can be concluded that even by simply removing a small cylindrical region (which is relatively easy to machine), we were able to keep the field variation for both the central and the off-centered ( $a/2$ ) profiles in the range of few %. It is, in principle, possible to "sculpture" the field even better if a conical slab is used – a more continuous variation for the dielectric constant  $\epsilon_r$  can be hence obtained in the transverse direction.

## 4.2 Loop-gap geometry with AMC

The goal of the following study is to implement the AMC in the case of the loop-gap geometry that was extensively covered in chapter 3. In this way we can combine the loop-gap compactness with the promising performance of the homogeneous  $TE_{010}$  mode. Alongside the AMC solution based on a dielectric filling, it is also possible to locally modify the structure of the cavity in the vicinity of the boundary. It is therefore interesting to investigate such an alternative solution in the case of the loop-gap geometry.

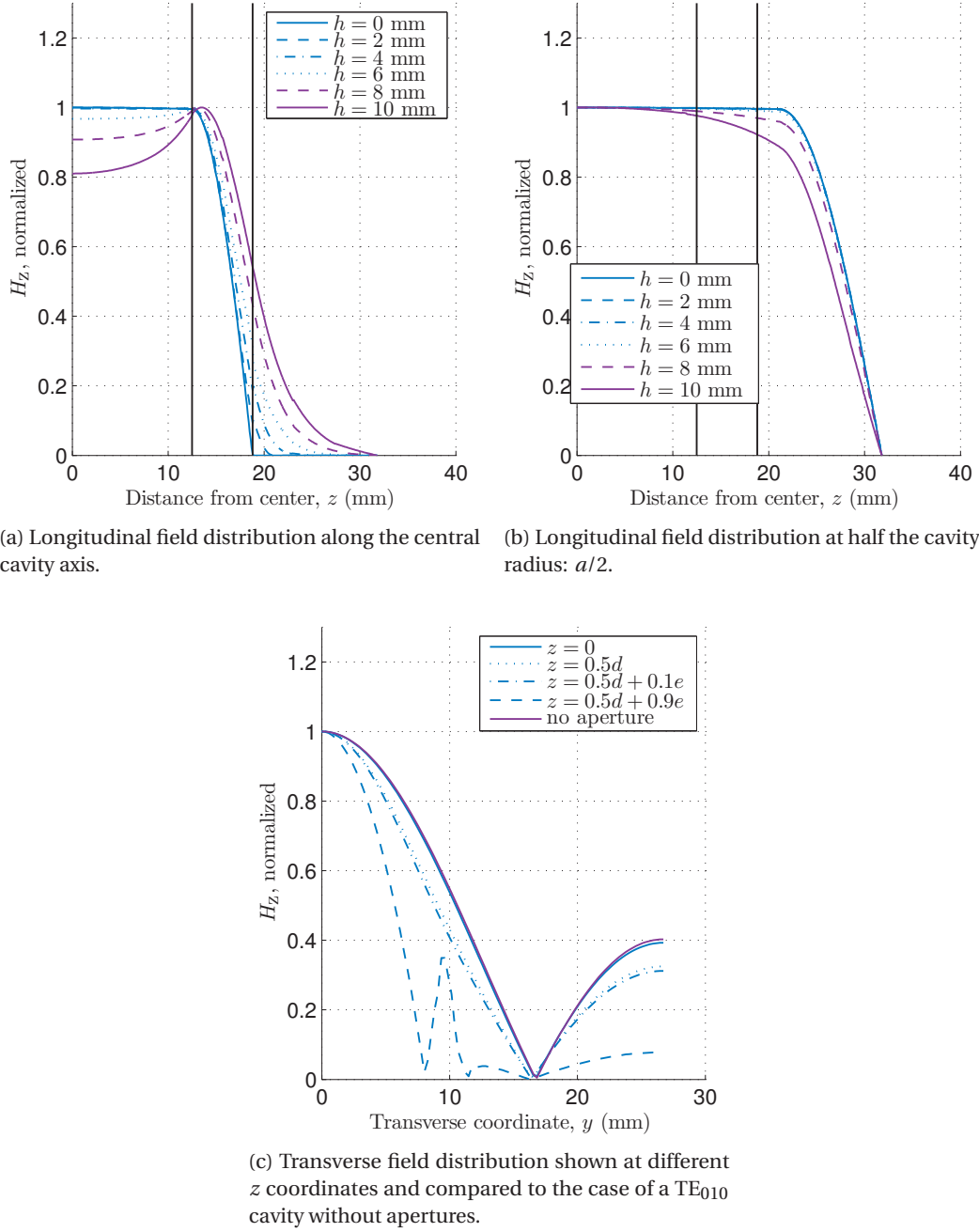
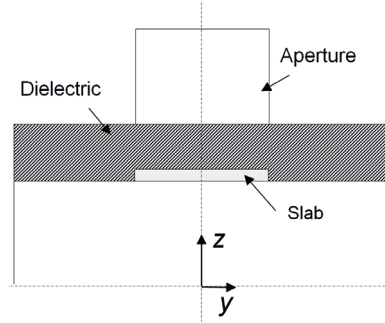


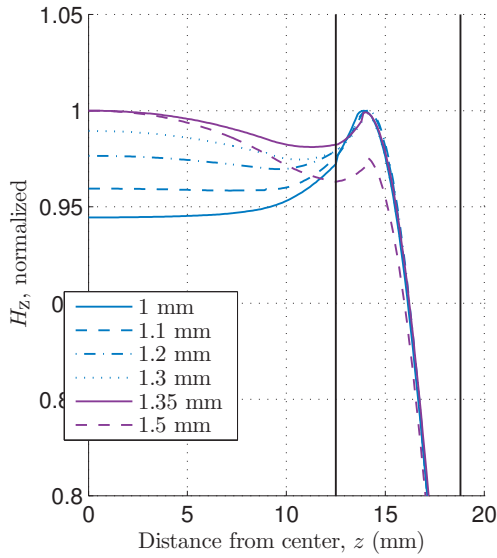
Figure 4.15 – Field distribution of the  $H_z$  component (amplitude), where  $h$  is the height of the aperture,  $d$  is the height of the central region,  $e$  is the height of the dielectric filling (depicted via the vertical lines).

#### 4.2.1 Implementation of AMC based on planar structures

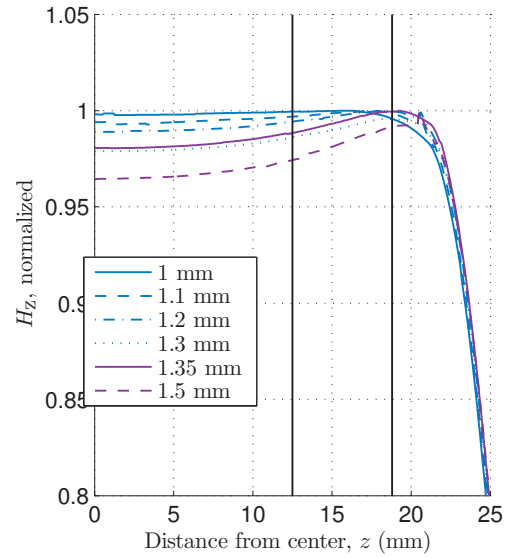
A common trait among the implementations of AMC is the utilization of some resonant behavior. In this sense, it is advantageous that the generic structure of the loop-gap cavity is



(a) A scheme of the dielectric segment where a small cylindrical slab of material is removed.



(b) Longitudinal field distribution along the central cavity axis.



(c) Longitudinal field distribution at half the cavity radius:  $a/2$ .

Figure 4.16 – Field distribution of the  $H_z$  component (amplitude) as function of the slab height. The radius of the slab is identical to the radius of the aperture  $h$ . The position of the dielectric is indicated via the vertical lines.

characterized by a longitudinal impedance discontinuity (the presence of the empty extensions at both sides of the central loop-gap region). For the mode of interest, the standing wave exists in the central region but it is under cutoff in the cylindrical extensions situated on both sides. However, since part of the field (mostly magnetic) leaks in the extensions, it is natural to assume that they can be engineered so that a unity reflection coefficient can be locally found. In our case this cannot be obtained by changing the external radius or shape of the cross section (due to the complicated structure of the physics package: dc coils, heating required for the vapor, magnetic shielding). It is instead possible to utilize a loop-gap structure similar to the one already used in the central region of the cavity – figure 4.17 [98].

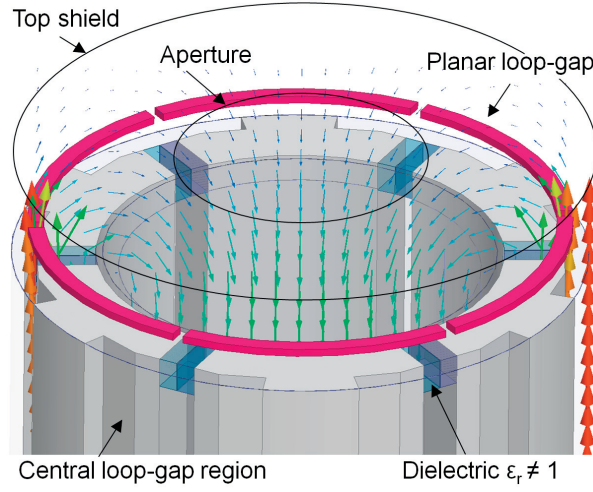


Figure 4.17 – The illustration shows some conceptual ways that can be used to modify the structure in order to obtain AMC boundary conditions in the case of the loop-gap geometry: the capacitance can be locally increased by including dielectrics in the gaps; the empty extension can be loaded with a resonant structure. The cell is completely enclosed inside the central loop-gap region where it is seen that the magnetic field is oriented along the  $z$ -axis. Image taken from [120].

Our idea is to use a planar design for which the metal loops (electrodes) can be realized based on a PCB technology where the dielectric substrate, in this case, is only used for a support – figure 4.18. Based on the approach established in section 3.2, we can design the planar loop-gap to resonate close to the requirement:  $f_{\text{int}} \approx f_{\text{clock}}$ . It is important to note that the planar loop-gap needs to have a larger diameter than the aperture required for the laser light. This means that it is appropriate to consider the interval of normalized radius  $r > 0.6$  (see figure 3.8). Placing it in the vicinity of the electrodes, couples it to the central loop-gap region since both structures support the mode of interest (as shown in figure 4.17). While in principle, the coupling problem is complicated to model, it is clear that the magnetic field leaking out of the central region contributes the most [115]. Therefore, it is mainly the distance between the planar structure and the main loop-gap region that controls the amount of coupling. In our case, due to structural reasons, it is preferred to fix the planar loop-gap close to the top and bottom walls of the vapor cell as shown in figure 4.18a. From a transmission line point of view the AMC boundary corresponds to an impedance  $Z \rightarrow \infty$  and hence the extensions (loaded with the planar loop-gap) can be modeled as a parallel  $LC$  circuit. Since we consider the planar AMC to apply at both ends of the central region, the magnetic/electric energy integrated over the whole volume of the loaded extensions is:  $W_e = W_h$ . However, because of the evanescent magnetic field, we have:  $W_e < W_h$  and hence the cavity resonates above the cutoff of the central region. This can be counteracted by decreasing the intrinsic frequency of the planar loop-gap, since the parallel  $LC$  is capacitive for:  $f > f_{\text{int}}$ . From figure 3.8 can be clearly seen that, in this case, we need to reduce the internal radius  $r$  of the planar loop-gap.

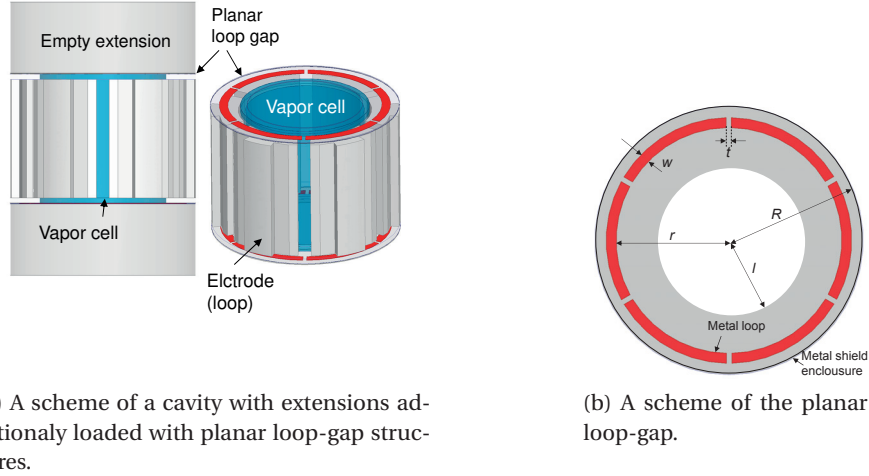


Figure 4.18 – A loop-gap cavity with AMC boundaries based on planar loop-gaps. The structures can be realized using PCB technology based on a standard substrate material (dielectric shown in grey). The circular aperture in the center (white), required for the laser light, needs to have a radius of  $l > 10$  mm.

Parameter	Size (mm)
radius of the shield, $R$	18
internal radius, $r$	16.8
thickness of the loop element, $w$	0.5
gap, $t$	1
number of gaps $n$	6
substrate ( $\epsilon_r = 2$ ) thickness	0.127
metal thickness	0.07

Table 4.4 – Dimensions of the planar loop-gap.

The balance between  $W_e$ ,  $W_h$  is easily obtained from simulations and it can be used as a design rule – figure 4.19a. It can be seen that the AMC condition is obtained for  $r \approx 0.72$ . For a lower  $r$ , the field is slightly evanescent towards the extensions and hence the cavity resonates lower than the cutoff. It is interesting to see that for the smallest radius considered, the magnetic energy starts increasing again, as well as the resonance frequency of the cavity. This is because, as seen in figure 3.8, in this case the intrinsic frequency of the planar loop-gap starts increasing again. In figure 4.20a we report the distribution of the required field obtained for the optimal case of the above-described planar AMC. It is seen that the central region of the cavity (close to the axis) is characterized by high homogeneity. The field is peaked at the vicinity of the planar structure, however the central region is unaffected. It can be also noticed that there is a significant field leakage found in the extensions.

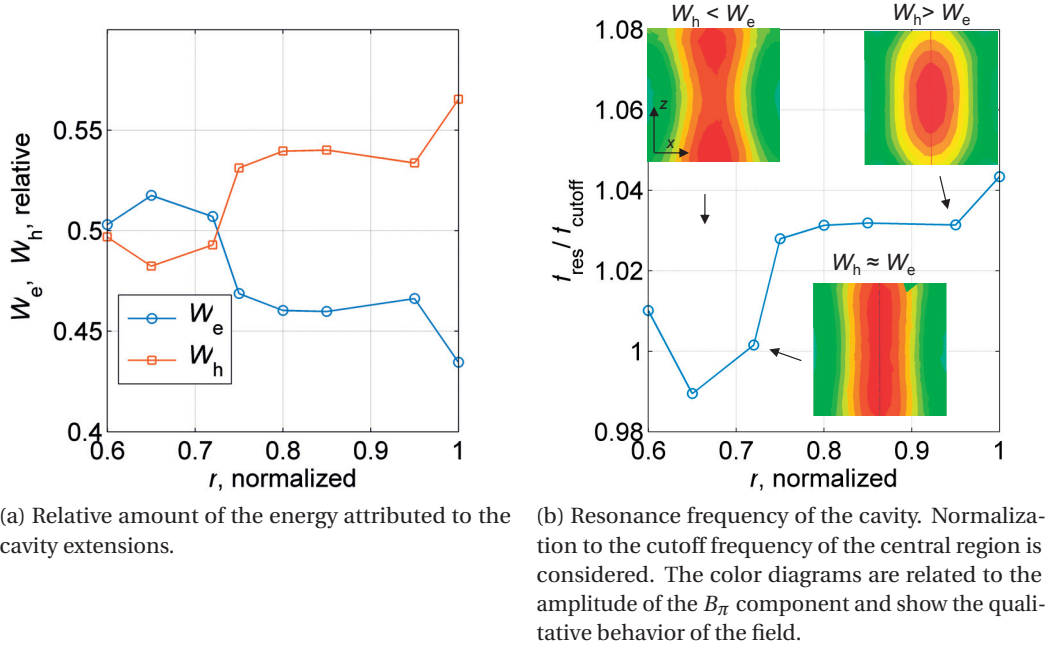
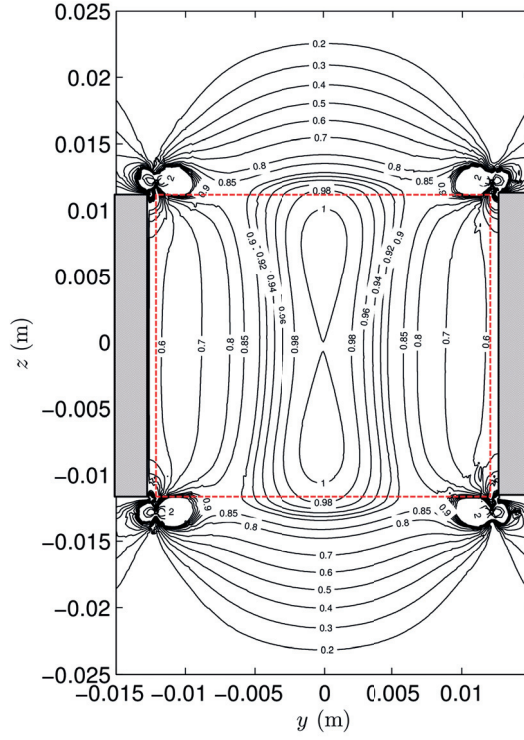


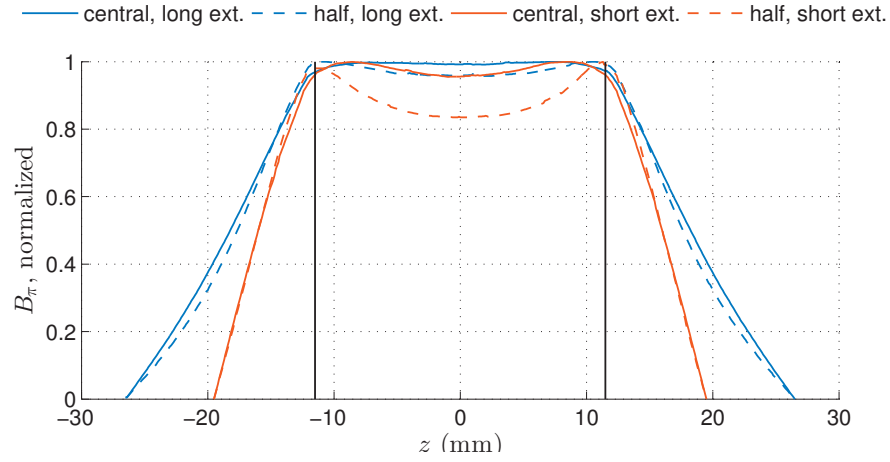
Figure 4.19 – The plots show what is the effect of scaling the internal radius  $r$  of the planar loop-gap. For normalized radius of  $\approx 0.72$  the mode in the central region is  $TE_{010}$  and the cavity resonates at the cutoff (of the central region). All dimensions are as the reported in table 4.4. The height of the extensions is 14 mm, the distance between the planar loop-gap and the central region is 1mm.

This is the reason why, generally, the planar AMC is found to work well when the extensions are chosen to be long enough (14 mm in the optimal case shown). The effect is demonstrated in figure 4.20b where we compare the longitudinal field distribution for two different extension lengths. It is seen that when the extensions are kept long (as reported for the case shown in figure 4.19) the field along the central axis is close to constant while the field considered at half the cell radius is within 5% variation. When extensions with half the length are considered, the distribution for the off-centered profile is degraded significantly ( $\approx 18\%$  field variation). It is possible, however, to try mitigate this effect by employing a second planar structure situated above the planar loop-gap and further tune the AMC condition.

In terms of fabrication, the above-described solution is suitable since, for the frequency of interest, the planar technology has generally well-controlled tolerances and negligible losses. Furthermore, it is characterized by a small footprint and is hence less stringent to accommodate inside the cavity. A variety of such structures can be easily developed, allowing us to retrofit the cavity without complicated machining. However, for a highly compacted design, a solution based on a dielectric filling is found to have a better performance.



(a) A 2d contour map of the  $yz$  ( $x = 0$ ) cavity plane. The volume occupied by the Rb vapor is depicted by the (red) dashed contour. The electrodes are shown in gray. The result is with a dielectric cell included (not shown for clarity).



(b) Longitudinal field distribution. The field profiles correspond to the central axis as well as to half the radius of the vapor cell. The dimensions of the vapor cell are indicated by vertical lines. The height of the extensions is: 14 mm (long), 7 mm (short). A normalization to the max. amplitude is separately considered for each case.

Figure 4.20 – Field distribution (amplitude) of the required  $B_\pi$  component for a cavity based on a planar AMC solution.



### 4.2.2 Implementation of a variable tuning in the case of the loop-gap geometry

A major concern in the practical realization of the atomic clock cavity are the various productions tolerances. Among all, the dimensions of the vapor cell usually vary the most where production differences of up to  $\approx 0.5$  mm are not unusual. In section 3.2.2 we showed that the vapor cell has a quite significant effect on the resonance frequency – a dedicated numerical study is included in appendix B. It is therefore evident that, in order to obtain the resonance condition, it is crucial to include a possibility for a variable tuning mechanism.

The usual way to achieve this is to simply change the height of the cavity by inserting one of its caps. The resolution of the tuning is therefore determined by the thread pitch used. In more compact geometries, the cell can be attached directly to the cap and hence, in this case, tuning is obtained by loading the cavity (see section 3.3.3). Depending on the design, the insertion of the cell may slightly alter the amount of magnetic flux interacting with the Rb atoms and thus perturb the clock signal. Furthermore, such a tuning mechanism is not azimuthally symmetric because the vapor cell has one (or more) dielectric stems, rotation may also lead to unwanted redistribution of the field (we have studied this effect for the case of the currently used loop-gap geometry and the results are included in appendix B).

We want to emphasize that, in the here-considered case, two requirements should be fulfilled at the same time: both the resonance frequency and the condition for the homogeneous mode need to be met for the required clock frequency. This is in fact one of the most challenging aspects of the  $TE_{010}$  cavity since, strictly speaking, the mode is only defined for a single frequency. Because we only have access to the resonance frequency (in principle imaging experiments can be used to confirm the homogeneity – see section 3.3.1) we need to make sure that the cavity provides a well-controlled, close to homogeneous field in a reasonable frequency range around  $f_{Rb}$ . For achieving this, we foresee two separate ways that can be used in order to influence the resonance frequency: altering the AMC boundary conditions or alternatively modifying the transverse propagation constant in the central region  $k_c$ .

In section 4.1 we showed how changing the length of the dielectric region (in the case of AMC based on a dielectric material) alters the resonance frequency. One can thus imagine a tuning solution that works with a variable dielectric region at one of the AMC boundaries (figure 4.21). This is however a very unstable configuration because, in this case, there is an imbalance between the two (top and bottom) dielectric segments. Since we operate very close to the cutoff, it is highly probable to have evanescent field in the central region. While, in principle, the cavity can be tuned in this way the field distribution can be very far from the optimal, as seen from figure 4.21. An additional difficulty comes from the fact that such an approach restricts further the positioning of the feeding mechanism.

In order to cope with this issue, the transverse boundary of the loop-gap can be locally perturbed: e.g. in [35] tuning screws are attached to the lateral walls of the loop-gap while in [72] capacitive tuning is similarly used where the gap is variably loaded via insertion of a dielectric slab. We have found that, since in our case the radius of the central loop-gap is relatively large, such a localized transverse perturbation cannot be utilized without a significant degradation of the required mode.



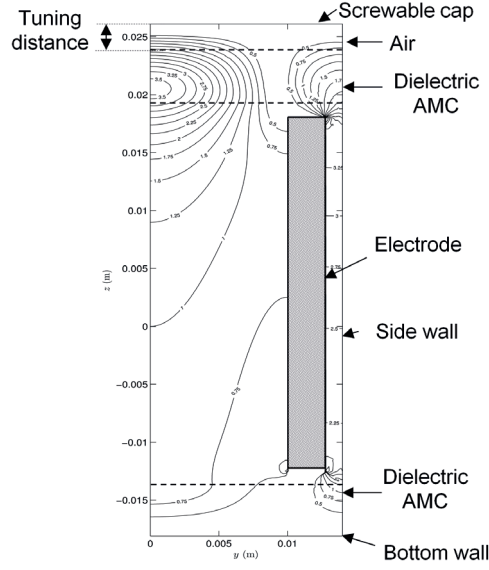


Figure 4.21 – A scheme of a loop-gap  $TE_{010}$  cavity with a tuning mechanism based on insertion of the top cap. Changing the tuning distance alters the effective length of the dielectric and hence influences  $f_{\text{res}}$ . In the case shown, the cavity resonates such that:  $f_{\text{res}} < f_{\text{cut}}$ . The contour lines shown, correspond to the normalized  $B_{\pi}$  field. The  $yz$  plane is shown, where symmetry along the central axis of the cavity is considered.

Instead, we propose a mechanism that can directly tune the transverse propagation constant  $k_c$  (or the cutoff  $f_{\text{cut}}$ ) of the central region in a more controlled way. The idea is to include an additional loop-gap structure that can be mechanically rotated relative to the main loop-gap of the cavity. It is hereafter referred as "rotator" and it is shown in figure 4.22. In this way, the return flux (the magnetic field in the volume between the main loop-gap electrodes and the outer cylindrical cavity shield) of the cavity can be perturbed in a symmetrical manner. Because the active volume relevant for clock operation is located within the electrodes around the cavity's central axis (see figure 3.3) and due to the rotator's identical symmetry (6-fold rotational symmetry in the structure chosen), the homogeneity of the relevant field in the active volume is found stable with respect to this frequency tuning method.

One additional advantage of such a tuning mechanism is its flexibility. The thickness and the size of the tuning electrodes (figure 4.22b), can be used to engineer the required frequency interval as well as the resolution of tuning. In figure 4.23 we show how the cutoff frequency of the loop-gap is influenced by the position of the rotator. It can be concluded that the most usable rotation range is approx. between 15 and 30 deg., where this is the most restrictive characteristic of this tuning mechanism. Some improvement can be obtained, for example, by altering the width  $r_w$  as well as the shape of the electrodes, where one can imagine that this range is going to be larger for a geometry with lower number of gaps. In terms of the resolution, from figure 4.23, it can be evaluated that the rotator can be easily designed for a large enough tuning range – anywhere from few to several hundred MHz.

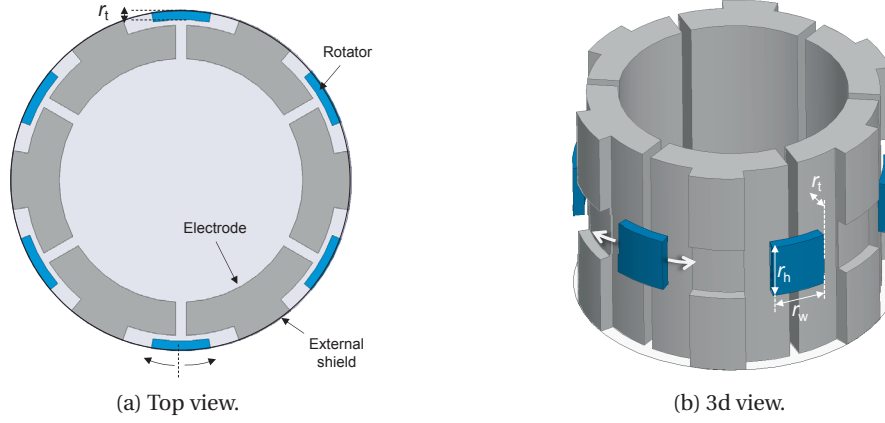


Figure 4.22 – A scheme of a loop-gap structure with (mechanically) variable  $f_{\text{cut}}$ . A set of symmetrically situated electrodes (referred as "rotator" and depicted in blue) can be designed such that rotation with respect to the  $z$ -axis of the cavity results in variation of the transverse propagation constant associated to the central region. The parametrization is as following:  $r_h$  – height;  $r_w$  – width;  $r_t$  – thickness.

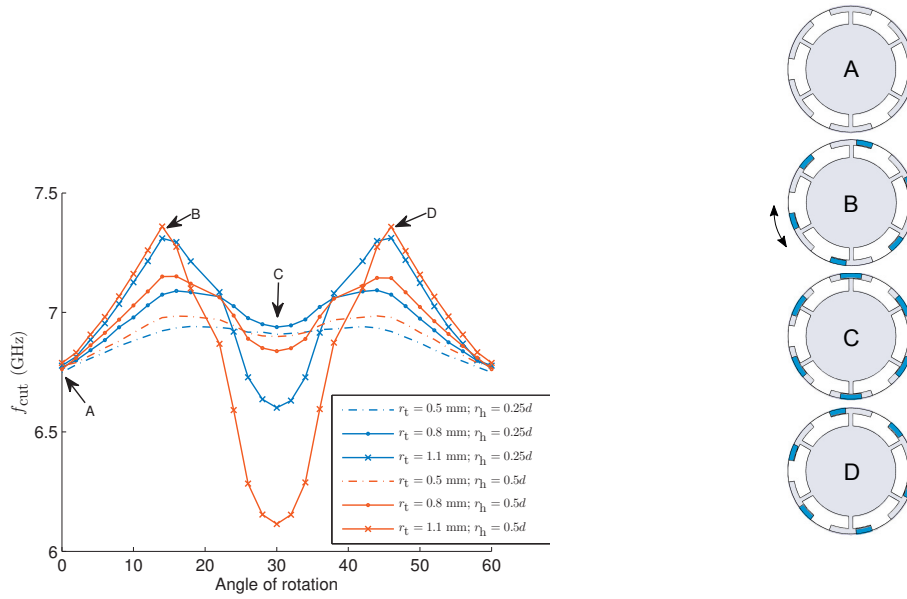


Figure 4.23 – Variation of the cutoff frequency as function of the rotator position angle. The height of the rotator  $r_h$  is normalized to the height of the main loop-gap region. In the range  $A \rightarrow B$  the rotator effectively increases the width of the main loop (electrode)  $w$  and hence increases the frequency – a similar effect was already discussed in section 3.2.2. In the range  $B \rightarrow C$  the frequency is reduced because the rotator electrode is close enough to the gap, couples to the electric field creating a high capacitance region with respect to the loop wall.

It is evident that, the larger is the targeted interval (relative to the desired  $f_{\text{RB}}$ ), the more sensitive is the geometry and the lower the resolution is. Nevertheless, for a frequency interval of  $\pm 200$  MHz, we have  $\approx 60$  MHz/deg which is on a par with the previously discussed loop-gap geometries (see section 3.3.3).

In this study we initialized the general requirements for the tuning mechanism as well as the challenges that apply to the  $\text{TE}_{010}$  mode specifically. The proposed solution is found to be appropriate and it proved to be very flexible in terms of design freedom. Moreover, a sufficient tuning range is achieved without displacing the vapor cell.

### 4.3 Complete cavity design

Up to now in this chapter, we extensively covered the design aspects but also the practical issues relevant to the  $\text{TE}_{010}$  mode of interest. Based on this, in this final part, a realistic cavity design is proposed where we take into account the full complexity of the problem.

#### 4.3.1 Description of the proposed design

A detailed scheme of the proposed cavity with the vapor cell is presented in figure 4.24. For the central region (referred as "main loop-gap") of the cavity, a loop-gap geometry based on 6-gaps is preferred. This particular choice is mainly dictated by a requirement of compatibility with a physics package previously customized. A 4-gap geometry is also a good candidate, a 2-gap might be too restrictive on the tuning while a 8-gap geometry might be structurally too weak, depending on the technology used for production. The height of the electrodes is chosen to be similar to the height of the vapor cell because, in this way, the magnetic field is well-guided throughout the full length of the cell. From figure 4.24 can be seen that the support needed for the electrodes of the main loop-gap is removed in the center. This is required so that the rotator electrodes can be accommodated. Note that, the bottom part of the cylindrical shield is physically attached to the electrodes (depending on the technology it can be machined together) and hence provides a structural support. The rotator is implemented via the top cylindrical shield, where the tuning electrodes are embedded on its internal wall. The width of the electrodes (as defined in figure 4.22b) is such that it can be inserted and freely rotated azimuthally (no thread is used). This is possible because the support elements, at the top of the main loop-gap, are slightly thinner and hence allow the rotator to move freely with respect to the bottom part. The latter is illustrated in the transverse cut, shown in figure 4.24, where it is referred as a "rotator gap". It is worth noting that the discontinuity formed between the fixed bottom part of the shield and the rotator will not affect the field much because, in this region, the wanted mode is characterized by azimuthal currents.

In this implementation, we have chosen to use AMC made of dielectric since such a solution is found more beneficial in preventing heat loss. The optimal dimension is initially based on the result for the canonical case. Using simulations, the optimal dielectric segments are obtained where the presence of the apertures is also taken into account. However, the cavity is designed such that the previously discussed planar AMC solution can be also accommodated with a minimal modification.

The top and bottom dielectric segments are kept in place using two dielectric rings such that a layer of air exists between them and the metal caps. If required, the caps can be made movable so that, depending on the availability of the materials used, we are able to obtain the effective length for which the  $TE_{010}$  mode is defined. Relatively large light apertures are considered (a radius of 9 mm) since the quality of the field allows to sample a larger region of the cell volume. Close to the aperture, the thickness of the dielectric is modified, as explained in section 4.1, so that the apertures have a negligible effect on the longitudinal homogeneity of the field. The vapor cell used in this cavity is similar to the previously shown two-stem design (see section 3.3.3). It is characterized by a significant dielectric discontinuity (due to the two dielectric stems) which could contribute to the excitation of unwanted modes (a study of this effect is included in appendix B). This is the reason why, in the current design, we put emphasis on keeping all non-symmetric structures fixed and hence the field better controlled. Namely, the stems are accommodated through holes in the dielectric segment where the cell is fixed (it can be also glued) to the bottom dielectric segment which is kept fixed too. In this way, the process of tuning is independent of the vapor cell position and, therefore, does not perturb the overall quality of the field.

Due to the large cell tolerances, typically, a whole set of electrode structures with different gaps is required. In this way, it can be ensured that the cavity will meet the resonance condition. This is a significant difficulty because a complete disassembling of the cavity-cell package is required. In the here proposed design, it is instead possible to use rotator realizations with different electrode thickness. In this case, when needed, the resonance condition can be met simply by using a different rotator structure – no disassembling is needed and both the feeding and the cell can be kept in place. The latter is not negligible, since the process of accommodating the vapor cell is often involved with gluing, resulting in a fairly complicated procedure.

### 4.3.2 Cavity modes

It is unfortunate that cavities with such a complicated structure are usually found to support an abundance of unwanted modes that can significantly degrade the performance. In fact, the latter is valid even if we take the simplest form of our 6-gap structure (neglecting supports, dielectrics, top extensions etc.) since the mode we are interested in is not the fundamental. After we have all details of the design clarified it is now appropriate to investigate what modes exist besides the  $TE_{010}$ -like mode of interest. In figure 4.25 we report what is the field distribution associated to three such unwanted modes that are found near the required resonance frequency  $f_{\text{res}} = f_{\text{Rb}}$ . Clearly, the modes shown in the figure are incompatible to the optimal clock operation and hence we need to ensure that they are well isolated from the mode of interest. Among them, mode (1) is of the TM type while both modes (2) and (3) have regions with longitudinal components of the magnetic field.

Lets see which design parameters are suitable to use in order to obtain the required mode with enough separation. Since the dimensions of the vapor cell are fixed (hence the internal radius  $r$  of the loop-gap), it is found appropriate to employ the size of the external cavity radius  $R$  and the size of the gap  $t$ .

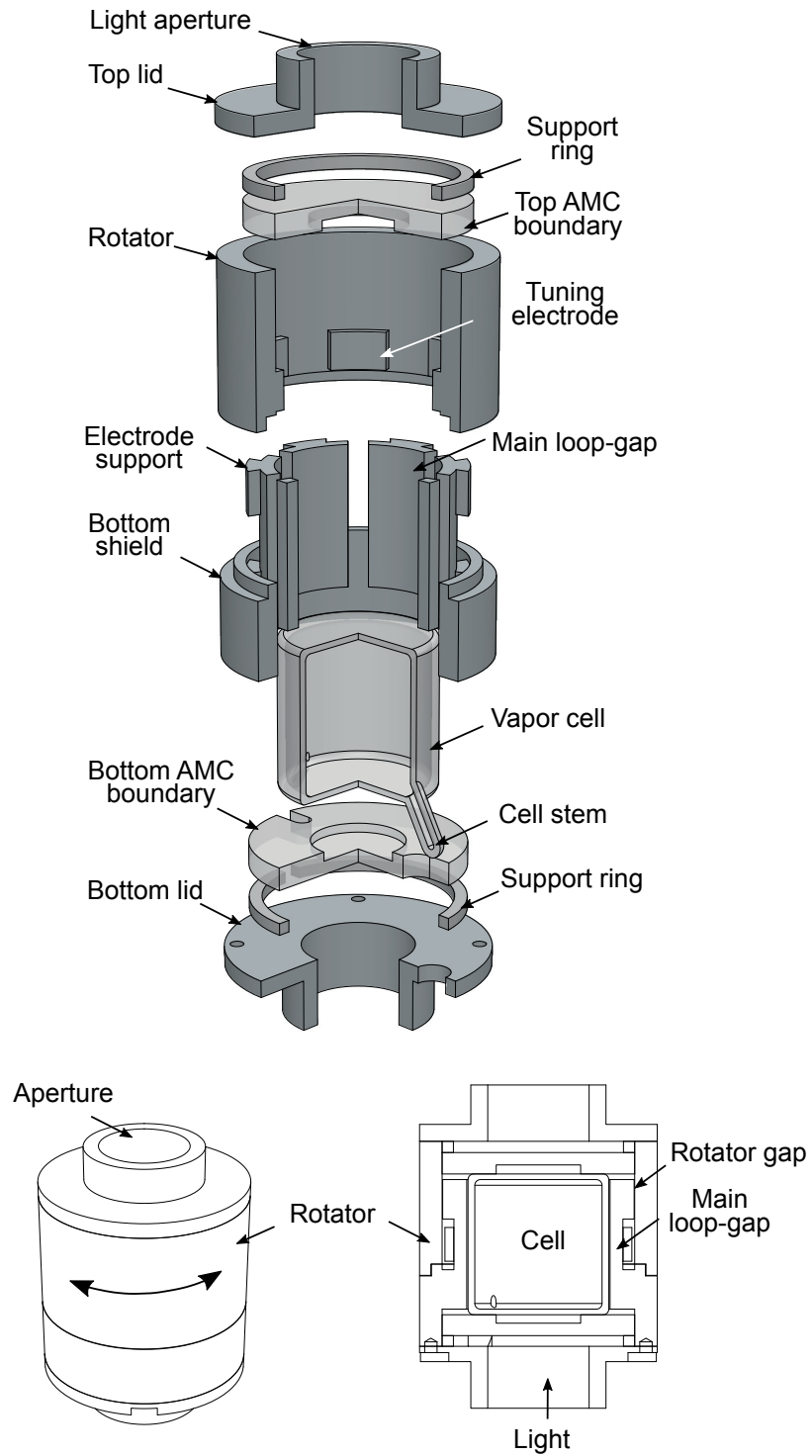


Figure 4.24 – A detailed scheme of the proposed design. The dimensions of the structure are reported in table 4.5. The design of the cell is based on two stems (one of which is not seen for the chosen view). The feeding is separately discussed in section 4.3.4.

## Chapter 4. Implementation of AMC boundary conditions

parameter	value
number of electrodes, $n$	6
loop-gap internal radius, $r$	12.7 mm
loop-gap external radius, $R$	17 - 18 mm
loop-gap height, $d$	23 mm
gap thickness, $t$	2.5 - 3.2 mm
aperture radius, $h$	9 mm
dielectric segment thickness, $e$	3.6 - 3.7 mm
cell radius, $b$	12 mm
cell height, $l$	25 mm
cell thickness	1 mm
rotator electrodes thickness, $r_t$	0.5 - 1.75 mm
rotator electrodes height, $r_h$	6 mm
rotator electrodes width, $r_w$	8 - 9.5 mm

Table 4.5 – Dimensions associated with the structure shown in figure 4.24. The material used for the dielectric segment (Pyrex) is assumed identical to the one used for the vapor cell (with a measured dielectric constant of:  $\epsilon_r = 5.02 \pm 0.01$ ). The volume of the cavity is  $V_{\text{cavity}} \approx 65 \text{ cm}^3$ .

In figure 4.26 we show the resonance frequency as a function of the external radius  $R$  for a gap size  $t$  of: 2.6, 2.8 and 3 mm accordingly. For the interval considered, a cavity with a gap size of  $t = 3 \text{ mm}$  is found to be able to obtain the required  $f_{\text{Rb}}$  where it can be seen that the first, lower, (unwanted) mode is separated by  $\approx 80 \text{ MHz}$  and the first, upper, is  $\approx 150 \text{ MHz}$  away. We find this separation to be sufficient enough, given the fact that the half-power line-width is found to be  $\approx 50 \text{ MHz}$  for all the modes discussed.

However, we still need to make sure that the tuning mechanism is not going to lead to any further overlap. Its influence can be seen in figure 4.27, where we consider cavities with two separate values for the gap size:  $t = 3.3$  and  $3 \text{ mm}$ . As expected (previously shown in figure 4.23), the thickness of the rotator electrodes determines the dynamic range of the frequency tuning. The latter can be made symmetric to the target frequency by slightly altering the gap distance – e.g. from figure 4.27 can be seen that an increase of the gap size brings down the tuning curve. The latter applies less to the unwanted modes since the gap size affects selectively the capacitance of the  $\text{TE}_{010}$ -like mode. It is therefore enough to use the two parameters in order for the tuning mechanism to be conveniently engineered.

It would be optimal if all the unwanted modes have an opposite slope to the  $\text{TE}_{010}$  mode of interest. Unfortunately we can see that this is the case only for the unwanted mode (3) – figure 4.27. The least amount of separation between the wanted mode and modes (1) and (2) is found when the rotator electrodes are in front of the gap (for an angle of  $30 \text{ deg.}$  corresponding to the position marked by "C" shown in figure 4.23). However, in terms of resonance frequency, the unwanted modes are generally less sensitive to the perturbation of the rotator, especially for a larger  $r_t$ .

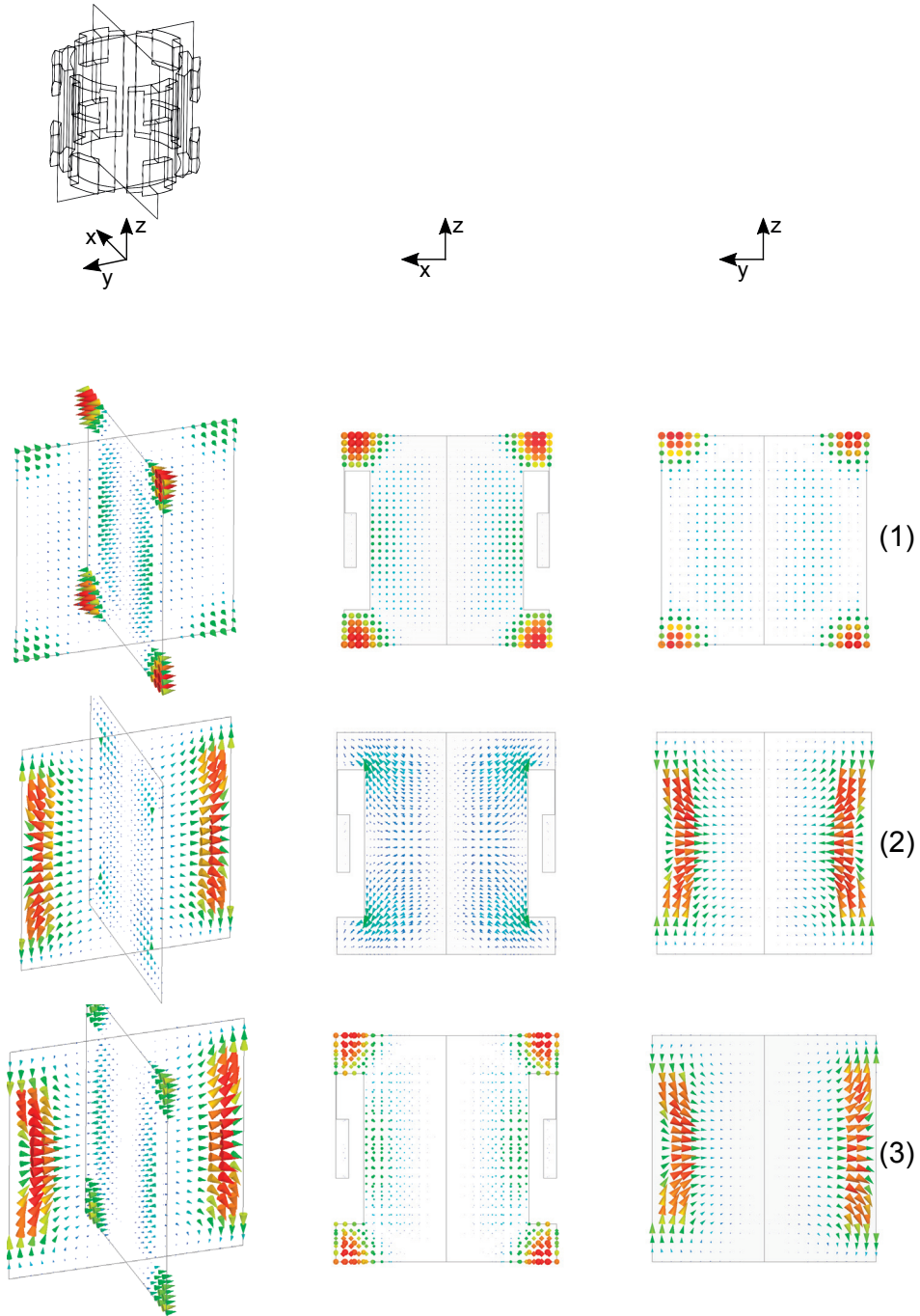


Figure 4.25 – Magnetic field distribution associated to the unwanted modes found near the required resonance frequency  $f_{\text{res}}$ . Each row corresponds to a given mode which is hereafter referred according to the numbering shown.



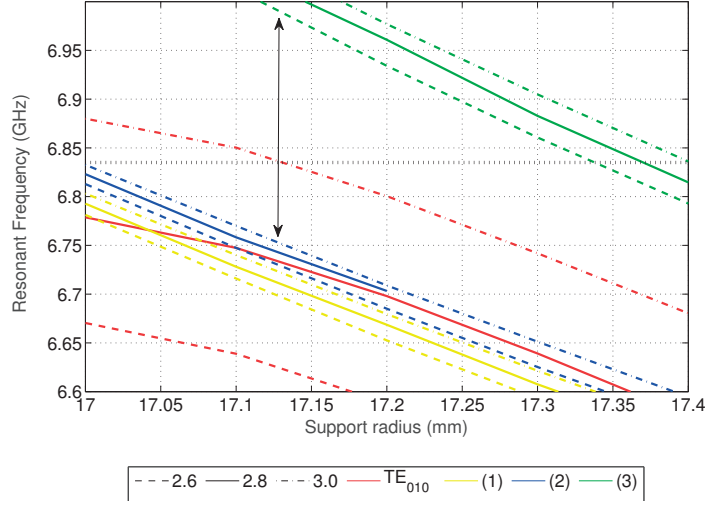


Figure 4.26 – Resonance frequency as function of the external cavity radius  $R$  shown for various gap sizes  $t$ . The modes are color-coded while the different gap sizes are indicated by the family of curves. The target frequency  $f_{Rb}$  is represented by the horizontal (dotted) line. The rotator electrodes are considered with a thickness  $r_t$  of 1.5 mm.

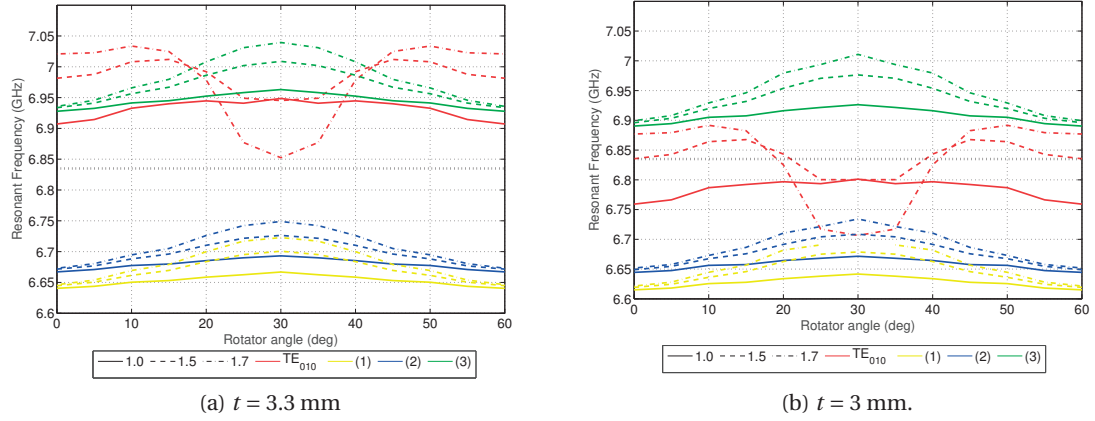


Figure 4.27 – Resonance frequency as function of the rotator position shown for two different cases of the gap sizes  $t$ . In both plots we consider rotators with a thickness  $r_t$  of: 1, 1.5 and 1.7 mm. The modes are color-coded while  $r_t$  is indicated by the family of curves. The positions of the rotator, corresponding to the different angles, are visualized in figure 4.23. The target frequency  $f_{Rb}$  is represented by the horizontal (dotted) line.



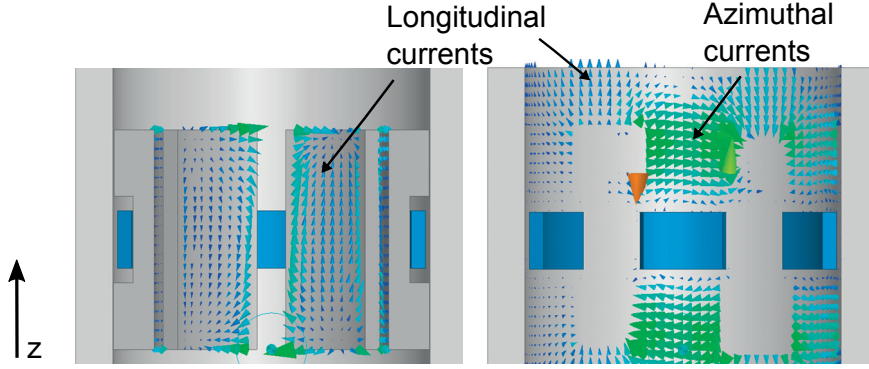


Figure 4.28 – Surface current distribution found for the unwanted mode (3). Regions with purely  $z$ -oriented currents are found at the internal electrode surface as well as at the internal surface of the rotator.

This allows us to tune the cavity while preserving the modal isolation. Moreover, because the vapor cell is kept stationary, in the process of tuning, both the quality of the field and the amount of modal overlapping are very well-controlled.

#### 4.3.3 Second design proposal – cavity with corrugations

It is possible to further increase the interval for which the tuning of the resonance frequency can be obtained without a modal overlap. We do this by adding an additional design feature – selected regions of the internal cavity walls are made corrugated. The corresponding structure is shown in figure 4.29. The effect can be easily understood by analyzing the distribution of the surface currents associated to the unwanted modes (figure 4.28). Since in the central region the mode of interest is only characterized by a longitudinal magnetic field, the associated azimuthal currents are relatively unperturbed by the discontinuity of the ridges. On the other hand, as seen from figure 4.28, the unwanted modes are found to have longitudinal components. By introducing the corrugations, we make the current path effectively longer and hence the resonance frequency lowers. The region where the corrugation is applied is chosen such that only the unwanted currents are affected. In figure 4.30 we compare the simulated  $S_{11}$  parameter for the case of the cavity with and without corrugations (in both cases the rotator position is considered to be at 30 deg). It is immediately seen that the unwanted (3) mode is down-shifted by  $\approx 300$  MHz, while the unwanted (2) mode is shifted (down) by more than 600 MHz and it is therefore not seen on the plot. In fact, another upper mode is seen, brought down due to the corrugation – referred as (4) in the plot shown in figure 4.30. Moreover, it can be seen that, for the interval of 6.7–7 GHz, the wanted mode is well-defined for the cavity with corrugations and for the sufficient tuning range of  $\approx 150$  MHz (for 30 – 15 deg position of the rotator) no overlap is observed.

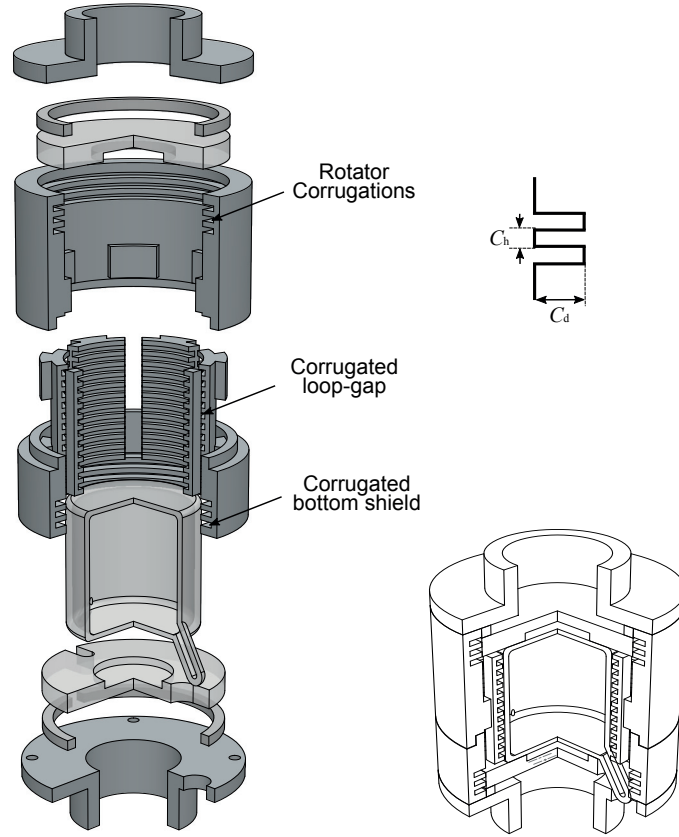


Figure 4.29 – A detailed scheme of the proposed design of a loop-gap cavity with corrugations. The depth of the corrugation  $C_d$  is in the range of 1.3 – 2.6 mm; The height of the corrugation  $C_h$  is in the range of 0.8 – 1.2 mm.

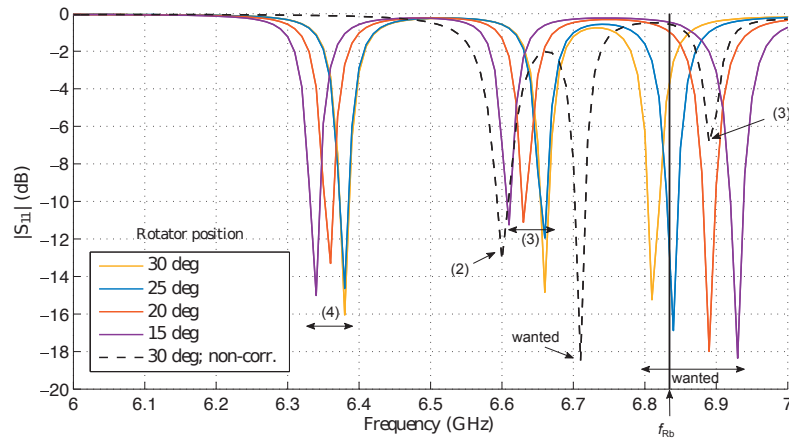


Figure 4.30 –  $S_{11}$  frequency response shown for several positions of the rotator. A cavity with corrugations and a single feed is considered. The  $S_{11}$  parameter for the case of the non-corrugated cavity is shown (dashed line) for a rotator angle of 30 deg. The target frequency  $f_{Rb}$  is indicated by the vertical (black) line.

#### 4.3.4 Feeding mechanism

In our design the feeding mechanism serves two important purposes: we aim at efficient power transfer to the mode of interest and we also want to use the feed design as an additional feature in order to suppress the appearance of unwanted modes. The compact size, the tuning mechanism, the apertures and the AMC boundary conditions all limit the design and the position of the feed. An optimal choice is to use a feeding mechanism based on a small loop. In our case it is logical to use a planar technology – the dimensions of the loop are otherwise too small to obtain precise control. Our idea is to use a Printed Circuit Board (PCB) technology in order to be able to realize a feeding mechanism based on a planar loop. It can be placed close to the external shield so that the mode can be driven in the area of the returned magnetic flux (figure 4.31). We think this approach is favorable because this technology allows a very good control of the dimensions.

In this case, the plane of the feeding loop needs to be oriented perpendicular to the  $z$ -axis since the wanted mode is  $z$ -independent. The feed can be positioned anywhere along the height for which the magnetic flux is present. Moreover, from figure 4.25 it is seen that because the unwanted mode (1) is of a TM-type it will not couple to the feeding loop (if the loop is perfectly aligned). If the feed is positioned in the middle of the  $z$ -axis, it is clear that the unwanted modes (2) and (3) are not coupled either – in that region, their magnetic flux is found orthogonal to the one of the feed.

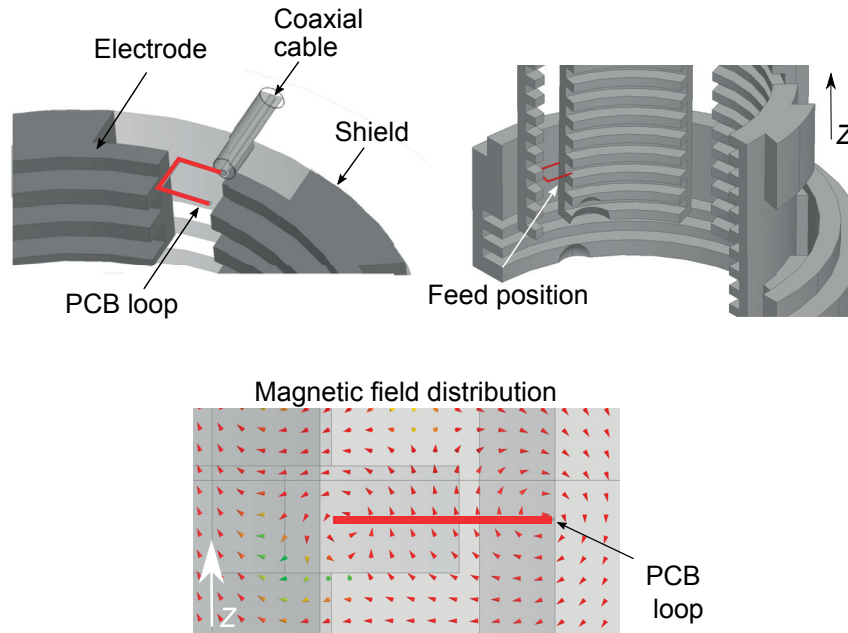


Figure 4.31 – A scheme of the planar-based, PCB feeding loop and its position inside the cavity. The loop is floating (not closed) and it is based on a standard dielectric substrate (not shown for clarity). The dimensions of the feed are: 2 mm x 2.6 mm, 200  $\mu\text{m}$  line thickness, 17  $\mu\text{m}$  thickness of the metal, where a standard substrate material, "Rogers RO4003C", is considered.

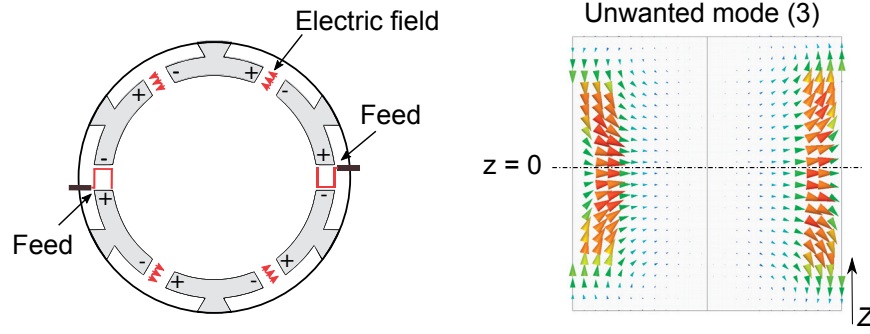


Figure 4.32 – Distributed feeding based on two loops. (Left) For the mode of interest the orientation of the loops is chosen so that the direction of the magnetic flux is identical for both feeds, when both receive signals that are in phase. (Right) For  $z \neq 0$ , the magnetic flux attributed to the unwanted mode (3) is antisymmetric with respect to the central axis of the cavity and it will not be coupled by the feeds.

However, we note that, this location is not possible since in this case, the rotator electrodes cannot be accommodated. It can be concluded that the most optimal position of the considered feeding loop is situate it as close to the center as it can be practically achieved.

It is worth noting that the above-described solution can be further improved if the feed is distributed azimuthally. This approach is used, for instance in [116], in order to limit the modes that contribute to losses and hence minimize the cavity phase shift. In our case, its simplest implementation would be to include one additional feed to the structure (figure 4.32) for which the unwanted mode (3) will not be coupled and the tuning range can be increased even further.

#### 4.3.5 Quality of the obtained field

**Field homogeneity** After it was ensured that the main performance requirements are met, the next step is to evaluate the quality of the field relevant for the atomic clock operation. In figure 4.33 we report the field distribution at the target frequency  $f_{\text{Rb}}$  (for a rotator position of  $\approx 25$  deg) found for a cavity with one feed. We can see that the distribution is quite close to the ideal, non-driven,  $\text{TE}_{010}$ -like case – along the direction of light propagation the field is nearly constant. In fact, the field amplitude found in the central region of the cavity is seen to vary as little as 2% from the maximum. Moreover, the transverse distribution of the field is not too compromised by the proximity of the rotator electrodes (for the case shown they are situated in front of the main electrode gap which can be considered as the worst case of perturbation). One issue is that the field is skewed towards the feed – the lack of azimuthal symmetry for the feed and the cell can lead to the field maximum slightly offset from the center. The latter is easily seen in the transverse field maps shown in figure 4.34.

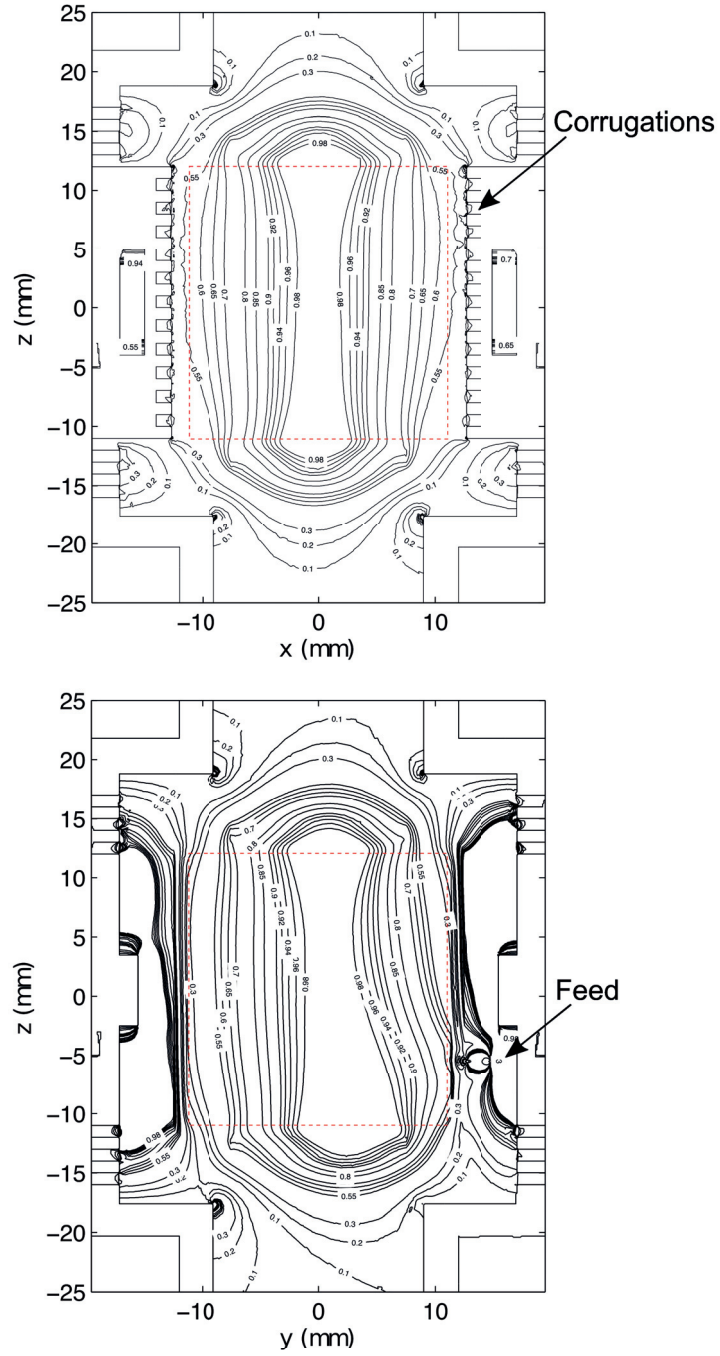


Figure 4.33 –  $H_z$  field (amplitude) distribution normalized to the center. Two longitudinal planes are considered:  $xz$ - plane for  $y = 0$  and  $yz$ -plane for  $x = 0$ . The cell interior is indicated via the (red) dashed line. The transverse variation of the field is more pronounced for the  $yz$ -plane since in our case this plane is situated across the gap.

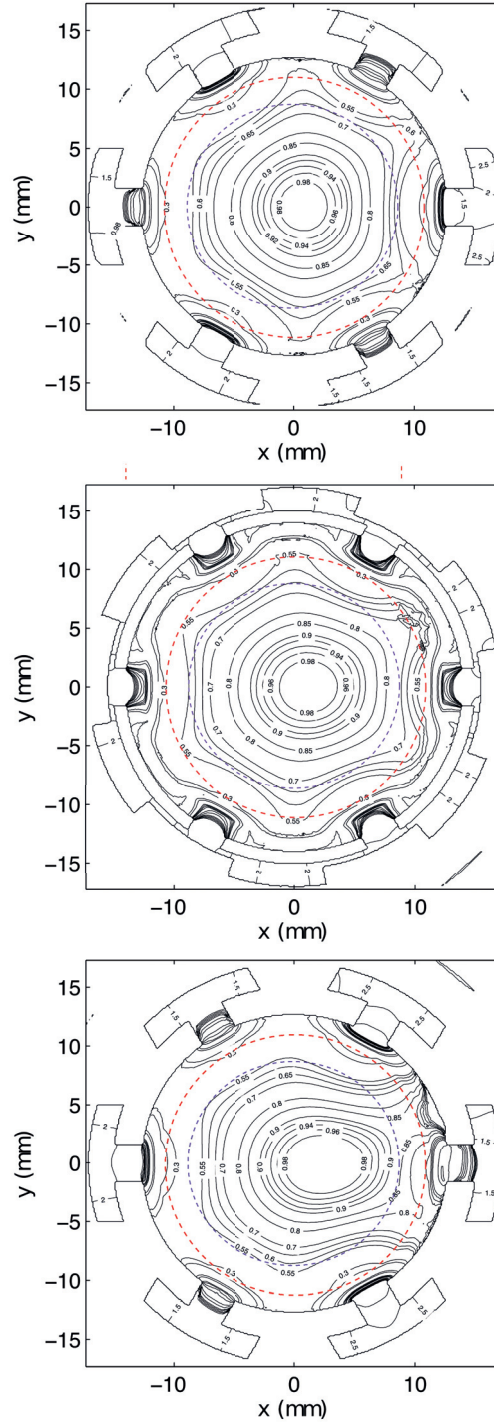


Figure 4.34 –  $H_z$  field (amplitude) distribution normalized to the center. Three transverse ( $xy$ ) planes are considered at heights:  $z = 0.1l$  (bottom);  $z = 0.5l$  (middle);  $z = 0.9l$  (top), where  $l$  is the height of the vapor cell. The cell interior is indicated via the (red) dashed line, the light aperture is indicated via the (purple) dashed line.



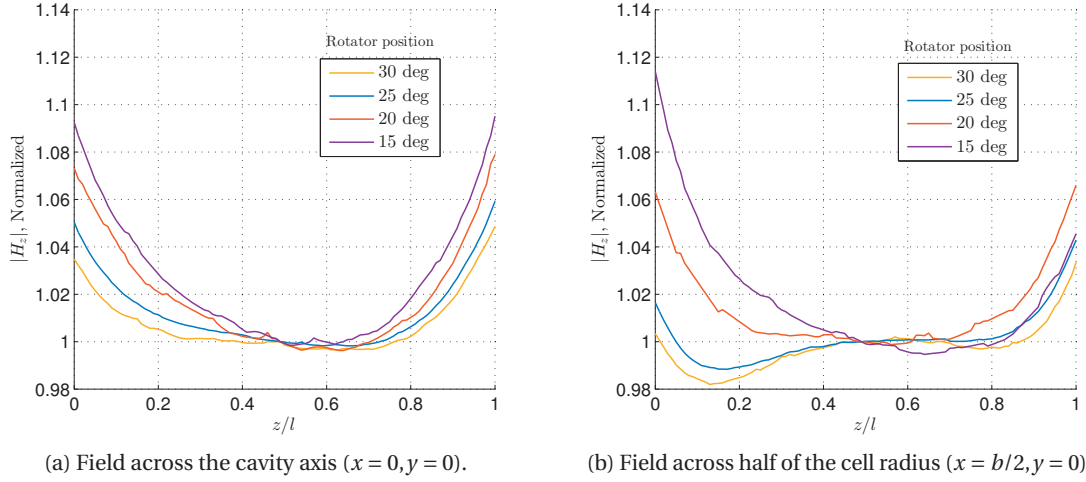


Figure 4.35 –  $H_z$  field distribution (amplitude) along the height of the vapor cell. The result corresponds to the corrugated cavity where the rotator positions from figure 4.30 are considered. The field profiles are case-wise normalized to the amplitude found in the center.

**Stability of the field homogeneity** By definition, the process of tuning changes the resonance frequency and influences the homogeneity in our cavity for which, in principle, the  $TE_{010}$  mode is defined for a single frequency. It is worthwhile to check if the field homogeneity is preserved in the full-tuning range considered in figure 4.30. The result is reported in figure 4.35 where we show the  $H_z$  component for two longitudinal profiles along the height of the cell interior. It can be seen that, for the considered frequency range of  $\approx 130$  MHz, the  $z$ -variation of the field stays in the 10% range. The slight imbalance, with respect to the center, seen in figure 4.35b, is attributed to the presence of the rotator gap (see figure 4.24).

**Field orientation factor** In figure 4.36 we show the distribution of the unwanted magnetic field. As expected for the  $TE_{010}$  mode, the transverse field is well-contained within the dielectric segments with the exception of some regions for which the amplitude is not more than 10%, relative to the amplitude of the  $H_z$  field (found in the center). For the  $xz$ -plane, shown in figure 4.36, it is seen that these regions are quite symmetric with respect to the cavity axis. Such an effect can be attributed to the small gap included in the upper part of the electrode supports, needed to allow rotation. From the distribution for the  $xz$ -plane, shown in figure 4.36, we see that the rotator electrodes do not introduce unwanted field in the central region. However, it can be seen that this is not the case for the feeding loop, which seems the main reason for the slight degradation of the FOF. Nevertheless, we would like to report that the FOF found for this cavity is still very high – approx. 98% of the available in the cell field is used to drive the wanted  $\pi$ -transition.

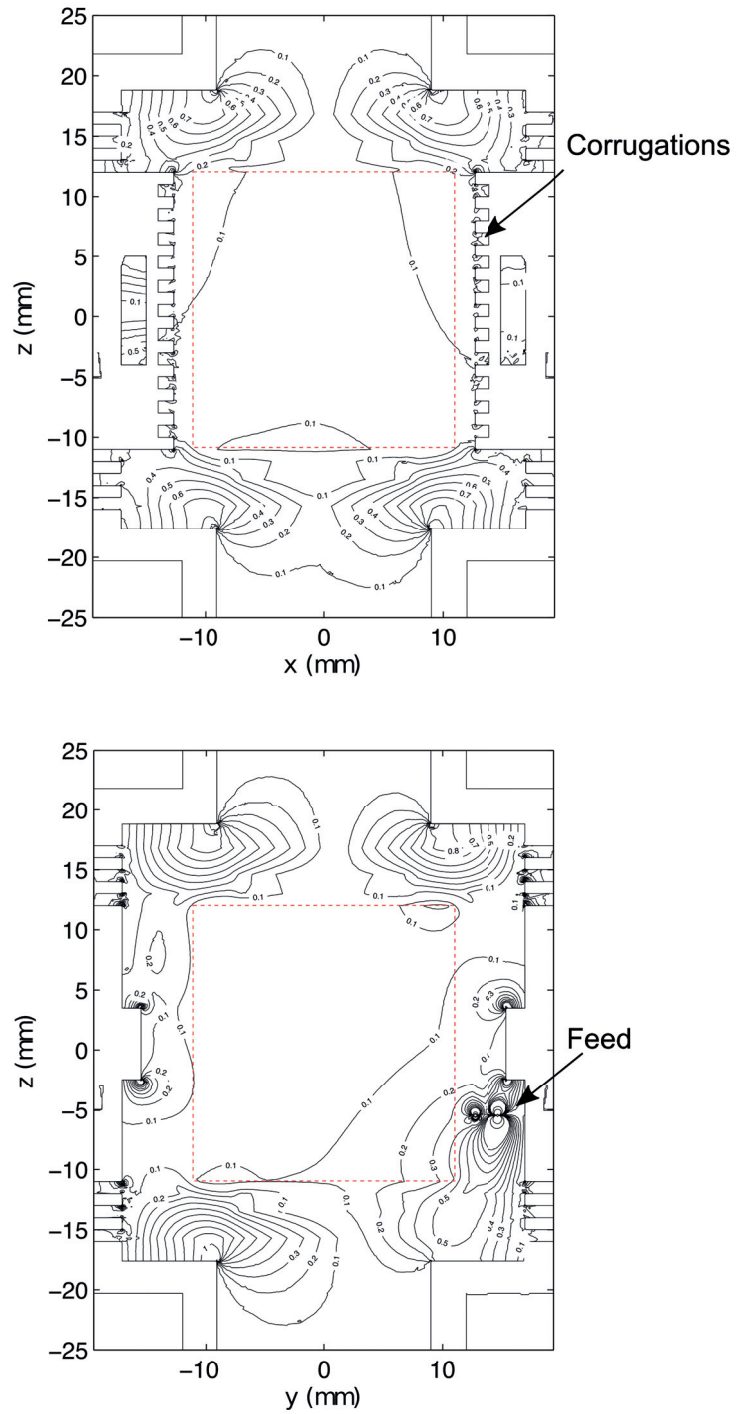


Figure 4.36 – Unwanted field (amplitude) distribution. Two longitudinal planes are considered:  $xz$ -plane for  $y = 0$  and  $yz$ -plane for  $x = 0$ . The cell interior is indicated via the (red) dashed line.



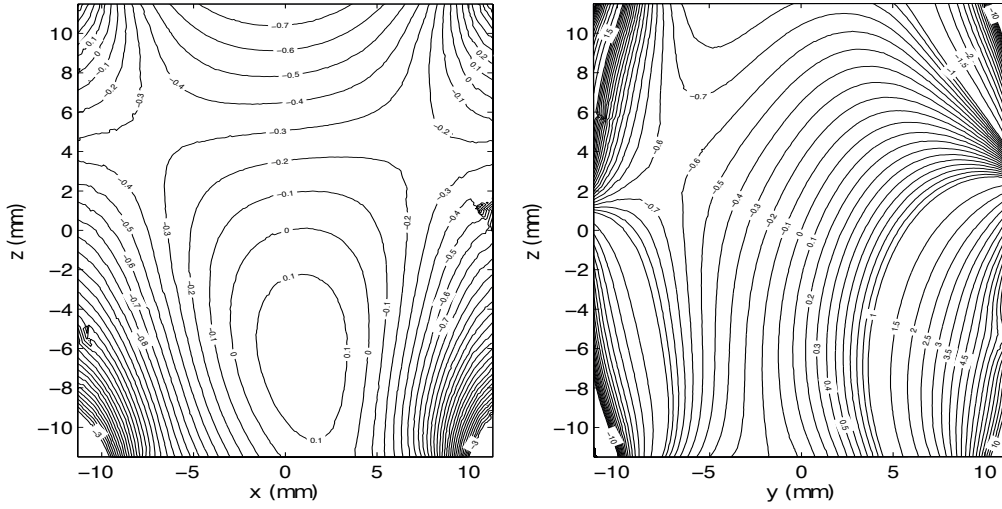


Figure 4.37 – Distribution of the phase shift (degrees) associated to  $H_z$  found inside the vapor cell. Two longitudinal planes are considered for the cell interior:  $xz$ -plane for  $y = 0$  and  $yz$ -plane for  $x = 0$ .

**Q-factor** A Q-factor of  $\approx 170$  is found from the simulations, where we have considered losses in the metal (aluminum), as well as in the vapor cell (Pyrex). At the apertures and the openings required for the stems, a radiation boundary condition is used.

**A note on the phase distribution** For completeness, we are interested in the phase distribution associated to the  $H_z$  field. Albeit, in principle, this is not among the major concerns in our studies, it was recently reported that such an effect might be relevant for the performance of POP clocks [117]. In figure 4.37 we show the amount of phase shift defined relative to the center of the vapor cell interior. The presence of the corrugations is not found to have a too significant effect. It can be seen that, for the region of interest, the feed has the biggest impact on the phase shift.

#### 4.3.6 Design realization and stage of development

We want to note that, in general, both versions of the cavity (with/without corrugations) are suitable to implement, where the corrugated one is generally more preferable since it allows larger tolerances for the vapor cell implementation. It is clear that, assuming the traditional methods used, the corrugated cavity is the more difficult to machine. However, we think that, for the overall size of this structure (a realistic feel can be obtained from a mockup design shown in figure 4.38) the suitable approach is a realization based on additive manufacturing [118]. We have considered two types of solutions: The cavity can be 3D-printed directly in aluminum, based on a Selective Laser Melting (SLM) process. Alternatively, a more traditional, Stereolithography-based process (SLA) can be applied combined with metalization.



Figure 4.38 – A mockup design of the corrugated cavity made using a standard 3D-printed technique. Using such an approach allows for a more intuitive analysts in line with the realization as well as the the various requirements of the physics package.

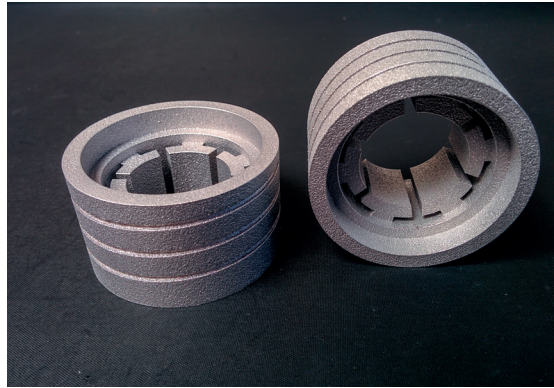


Figure 4.39 – A first prototype based on a SLM-type 3D printing. In the this case the printing process is realized directly in Aluminum.

In the domain of atomic clock cavities using additive manufacturing is a novel approach. This means that some additional preliminary studies are needed before applying this method to the case of the finally proposed solution. In order to investigate, we first considered a 3D-printed realization of a more generic loop-gap geometry where only the main loop-gap region was 3D-printed (figure 4.39). This allowed us to inspect the realization and to compare the performance with a similar, conventionally-realized, structure. The first results show that, considering the tolerance requirements, the structure is identical to the previous realization. The resonance performance of this first cavity prototype was initially measured and showed a close to identical performance in terms of the measured return loss. It can be concluded that a realization based on additive manufacturing is indeed a suitable solution for the implementation of the finally proposed design.

## Summary and conclusions

Modern vapor-cell clocks are now developed up to the point that approach the performance of passive masers for a fraction of their volume. However, in order to obtain such a high stability, the requirements for the components that constitute the clock have also increased. The microwave cavity is a limiting component both in terms of performance and compactness. Moreover, a new generation of pulsed vapor-cell clocks can reach stabilities for which even small imperfections of the required field quality, namely amplitude and orientation, can lead to a significant degradation of the clock signal. We propose a compact solution that solves this problem by combining a loop-gap type geometry with an implementation of AMC boundary conditions. This allows the cavity to resonate at a favorable  $TE_{010}$  mode characterized by a constant field amplitude and a fully parallel orientation along the quantization axis. Two general directions have been followed throughout the research process:

- Investigation and optimization of the loop-gap geometry
- Analysis and implementation of the  $TE_{010}$  mode

**Investigation and optimization of the loop-gap geometry** For the majority of implementations in the community of atomic clocks the (standard) cylindrical geometry is preferred where various modifications exist, however they cannot usually combine performance with compactness. One notable exception is the loop-gap geometry which is known, yet not fully adopted. As an initial reference point, in our studies, we used such a previously realized loop-gap cavity which was investigated via a field imaging experiment and temperature stability measurements.

The results from the imaging experiment showed that the transverse distribution of the wanted field in the loop-gap cavity is similar to the much larger standard cylindrical cavity which confirmed the potential of the loop-gap geometry to provide a well-controlled field. However, it was seen that the field distribution driving the clock transition has an offset from the cavity axis. Such an effect has the potential of degrading the clock performance and it was hence important to investigate. It was shown to be attributed mainly to the fact that the mechanism of tuning is based on rotating (and inserting) the non-symmetric vapor cell.

## Summary and conclusions

---

The experimentally imaged unwanted field showed a non-negligible amplitude close to the center and moreover, the two left/right circularly polarized transverse components were found non-symmetric – an unwanted effect which leads to degradation of the FOF factor. Since a similar result was not seen in the general, full-wave, analysis we made a hypothesis of a possible misalignment existing between the static magnetic field the optical beam and the cavity axis. In order to check, the simpler case of a circular geometry was considered, for which the field misalignment was numerically implemented in a way that physically resembles the imaging experiment. As expected, it was seen that even a small misalignment might, in fact, lead to a non-negligible coupling of the unwanted field along the central axis of the cavity. Moreover, it was shown that the most plausible explanation for the distribution of the unwanted field, seen in the experiment, is a misalignment of the optical beam. However, the observed difference between the circularly polarized components could not be explained by the effect of misalignment and it was attributed to mechanical noise present at the time of the experiment. It was also unexpected to find that a misalignment of the optical beam can effectively improve the field homogeneity, which is an important conclusion since it means that the imaging experiment tends to overestimate the field homogeneity in the presence of an optical beam tilt. Overall this model was found useful in terms of realistically representing the field misalignment and allowed quantifying its effect based on the various figures of merit. It is simple to implement and in the future can be used as a tool in the interpretation of such imaging experiments.

After the field distribution found via numerical simulations was experimentally confirmed it was logical to further (numerically) investigate what is the intrinsic homogeneity that could be achieved in the different possible implementations of the loop-gap cross section. A little surprising is the fact that structures with a lower number of gaps were found to perform somewhat better, conversely to some of the reported results available in the literature. In fact, not many studies were found that aim at improving this type of cavities (in contrast to lower frequency resonance structures used in MRI for example). It was also understood that the loop-gap has a surprising potential for miniaturization, mainly because of its many degrees of freedom. In the literature, the most prominent work related was found from the EPR community. In our case, based on a relatively simplified lumped method approach we were able to get a good physical understanding which helped a lot in the design selection process.

Since the temperature stability of the cavity is important for the medium and long term performance of the clock, a dedicated experiment was used in order to verify the temperature coefficient of the loop-gap. It was measured to be a significantly better than the standard geometry and to be on a par with similar structures reported in the literature. In order to understand the temperature behavior, we used a simplified analysis which revealed an intrinsic feature of the design that allows engineering the slope of the temperature coefficient by properly choosing the diameter of the vapor cell. It can be concluded that, considering the temperature stability the loop-gap geometry is not a compromise in terms of performance.

Finlay, based on our experimental experience, it can be concluded that a common difficulty in the design of these structures comes from the presence of the unwanted modes. This can play a significant role in the degradation of the performance, especially given the fact that the vapor cell is usually characterized by considerable tolerances. This means that the design needs to always include an efficient mechanism to tune the resonance frequency in order to meet the resonance condition for the clock transition.

**Analysis and implementation of the  $TE_{010}$  mode** In our application, the intrinsic advantage of the  $TE_{010}$  mode stems from the fact that such a cavity resonates at the cutoff frequency associated with the cross section and, as a consequence, the magnetic field amplitude is spatially constant (along the height) and fully parallel to the cavity axis. Additional benefit is the possibility to compact or increase the height of the cavity without affecting the resonance frequency.

First in our analysis, we showed that for the ideal case of PMC boundaries applied to the top and bottom walls of a cylindrical cavity, it is possible to obtain such a mode for any arbitrary cross section. This is an important conclusion since it means that the concept is in principle applicable to a variety of structures. The next step was to consider a more realistic implementation (based on AMC boundaries) in the context of the clock application. In order to obtain a physical intuition, given the requirements of the physics package, we took the case of the canonical cylindrical geometry for which we intended to evaluate if the AMC boundary can be utilized successfully (implemented with a dielectric material transparent for the laser light). An interesting outcome of the study was that the main concerns of high sensitivity (in terms of dimensions) turned out not to be true and the mode was found not so restrictive when a realistic range of production tolerances is considered. Moreover, we also modeled the temperature stability which, due to an effect of compensation coming from the dielectric segments, was found to be considerably improved (with respect to the standard geometry). The latter is not unusual since selectively loading regions of the cavity is a well-known approach that can be used to improve the temperature performance. As expected, the presence of the light apertures was found to degrade the field homogeneity. However, because it effectively resembles an additional dielectric loading, we were able to diminish this effect simply by removing slabs from the dielectrics used for the AMC boundary condition. It is also worth noting that, even with this relatively simple implementation, the volume of the cavity was effectively reduced since the height is limited only by the vapor cell. The major difficulty in the implementation of the  $TE_{010}$  cavity comes from the fact that the mode is in principle defined only for a single frequency. Therefore, the mechanism chosen for the frequency tuning needs to allow obtaining the mode ideally at the target resonance frequency. However, the specifics of the  $TE_{010}$  mode is such that a solution based on the electrical length of the cavity was found unstable. Alternatively, a (local) perturbation of the circumferential walls was also studied as a possibility but it was found to have an even more negative impact on the distribution of the field. The conclusion at that stage is that such a simple cylindrical geometry (modified

## Summary and conclusions

---

with a dielectric material) can be in principle easily implemented for the  $TE_{010}$  mode and it is applicable for a high-performance vapor-cell atomic clock. However, no practical way to tune the resonance frequency of the cavity was found.

In the next stage of the work our goal was to apply the  $TE_{010}$  mode to the loop-gap type geometry. In this way it is possible to combine the excellent transverse homogeneity of the loop-gap cross section with the nearly constant field distribution along the height of the  $TE_{010}$  cavity and, moreover, we showed that in terms of temperature performance, compactness and FOF, such a cavity is a significant improvement. The specifics of the loop-gap structure were found very beneficial concerning the implementation of the tuning as well as the AMC boundaries.

Considering the important issue of frequency tuning, it was recognized that the specific symmetry of the loop-gap is actually an advantage for the tuning mechanism realization because it allows a flexible way to change the cross section. Our approach is to introduce an additional loop-gap structure that can be azimuthally displaced and hence the tuning is obtained via a perturbation of the returned magnetic flux. In the design of the tuning we aimed and achieved two main features: the solution is found very flexible in terms of design and it can be designed for a broad tuning range while at the same time preserving the azimuthal symmetry; it does not involve displacement of the cell, and hence provides a stable operation. Based on our studies, the latter proved to be of a crucial importance for the suppression of the unwanted modes.

Alternative ways to obtain the AMC boundaries were explored for the loop-gap  $TE_{010}$  cavity where a particularly interesting AMC solution based on a planar PCB structure was studied. It was found to be fairly easy to manufacture and it is characterized by low production tolerances and low losses. While, in principle, the size is significantly reduced compared to the solution based on a dielectric filling, it must be noted that the planar AMC performed well only if large enough extensions were included, which slightly diminished its compactness aspect. Finally, it can be also concluded that such a solution opens possibilities for size and cost reduction, hence it is worth further investigation.

**Final design** In the last stage of the work, based on our various studies and the lessons learned from the available experiments, we proposed a novel design suitable for high performance vapor-cell clocks. The cavity is designed to operate at the  $TE_{010}$  mode and it is based on a six loop-gap structure. The AMC boundaries are realized via dielectric segments in order to minimize heat loss and also to improve the temperature coefficient. The resonance frequency is tuned directly through the cutoff of the cross section which is realized using an additional loop-gap structure. In this way the tuning can be both azimuthally symmetric and symmetric to the AMC boundaries hence allowing the  $TE_{010}$  mode. Because the vapor cell is kept fixed (in the tuning process), the field is well controlled and the performance in



terms of homogeneity and FOF is very stable even for a significant tuning range. We have also used large apertures with additional cutoff extensions in order to decrease the field leakage. The dielectric segments used for the AMC are modified so that the field non-homogeneity arising from the apertures is well mitigated in the region sampled by the optical beam. The overall volume is about two times lower relative to the standard geometry which is a good achievement given the substantial improvement of the performance and the fact that, in our case the vapor cell is chosen to be relatively large. In order to tackle the potential problems related to the existence of unwanted modes, we provide two additional solutions that were able to significantly increase the isolating between the wanted and the unwanted modes: a cavity with added corrugations and a possibility for a distributed feed. Although they are not strictly necessary, depending on the technological limitations, they would improve the performance if implemented. Moreover, the proposed distributed feed is found to additionally improve the field homogeneity in the vicinity of feeding loop.

In terms of realization, we have chosen the novel approach of additive manufacturing which in our case is especially suitable since the proposed design is quite a challenge to machine. Using it we first realized a prototype based on a simplified design which, in terms of performance, was found comparable to a similar design based on conventional means of realization. For the feeding mechanism we consider to use a PCB structure, which is favorable in terms of tolerances, it can be easily reproduced and it allows for a relatively easy implementation of a distributed feed.

In conclusion: two versions of the design were proposed (with and without corrugations), which fulfill the requirements established in section 1.3.4 and provide homogeneity of the field amplitude of a few % in the central region sampled by the laser light as well as almost 97% proper orientation along the quantization axis. Our design can be compacted, if needed, since the resonance frequency is independent of the height.





## Prospective work

### Maximizing the performance of the $TE_{010}$ cavity

One possible direction of improvement is to simply increase the height of the  $TE_{010}$  cavity allowing for increased height of the vapor cell. This means that the number of atoms that "see" improvement of the field homogeneity will also increase hence improving the clock signal. From a purely electromagnetic point of view, the longer the height of the cavity is chosen to be, the more sensitive the  $TE_{010}$  mode is. Nevertheless, given the tolerances, the height of the cavity can be easily scaled by a factor of two while still preserving the field homogeneity. This means that, in principle, the amount of Rb vapor sampled by the light field is going to double. While such a geometry would increase the footprint of the cavity, the height will still be smaller than the standard geometry. One significant difficulty stems from the fact that obtaining a homogeneous temperature distribution in the vapor is more difficult in the case of larger volumes. Therefore, the problem of heating the vapor has to be modeled accordingly and the heating mechanism needs to be rethought. Finally, one needs to also consider that due to the longer path of the laser light (throughout the vapor) the clock operation might be prone to effects like position shift arising from inhomogeneities associated with the absorption of the light.

### Cavity based on planar loop-gaps

A potentially interesting line of development is related to the planar structure that was discussed in section 4.2. The goal here is to reduce the realization complexity of the loop-gap cavities and to explore the industrialization potential of the planar structure. It is realistic to imagine that the whole loop-gap cavity can be realized using a PCB technology. In fact, such planar loop-gap structures have been largely employed in EPR applications. In our case, it is possible to stack several planar resonators along the height of the vapor cell. By controlling the distance between the planar elements it is in principle possible to obtain the favorable  $TE_{010}$  mode. Moreover, if for the external shield a simple metal cylinder is used, it would be feasible for such a cavity to be produced fairly easy. While in terms of temperature stability this structure would be a tradeoff, given its simplicity, it is worth exploring.

### Modeling of the light absorption

In the interpretation of the field imaging experiment, the light signal absorbed by the rubidium vapor is considered according to the Beer-Lambert law. This mainly stems from the fact that

the imaging experiment was originally developed for an optically thin medium. It means that the variation of the optical density (and the driving fields) along the path of the light integration is negligible. For the case of the atomic clock cavity the vapor cell is no more optically thin however, the same approximation can be also used. Physically, it means that all differential volumes inside the cell contribute equally to the clock signal. It is worth noting that, in general, the application of the Beer-Lambert law implies that the light should not cause optical saturation or optical pumping. Therefore, in the actual clock implementation, especially for the case of longer cells, it is justified to use a model that is better suited to account for such effects. In this case, the figures of merit and the interpretation of the field imaging experiment can be updated accordingly so that a more physical notion is obtained for the optimal design.

## A Field misalignment

**Laser beam misalignment** When the integration procedure is performed in a cavity with axis perfectly aligned to the direction of the light, the resulting 2D image of the field distribution represents the traverse variation of the field (e.g. if we take the ideal case for which the longitudinal field variation is identical for all points from the cross section, we will obtain the 2D Bessel profile in the case of the circular cavity). A laser beam misalignment results in a horizontal displacement of the averaging direction, spread of the shape of the peak of the averaged field and reduced amount of the useful signal. We calculate the driving fields for a set of voxels with coordinates created on a standard 3D rectangular grid inside the volume of the cavity. All voxels corresponding to the same transverse coordinates represent arrays where the first array element is considered situated at the plane of the light source and the last is at the plane of the detector – figure A.1. In this case, for example, the value corresponding to the pixel  $x_1, y_1$  from the detector plane is obtained by calculating the Riemann sum from the corresponding array:

$$A_{x_1, y_1} = \sum A(x_1, y_1, z_i) \Delta z, \quad (\text{A.1})$$

where  $A$  is the considered driving field that can be evaluated analytically everywhere in the cylindrical cavity. Physically this corresponds to the signal that will be detected by the detector at the top plane of the cavity. The displaced direction of the laser light and thus the direction of the field integration can be represented by applying a shear-type mapping to the initial rectangular grid – figure A.2. In 3D, the shearing transformation, performed with respect to the  $z$  axis, preserves the volume and the cross section of the laser beam and it will not change the  $z$ -coordinate of the grid points. The transformation can be represented by the matrix equation:

$$\begin{pmatrix} x' \\ y' \\ z' \\ 1 \end{pmatrix} = \begin{pmatrix} 1 & 0 & a & 0 \\ 0 & 1 & b & 0 \\ 0 & 0 & 1 & 0 \\ 0 & 0 & 0 & 1 \end{pmatrix} \begin{pmatrix} x \\ y \\ z \\ 1 \end{pmatrix}, \quad (\text{A.2})$$

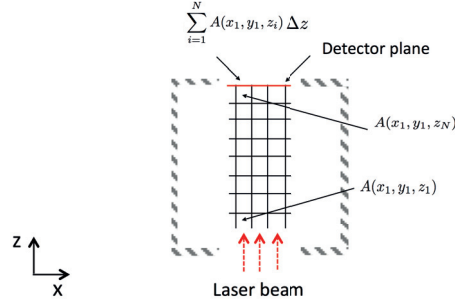


Figure A.1 – The 3D rectangular grid in the cavity is shown for the x-z plane. The elements at the plane of the light source and at the plane of the detector are pointed out.

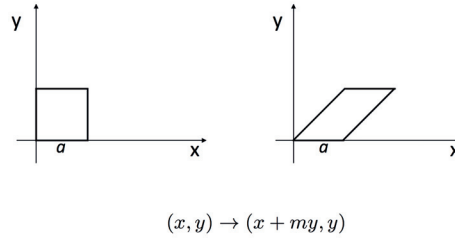


Figure A.2 – An example of shear mapping performed in 2D — a unit square before and after the transformation. Every point that is not found on  $a$  will be displaced along  $x$  by a distance proportional to its perpendicular distance to  $a$ ;  $m$  - shearing factor.

where  $x'y'z'$  are the sheared coordinates and  $xyz$  are the coordinates of the initially created, 3D rectangular grid. The shearing parameters  $a$  and  $b$  can be assigned any real values. The effect of this transformation is to displace the initial  $x$ ,  $y$  coordinates by an amount that is proportional to the  $z$  coordinate, while leaving  $z$  unchanged. After the sheared grid is obtained the total field inside the cavity is calculated for the sheared coordinates. A scheme of the transformed grid can be seen in figure A.3. The integrated value obtained at the plane of the detector is associated to the transformed coordinates which depend on the misalignment of the laser beam and will be different from the original pixel coordinates of the detector (the detector is fixed and aligned to the axis of the cavity). This is solved by applying interpolation that maps the integrated field obtained at the plane of the detector to the actual pixel coordinates.

**Influence of the phase difference** It is of interest to see what is the distribution attributed to the unwanted  $B_-$  and  $B_+$  components if a constant phase difference is (artificially) introduced between the  $B_x$  and  $B_y$  components in the cavity. From figure A.4 is seen that in this case the integrated images corresponding to the  $B_+$  and  $B_-$  components appear rotated. In a realistic cavity such a phase difference may in principle be seen localized in the vicinity of the feeding loop.

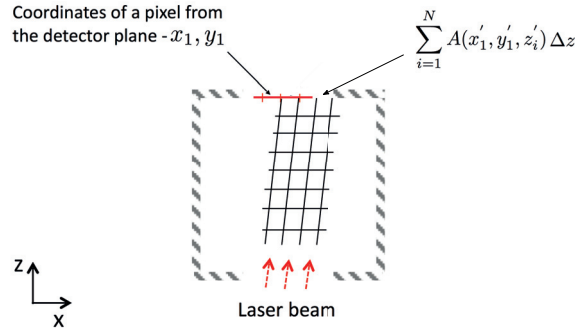


Figure A.3 – The transformed 3D rectangular grid in the cavity is shown for the x-z plane. The vertical array of voxels used to calculate the integrated field quantity at the detector plane is obtained for arbitrary displacement of the laser beam. All arrays with voxels having coordinates outside the radius of the beam aperture are discarded.

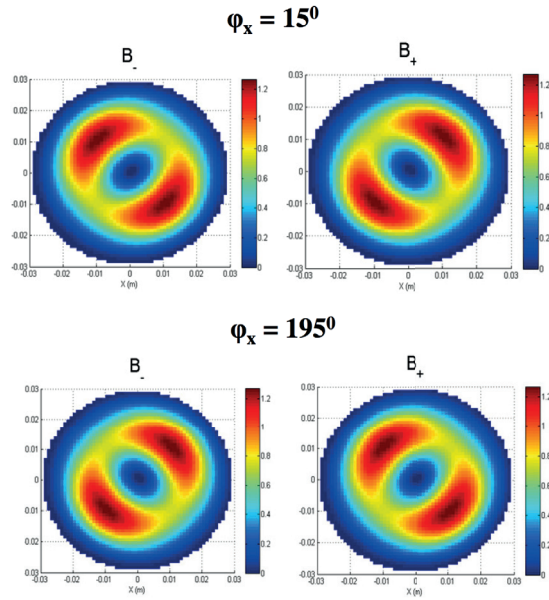


Figure A.4 – 2D integrated profiles found for  $B_+$  and  $B_-$  assuming a phase difference  $\phi_x$  between the transverse magnetic field components in the cavity.



## B Vapor cell study. Stability of the resonance condition

### B.0.1 Variation of the vapor cell dimensions

In this part we study what is the effect of the tolerances associated to the produced vapor cells. Based on the provided measurements (see figure B.1) we have determined what are the worst case deviations concerning the radius and the length of the vapor cell (table B.1).

In order to represent this dimension variations in our simulations we have scaled the nominal

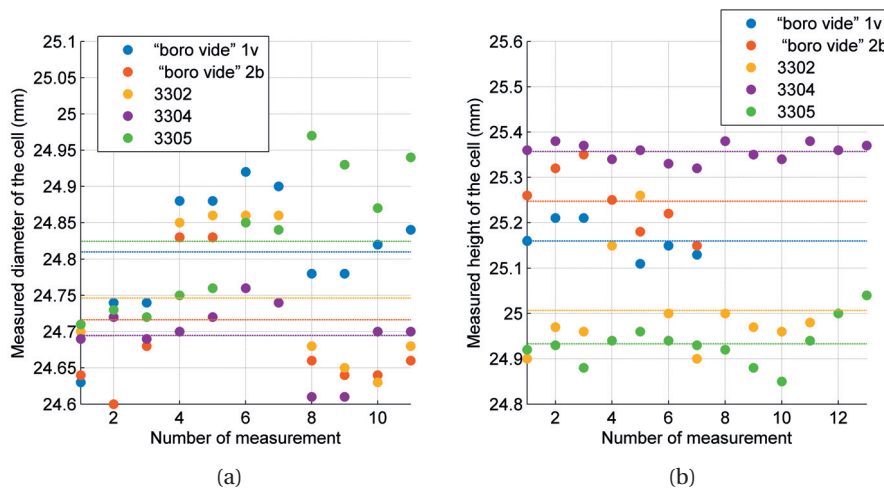


Figure B.1 – Measured dimension data for different vapor cell realizations. The dashed lines indicate the mean values. The nominal value for both the radius and the height is 25 mm.

	External height	External diameter
nominal	25	25
min	24.85	24.6
max	25.38	24.97

Table B.1 – The extreme values found for the measured dimensions of the vapor cell (mm).

## Appendix B. Vapor cell study. Stability of the resonance condition

---

vapor cell geometry in height (along  $z$ ) and width (perpendicular to  $z$ ). The scaling coefficients are defined relative to the nominal dimensions (table B.2). Based on this, in order to study the effect on the resonance frequency we have grouped four different cases (table B.3). In this way we are able to cover the worst-case combinations of tolerances that apply to the cell. In order to obtain the resonance condition for these 4 cases, we have chosen the two extreme cases for the gap size: 2.5 and 2.6 mm. This choice is justified because for these cases the separation between the modes is the smallest. It can be seen (figure B.3) that the wanted resonance is not too influenced for cases 2 and 4, where the resonance condition is obtained for tuning distance close to the nominal case. On the other hand cases 1 and 3 cannot reach resonance condition at all.

### Worst realizations in terms of the wanted mode

It can be directly seen that cases 1 and 3 differ to 2 and 4 in terms of the transverse scaling. It can be concluded that the worst realizations are the ones that have the minimum value found for the diameter (in other words the largest deviation). Size variation in terms of length is not so crucial – the difference between the separate cases 1 and 3 is not so pronounced (the same is valid when the separate cases 2 and 4 are compared). It can be thus concluded that the worst cells are the ones that have the smallest diameter with respect to the nominal (that would be also the case if they had larger but, as previously discussed, this is not allowed because of the production technology).

### Worst realizations in terms of the unwanted mode

From figure B.3, for the unwanted mode, can be seen that for large positive tuning cap distances (when the cell is removed away) all simulated cases converge close to the nominal one. However, when the tuning cap is inserted, cases 1 and 2 remove away the unwanted mode from the nominal (hence they are favorable) while cases 3 and 4 bring the unwanted mode closer and hence they are not favorable. If for example, cases 2 and 4 are taken from table B.3. It can be seen that both are characterized by the same scaling for the radius but different scaling for the heights. It can be thus concluded that the height of the cell is the main reason that plays a role in bringing the unwanted resonance closer when the cell is deeply inserted. Furthermore, it can be seen that the cells having longer than the nominal height are the worse ones.

So considering the above analysis, it can be finally concluded that, the worst case corresponds to case 3 from table B.3, where we have somewhat put more importance into obtaining the resonance condition rather than the separation of the modes.

### Separate cell realizations

According to the above discussion and considering the cell dimensions in table B.4 we consider cell the "3304" to be a representation of the worst case that is considered in the simulations. It can be seen that this corresponds to the case 3, reported in table B.3.



	Scaling along $z$	Scaling transverse to $z$
nominal	1	1
min	0.994	0.984
max	1.0152	0.9988

Table B.2 – Scaling factors applied to the cell dimensions in the simulations. The scaling along  $z$  is related to the height of the cavity, while the scaling transverse to  $z$  is needed for the radius. From the values it can be concluded that the relative variation of the radius is in the range:  $-0.12\% \div -1.6\%$ , while for the height we have:  $-1.5\% \div +0.6\%$ .

Simulated cell	Scaling along $z$	Scaling transverse to $z$
case 1	0.994 (min)	0.984 (min)
case 2	0.994 (min)	0.9988 (max)
case 3	1.0152 (max)	0.984 (min)
case 4	1.0152 (max)	0.9988 (max)

Table B.3 – Four separate cases of the simulated cell.

### B.0.2 Variation of the cell permittivity $\epsilon_d$

The influence of a potential deviation from the nominal dielectric constant (associated to the vapor cell) is shown in figure B.4. It can be seen that both the wanted and unwanted modes are affected in a similar way.

Name of the cell	Max height	Min height	Max diameter	Min diameter
“boro vide” 1v	25.21	25.11	24.92	24.63
“boro vide” 2b	25.35	25.15	24.86	24.60
3302	25.26	24.9	24.86	24.63
3304	25.38	25.32	24.76	24.61
3305	25.04	24.85	24.97	24.71

Table B.4 – Extreme values for the measured cell dimensions (mm).

## Appendix B. Vapor cell study. Stability of the resonance condition

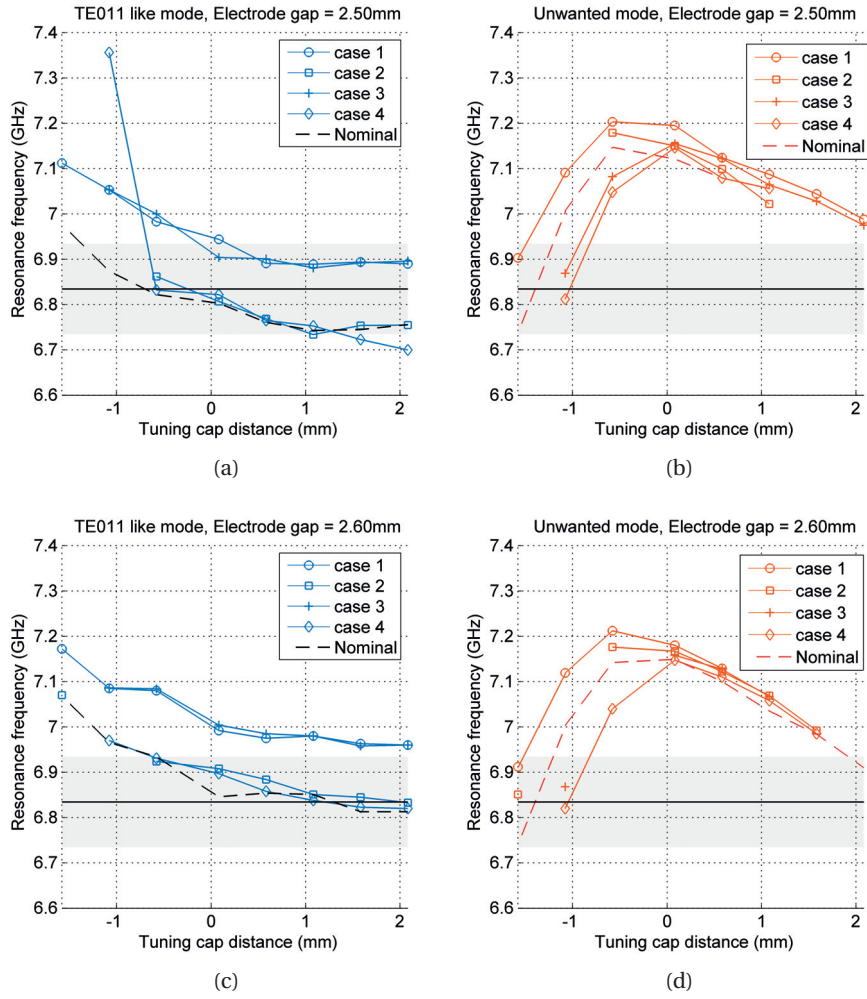


Figure B.2 – Resonance frequency as function of the tuning cap distance for cavities with gaps 2.5 and 2.6 mm. The four different cases correspond to the dimensions of the vapor cell scaled according to table B.3. The nominal case is indicated by the dashed line and corresponds to the result shown in B.3. The resonance frequency required for the clock transition  $f_{\text{res}} = 6.835$  GHz is indicated via the black line.

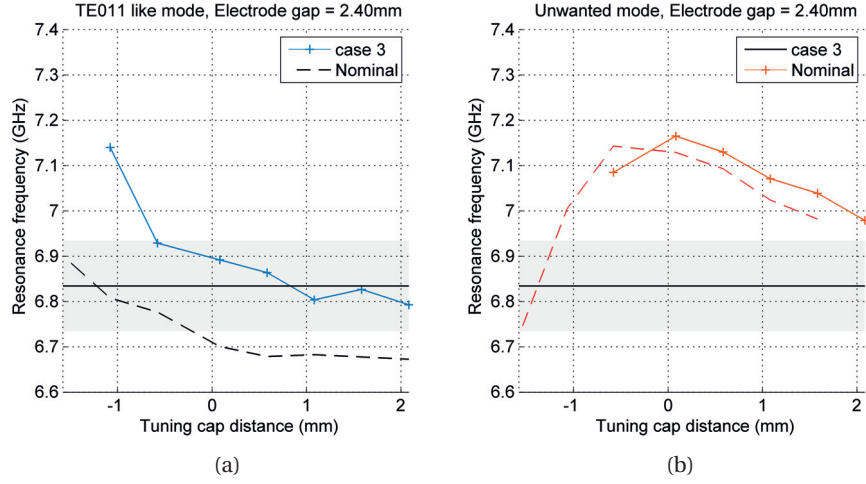


Figure B.3 – Resonance frequency as function of the tuning cap distance for a cavity with a gap of 2.4 mm. The case shown corresponds to the cell "3304" which is considered as the worst case (case 3 reported in table B.3). The nominal case is indicated by the dashed line. The resonance frequency required for the clock transition  $f_{\text{res}} = 6.835$  GHz is indicated via the black line.

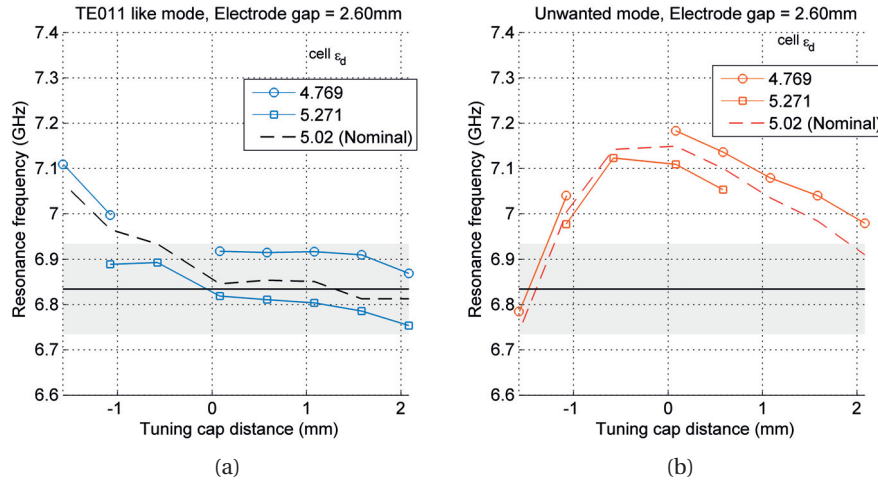


Figure B.4 – Resonance frequency as function of the tuning cap distance for a cavity with gap 2.6 mm. The cases shown correspond to  $\pm 5\%$  variation of the cell dielectric constant with respect to the nominal case (indicated by the dashed line). The resonance frequency required for the clock transition  $f_{\text{res}} = 6.835$  GHz is indicated via the black line.



# Bibliography

- [1] J. Vanier and C. Mandache, "The passive optically pumped rb frequency standard: the laser approach," *Applied Physics B*, vol. 87, no. 4, pp. 565–593, 2007.
- [2] R. Wynands and S. Weyers, "Atomic fountain clocks," *Metrologia*, vol. 42, no. 3, p. S64, 2005.
- [3] L. S. Cutler, "Fifty years of commercial caesium clocks," *Metrologia*, vol. 42, no. 3, p. S90, 2005.
- [4] J. R. Vig, "Quartz crystal resonators and oscillators for frequency control and timing applications. a tutorial," *NASA STI/Recon Technical Report N*, vol. 95, 1994.
- [5] S. Micalizio, C. E. Calosso, A. Godone, and F. Levi, "Metrological characterization of the pulsed rb clock with optical detection," *Metrologia*, vol. 49, no. 4, p. 425, 2012.
- [6] S. Kang, C. Affolderbach, F. Gruet, M. Gharavipour, C. E. Calosso, and G. Mileti, "Pulsed optical pumping in a rb vapor cell using a compact magnetron-type microwave cavity," in *2014 European Frequency and Time Forum (EFTF)*, pp. 544–547, June 2014.
- [7] S. Kang, M. Gharavipour, C. Affolderbach, F. Gruet, and G. Mileti, "Demonstration of a high-performance pulsed optically pumped rb clock based on a compact magnetron-type microwave cavity," *Journal of Applied Physics*, vol. 117, no. 10, p. 104510, 2015.
- [8] F. Riehle, *Frequency Standards: Basics and Applications*. Wiley, 2006.
- [9] T. N. Bandi, *Double-resonance studies on compact, high-performance rubidium cell frequency standards*. PhD thesis, Université de Neuchâtel, 2013.
- [10] W. Riley, P. L. U. Time, and F. Division, *Handbook of Frequency Stability Analysis*. NIST special publication, U.S. Department of Commerce, National Institute of Standards and Technology, 2008.
- [11] M. Lombardi, "The accuracy & stability of quartz watches," *Horological Journal*, vol. 57, p. 150(2), 2008.
- [12] J. Camparo, "The Rubidium Atomic Clock and Basic Research," *Physics Today*, vol. 60, no. 11, pp. 33–39, 2007.

## Bibliography

---

- [13] D. A. Steck, “Rubidium 87 D line data,” revision 2.1.4, 23 December 2010. <http://steck.us/alkalidata>.
- [14] J. Vanier and C. Audoin, *The quantum physics of atomic frequency standards*. No. v. 1 in The Quantum Physics of Atomic Frequency Standards, A. Hilger, 1989.
- [15] J. Vanier and C. Tamescu, *The quantum physics of atomic frequency standards. Recent Developments*. No. v. 3 in The Quantum Physics of Atomic Frequency Standards, Taylor and Francis Group, 2016.
- [16] C. Stefanucci, T. Bandi, F. Merli, M. Pellaton, C. Affolderbach, G. Mileti, and A. K. Skrivervik, “Compact microwave cavity for high performance rubidium frequency standards,” *Review of Scientific Instruments*, vol. 83, no. 10, 2012.
- [17] T. Bandi, C. Affolderbach, C. E. Calosso, and G. Mileti, “High-performance laser-pumped rubidium frequency standard for satellite navigation,” *Electronics Letters*, vol. 47, pp. 698–699, June 2011.
- [18] S. Micalizio, A. Godone, F. Levi, and C. Calosso, “Pulsed optically pumped rb 87 vapor cell frequency standard: A multilevel approach,” *Physical Review A*, vol. 79, no. 1, p. 013403, 2009.
- [19] J. Vanier and L.-G. Bernier, “On the signal-to-noise ratio and short-term stability of passive rubidium frequency standards,” *IEEE Transactions on Instrumentation and Measurement*, vol. IM-30, no. 4, pp. 277–282, 1981.
- [20] F. G. Major, *The Quantum Beat*, vol. 1. Springer, New York, USA, 2010.
- [21] A. Godone, S. Micalizio, F. Levi, and C. Calosso, “Microwave cavities for vapor cell frequency standards,” *Review of Scientific Instruments*, vol. 82, no. 7, 2011.
- [22] P. Collin and R. Collin, *Foundations for Microwave Engineering*. IEEE Press Series on Electromagnetic Wave Theory, John Wiley & Sons Australia, Limited, 2004.
- [23] L. Felsen and N. Marcuvitz, *Radiation and Scattering of Waves*. IEEE Press Series on Electromagnetic Wave Theory, Wiley, 1994.
- [24] N. Marcuvitz and I. of Electrical Engineers, *Waveguide Handbook*. Electromagnetics and Radar Series, P. Peregrinus, 1951.
- [25] D. Pozar, *Microwave Engineering, 4th Edition*. Wiley, 2011.
- [26] P. Böhi, M. F. Riedel, T. W. Hänsch, and P. Treutlein, “Imaging of microwave fields using ultracold atoms,” *Applied Physics Letters*, vol. 97, no. 5, pp. 10–13, 2010.
- [27] G. Mei, D. Zhong, S. An, F. Zhao, F. Qi, F. Wang, G. Ming, W. Li, and P. Wang, “Main features of space rubidium atomic frequency standard for beidou satellites,” in *2016 European Frequency and Time Forum (EFTF)*, pp. 1–4, April 2016.

- 
- [28] S. Li, Q. X. Yang, and M. B. Smith, "Rf coil optimization: Evaluation of b1 field homogeneity using field histograms and finite element calculations," *Magnetic Resonance Imaging*, vol. 12, no. 7, pp. 1079 – 1087, 1994.
  - [29] D. Goujon, P. Rochat, P. Mosset, D. Boving, A. Perri, J. Rochat, N. Ramanan, D. Simonet, X. Vernez, S. Froidevaux, and G. Perruchoud, "Development of the space active hydrogen maser for the aces mission," in *EFTF-2010 24th European Frequency and Time Forum*, pp. 1–6, April 2010.
  - [30] A. Jones, *Splitting The Second: The Story of Atomic Time*. CRC Press, 2000.
  - [31] Q. Wang, Z. Zhai, W. Zhang, and C. Lin, "An experimental study for the compact hydrogen maser with a TE<sub>111</sub> septum cavity," *IEEE Transactions on Ultrasonics, Ferroelectrics, and Frequency Control*, vol. 47, pp. 197–200, Jan 2000.
  - [32] J. Deng, "Subminiature microwave cavity for atomic frequency standards," in *Proceedings of the 2001 IEEE International Frequency Control Symposium and PDA Exhibition (Cat. No.01CH37218)*, pp. 85–88, 2001.
  - [33] T. Kwon and H. Williams, "Cavity resonator for atomic frequency standard," Jan. 22 1985. US Patent 4,495,478.
  - [34] T. Sphicopoulos, L.-G. Bernier, and F. Gardiol, "Theoretical basis for the design of the radially stratified dielectric-loaded cavities used in miniaturised atomic frequency standards," in *Microwaves, Optics and Antennas, IEE Proceedings H*, vol. 13J, pp. 94–98, April 1984.
  - [35] M. Violetti, M. Pellaton, C. Affolderbach, F. Merli, J. F. Zürcher, G. Miletì, and A. K. Skrivervik, "The microloop-gap resonator: A novel miniaturized microwave cavity for double-resonance rubidium atomic clocks," *IEEE Sensors Journal*, vol. 14, pp. 3193–3200, Sept 2014.
  - [36] J. G. Hartnett, M. E. Tobar, P. L. Stanwix, T. Morikawa, D. Cros, and O. Piquet, "Designs of a microwave te/sub 011/ mode cavity for a space borne h-maser," *IEEE Transactions on Ultrasonics, Ferroelectrics, and Frequency Control*, vol. 52, pp. 1638–1643, Oct 2005.
  - [37] P. Rochat, F. Droz, P. Mosset, G. Barmaverain, Q. Wang, D. Boving, L. Mattioni, M. Belloni, M. Gioia, U. Schmidt, T. Pike, and F. Emma, "The onboard galileo rubidium and passive maser, status and performance," in *Proceedings of the 2005 IEEE International Frequency Control Symposium and Exposition, 2005.*, pp. 26–32, Aug 2005.
  - [38] B. Xia, D. Zhong, S. An, and G. Mei, "Characteristics of a novel kind of miniaturized cavity-cell assembly for rubidium frequency standards," *IEEE Transactions on Instrumentation and Measurement*, vol. 55, pp. 1000–1005, June 2006.
  - [39] H. Qiang, L. Wenbing, H. Shengguo, L. Jianfeng, W. Pengfei, and M. Ganghua, "A physics package for rubidium atomic frequency standard with a short-term stability of  $2.4 \times 10^{-13} \tau^{-\frac{1}{2}}$ ," *Review of Scientific Instruments*, vol. 87, no. 12, p. 123111, 2016.

## Bibliography

---

- [40] Y. Koyama, H. Matsuura, K. Atsumi, Y. Nakajima, and K. Chiba, "An ultra-miniature rubidium frequency standard with two-cell scheme," in *Proceedings of the 1995 IEEE International Frequency Control Symposium (49th Annual Symposium)*, pp. 33–38, May 1995.
- [41] J. Deng, "Subminiature microwave cavity," Oct. 17 2000. US Patent 6,133,800.
- [42] H. E. Williams, T. M. Kwon, and T. McClelland, "Compact rectangular cavity for rubidium vapor cell frequency standards," in *37th Annual Symposium on Frequency Control*, pp. 12–17, June 1983.
- [43] T. Morikawa, K. Takahei, M. Uehara, K. Mori, and M. Tsuda, "Design analysis of a sapphire loaded cavity for a spaceborne hydrogen maser," in *Conference on Precision Electromagnetic Measurements. Conference Digest. CPEM 2000 (Cat. No.00CH37031)*, pp. 50–51, May 2000.
- [44] L.-G. Bernier, "Preliminary design and breadboarding of a compact space qualified hydrogen maser based on a sapphire loaded microwave cavity," in *Proc. 8th European Frequency and Time Forum, Munich*, pp. 965–980, March 1994.
- [45] Y. Koyama, H. Matsuura, K. Atsumi, K. Nakamuta, M. Sakai, and I. Maruyama, "An ultra-miniature rubidium frequency standard," in *Proceedings of the 2000 IEEE/EIA International Frequency Control Symposium and Exhibition (Cat. No.00CH37052)*, pp. 694–699, 2000.
- [46] H. Peters, "Atomic standard with reduced size and weight," Oct. 31 1978. US Patent 4,123,727.
- [47] H. E. Peters, "Small, very small, and extremely small hydrogen masers," in *32nd Annual Symposium on Frequency Control*, pp. 469–476, May 1978.
- [48] A. Belyaev and V. Savin, "Calculation and analysis of frequency properties of special axisymmetric resonators of hydrogen quantum frequency discriminators," *Meas. Tech. (Engl. Transl.); (United States)*, vol. 30:2, Jul 1987.
- [49] T. Sphicopoulos and F. Gardiol, "Slotted tube cavity: a compact resonator with empty core," *IEE Proceedings H - Microwaves, Antennas and Propagation*, vol. 134, pp. 405–410, October 1987.
- [50] H. T. M. Wang, J. B. Lewis, and S. B. Crampton, "Compact cavity for hydrogen frequency standard," in *33rd Annual Symposium on Frequency Control*, pp. 543–548, May 1979.
- [51] L. Mattioni *et al.*, "The developement of a passive hydrogen maser clock for the galileo navigation system," in *34th Annual Precise Time and Time Interval (PTTI) Meeting*, December 2002.



- 
- [52] P. Berthoud, I. Pavlenko, Q. Wang, and H. Schweda, "The engineering model of the space passive hydrogen maser for the european global navigation satellite system galileo," in *IEEE International Frequency Control Symposium and PDA Exhibition Jointly with the 17th European Frequency and Time Forum, 2003. Proceedings of the 2003*, pp. 90–94, May 2003.
- [53] Q. Wang, P. Mosset, F. Droz, P. Rochat, and G. Busca, "Verification and optimization of the physics parameters of the onboard galileo passive hydrogen maser," in *Proceedings of the 38th Annual Precise Time and Time Interval Systems and Applications Meeting*, pp. 81–94, December 2006.
- [54] A. Belyaev *et al.*, "Passive hydrogen maser—prospective glonass satellite clocks," in *6th International Symposium "Metrology of Time And Space"*, 2012.
- [55] G. Mileti, I. Rueedi, and H. Schweda, "Line inhomogeneity effects and power shift in miniaturized rubidium frequency standards," in *ESA Special Publication* (J. J. Hunt, ed.), vol. 340 of *ESA Special Publication*, June 1992.
- [56] H. Schweda, G. Busca, and P. Rochat, "Atomic frequency standard," Feb. 7 1995. US Patent 5,387,881.
- [57] X. Huang, B. Xia, D. Zhong, S. An, X. Zhu, and G. Mei, "A microwave cavity with low temperature coefficient for passive rubidium frequency standards," in *Proceedings of the 2001 IEEE International Frequency Control Symposium and PDA Exhibition (Cat. No.01CH37218)*, pp. 105–107, 2001.
- [58] J. Hu, B. Xia, Y. Xie, Q. Wang, D. Zhong, S. An, and G. Mei, "A subminiature microwave cavity for rubidium atomic frequency standards," in *2007 IEEE International Frequency Control Symposium Joint with the 21st European Frequency and Time Forum*, pp. 599–601, May 2007.
- [59] S. Kang *et al.*, "Study of the physics package for high performance rubidium frequency standards," in *Proceedings of the China Satellite Navigation Conference (CSNC)*, pp. 563–570, 2012.
- [60] N. R. Wang, R. F. Yang, T. Z. Zhou, and L. S. Gao, "Frequency–temperature compensated sapphire loaded cavity for compact hydrogen masers," *Metrologia*, vol. 45, no. 5, p. 534, 2008.
- [61] R. f. Yang, T. z. Zhou, H. b. Chen, N. r. Wang, and L. s. Gao, "A new method to reduce frequency-temperature coefficient of sapphire-loaded cavities for compact hydrogen masers," *IEEE Transactions on Ultrasonics, Ferroelectrics, and Frequency Control*, vol. 57, pp. 583–586, March 2010.
- [62] H. Chen, J. Li, Y. Liu, and L. Gao, "A study on the frequency–temperature coefficient of a microwave cavity in a passive hydrogen maser," *Metrologia*, vol. 49, no. 6, p. 816, 2012.

## Bibliography

---

- [63] M. Gharavipour, A. E. Ivanov, C. Affolderbach, A. K. Skrivervik, and M. G., “Microwave cavity characterization for rubidium frequency standards,” in *2016 European Frequency and Time Forum (EFTF)*, April 2016.
- [64] G. A. Rinard and G. R. Eaton, “Loop-gap resonators,” in *Biomedical EPR, Part B: Methodology, Instrumentation, and Dynamics*, pp. 19–52, Springer, 2005.
- [65] A. Webb, “Cavity- and waveguide-resonators in electron paramagnetic resonance, nuclear magnetic resonance, and magnetic resonance imaging,” *Progress in Nuclear Magnetic Resonance Spectroscopy*, vol. 83, pp. 1 – 20, 2014.
- [66] J. Mispelter and M. Lupu, “Homogeneous resonators for magnetic resonance: A review,” *Comptes Rendus Chimie*, vol. 11, no. 4–5, pp. 340 – 355, 2008. {GERM} 2007.
- [67] H. J. Schneider and P. Dullenkopf, “Slotted tube resonator: A new nmr probe head at high observing frequencies,” *Review of Scientific Instruments*, vol. 48, no. 1, pp. 68–73, 1977.
- [68] W. N. Hardy and L. A. Whitehead, “Split-ring resonator for use in magnetic resonance from 200–2000 mhz,” *Review of Scientific Instruments*, vol. 52, no. 2, pp. 213–216, 1981.
- [69] G. Collins, *Microwave magnetrons*. Radiation Laboratory series, McGraw-Hill Book Co., 1948.
- [70] R. Feynman, R. Leighton, and M. Sands, *The Feynman Lectures on Physics*. No. v. 2 in The Feynman Lectures on Physics, Addison-Wesley, 1963.
- [71] W. Froncisz and J. S. Hyde, “The loop-gap resonator: a new microwave lumped circuit esr sample structure,” *Journal of Magnetic Resonance (1969)*, vol. 47, no. 3, pp. 515 – 521, 1982.
- [72] M. Mehdizadeh, T. K. Ishii, J. S. Hyde, and W. Froncisz, “Loop-gap resonator a lumped mode microwave resonant structure,” *IEEE Transactions on Microwave Theory and Techniques*, vol. 31, pp. 1059–1064, Dec 1983.
- [73] W. Froncisz, T. Oles, and J. S. Hyde, “Q-band loop-gap resonator,” *Review of Scientific Instruments*, vol. 57, no. 6, pp. 1095–1099, 1986.
- [74] S. Pfenninger, J. Forrer, A. Schweiger, and T. Weiland, “Bridged loop-gap resonator: A resonant structure for pulsed esr transparent to high-frequency radiation,” *Review of Scientific Instruments*, vol. 59, no. 5, pp. 752–760, 1988.
- [75] W. Piasecki and W. Froncisz, “Field distributions in loop-gap resonators,” *Measurement Science and Technology*, vol. 4, no. 12, p. 1363, 1993.
- [76] M. Mehdizadeh and T. K. Ishii, “Electromagnetic field analysis and calculation of the resonance characteristics of the loop-gap resonator,” *IEEE Transactions on Microwave Theory and Techniques*, vol. 37, pp. 1113–1118, Jul 1989.

- 
- [77] A. Sotgiu, "Resonator design for in vivo esr spectroscopy," *Journal of Magnetic Resonance* (1969), vol. 65, no. 2, pp. 206 – 214, 1985.
- [78] G. Rinard, R. Quine, S. Eaton, G. Eaton, and W. Froncisz, "Relative benefits of overcoupled resonators vs inherently low-q resonators for pulsed magnetic resonance," *Journal of Magnetic Resonance, Series A*, vol. 108, no. 1, pp. 71 – 81, 1994.
- [79] W. Piasecki, W. Froncisz, and W. L. Hubbell, "A rectangular loop-gap resonator for epr studies of aqueous samples," *Journal of Magnetic Resonance*, vol. 134, no. 1, pp. 36 – 43, 1998.
- [80] W. Piasecki, W. Froncisz, and J. S. Hyde, "Bimodal loop-gap resonator," *Review of Scientific Instruments*, vol. 67, no. 5, pp. 1896–1904, 1996.
- [81] C. P. Lin, M. K. Bowman, and J. R. Norris, "A folded half-wave resonator for esr spectroscopy," *Journal of Magnetic Resonance* (1969), vol. 65, no. 2, pp. 369 – 374, 1985.
- [82] J. Forrer, S. Pfenninger, J. Eisenegger, and A. Schweiger, "A pulsed endor probehead with the bridged loop-gap resonator: Construction and performance," *Review of Scientific Instruments*, vol. 61, no. 11, pp. 3360–3367, 1990.
- [83] M. Ono, T. Ogata, K.-C. Hsieh, M. Suzuki, E. Yoshida, and H. Kamada, "L-band esr spectrometer using a loop-gap resonator for in vivo analysis," *Chemistry Letters*, vol. 15, no. 4, pp. 491–494, 1986.
- [84] F. Momo, A. Sotgiu, and R. Zonta, "On the design of a split ring resonator for esr spectroscopy between 1 and 4 ghz," *Journal of Physics E: Scientific Instruments*, vol. 16, no. 1, p. 43, 1983.
- [85] B. T. Ghim, G. A. Rinard, R. W. Quine, S. S. Eaton, and G. R. Eaton, "Design and fabrication of copper-film loop-gap resonators," *Journal of Magnetic Resonance, Series A*, vol. 120, no. 1, pp. 72 – 76, 1996.
- [86] M. Mehring and F. Freysoldt, "A slotted tube resonator (str) for pulsed esr and odmr experiments," *Journal of Physics E: Scientific Instruments*, vol. 13, no. 8, p. 894, 1980.
- [87] N. Benabdallah, N. Benahmed, B. Benyoucef, R. Bouhmidi, and M. Khelif, "Electromagnetic analysis of the slotted-tube resonator with a circular cross section for mri applications," *Physics in medicine and biology*, vol. 52, no. 16, p. 4943, 2007.
- [88] F. R. da Silva, J. C. Sartori, M. A. Romero, and O. R. Nascimento, "Design and characterization of bridged loop-gap resonators for use in electron paramagnetic resonance measurements," *Review of Scientific Instruments*, vol. 79, no. 1, p. 016104, 2008.
- [89] M. F. Koskinen and K. R. Metz, "The concentric loop-gap resonator—a compact, broadly tunable design for nmr applications," *Journal of Magnetic Resonance* (1969), vol. 98, no. 3, pp. 576 – 588, 1992.

## Bibliography

---

- [90] A. Sotgiu and G. Gualtieri, "Cavity resonator for in vivo esr spectroscopy," *Journal of Physics E: Scientific Instruments*, vol. 18, no. 11, p. 899, 1985.
- [91] R. L. Wood, W. Froncisz, and J. S. Hyde, "The loop-gap resonator. ii. controlled return flux three-loop, two-gap microwave resonators for endor and esr spectroscopy," *Journal of Magnetic Resonance (1969)*, vol. 58, no. 2, pp. 243 – 253, 1984.
- [92] J. W. Sidabras, R. R. Mett, W. Froncisz, T. G. Camenisch, J. R. Anderson, and J. S. Hyde, "Multipurpose epr loop-gap resonator and cylindrical te<sub>011</sub> cavity for aqueous samples at 94ghz," *Review of Scientific Instruments*, vol. 78, no. 3, p. 034701, 2007.
- [93] J. S. HYDE and W. FRONCISZ, "ch7 - loop gap resonators," in *Advanced EPR* (A. Hoff, ed.), pp. 277 – 305, Amsterdam: Elsevier, 1989.
- [94] T. Ichikawa, H. Yoshida, and J. Westerling, "Coupling structure for the loop-gap resonator," *Journal of Magnetic Resonance (1969)*, vol. 85, no. 1, pp. 132 – 136, 1989.
- [95] R. R. Mett, J. W. Sidabras, and J. S. Hyde, "Coupling of waveguide and resonator by inductive and capacitive irises for epr spectroscopy," *Applied Magnetic Resonance*, vol. 35, no. 2, pp. 285–318, 2009.
- [96] R. Sorrentino and T. Itoh, "Transverse resonance analysis discontinuities of finline discontinuities," *IEEE Transactions on Microwave Theory and Techniques*, vol. 32, pp. 1633–1638, Dec 1984.
- [97] C. W. Kuo and T. Itoh, "Characterization of the coplanar waveguide step discontinuity using the transverse resonance method," in *1989 19th European Microwave Conference*, pp. 662–665, Sept 1989.
- [98] G. M. A. K. S. Anton E. Ivanov, Christoph Affolderbach, "Design of atomic clock cavity based on a loop-gap geometry and modified boundary conditions (accepted)," *International Journal of Wireless and Microwave Technologies*, 2017.
- [99] P. Böhi, M. F. Riedel, T. W. Hänsch, and P. Treutlein, "Imaging of microwave fields using ultracold atoms," *Applied Physics Letters*, vol. 97, no. 5, p. 051101, 2010.
- [100] P. Böhi and P. Treutlein, "Simple microwave field imaging technique using hot atomic vapor cells," *Applied Physics Letters*, vol. 101, no. 18, p. 181107, 2012.
- [101] A. Horsley, G.-X. Du, M. Pellaton, C. Affolderbach, G. Mileti, and P. Treutlein, "Imaging of relaxation times and microwave field strength in a microfabricated vapor cell," *Phys. Rev. A*, vol. 88, p. 063407, Dec 2013.
- [102] C. Affolderbach, G. X. Du, T. Bandi, A. Horsley, P. Treutlein, and G. Mileti, "Imaging microwave and dc magnetic fields in a vapor-cell rb atomic clock," *IEEE Transactions on Instrumentation and Measurement*, vol. 64, pp. 3629–3637, Dec 2015.

- 
- [103] A. Ivanov, T. Bandi, G. X. Du, A. Horsley, C. Affolderbach, P. Treutlein, G. Mileti, and A. K. Skrivervik, "Experimental and numerical study of the microwave field distribution in a compact magnetron-type microwave cavity," in *2014 European Frequency and Time Forum (EFTF)*, pp. 208–211, June 2014.
- [104] A. E. Ivanov, C. Affolderbach, G. Mileti, and A. K. Skrivervik, "Study of field misalignment in a cavity used for atomic clock applications," in *2016 URSI International Symposium on Electromagnetic Theory (EMTS)*, pp. 308–311, Aug 2016.
- [105] Y. Millot and P. P. Man, "Active and passive rotations with euler angles in nmr," *Concepts in Magnetic Resonance Part A*, vol. 40A, no. 5, pp. 215–252, 2012.
- [106] A. E. Ivanov, "Microwave Cavity Characterization for Rubidium Frequency Standards," in *30th European Frequency and Time Forum EFTF 2016*, 2016.
- [107] A. P. Feresidis, G. Goussetis, S. Wang, and J. C. Vardaxoglou, "Artificial magnetic conductor surfaces and their application to low-profile high-gain planar antennas," *IEEE Transactions on Antennas and Propagation*, vol. 53, pp. 209–215, Jan 2005.
- [108] D. Dancila, X. Rottenberg, H. A. C. Focant, N. and Tilmans, W. De Raedt, and I. Huynen, "Compact cavity resonators using high impedance surfaces," *Applied Physics A*, vol. 103, no. 3, pp. 799–804, 2011.
- [109] R. R. Mett, W. Froncisz, and J. S. Hyde, "Axially uniform resonant cavity modes for potential use in electron paramagnetic resonance spectroscopy," *Review of Scientific Instruments*, vol. 72, no. 11, p. 4188, 2001.
- [110] J. R. Anderson, R. R. Mett, and J. S. Hyde, "Cavities with axially uniform fields for use in electron paramagnetic resonance: II. Free space generalization," *Review of Scientific Instruments*, vol. 73, no. 8, p. 3027, 2002.
- [111] J. S. Hyde, R. R. Mett, and J. R. Anderson, "Cavities with axially uniform fields for use in electron paramagnetic resonance. III. Re-entrant geometries," *Review of Scientific Instruments*, vol. 73, no. 11, p. 4003, 2002.
- [112] R. R. Mett, J. W. Sidabras, and J. S. Hyde, "Uniform radio frequency fields in loop-gap resonators for epr spectroscopy," *Applied Magnetic Resonance*, vol. 589, pp. 573–589, 2007.
- [113] I. Gurman, Y. Soreq, R. Shavit, M. Givon, G. Aviv, D. Groswasser, and R. Folman, "Dual frequency cavity resonator for atomic manipulation and spectroscopy," in *Microwaves, Communications, Antennas and Electronics Systems, 2009. COMCAS 2009. IEEE International Conference on*, pp. 1–6, Nov 2009.
- [114] G. Pisano, P. A. R. Ade, and C. Tucker, "Experimental realization of an achromatic magnetic mirror based on metamaterials," *Appl. Opt.*, vol. 55, pp. 4814–4819, Jun 2016.

## Bibliography

---

- [115] Y. Sakamoto, H. Hirata, and M. Ono, "Design of a multicoupled loop-gap resonator used for pulsed electron paramagnetic resonance measurements," *IEEE Transactions on Microwave Theory and Techniques*, vol. 43, pp. 1840–1847, Aug 1995.
- [116] R. Li and K. Gibble, "Phase variations in microwave cavities for atomic clocks," *Metrologia*, vol. 41, no. 6, p. 376, 2004.
- [117] A. Godone and S. Micalizio, "Phase-shift in vapor cell and compact cold-atom frequency standards," *ArXiv e-prints*, May 2017.
- [118] R. Sorrentino, P. Martin-Iglesias, O. A. Peverini, and T. M. Weller, "Additive manufacturing of radio-frequency components [scanning the issue]," *Proceedings of the IEEE*, vol. 105, pp. 589–592, April 2017.

## List of publications

- [119] A. E. Ivanov, C. Affolderbach, G. Mileti, and A. K. Skrivervik, “Design of atomic clock cavity based on a loop-gap geometry and modified boundary conditions (accepted),” *International Journal of Wireless and Microwave Technologies*, 2017.
- [120] A. E. Ivanov, A. K. Skrivervik, C. Affolderbach, and G. Mileti, “Compact microwave cavity with increased magnetic field homogeneity,” in *2016 10th European Conference on Antennas and Propagation (EuCAP)*, pp. 1–5, April 2016.
- [121] M. Gharavipour, A. E. Ivanov, C. Affolderbach, A. K. Skrivervik, and M. G., “Microwave cavity characterization for rubidium frequency standards,” in *2016 European Frequency and Time Forum (EFTF)*, April 2016.
- [122] A. Ivanov, T. Bandi, G. X. Du, A. Horsley, C. Affolderbach, P. Treutlein, G. Mileti, and A. K. Skrivervik, “Experimental and numerical study of the microwave field distribution in a compact magnetron-type microwave cavity,” in *2014 European Frequency and Time Forum (EFTF)*, pp. 208–211, June 2014.
- [123] A. E. Ivanov, C. Affolderbach, G. Mileti, and A. K. Skrivervik, “Study of field misalignment in a cavity used for atomic clock applications,” in *2016 URSI International Symposium on Electromagnetic Theory (EMTS)*, pp. 308–311, Aug 2016.
- [124] A. Ivanov, C. Affolderbach, G. Mileti, and A. Skrivervik, “Study of the misalignment between electromagnetic fields interacting with rb atoms in a cavity with losses,” in *2016 European Frequency and Time Forum (EFTF)*, 2016.
- [125] A. E. Ivanov and A. K. Skrivervik, “Design of resonance structures for the next generation vapor cell atomic clocks,” in *COST IC1102 Vista 8th WG Meeting & Technical Workshop, Sofia, Bulgaria*.

